DISSERTATION

submitted to the
Combined Faculty of Mathematics, Engineering
and Natural Sciences
of Heidelberg University, Germany
for the degree of
Doctor of Natural Sciences

Put forward by
Eleonora Lippi
born in: Firenze, Italy

Oral examination: October 17th, 2024

^{133}Cs ATOMS IN A ^{6}Li FERMI SEA FOR EXPLORING POLARON PHYSICS IN THE HEAVY IMPURITY LIMIT

Referees: Prof. Dr. Matthias Weidemüller
Prof. Dr. Markus Oberthaler

Abstract. The thesis deals with the experimental study of dilute ultracold gases of ^{133}Cs atoms mixed with a degenerate Fermi Sea of ^{6}Li atoms. It focuses on the problem of the coupling of an impurity to a surrounding quantum bath, which can be described as a quasi-particle known as polaron. The large mass imbalance between the impurity (Cs) and the bath (Li) leads to unique many-body phenomena, but also poses significant experimental challenges for mixing the two species at ultracold temperature where Li is quantum degenerate. In this work, we realize a mixture of a degenerate Li Fermi Sea and a dilute thermal Cs gas by adopting a bichromatic trapping approach and implementing a tightly confining and movable single beam trap for Li at the Cs tune-out wavelength. This allows the sequential preparation of the Li Fermi Sea, which can be overlapped with Cs atoms in a controlled manner, compensating for the differential gravitational sag between the two species. To probe the Fermi-polaron scenario, an optical spectroscopic method based on two-photon Raman transitions between the two lowest Zeeman states of Cs is implemented. Guided by theoretical predictions of the polaron spectral function, ejection spectroscopy on Cs impurities is performed to map the polaron energy spectrum as a function of interaction strength near a Li-Cs Feshbach resonance at 890 G, which provides high tunability of the interspecies interactions. Limitations to this kind of experiments and strategies to overcome them are discussed, laying the groundwork for exploring polaron physics with heavy mass impurities.

Zusammenfassung. Die Arbeit befasst sich mit der experimentellen Untersuchung verdünnter ultrakalter Gase aus ^{133}Cs-Atomen, die mit einem entarteten Fermi-See aus ^{6}Li-Atomen gemischt sind. Im Mittelpunkt steht das Problem der Kopplung einer Verunreinigung an ein umgebendes Quantenbad, das als Quasiteilchen, als Polaron, beschrieben werden kann. Das große Massenungleichgewicht zwischen der Verunreinigung (Cs) und dem Bad (Li) führt zu einzigartigen Vielkörperphänomenen, stellt aber auch eine große experimentelle Herausforderung für die Mischung der beiden Spezies bei ultrakalten Temperaturen dar, bei denen Li quantendegeneriert ist. In dieser Arbeit realisieren wir eine Mischung aus einem entarteten Li-Fermi-See und einem verdünnten thermischen Cs-Gas, indem wir eine bichromatische Falle verwenden, wofür wir eine eng begrenzte und bewegliche optische Einzelstrahlfalle für Li bei der Cs tune-out-Wellenlänge implementieren. Dies ermöglicht die sequenzielle Präparation eines Li-Fermi-Sees, der auf kontrollierte Weise mit Cs-Atomen überlagert werden kann, wodurch die unterschiedliche gravitative Verschiebung zwischen den beiden Spezies kompensiert wird. Um das Fermi-Polaron-Szenario mithilfe optischer Spektroskopie zu untersuchen, wird ein Zwei-Photonen-Raman-Übergang zwischen den beiden niedrigsten Zeeman-Zuständen von Cs eingesetzt. Geleitet von theoretischen Vorhersagen der Polaron-Spektralfunktion wird Ejektionsspektroskopie an Cs-Verunreinigungen durchgeführt, um das Energiespektrum des Polarons als Funktion der Wechselwirkungsstärke abzubilden. Dabei ermöglicht eine Li-Cs-Feshbach-Resonanz bei 890 G die hohe Einstellbarkeit der Wechselwirkung zwischen den Spezies. Beschränkungen dieser Art von Experimenten und Möglichkeiten zu deren Überwindung werden erörtert, wodurch die Grundlage für die Erforschung der Polaronphysik mit schweren Verunreinigungen geschaffen wird.

Parts of this thesis are based on the following manuscript and publication:

- **A platform for the creation and manipulation of a mixture of ^{6}Li and ^{133}Cs atoms**
  E. Lippi *et al.*, Manuscript in preparation
- **Scattering of two heavy Fermi polarons: Resonances and quasibound states**
  T. Enss, B. Tran, M. Rautenberg, M. Gerken, E. Lippi, M. Drescher, B. Zhu, M. Weidemüller, and M. Salmhofer, Physical Review A **102**, 063321 (2020)

The author furthermore contributed to the following publications:

- **Anomalous loss behavior in a single-component Fermi gas close to a p-wave Feshbach resonance**
  K. Welz, M. Gerken, B. Zhu, E. Lippi, M. Rautenberg, L. Chomaz, and M. Weidemüller, Physical Review A **107**, 053310 (2023)
- **Fermions Meet Two Bosons—the Heteronuclear Efimov Effect Revisited**
  B. Tran, M. Rautenberg, M. Gerken, E. Lippi, B. Zhu, J. Ulmanis, M. Drescher, M. Salmhofer, T. Enss, and M. Weidemüller, Brazilian Journal of Physics **51**, 316–322 (2021)

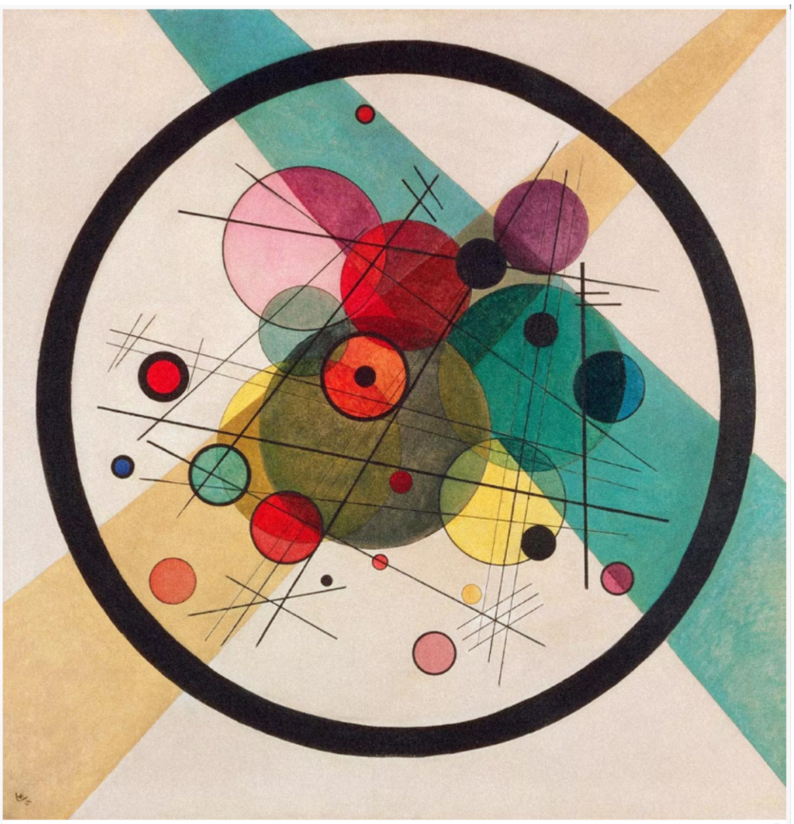

Vasily Kandinsky - "'Circles in a Circle"' (1923)
98.7 x 95.6 cm, Oil on canvas
© Philadelphia Museum of Art

"Siamo una strana pattuglia di moderni esploratori, quelli che la gente chiama scienziati, truppe speciali della conoscenza che l'umanità manda in avanscoperta a capire come funziona la natura. Ai confini della conoscenza ti trovi da solo, in un mondo in cui riecheggiano solo le intuizioni dei poeti e le voci dei pazzi. Sono gli unici esseri umani che, come noi, non hanno paura di perlustrare i luoghi sconosciuti. Anche noi, come loro, siamo funanboli che corrono sul filo senza gancio di sicurezza."

Guido Tonelli - "'La nascita imperfetta delle cose"'

Contents

Introduction

Understanding the behavior of many-body systems requires to consider the complex influence that each particle has on the behavior of all the others. The problem of strongly coupled many-body systems can be described by using the concept of elementary excitations, which are often divided into the two categories of *collective excitations* and *quasi-particles* [Mattuck, 1976]. The *quasi-particles* identify a special kind of elementary excitations that resemble real particles quite closely. Nevertheless, the properties of the real particle, such as energy, effective mass, lifetime and particle-particle interactions are modified due to the interaction with the many-body environment. In this picture, the overlap between the quasi-particle and the bare particle is encoded in the *quasi-particle weight*. The quasi-particle concept has been used by Landau [Landau, 1933] to describe electrons interacting with phonons in crystals. The electron moving through the ionic crystal lattice displaces the surrounding ions and becomes *dressed* with the phononic excitations of the lattice, resulting in a quasi-particle called *polaron*. More generally, the problem of an impurity coupled to a quantum medium shows similarities with many famous condensed matter problems, such as the Kondo effect [Mahan, 2000], the X-rays singularities in metals [Nozières and De Dominicis, 1969], the mobility of ions [Prokof'ev, 1995] and of ^{4}He [Arias de Saavedra *et al.*, 1994] in ^{3}He. Nowadays, this concept finds applications in many diverse areas of physics, such as semiconductors [Sidler *et al.*, 2017; Muir *et al.*, 2022], conducting polymers [Bredas and Street, 1985; Schott *et al.*, 2019], high-temperature superconductivity [Mott, 1993; Dagotto, 1994] and neutron matter [Forbes *et al.*, 2014; Nakano *et al.*, 2020; Vidaña, 2021].

In the last fifteen years the concept of *polaron* has been applied successfully to describe atomic impurities immersed in either a Bose-Einstein condensate (BEC) or Fermi Sea of ultracold atoms. Indeed, ultracold atoms offer a very well suited playground for polaron physics [Grusdt and Demler, 2016; Schmidt *et al.*, 2018; Scazza *et al.*, 2022] thanks to the great insulation from the external environment, the possibility to exploit the full toolbox provided by atomic physics and to control relevant parameters with high accuracy, such as quantum statistics, impurities concentration and interactions. By experimentally manipulating these parameters, it is possible to study many-body effects that are difficult to access in other systems. First of all, depending on whether the quantum medium consists of fermions or bosons, one speaks of a Fermi or Bose polaron and the impurities create excitation in the medium in the form of Bogoliubov modes or particle-holes excitations, respectively. The Bose polaron is more similar to the solid state physics with the collective phonon excitation of the BEC that can be mapped onto the Hamiltonian of the Fröhlich model [Fröhlich, 1954], whereas the Fermi polaron is rather an exemplary realization of Landau's Fermi liquid theory [Mahan, 2000]. Second, while for the classical solid state polaron the strength of interactions is weak and fixed by nature, the tunability of the interactions via Feshbach resonances [Chin *et al.*, 2010] enables experiments where the coupling between the impurity and the medium can be tuned by magnetic fields from weakly [Catani *et al.*, 2012; Rentrop *et al.*, 2016] to strongly interacting regimes [Schirotzek *et al.*, 2009; Kohstall *et al.*, 2012; Jørgensen *et al.*, 2016; Hu *et al.*, 2016; Yan *et al.*, 2020; Etrych *et al.*, 2024]. Third, in contrast to the attosecond timescales typical of condensed matter systems, the degeneracy of the system ensures that all interesting many-body processes occur on the experimentally accessible microsecond timescale, allowing the study the dynamics of impurities in a many-body environment [Cetina *et al.*, 2015, 2016; Skou *et al.*, 2021] as well as the emergence of mestable states with finite lifetime [Scazza *et al.*, 2017; Darkwah Oppong *et al.*, 2019; Skou *et al.*, 2022]. Moreover, by tuning the temperature it was studied how degenerate, i.e. *quantum*, the environment needs to be to observe the emergence of polarons [Yan *et al.*, 2019], and by using tailored optical potentials it was also possible to obtain information on how much reduced dimensionality influences the energy of the quasi-particle [Zhang *et al.*, 2012; Koschorreck *et al.*, 2012]. Recently, interactions between polarons [Baroni *et al.*, 2024a] as well as regimes of transitions between polarons and molecules in Fermi polarons [Ness *et al.*, 2020] have also been studied by varying the impurity concentration and by adapting sophisticated spectroscopic schemes, respectively.

Most of the experiments cited above were performed with homonuclear mixtures. There, the medium and the impurity belong to the same atomic species but differ in the selected spin state. With the introduction of an asymmetry in the mass between the atomic impurity and the quantum medium, the impurity problem changes qualitatively and new phenomena that do not occur in single species experiments appear [Baroni *et al.*, 2024b]. For lightweight impurities in a Bose gas, signatures of the crossover between few-body and many-body physics are predicted [Levinsen *et al.*, 2015; Sun *et al.*, 2017; Sun and Cui, 2017]. Here, the polaron state is expected to smoothly crossover into a dressed Efimov state. Similarly, lightweight impurities in a Fermi gas are good candidates for observing new types of quasi-particles associated with few-body physics [Mathy *et al.*, 2011; Liu *et al.*, 2022]. In the opposite limit of an infinitely heavy impurity in a Fermi gas, the overlap between the state describing the interacting many-body system and the noninteracting one is expected to vanish, leading to the Anderson *orthogonality catastrophe* [Anderson, 1967; Schmidt *et al.*, 2018]. A similar phenomenon is also expected in a noninteracting Bose gas [Guenther *et al.*, 2021]. Among heteronuclear mixtures, the full Fermi polaron spectrum has been recorded for both Fermi-Fermi mixtures of ^{6}Li-^{40}K [Kohstall *et al.*, 2012; Cetina *et al.*, 2015, 2016] and Fermi-Bose mixtures of ^{6}Li-^{41}K [Fritsche *et al.*, 2021; Baroni *et al.*, 2024a]; the Bose polaron spectrum was instead studied in Fermi-Bose mixtures of ^{87}Rb-^{40}K [Hu *et al.*, 2016] and ^{23}Na-^{40}K [Yan *et al.*, 2020]. However, since the atomic mixtures used so far have moderate mass ratios, the aforementioned phenomena remain largely unexplored.

In this work we study heteronuclear Fermi-Bose quantum mixtures of ^{6}Li and ^{133}Cs atoms. These atomic species exhibit the highest mass ratio among all stable alkali isotopes, thereby providing access to both physically relevant limits of light impurities coupled to a Bose-Einstein condensate and heavy particles coupled to a degenerate Fermi Sea. These are non-trivial paradigms of many-body systems. The very well-suited interplay of Feshbach resonances at high magnetic fields, between 800 G and 1000 G [Repp *et al.*, 2013; Tung *et al.*, 2013; Pires *et al.*, 2014a], potentially allows for the preparation of stable Bose and Fermi polarons, respectively. This mixture has been widely used as a test bed for few-body Efimov physics [Pires *et al.*, 2014b; Tung *et al.*, 2014; Ulmanis *et al.*, 2015, 2016a,b,c; Häfner *et al.*, 2017; Johansen *et al.*, 2017] and p-wave two-body physics [Zhu *et al.*, 2019a,b]. Experiments by [DeSalvo *et al.*, 2017, 2019; Patel *et al.*, 2023] have studied double-degenerate mixtures where the Cs Bose-Einstein condensate is embedded in a Li-Fermi sea. Recently, also Bose-Bose degenerate mixtures of ^{7}Li -^{133}Cs with tunable interactions have been realized [Li *et al.*, 2022; Chen *et al.*, 2023]. However, even though Li-Cs mixtures have been considered in many theoretical studies as an exemplary application of various polaron experiments, for example by Levinsen *et al.* [2015], Sun *et al.* [2017], Christianen *et al.* [2022] and Rose and Schmidt [2022], polarons have not yet been studied experimentally with such a high mass imbalance mixture. The ^{6}Li-^{133}Cs mixture offers intriguing directions of study, including the following three: (i) the study of signatures of Efimov physics in the polaron spectrum, in the Bose polaron scenario, (ii) the study of the breakup of the infinite series of Efimov states due to bath-mediated interactions as well as the occurrence of resonances in the impurity-impurity scattering length, and (iii) many-body dynamics near the orthogonality catastrophe limit for the Fermi polaron scenario. In the following, I will explain these three motivations in more detail and then outline the contents and the structure of this work.

How does many-body polaron physics build up from the few-body system? In the three-body system, it has been observed the existence of peculiar three-body bound states known as Efimov states. Those trimer states, originally proposed in the context of nuclear systems [Efimov, 1970], have been created and observed in ultracold gases in both homonuclear [Kraemer *et al.*, 2006; Williams *et al.*, 2009; Zaccanti *et al.*, 2009; Gross *et al.*, 2009; Pollack *et al.*, 2009; Knoop *et al.*, 2009; Lompe *et al.*, 2010; Nakajima *et al.*, 2010; Roy *et al.*, 2013] and heteronuclear systems [Barontini *et al.*, 2009, 2010; Bloom *et al.*, 2013; Pires, 2014; Tung *et al.*, 2014]. A natural question to ask is whether the few-body Efimov states would persist in a many-body environment. This problem was introduced by Levinsen *et al.* [2015] describing the system by a variational ansatz including the dressing of the impurity by one or two Bogoliubov excitations. The energy of the many-body ground state is influenced by an avoided crossing between the Bose polaron state and a dressed Efimov state. The crossover manifests itself in the quasi-particle weight, which is the overlap between the interacting and non-interacting particle. The favorable conditions for the observation of Efimov physics in the Bose polaron depends on the ratio between two relevant lengthscales, the characteristic size of the Efimov state l_T and the mean distance d between the atoms of the bath [Sun *et al.*, 2017; Sun and Cui, 2017]. The studied systems of ^{39}K-^{39}K [Jørgensen *et al.*, 2016] and ^{40}K-^{87}Rb [Hu *et al.*, 2016] are characterized by large Efimov scaling factors λ, which limit their detection. In these cases, we do not expect any signature of few-body correlations in the many-body observables. Strong signatures are instead expected in Efimov favored systems, as for example the experimentally well studied combinations ^{7}Li-^{87}Rb [Maier *et al.*, 2015] and ^{6}Li-^{133}Cs[Ulmanis *et al.*, 2016b], where the large mass imbalance drastically reduces the Efimov scaling factor λ, thus leading to a dense spectrum of Efimov states and a large binding energy of the ground state trimer. Hence, as calculated in [Sun *et al.*, 2017], it is likely that one of the Efimov states fulfills the condition $l_T \approx d$ and manifests itself in the many-body spectrum.

How does a Fermi Sea mediate the interactions between heavier particles? Contrarily to the Bose polaron case, a crossover between a quasi-particle and a trimer state is not possible in a Fermi Sea because Pauli blocking prevents the formation of bound states. Indeed, by using the Born-Oppenheimer approximation [Nishida, 2009], it has been calculated that, for sufficiently large Fermi momentum, the formation of bound states is suppressed by the presence of the Fermi Sea and the discrete Efimov state is violated [Sun and Cui, 2019; Tran *et al.*, 2021]. However, a new scaling can be formulated including the Fermi momentum as an additional length scale [Sun and Cui, 2019; Tran *et al.*, 2021]. On the other hand, interesting scattering properties arise in this scenario, which at zero-temperature can be solved exactly [Enss *et al.*, 2020]. For weak interactions, the outcome is similar to the results obtained by perturbation theory and it is consistent with experimental findings in ^{6}Li-^{133}Cs [DeSalvo *et al.*, 2019] and ^{87}Rb-^{40}K [Edri *et al.*, 2020] mixtures. For strong interactions, instead, we found, for the first time, a resonant behaviour in the induced scattering length between two heavy bosons in a Fermi Sea. The resonances are found at interspecies scattering lengths at which the Efimov state crosses the scattering continuum in the medium. This repulsive interaction suggests a large suppression of losses and an enhanced stability near resonance. Recent experiments on Bose-Fermi mixtures of ^{23}Na-^{40}K [Yan *et al.*, 2020; Chen *et al.*, 2022] and ^{6}Li-^{133}Cs [Patel *et al.*, 2023] have observed a strong suppression of the losses, which could be explained by our predictions. Moreover, mediated interaction by a Fermi Sea in strongly interacting regimes have been observed recently in both ^{6}Li-^{40}K Fermi-Fermi and ^{6}Li-^{41}K Bose-Fermi mixtures by Baroni *et al.* [2024a]. However, interactions between either Fermi or Bose polarons induced by the medium remain experimentally largely unexplored.

What is the role of the mass of the impurity? On the one hand, as discussed above, lightweight ^{6}Li impurities in the ^{133}Cs bosonic medium is a well suited system for studying the emergence of few-body physics in the many-body polaron spectrum. On the other hand, heavy ^{133}Cs impurities in a ^{6}Li Fermi Sea resembles quite closely the fully solvable problem of an infinitely heavy fixed impurity in a Fermi Sea. In the thermodynamic limit, for infinitely heavy impurity and zero temperature the quasi-particle weight is expected to vanish, leading to the Anderson orthogonality catastrophe [Anderson, 1967]. Although the orthogonality catastrophe is an idealization, its signatures can still be observed in realistic experimental scenarios with finite impurity mass and finite temperature [Knap *et al.*, 2012; Schmidt *et al.*, 2018]. Notably, it results in a universal evolution of the quasi-particle properties during the early-time dynamics following a quench of the interaction. This evolution exhibits a characteristic power-law dependence, where the exponent is determined solely by the strength of the interspecies interaction. The temporal evolution of heavy impurities in a Fermi Sea has been studied for a ^{41}K-^{6}Li mixture by Cetina *et al.* [2015] and Cetina *et al.* [2016]. However, the timescale on which the universal dynamics take place, set by the Fermi energy, is limited by the timescale on which thermal and finite mass effects become relevant. Larger mass ratio, as in a ^{133}Cs-^{6}Li mixture, would allow accessing the power-law scaling behaviour in a larger time window. An impurity of infinite mass can also be realized experimentally by trapping one species with a species-selective potential. Pinning down Li atoms with an optical tweezer realizes the scenario of a heavy impurity in a Bose-Einstein condensate, complementary to the previous case. Here, the real-time dynamics of a Bose-Einstein condensate after a sudden quench has recently been calculated by Drescher *et al.* [2019] using a variational coherent state ansatz and long-lived quantum coherent oscillations are predicted on the repulsive side of the Feshbach resonance. As a consequence, an impurity introduced at a finite velocity exhibits a stop-and-go motion and a characteristic density profile. These deformations have never been observed because, again, they are difficult to access experimentally as they requires the spatial scale of the healing length of the Bose-Einstein condensate to be larger than the period of these density oscillations. Detection might be possible either with high-resolution imaging combined with two-dimensional confinement, or by Bragg spectroscopy on the medium in the presence of impurities.

Overview of the work presented in the thesis. The focus of this thesis is the study of low-density samples of Cs atoms mixed to a degenerate Fermi Sea of Li atoms. In this regime, we aim to spectroscopically probe thermal Cs impurities immersed in a degenerate Fermi gas of Li while tuning the interspecies interactions, in order to map out the Fermi polaron spectrum in a Li-Cs mixture.

A considerable effort has been made in reconstructing the experiment to implement a tightly confining and movable single-beam trap for Li at the Cs tune-out wavelength, which was originally designed to create the Bose polaron scenario allowing to confine Li inside a Cs Bose-Einstein condensate. This trap allowed for the sequential preparation of a Li Fermi gas deep in the degenerate regime that can be overlapped with Cs atoms in a controlled way. A major focus of the design was the resulting symmetry of the two clouds, which allows for the compensation of the relative gravitational sag. This ensures a good spatial overlap at arbitrary temperatures, which is a persistent challenge for atomic mixtures with large mass ratio. After the implementation of this new Li trap, a degradation of the Cs source was observed and a Cs Bose-Einstein condensate could no longer be produced. Since replacing the source would have caused a significant delay, in addition to the delay already caused by the pandemic, we decided to shift the focus of our experimental efforts from the Bose to the Fermi polaron scenario. Nevertheless, we maintained the newly implemented Li trap, as it is versatile and suitable for producing a deeply degenerate Li Fermi sea.

In order to probe the Fermi-polaron scenario, two ingredients are needed:

1. the ability to fine tune the magnetic field strength in the vicinity of favorable interspecies Feshbach resonances,
2. the ability to probe the energy of the impurity as a function of the interaction strength, which is generally done by an energy-selective transfer of the impurity from a non-interacting state to an interacting one or viceversa (*injection* or *ejection* spectroscopy).

Concerning the first point, great efforts have been made to (i) characterize the magnetic field topology in the region where the atoms are confined, (ii) map out the loss signal of interspecies interaction in the vicinity of the broad Li-Cs Feshbach resonances around 888.6 G, and (iii) take into account if and how inelastic two-body loss channels might limit the typical timescale of polaron experiments.

Concerning the second point, after some effort in adapting our existing radio-frequency (RF) setup to the Cs transition frequencies (around 260 MHz at the relevant magnetic fields), we abandoned this approach because it turned out not to be feasible due to bad coupling of the RF fields into our steel vacuum chamber. We have adopted an optical method in which two co-propagating laser beams allow probing two-photon Raman transitions between the two lowest hyperfine states of Cs atoms. Additionally, Raman spectroscopy allows for local addressability of the atomic cloud and for finite momentum-transfer [Veeravalli *et al.*, 2008; Shkedrov *et al.*, 2020], which opens up to investigating polaron momentum-dependent properties [Ness *et al.*, 2020; Diessel *et al.*, 2024] that cannot be studied with RF. The Raman technique on Cs, together with our ability to prepare Li in either of its two lowest hyperfine states via radiofrequency transitions, allows for versatile preparation and interrogation of the mixture in different states. Guided by numerical predictions of the polaron spectral function at finite temperatures calculated by the functional determinant method by our theoretical collaborators, we sought to identify the Fermi polaron signature.

The thesis is organized as follows:

Chapter 1 - A platform for creating an ultracold Li-Cs mixture. Ultracold experiments rely on complex experimental setups. We present the apparatus in Heidelberg designed for cooling, trapping, and manipulating the highly mass-imbalanced mixture made of Li and Cs atoms. Given that the core of this dual-species experiment was built over a decade ago, we quickly review its primary functions and focus on recent updates, including a revision of the performance of the Zeeman slower, the tomography of our magnetic fields for Feshbach tuning of the interparticle interactions and the implementation of a new dipole trap for Li atoms. Indeed, this thesis introduces a new bichromatic approach for trapping both species and implements a tightly confining movable trap for Li at the Cs tune-out wavelength. We then discuss our standard detection tools, such as radiofrequency, microwave, and dual-species absorption imaging, emphasizing their roles in the experiment.

Chapter 2 - Li Fermi Sea with Cs impurities. We describe the experimental realization of the effective mixing sequence for creating a Fermi Sea of Li atoms combined with dilute samples of Cs atoms. First, we review fundamental concepts of Bose and Fermi gases in harmonic potentials as well as basic two-body scattering theory applied to Li-Cs mixtures. Then, we discuss the issues for the creation of ultracold Li-Cs mixtures and outline the main solutions implemented in the course of this work. Therefore, we provide a detailed, step-by-step explanation of our subsequent individual preparation of the two species combined with the bichromatic approach for mixing them. We describe cooling and trapping, first for Li towards the creation of a deeply degenerate Fermi Sea, then for Cs, for the creation of ultracold dilute Cs samples. We describe how we overlap them in a controlled way and cancel the differential gravitational sag. Finally, we examine the loss processes, primarily dominated by Raman spontaneous scattering on Cs atoms at the tune-out wavelength and three-body losses near the Feshbach resonance at 888.6 G. We summarize the highlights and discuss the criticalities of the described mixing procedure and, propose the next steps towards the achievement of a thermalized mixture.

Chapter 3 - Heavy Fermi polarons. We investigate heavy Fermi polarons and detail our detection protocol on Cs impurities. We theoretically compare the case of heavy Cs impurities in a light Li Fermi Sea with the case of an infinite mass impurity. We use the Chevy variational ansatz to calculate the ground state polaron energy at zero temperature for a mass imbalance between the impurity and the bath of $m_I/m_b = 22$ and compare it with the analytical result obtained for the case of an impurity with infinite mass $m_I/m_b = \infty$. Additionally, we discuss numerical predictions of the polaron spectral function at finite temperatures calculated by our theoretical collaborators using the functional determinant method. We then present the implementation for a Li-Cs system, looking at the relevant timescales, at the constraints given by two-body inelastic loss channels and draw conclusions about *ejection* and *injection* spectroscopy schemes. We also introduce the Raman spectroscopy setup, which allows us to address the two lowest hyperfine states of Cs. We provide an example from the first series of measurements based on an ejection spectroscopy protocol aimed at detecting the polaron signal. We discuss the limitations of these experiments and, based on our findings, we propose modifications to the experimental setup to detect the Fermi polaron. Finally, we explore future directions in few- and many-body physics within the Li-Cs system.

Chapter 1

A platform for creating an ultracold Li-Cs mixture

Parts of this chapter are based on the following manuscript:

A platform for the creation and manipulation of a mixture of ^{6}Li and ^{133}Cs atoms
E. Lippi, et *al.* Manuscript in preparation

The Li-Cs experiment in Heidelberg is a dual-species experimental apparatus whose construction has started more than a decade ago. With each generation of Ph.D. students, the experiment has been adapted to overcome the challenges of that generation. The challenge during this Ph.D. work was to produce a mixture of a degenerate atomic sample of either Li or Cs mixed with a dilute and non-degenerate sample of atoms of the other species in strongly interacting regimes, and to develop some of the tools for the characterization of our samples.

In this chapter I introduce our experimental apparatus and describe some of the upgrades and analyses made during my time on the experimental machine. In Sec. 1.1 I will give an overview of the experimental apparatus, using a block diagram for summarizing the functions that the experiment must fulfill. In the other sections, I delve into specific topics. In Sec. 1.2 I describe the characterization of the performance of the existing double-species Zeeman slower, starting from a modeling of the deceleration process. This plays a key role for loading Li and Cs clouds in their respective magneto-optical traps (MOTs). In Sec. 1.3 I describe our optical dipole trap management, focusing on the implementation of a bichromatic scheme based on a tightly confined movable optical trap for Li atoms realized at the Cs tune-out wavelength. In Sec. 1.4 I present how we characterize the homogeneity and calibrate the magnetic fields generated by the homogeneous Feshbach coils. These are important prerequisite for controlling and tuning the intra- and inter-species scattering lengths via magnetic Feshbach resonances. In Sec. 1.5 I describe the detection tools needed for the characterization of ultracold quantum gases and for the detection of polarons, such as imaging detection techniques and spectroscopic setups.

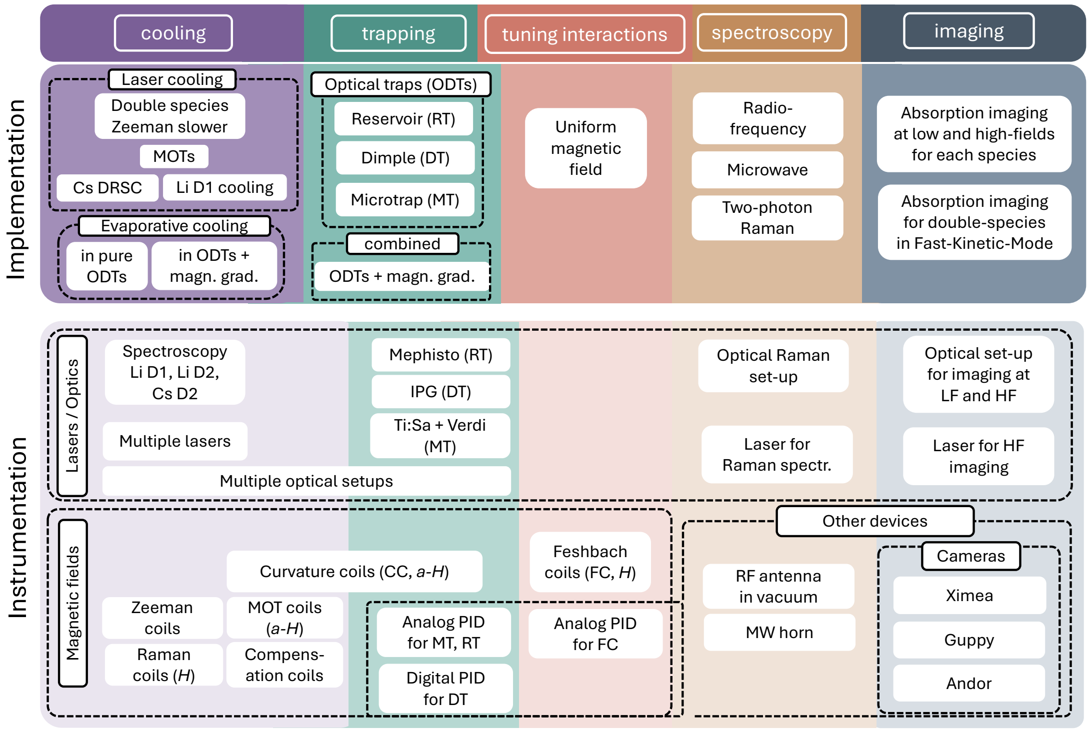

FIGURE 1.1: Block diagram summarizing the complex structure of our experimental apparatus. The block scheme is organized into five vertical sections, each representing a specific function of our experimental apparatus and coded in a different colour: cooling (violet), trapping (green), tuning interactions (orange), spectroscopy (yellow) and imaging (blue). The schema is divided horizontally into two layers. The implementation layer outlines the different techniques and setups used to implement the different functions of the experimental apparatus. The instrumentation layer lists the specific equipment and devices required to realize each implementation of a particular function.

1.1 An overview of a double species experiment

In order to give an overview of the complexity of our experiment, I will follow the block scheme in Fig. 1.1, which summarizes the structure of the experimental apparatus. The block scheme is organized into five vertical sections, each representing a specific function of our experimental apparatus and coded in a different colour: cooling (violet), trapping (green), tuning interactions (orange), spectroscopy (yellow) and imaging (blue). The schema is divided horizontally into two layers called Implementation and Instrumentation. The implementation layer outlines the various techniques and setups used to implement the different functions of the experimental apparatus. The instrumentation layer lists the specific equipment and devices required to realize each implementation of a particular function. In some cases, the same techniques and setups are used to implement different functions, and the same equipment and devices are used for different implementations. The instrumentation consists of external magnetic fields, lasers for cooling, trapping and probing, CCD cameras for detection, source of oscillating electromagnetic fields (radio frequency antenna and microwave horn).

Vacuum apparatus. A schematic overview of the core of the ultra-high vacuum (UHV) apparatus for the production of ultracold ^{6}Li-^{133}Cs mixtures is shown in Fig. 1.2. The two atomic beams are generated by a double-species effusive oven, decelerated by a double-species Zeeman slower consisting of four interleaving helical coils with variable pitch and captured in a magneto-optical trap inside the main experimental chamber by means of a sequential loading scheme. The oven region and the main chamber are connected by two differential pumping stages, allowing for pressure differences between the two parts. We refer the reader to [Repp, 2013] for a more detailed description of our vacuum system.

Double species effusive oven. For the thermal source beam we use an effusive double-species oven with a similar design to the one presented by [Stan and Ketterle, 2005]. It enables element selective control over the fluxes up to ten orders of magnitude, regardless of the difference between vapor pressures of $p_{Li} = 1 \times 10^{-5}$ Torr and $p_{Cs} = 4 \times 10^{-3}$ Torr, at typical operation temperatures of $T_{oven,Li} = 625$ K and $T_{oven,Cs} = 375$ K [Gehm, 2003; Steck, 2023]. The oven is divided into three parts maintained at different temperatures in order to have individual control on fluxes and velocities of the two atomic species [Repp, 2013]. The atomic beams leave the oven through a nozzle with a diameter of 10 mm leading to atomic fluxes of $\Phi_{\mathrm{Li}} = 5 \times 10^{15}$ atoms/s and $\Phi_{\mathrm{Cs}} = 10^{14}$ atoms/s. Note that the velocity distribution in the atomic beams are strongly different for each species, due to the different temperature and mass for Li and Cs atoms.

Cooling. The atomic beam is first decelerated by a double species Zeeman slower, as explained in Sec. 1.2. A detailed characterization of the Zeeman slower can also be found in [Repp, 2013]. Doppler cooling is performed by loading a three-dimensional magneto-optical-trap (MOT). The cooling transitions for both Li and Cs are shown in Fig. 1.3. The Cs-MOT is realized by six individual laser beams coming from different optical fibers. The Li-MOT is realized by three retro-reflected laser beams with a beam diameter that matches the transversal expansion of the atomic beam after Zeeman deceleration. The details on the frequency preparation and laser setup can be found in [Repp, 2013]. We cool both species below their Doppler limit by applying different cooling schemes. The unresolved hyperfine structure of the excited $2^2\mathrm{P}_{3/2}$ state in Li prevents the application of simple sub-Doppler cooling schemes on the D_2 transition and temperatures of standard Li MOTs are limited by the Doppler temperature $T_{\mathrm{Li}} \approx 140\ \mu$K. We apply gray-molasses cooling to achieve samples at a temperature of 40 μK. The optical setup that allow $\mathcal{D}_1$ cooling is described in [Gerken, 2016; Häfner, 2017; Neiczer, 2018]. Details on the loading process after $\mathcal{D}_1$ cooling is detailed in [Neiczer, 2018; Gerken, 2022] and briefly summarized in Sec. 2.2.1. Cs atoms are cooled and spin polarized into their energetically lowest state by applying degenerate Raman sideband cooling (DRSC). The procedure is

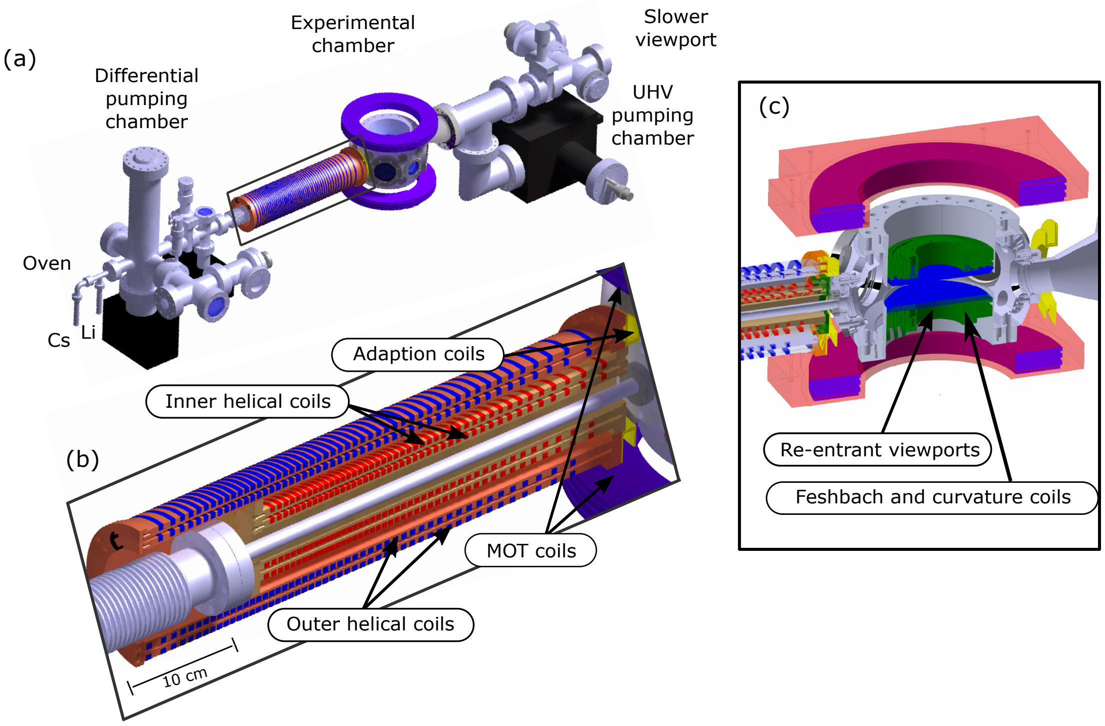

FIGURE 1.2: (a) Experimental apparatus: an atomic beam is generated in the oven chamber and decelerated by a double-species Zeeman slower for the loading of MOTs in the experimental chamber. Various ion pumps (black) in combination with differential pumping stages enable a pressure difference between the oven region and the experimental chamber. (b) Schematic cut through the first part of the Zeeman slower. On the left hand side a schematic of the four helical coils, consisting of two inner ones (red) and two outer ones (blue), is shown. The magnetic fields for the last part of the Zeeman slower are generated by the radial fields of the MOT coils (violet) and a good matching of the fields is obtained by the adaption coil (yellow). (c) Schematic cut through the experimental chamber: Feshbach and Curvature coils are placed inside the recess of the re-entrant viewport. The picture is adapted from [Repp, 2013].

described in Repp [2013] and Tran [2022]. Main cooling steps within the sequence used for our mixing scheme are sketched in Sec. 2.2.2.

Six diode lasers provide light for cooling Cs and Li: at 852 nm, Toptica TA Pro for Cs MOT cooler beams and Toptica DL 100 Pro for Cs MOT repumping beams; at 671 nm two Toptica TA, one for Li MOT cooler beams and one for $\mathcal{D}_1$ cooling, two home-built TAs, one for the amplification of the MOT repumping beams and another for the amplification of the in-plane beams for $\mathcal{D}_1$ cooling.

The external magnetic fields required for cooling the atoms are provided by a set of both homogeneous and quadrupole magnetic fields. The quadrupole magnetic fields required for MOT are generated by two coils connected in anti-Helmholtz configuration. Raman coils are installed along the vertical direction to generate a small homogeneous magnetic field used for DRSC and fast displacement of the MOT position. Compensation cage coils are implemented to compensate for earth and magnetic stray fields. Offset coils mounted on the large horizontal view-ports of the experimental chamber allow the MOT to be moved in plane. [Repp, 2013; Pires, 2014; Häfner, 2017; Gerken, 2022; Tran, 2022].

Trapping. Optical dipole traps provide trapping potentials for neutral atoms which are almost independent from the internal state occupied by the atoms (see Sec. 1.3). For trapping Li and Cs atoms we use three different dipole traps, namely dimple trap, microtrap and reservoir trap, which are produced by three high power lasers: a fiber laser IPG at 1070 nm, a Ti:Sa laser by Coherent tuned at 880 nm and pumped by a Verdi V-18 at 532 nm, and a Mephisto MOPA at 1064 nm. These dipole traps are described in detail in Sec. 1.3. For specific needs, optical trapping can be also combined with magnetic field gradients. An example is given by the trapping scheme for Cs when loaded into the Reservoir trap, explained in Sec. 2.2.2. Such a magnetic field gradient is provided by the Curvature Coils (Fig. 1.2 (c)). They consist of a pair of coils of two layers with two windings each, which is placed inside the Feshbach coils. The implementation and construction procedure is similar to the one for the Feshbach coils and can be found in [Pires, 2014]. In the course of this work, an H-bridge was implemented and connected to these coils to allow switching the gradient direction. This makes possible to create a magnetic field gradient that pulls down both species, compensating the gravitational sag while trapping both species in the same trapping potential. Details on the implementation of the H-bridge and on the calibration of the magnetic fields produced by the Curvature coils can be found in [Freund, 2019]. In Appendix A I show a measurement where the center of mass of Cs atoms trapped in this combined potential is effectively pushed down as expected.

Tuning interactions. To tune intra- and inter-species interactions in a Li-Cs mixture we need to generate homogeneous magnetic fields up to 1000 G. A homogeneous magnetic field is produced by a couple of coils mounted in Helmholtz configuration within the re-entrant view-ports of the main chamber, as shown in Fig. 1.2 (c). The coils consist of 4×6 windings, with a minimal radius of 39.1 mm and a distance from the center of the chamber of 19.5 mm. They generate magnetic fields up to 1350 G, corresponding to the maximum available current of 400 A. The temperature of the coils is stabilized by cooling water supplied from a custom made industrial cooling unit and the current, measured by a current transducer, is actively stabilized with a PID controller. The construction procedure is shown in [Pires, 2014]. The characterization of the residual field curvature and magnetic field resolution is presented in Sec. 1.4.

Detection. The relevant information on our experiment, such as atom number, temperature and density distributions, are obtained by means of absorption imaging, which is described in Sec. 1.5.2. Absorption imaging at high magnetic field is possible thanks to dedicated lasers and optical setups. We use three CCD camera, one horizontally (Ximea) and two vertically (Guppy and Andor). Andor camera can perform high-resolution absorption imaging in fast kinetic mode, which allows the acquisition of images of both atomic clouds within the same experimental cycle. Moreover, to obtain detailed information on the physical properties of ultracold gases, we employ also various spectroscopic methods. Techniques such as radio-frequency and microwave spectroscopy are primarily

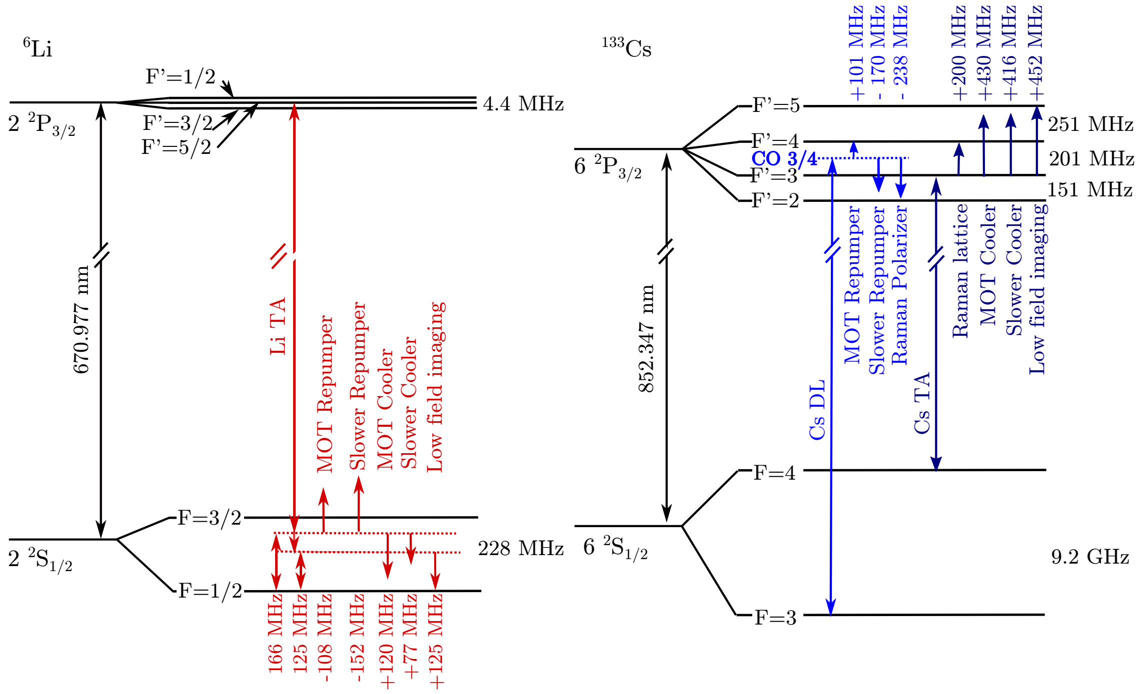

FIGURE 1.3: Hyperfine structure for the $\mathcal{D}_2$ cooling line for Li and Cs. The arrows and the labels (red, blue, dark blue) mark the laser light frequencies and frequency shifts by AOMs by the diode lasers named Li TA, Cs TA Cs DL, respectively. The figure is taken from [Tran, 2022].

implemented to calibrate magnetic fields and to probe the polaron energy, as discussed in Sec. 1.5.1. In addition, Raman spectroscopy, which was implemented in the course of this thesis, is described in detail in section 3.2.2 and is used to probe Fermi polarons on Cs impurities. Together, imaging and spectroscopy, provide a comprehensive toolkit for investigating the complex behavior and properties of ultracold gases under different experimental conditions, as summarized in Sec. 1.5.

1.2 Double species Zeeman slower

The atomic beam produced by the effusive oven has mean velocities corresponding to 1.48×10^3 m/s (Li) and 244 m/s (Cs), which are a factor of 10 and 30 respectively larger than the capture velocity of a MOT. One of the standard techniques to mitigate such a large gap is to use a Zeeman slower [Phillips and Metcalf, 1982; Metcalf and van der Straten, 1999], where radiative light forces are used to decelerate the hot atoms while the changing Doppler shifts are compensated by the Zeeman shifts produced by a position-dependent magnetic field B(z) along the atomic beam direction z. The optimal field profile has a total range which is expected to scales with $1/\sqrt{m}$ [Metcalf and van der Straten, 1999], where m is the atomic mass. Therefore widely different magnetic field profiles are needed for decelerating either Cs or Li atoms.

For the exact design and the technical details on the implementation of the coils, I address the reader to [Repp, 2013]. The description provided here is limited to the main concepts that are useful to explain the calculated magnetic fields profiles presented in Sec.1.2.1 and the measurements of the performance of the Zeeman slower by measuring the MOT loading rates as reported in Sec.1.2.2.

1.2.1 Modeling of atom deceleration in the Zeeman slower

Design of the double-species Zeeman slower. To create two different field profiles, we extended the approach presented by Bell *et al.* [2010] for a single species Zeeman slower. Our design consists of four interleaving layers of helical coils, where each layer is implemented as a single winding with a helical conductor profile of variable pitch. Moderate currents of 30 A in the outer two layers generate the magnetic field profile for decelerating Cs atoms. Much higher currents and differently shaped magnetic fields are reached for cooling Li atoms by increasing the current to 75 A in the outer two layers and simultaneously adding a magnetic field created by the same current value though the inner two coils. The magnetic fields in the last part of our Zeeman slower are generated by the radial fields of the MOT coils [Schünemann *et al.*, 1998]. The perfect matching between the fields generated by the helical coils and the MOT coils is ensured by an additional thin adaption coil mounted in the overlap region between the Zeeman slower and the MOT coils. The smooth overlap between the magnetic fields is beneficial to minimize the transverse expansion of the atomic beam [Joffe *et al.*, 1993], which is particularly critical for light elements like lithium. Compared to other solutions [Marti *et al.*, 2010], this scheme allows avoiding regions along the slower where the atomic beam is not decelerated and thus expands.

The small inductance due to a small number of windings allows for fast switching between loading Li or Cs. We measure switching times of the helical coils by recording the voltage response at the connectors while varying the control parameter of our power supplies. The 90% level of the final voltage is reached within less than 2 ms, whereas for switching off, the induced voltage vanishes in less than 15 ms. Sub-ms time-scales can also be reached switching off the coils by electronically short-circuiting them.

Modeling the deceleration of Li and Cs atoms. The required individual fields for decelerating Li and Cs atoms were calculated by studying the equations of motion via a numerical simulation. The deceleration is provided by the dissipative light force $F_D = \hbar k \gamma_p$, where k is the wave-vector of the light and γ_p is the excitation rate for a two level atomic system [Metcalf and van der Straten, 1999]. F_D has to be maintained, at each position, constant and smaller than the limit-acceleration provided at saturation by the on-resonance photon scattering $F_{\mathrm{D}}^{\mathrm{max}} = \hbar k \gamma/2$, where γ is the natural linewidth of the excited state. This requirement can be quantified with an adimensional deceleration $\eta = F_{\mathrm{D}}/F_{\mathrm{D}}^{\mathrm{max}} = a/a_{max}$ that must be kept <1 in order to fulfill the resonance condition in any position.

In Tab. 1.1 the design parameters used for simulating the optimal field for the two species are listed. For simplification, the deceleration process was inverted by virtually accelerating the two species separately towards the oven, starting at the MOT center with

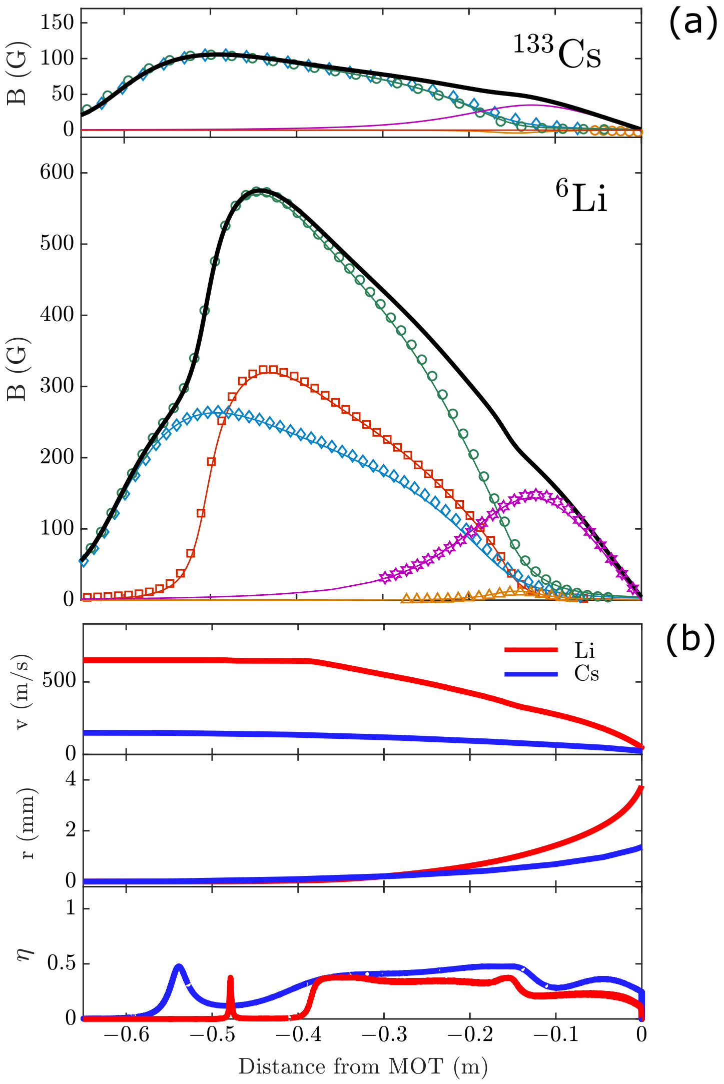

FIGURE 1.4: (a) Magnetic fields for the deceleration of Cs (upper panel) and Li (lower panel). The measured field (green circles) of the helical coils and the adaptation coil is a sum of the fields from the inner helical coils (red squares), the outer helical coils (blue diamonds) and a small field from the adaption coil (orange triangles). The transverse expansion of the atomic beam is minimized by generating the last part of the total field for slowing via the radial field of the MOT coils (violet hexagrams). The colored lines represent the results from the calculation for the single coils, while the black lines depict the calculated total field of all coils. The only free parameters are the zero positions of the measurements. (b) Simulations of the deceleration process for Cs (blue) and Li (red). The longitudinal velocity (upper panel), the beam radius due to the transverse heating (middle panel) and the dimensionless acceleration η (lower panel) are shown for atoms near to the capture velocity of the Zeeman slower, corresponding to $v_{\mathrm{Li}}^{\mathrm{cap,ZS}} = 650$ m/s for Li (m_I=-1) and to $v_{\mathrm{Cs}}^{\mathrm{cap,ZS}} = 150$ m/s for Cs (m_f=3). Figure (a) is adapted by Repp [2013].

Design parameters		**Cs**	**Li**
Current MOT Coils (A)	I^{MOT}	30	97.7
Current External Helical Coils ZS (A)	I^{ext}	30	75
Current Internal Helical Coils ZS (A)	I^{int}	0	75
Current Adaption Coils (A)	I^{A}	4.5	-1
Magnetic gradient MOT Coils (G/cm)	$\partial B/\partial z$	9.5	31.0
Saturation parameter	S^0	10	2.5
Detuning slower laser (MHz)	$\delta/2\pi$	-35	-70
Adimensional acceleration	η	0.5	0.5
Initial velocity (m/s)	v^{in}	23	48
Minimal distance (cm)	d^{min}	7.5	12.5

TABLE 1.1: Design parameters used for simulating the optimal fields for the two species. The adimensional deceleration η is fixed to 0.5. The differences in S_0 arise from different available laser powers on the experiment and the differences in v_{start} are assuming higher MOT capture velocities for Li than for Cs, due to the smaller mass. The table has been taken from Repp [2013].

the assumed capture velocities of $v_{\mathrm{Cs}}^{\mathrm{cap,MOT}} = 25$ m/s and $v_{\mathrm{Li}}^{\mathrm{cap,MOT}} = 48$ m/s of our Cs and Li MOT, respectively. The simulation started by first accelerating the atoms only by the radial fields of the MOT coils at the given currents. The design values for the magnetic gradients of the MOT along the axial direction are $\partial B_{\mathrm{Cs}}/\partial z = 9.5$ G/cm and $\partial B_{\mathrm{Li}}/\partial z = 31.0$ G/cm, which enables the levitation of Cs atoms [Weber *et al.*, 2003] while simultaneously loading a Li MOT. After a distance of about 100 mm, where the chamber geometry allows for generating magnetic fields by additional coils, the photon scattering rate and thus the acceleration at each position afterward was maximized in the simulation to $\eta \cdot a_{max}$ via optimizing the Zeeman shift. For typical magnetic field values, the Zeeman shift of Li is larger than the hyperfine splitting and thus closed optical transitions within the Pashen-Back regime were used in the calculation. To maximize the atomic flux, the field was selected in such a way that all three lowest m_{I} sub-levels are decelerated.

The calculated magnetic field profiles are shown in Fig. 1.4, together with the longitudinal velocity, the beam radius due to the transverse heating and the dimensionless acceleration η for atoms near to the capture velocity of the Zeeman slower, corresponding to $v_{\mathrm{Li}}^{\mathrm{cap,ZS}} = 650$ m/s for Li (m_I=-1) and to $v_{\mathrm{Cs}}^{\mathrm{cap,ZS}} = 150$ m/s for Cs (m_f=3), calculated considering the total field of all the coils (black lines). One can notice that at the position of the junction of the helical coils with the MOT coils, where the adaption coils are located, the deceleration remains constant at around the designed value of 0.5 even inside the experimental chamber, ensuring an efficient deceleration of the atoms until they reach the MOT center. As a consequence, the radial extension of the Li beam reaches a radius of almost 4 mm, corresponding to the extension of the MOT laser beams and guaranteeing a smooth loading into the MOT. The measured magnetic fields profiles are shown in Fig. 1.4. The magnetic fields resulting for both configurations have been measured with a standard Hall probe [Repp, 2013]. The maximum discrepancy between the calculated and measured fields is only 10 G, thanks to the high accuracy of the CNC-based manufacturing process for the helical coils.

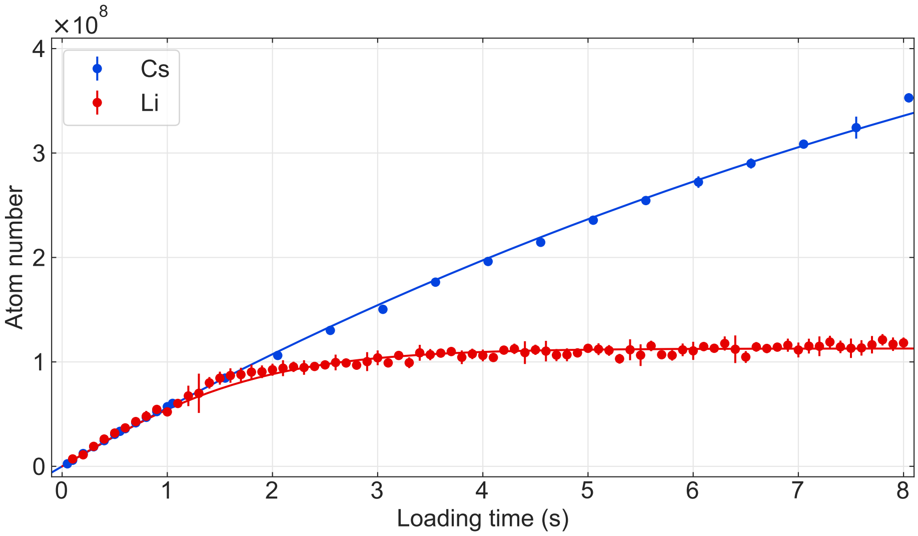

FIGURE 1.5: Time dependence of the number of Cs (blue) and Li (red) atoms loaded into their respective MOTs. Data (circles) are recorded by performing absorption imaging and the curves are the best fit to the models described in the text. A loading rate of 5.9×10^7 atoms/s for either Li and Cs atoms is deduced by the fit.

1.2.2 Performance of the Zeeman slower

In order to obtain fast cycle rates and having an efficient sub-sequential loading, a high loading rate is desired. We test the performances of the Zeeman slower by recording curves for a Li and Cs MOT via standard absorption imaging, as shown in Fig. 1.5 for $T_{oven,Li} = 635$ K and $T_{oven,Cs} = 375$ K. Details on the preparation of the MOT in our experiment can be found in [Repp, 2013].

For Cs atoms, we make a fit (blue solid line) of the measured loading curves with an exponential growth

$$N(t) = \frac{R_{\mathrm{Cs}}}{\alpha_{\mathrm{Cs}}}(1 - e^{-\alpha_{\mathrm{Cs}} t}) \tag{1.1}$$

taking into account the interplay between the increasing of the number of atoms via decelerated atoms at rate R and the density independent one-body loss mechanisms at rate α_{Cs}. A typical loading curve for Cs results in a MOT loading rate of $R_{\mathrm{Cs}} = 5.9 \times 10^7$ atoms/s and with one-body loss rate of α_{Cs} =0.09 s^{-1}. The $1/e$-lifetime of $\sim$11 s is close to the vacuum-limited value. For a typical MOT loading time of 1 s, temperatures of $T_{\mathrm{Cs}} \approx T_{Doppler} = 125\ \mu$K are generally reached at this stage with corresponding atomic densities of 3.1×10^{10} cm^{-3}.

In the case of Li, on the other hand, high densities result in non-negligible two-body losses induced by multiple scattering of photons and light-assisted collisions. Indeed, a maximal peak density of 7.2×10^{10} cm^{-3} leads to saturate the atom number at 1.2×10^8 for loading times longer than 2 s. Here, we describe the evolution of the atom number as

$$\dot{N}(t) = R_{\mathrm{Li}} - \beta'_{\mathrm{Li}} N(t)^2 \tag{1.2}$$

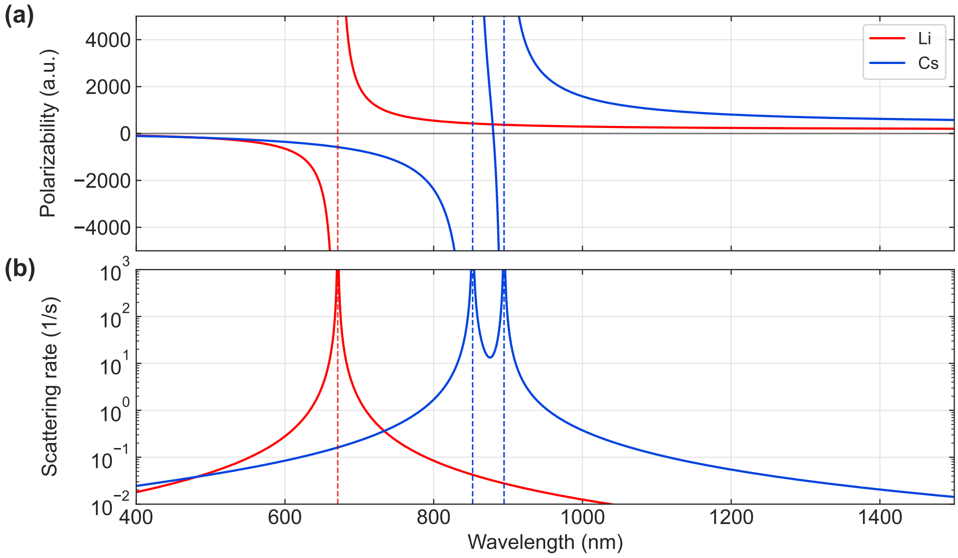

FIGURE 1.6: (a) Dynamic polarizability and (b) scattering rate for a typical intensity of 10^8 W/m^2 in dependence of the wavelength λ for ^{6}Li (red) and ^{133}Cs (blue). The wavelengths corresponding to the $\mathcal{D}_1$ and $\mathcal{D}_2$ transitions for each species are indicated by vertical dashed lines. The polarizabilty is expressed in atomic units, where 1 a.u. = $1/(4\pi\varepsilon_0 a_0^3)$.

with $\beta'_{\mathrm{Li}} = \beta_{\mathrm{Li}} V$ where β_{Li} is the two-body loss coefficient and $V = (\sqrt{2\pi}r)^3$ is the effective volume occupied by the cloud, where r is the $1/e^2$ size of the cloud averaged in the three spatial dimensions. The curve used for the fit (red solid line) is then given by

$$N(t) = \sqrt{R_{\mathrm{Li}}/\beta'_{\mathrm{Li}}} \tanh\left(t\sqrt{R_{\mathrm{Li}}\beta'_{\mathrm{Li}}}\right) \tag{1.3}$$

with a typical loading rate of $R_{\mathrm{Li}} = 5.9 \times 10^7$ atoms/s. In agreement with what reported in [Schünemann *et al.*, 1998] and [Schlöder *et al.*, 1999], we obtain a two-body loss coefficient of $\beta_{\mathrm{Li}} = 1.7 \times 10^{-11}$ cm^{-2}. Typical achieved temperatures are around 1.4 mK. In order to lower the temperature, after further 15 ms of compression the gradient fields are increased and provided by an additional set of coils with switching-off times below 1 ms. At the end of the compression phase, the laser intensity is reduced and the detuning of the cooler beam is decreased to half of the natural linewidth of the $\mathcal{D}_2$ transition. The temperatures are then reduced to $T_{\mathrm{Li}} \approx 400$ μK with an atom number of 7.8×10^7.

1.3 Dipole trap management

The two main quantities of interest for dipole traps are the time-averaged interaction energy of the induced dipole with the generating oscillating electric field of the light, and the photon scattering rate. Qualitatively, when an atom, considered as a simple oscillator, is placed in an electromagnetic field, like that of a laser beam, the electric field $\mathbf{E}(\mathbf{r},t) = \hat{\mathbf{e}}\, E(\mathbf{r}) \exp(-i\omega t) + c.c.$ induces an atomic dipole moment $\mathbf{p}(\mathbf{r},t) = \alpha(\omega)\mathbf{E}(\mathbf{r},t)$ that oscillates at the field frequency ω with a complex frequency-dependent polarizability

$\alpha(\omega)$. The dipole potential and the photon scattering rate are then given by

$$U_{dip}(\mathbf{r}) = -\frac{1}{2}\langle \mathbf{p}(\mathbf{r},t)\mathbf{E}(\mathbf{r},t)\rangle = -\frac{1}{2\epsilon_0 c},\Re e\{\alpha(\omega)\}I(\mathbf{r}) \tag{1.4}$$

$$\Gamma_{sc}(\mathbf{r}) = \frac{P_{abs}}{\hbar\omega} = \frac{1}{\hbar\epsilon_0 c}\Im m\{\alpha(\omega)\}I(\mathbf{r}), \tag{1.5}$$

respectively, where $P_{abs} = \langle \dot{\mathbf{p}}(\mathbf{r},t)\mathbf{E}(\mathbf{r},t)\rangle$ is the power absorbed by atoms from a stream of photons with energy $\hbar\omega$ and then re-emitted as dipole radiation, $I(\mathbf{r}) = 2/(\epsilon_0 c)|E(\mathbf{r})|^2$ is the position-dependent intensity, c the speed of light, and ϵ_0 the vacuum permittivity. Both quantities can be expressed following Grimm *et al.* [2000] as

$$U_{dip}(\mathbf{r}) = -\frac{3\pi c^2}{2\omega_0^3}\left(\frac{\Gamma}{\omega_0-\omega}+\frac{\Gamma}{\omega_0+\omega}\right)I(\mathbf{r}), \tag{1.6}$$

$$\Gamma_{sc}(\mathbf{r}) = \frac{3\pi c^2}{2\hbar^2\omega_0^3}\left(\frac{\omega}{\omega_0}\right)^3\left(\frac{\Gamma}{\omega_0-\omega}+\frac{\Gamma}{\omega_0+\omega}\right)^2 I(\mathbf{r}), \tag{1.7}$$

where ω_0 is the resonance frequency of the atomic transition and Γ is the natural linewidth. In the simplest case of a single focused beam, the laser light has a gaussian beam profile with peak intensity calculated via $I_0 = 2P/(\pi w_0^2)$, and the intensity profile is given by

$$I(x,y,z) = I_0\left(\frac{w_0}{w(x)}\right)^2 \exp\left(\frac{-2\,(y^2+z^2)}{w(x)^2}\right) \tag{1.8}$$

with $w(x) = w_0\sqrt{1+\left(\frac{x}{x_R}\right)^2}$, $x_R = \pi w_0^2/\lambda_0$ the Rayleigh length of the beam and w_0 the beam waist. Figure 1.6 (a) shows the polarizability $\Re(\alpha)$ of ^{6}Li and ^{133}Cs [Le Kien *et al.*, 2013] in their electronic ground state as a function of the laser wavelength. The polarizability of Li atoms exhibits a prominent resonance feature at a wavelength of 671 nm[1] and it remains positive for longer wavelengths. For Cs, two resonances are resolved clearly at the $\mathcal{D}_1$ (894.6 nm) and $\mathcal{D}_2$ (852.3 nm) lines. Above 894.6 nm, the dipole potential for Cs is attractive, whereas below 852.3 nm is repulsive. At a wavelength of 880.25(4) nm [Arora *et al.*, 2011; Ratkata *et al.*, 2021], the polarizability of Cs is zero, meaning that Cs atoms in their ground state do not experience any conservative light force. This wavelength is known as the tune-out wavelength and enables species-selective trapping [LeBlanc and Thywissen, 2007]. The wavelength dependent scattering rates of ^{6}Li and ^{133}Cs for a typical laser beam intensity of 10^8 Wm^{-2} are shown in Fig. 1.6 (b). The scattering rates at the $\mathcal{D}_1$ and $\mathcal{D}_2$ lines are severely enhanced, limiting the lifetime and minimum achievable temperature of the atomic samples. In general, it is beneficial to choose large detunings from the atomic resonances, while at the same time increasing the intensity to achieve sufficient trapping potentials. Light at the Cs tune-out wavelength, when it is in between the $\mathcal{D}_1$ and $\mathcal{D}_2$ lines, is characterized by large scattering rate (see Sec. 2.3.1).

---

[1] In fact we expect two resonance features located at the $\mathcal{D}_1$ and $\mathcal{D}_2$-lines. However, the small hyperfine splitting in ^{6}Li of only $\approx$ 10 GHz, or equivalently 0.015 nm, is not resolved in Fig. 1.6.

In the following, I introduce the optical dipole traps utilized in our experiment and employed for a bichromatic trapping scheme (see Sec. 1.3.1). Additionally, I provide a detailed description of a tightly confining dipole trap at the Cs tune-out wavelength (Sec. 1.3.2), which has been implemented in the course of this thesis work.

1.3.1 Bichromatic trapping scheme

Simultaneous optical trapping of highly mass-imbalanced atomic species has to satisfy very different requirements for each of them, especially for reaching ultra-low temperatures and for compensating for the gravitational sag. This section describes the optical dipole traps used for combining Li and Cs together, which are the dimple trap (DT) for Cs, and the microtrap (MT) for Li. The simultaneous exploitation of two distinct trapping potentials at different wavelengths is referred to as bichromatic or dual-color trapping. In this configuration, the MT is tuned to the Cs tune-out wavelength. Based on the method of species-selective trapping described by LeBlanc and Thywissen [2007], this wavelength allows for the independent control of the potentials of each species, as it does not impose any confining effect on Cs atoms. In particular, the simultaneous presence of both traps allows manipulating the Cs trapping potential without being deformed by the presence of the MT. Conversely, the potential depth of Li is predominantly determined by the MT potential, exhibiting only minor alterations due to the DT potential, as the volume ratio between the two traps is large. The relative trap depth and residual gravitational sag can be regulated by controlling the relative shifts and intensities of the two dipole traps. A detailed discussion of the challenges in producing Li and Cs mixtures can be found in 2.1.3.

Moreover, a third trapping potential is necessary to serve as a reservoir for loading Cs atoms after sub-Doppler cooling sequences. This is referred to as the reservoir trap (RT). The combination of these three distinct dipole traps is employed in our experiment, as illustrated in Fig. 1.7.

Dimple trap (DT). This optical dipole trap is formed by two crossed linearly polarized beams at a crossing angle of 8.5° with a beam waist of 62 μm. It comes out from a high power fiber laser IPG YLR-200-LP-WC with a wavelength of 1070 nm. This trap is used as a reservoir for Li atoms and as a final trapping potential for Cs atoms. At the maximum power of 100 W per beam, a maximum trap depth of 1.2 mK for Li is achieved, which is eventually required to transfer Li atoms directly from the MOT to the dipole trap. Moreover, the trap can dynamically change its trapping volume via frequency modulation of an acousto-optic modulator [Neiczer, 2018], providing a good mode matching for loading atoms from the gray molasses cooling to the dipole trap. The large trapping frequencies on the order of 10 kHz allow fast thermalization during loading and evaporative cooling. It also provides a small volume trap for Cs in the context of the dimple trick [Tran, 2022]. In the past it has also been used for monochromatic trapping of Li and Cs atoms. Recently, it has been stabilized at low power by a Red-Pitaya digital PID. The original optical setup can be found in [Heck, 2012].

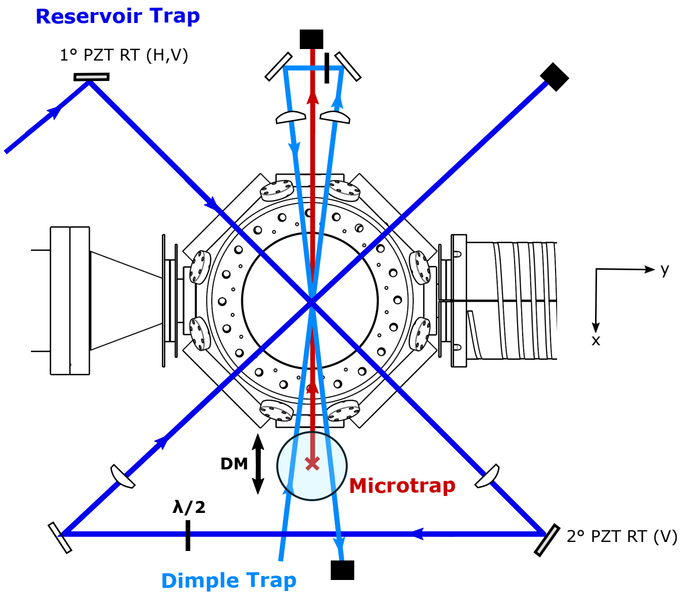

FIGURE 1.7: Schematic overview of the three optical dipole traps in our experiment: reservoir trap (blue), dimple trap (light blue) and microtrap (red). The microtrap is oriented along the axial direction of the dimple trap beams, which are combined together by the dichroic mirror (DM). The DM can be shifted horizontally producing a corresponding vertical displacement of the microtrap beam. The position of the reservoir trap can be adjusted with two piezo mirrors.

Microtrap (MT). This optical dipole trap,which has been designed and implemented during this thesis work, is formed by a single-beam trap with a beam waist of 10 μm operated at the Cs tune-out wavelength of 880 nm, which has been designed and implemented during this thesis work. The desired light is supplied by a titanium-sapphire (Ti:Sa) laser Coherent MBR-100, tunable in the wavelength in a range of 700 nm to 1030 nm, and delivering up to 3 W at 880 nm. The Ti:Sa laser is pumped by a Coherent-Verdi V-18 at 532 nm with a power of 18 W. This trapping potential is used to prepare and store Li Fermi gases, and combine them with the low-density Cs sample prepared in the dimple trap. The tight confinement favors high densities and it is optimal for obtaining a highly degenerate Li Fermi Sea. In addition, the beam can be translated along the z-direction (gravity-direction) by horizontally shifting a dichroic mirror (see Fig. 1.9) over a range of ± 6.5 mm, which is used to combine the microtrap with the dimple trap. This feature allows bringing the Li together with Cs and compensating for the differential gravitational sag between the two clouds. However, this trapping potential was originally designed with the aim of confining Li atoms in the center of a Cs Bose-Einstein condensate, with the intention of probing Bose polarons, which was the reason for choosing such a small beam waist of 10 μm[2]. The MT laser power is intensity stabilized via an analog PID to reduce intensity fluctuations in the laser power. In Sec. 1.7, I describe the full setup and the characterization of the main features, such as the achieved trapping frequencies and the efficiency in the transport.

---

[2] The name *microtrap* has historical reasons. Even though the current beam waist is not on the order of a few micrometers, we kept this name.

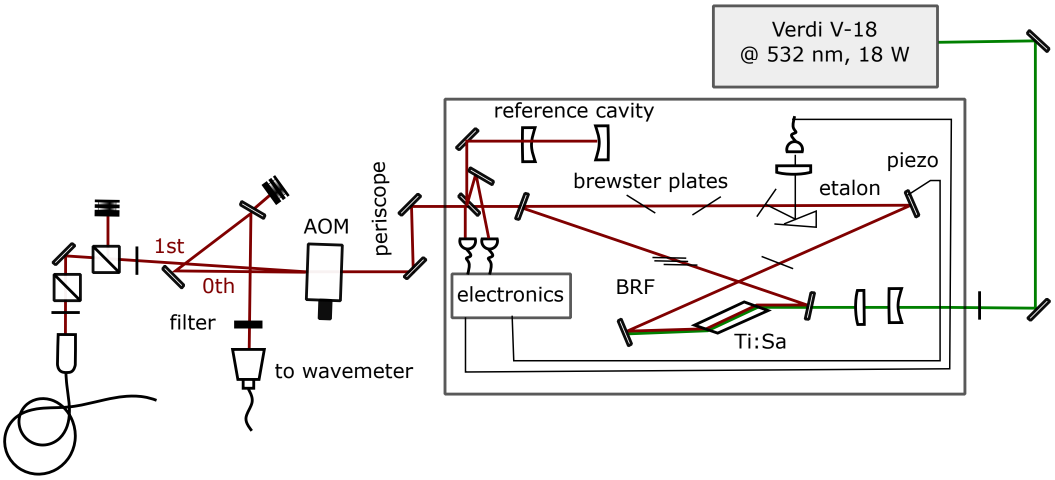

FIGURE 1.8: Schematic of the Ti:Sa laser-source. The green laser source output at 532 nm is injected into the Ti:Sa crystal placed into a bow-tie cavity aligned for having an output wavelength of 880 nm. After the cavity, which is a commercial system, the beam goes through an AOM and the 1*st* order goes through polarization optics and then is coupled into an optical fiber which brings it to the optical table. The 0*th* order is used to monitor the wavelength by a wavemeter.

Reservoir trap (RT). This optical dipole trap is formed by two crossed linearly polarized beams at a crossing angle of 90° with a beam waist of 300 μm. This large optical dipole trap is provided by a single beam out of a 55 W Mephisto MOPA Nd:YAG solid-state laser at 1064 nm and it is used for loading Cs atoms at trap depths on the order of 10 μK. This trapping potential is only used as a reservoir for Cs atoms, i.e. for collecting and storing them from the Raman lattice for degenerate Raman sideband cooling. The position of the intersecting foci can be displaced by a piezo-driven mirror and it was used in the past for combining the two species together by superimposing the RT with the dimple trap. Recently, the possibility of changing the beam waist between 300 μm and about 600 μm has been implemented, as well as a system for active power stabilization by means of an analog PID. The original optical setup and its characterization can be found in Arias [2014].

1.3.2 A tightly confining-movable optical trap

Here, I describe the implementation and characterization of the microtrap, evidencing its main features.

Idea and design. The microtrap was originally designed to confine Li atoms in the center of a Cs Bose-Einstein condensate, with the goal of probing Bose polarons. For this reason, a beam waist of 10 μm was chosen (see Freund [2022] for a detailed discussion of why we chose this size), in addition to the following specifications: (i) to enable the storage of the atoms away from the Cs MOT and the shifting of the Li trapping potential to compensate for the gravitational sag, (ii) to have a central geometry that is favorable to polaron detection, and (iii) to facilitate the independent manipulation of the density and

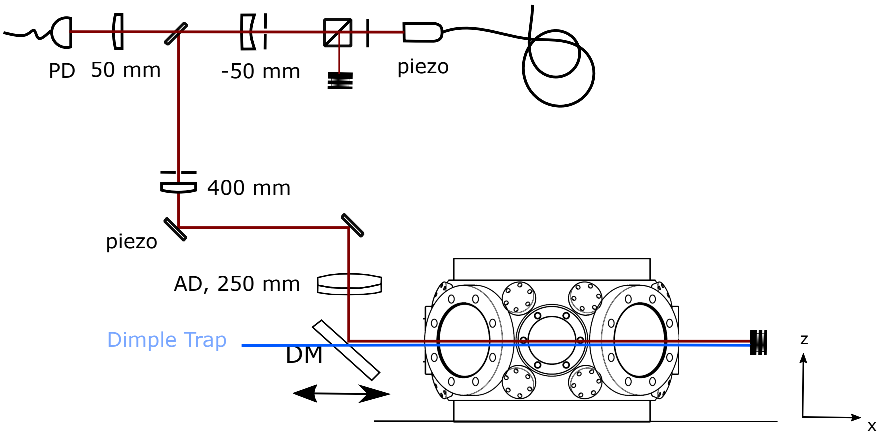

FIGURE 1.9: Schematic view of the microtrap setup in the xz plane. The microtrap light at 880 nm is prepared in the setup presented in Fig. 1.8 and comes out from an optical fiber on the experimental table. Here, the beam is spatially shaped in order to produce a tightly focused beam and is combined with the Dimple Trap beams at 1064 nm through a dichroic mirror (DM), which is mounted on a translational stage. As the stage moves horizontally, the microtrap beam shifts vertically while the dimple trap remains at a constant height.

temperature of Li and Cs. To address (i), the beam is designed to be movable along the vertical direction within a range of ± 6.5 mm; to address (ii), the beam is oriented along the symmetry axis of the dimple trap; for (iii), the Cs tune-out wavelength is selected. A detailed discussion about the challenges and solutions employed for the realization of a Li and Cs mixture can be found in Sec. 2.1.3.

Optical setup. The optical setup for preparing the beam of the microtrap is divided into two parts, one placed on the laser table shown in Fig. 1.8 and the other one on the experimental chamber table shown in Fig. 1.9. The large Ti:Sa laser system as well as the Verdi V-18 laser are kept far away from the experimental chamber due to the large size of the former and to the thermal effects associated with the dissipation of high intensities of the latter. Since the experimental chamber table is already quite packed, and the small 10 μm beam waist is sensitive to alignment, the setup was mounted on a portable aluminum breadboard (see Fig. 1.10 (a)), which allows the pre-alignment in a test setup. The shape and size of the breadboard was chosen to fit vertically in front of one of the small viewport of the chamber of science.

The beam coming out of the Ti:Sa, after a periscope, passes through an AOM[3], which we use to turn the laser beam on and off as well as controlling intensity. The 0*th* order of the AOM is used to monitor the wavelength of the free-running laser with a wavelength meter[4]. The 1*st* order of the AOM passes through two polarizing beam splitters (PBSs) and it is then coupled[5] to a polarization-maintaining single mode fiber[6], which brings

---

[3] Crystal Technology 3100-125

[4] HighFinesse WS7

[5] Schäfter+Kirchhoff 60FC-4-A8-07

[6] Thorlabs P3-780PM-FC-10

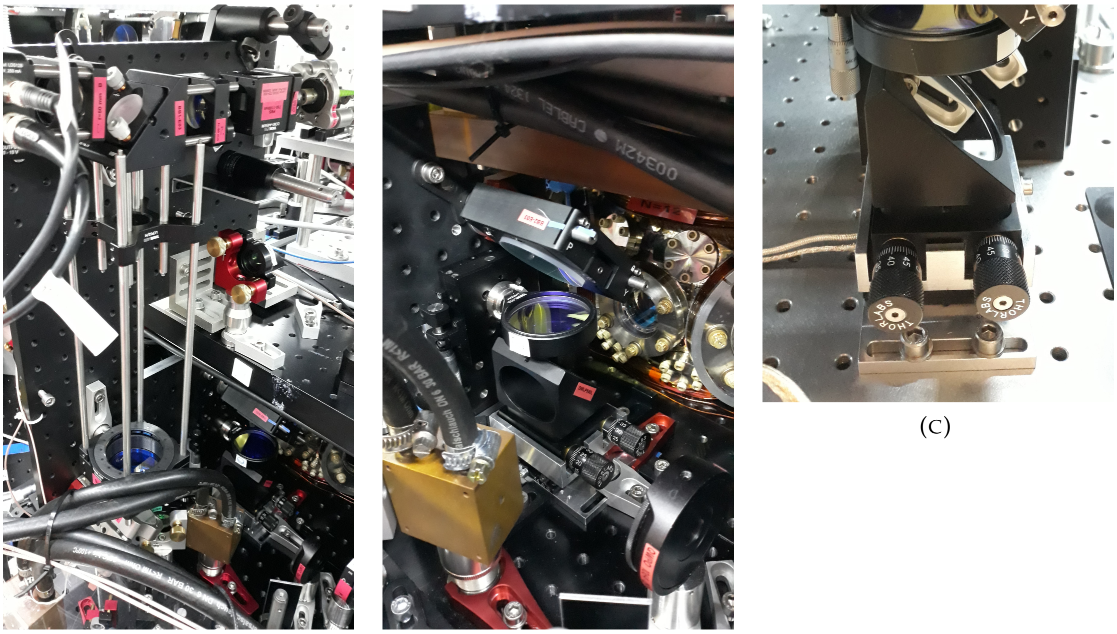

FIGURE 1.10: Photos of the microtrap setup: (a) the vertical breadbord implemented into the pre-existing experimental apparatus; (b) enlargement of the optics in front of the small central window of the chamber of science (second-last mirror, focusing lens, dichroic mirror); (c) view of the custom-made holder for the dichroic mirror mounted on top of the translational stage.

the light to the setup on the experimental chamber table. A fiber outcoupler[7] with a focal length of 12 mm produces a collimated beam of 850(4) μm, which is linearly p-polarized and has circular symmetry at any distance from the collimator. Afterwards, the beam passes through a lambda half-wave plate and a polarizing beam splitter mounted on a small cage system to maximize and clean the transmitted light, respectively[8]. The beam is then magnified by a telescope consisting of two lenses mounted into a cage system, with a focal length of -50 mm[9] and 200 mm[10] respectively, placed at a distance of 350 mm and resulting in a magnification of the beam of a factor of 8, corresponding to a beam waist of 6.8(2) mm. Before each of the two lenses, there are apertures for alignment purposes. The beam is then directed by a two-inch piezo-controlled mirror[11], used for remote fine alignment on the atomic cloud, to a fixed two-inch industrial mirror, which directs it to the focusing lens, as shown in Fig. 1.10 (b). Using a two-inch achromatic doublet [12] with a focal length of 250 mm, the desired beam waist of 10.3(3) μm is reached. The achromatic lens is placed on a manual translation stage[13] with a maximum traveling range of 12.7

---

[7] Schäfter+Kirchhoff 60FC-4-M12-10

[8] Here, it is left on purpose some space to mount on the cage a second half-wave plate for turning the polarization in case of need.

[9] Thorlabs: LC1715-B

[10] Thorlabs: LA1725-B

[11] During the construction of the setup, it was proposed that this mirror, together with the one-inch piezo-mirror holder on which the outcoupler is mounted, could be used for active beam pointing stabilization.

[12] Thorlabs AC508-250-B

[13] Thorlabs: MT1/M

mm, which allows shifting the focal position along the axial direction of the beam. The microtrap is then combined with the dimple trap by a dichroic mirror[14] mounted on a compact, high resolution translation stage[15] (see Klaus [2019] for the criteria of this choice). The dichroic mirror has a cut-off wavelength at 950 nm such that it reflects the microtrap light while transmits the dimple trap light. The stage on which the dichroic mirror is mounted allows the vertical displacement of the beam over a maximum travel range of 13 mm, resulting in a diagonal movement of the focus and thus of the trapped atomic cloud (see Fig. 1.12 (a) and (b), top). It should be noted that this mirror shows a slight astigmatic character, which results in a displacement of the focus position between the two transversal direction of the beam of $2.3(2)\times10^2$ μm (see Freund [2022] for the characterization of this effect). The mirror holder, shown in Fig. 1.10 (c), is custom made to fit into the existing setup, matching the correct height of the dimple trap beams and allowing both of them to pass through. The mirror holder is placed on a 2D gimbal mount, which allows for adjusting the pointing of the beam after the lens before entering the experimental vacuum chamber.

Behind the first mirror after the outcoupler, the light is collected by a lens and focused on a photodiode[16]. This photodiode is used to measure the power of the microtrap's beam and is connected to the AOM via an analog PID controller. This allows the power in the microtrap beam to be stabilized. The 3 dB bandwidth, defined as the frequency at which the power drops to half of its initial value at low frequencies, corresponds to a power of 220 mW and a trapping frequency of 25 kHz. As laser noise at a frequency $2\nu_{tr}$ would excite the trap at ν_{tr}, in presence of laser noise at 25 kHz we would expect to observe noise in the trapping frequency at 12.5 kHz. Taking the 3 dB bandwidth as the limit for intensity stabilization, we can then stabilize frequencies up to 12.5 kHz. In the scheme described in 2.2.1 we use a power of 60 mW for loading the microtrap from the dimple trap and a power of 147 mW for compression during the storage phase, and therefore, the laser intensity noise should not cause significant heating.

The frequency of the Ti:Sa laser can fluctuate around the set center frequency $\nu = (340.576 \pm 0.015)$ THz due to the strong sensitivity of the cavity inside the Ti:Sa laser[17]. However, the laser source shows frequency fluctuations smaller than 2 GHz [Matthies, 2018], for which the ratio of the trap depths $U_{\mathrm{Li}}/U_{\mathrm{Cs}} > 500$ and, therefore, the trapping effect on Cs atoms is still negligible.

Trapping frequencies vs. laser power. It is of great importance to accurately determine the trapping frequencies, as they directly influence the density and Fermi energy of the cloud. A calibration of the microtrap trapping frequencies as a function of power is here provided, for both axial and radial confinement. Axial trapping frequencies of the MT are measured by exciting the breathing mode of a non-interacting gas. This is done by rapidly increasing the trap depth, causing the cloud to compress and oscillate in size

---

[14] Thorlabs DMLP950L

[15] Physik Instrumente Q-545.140

[16] Thorlabs: PDA30B2

[17] We take the value of the tune-out wavelength $\lambda = 880.25(4)$ nm from [Arora *et al.*, 2011].

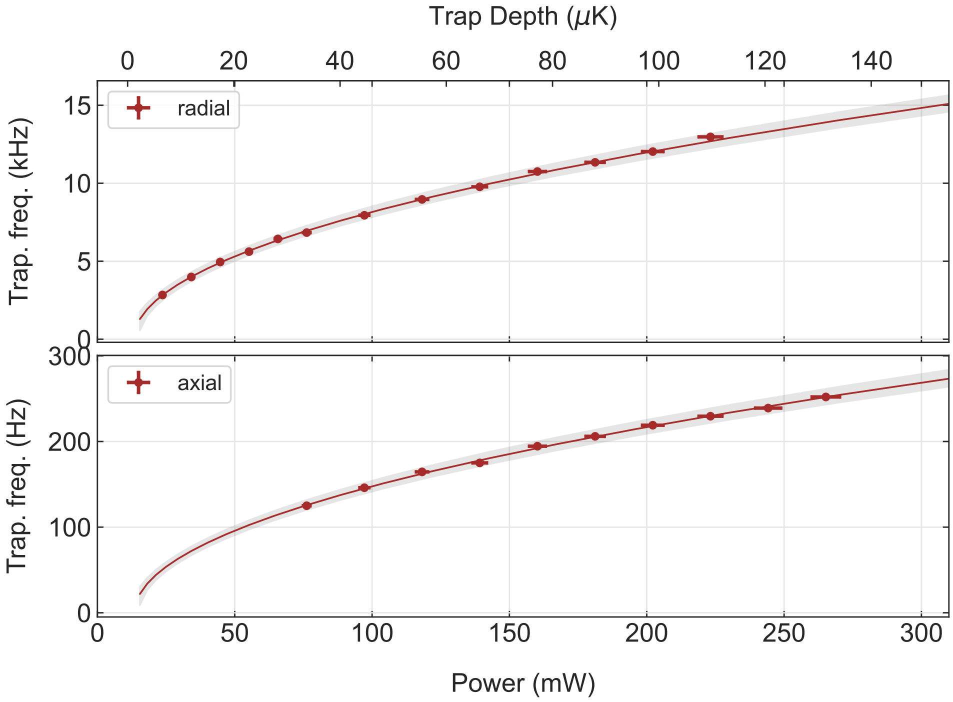

FIGURE 1.11: Trapping frequencies for Li atoms trapped in the microtrap as a function of the power: (a) along the radial direction, and (b) along the axial direction. A secondary x-axis indicates the corresponding trap depths. The radial trapping frequency has been extracted from a parametric heating measurement at twice the trapping frequency, while the axial trapping frequency has been extracted from breathing modes obtained by an intensity kick. The uncertainty in the fit is marked by the shaded area, which is calculated including the statistical error in the power.

at twice of the trapping frequencies. Radial trapping frequencies are characterized by parametric heating of an interacting cloud. Here the power of the microtrap beam, and thus the trap depth, is modulated by a sinusoidal signal at a certain frequency. Heating increases as the modulation frequency approaches the excitation frequency of one of the collective modes [Grimm, 2007]. Assuming to be in the unitary limit $1/(k_F a) \approx 0$ as well as in the hydrodynamic regime, the frequency of the radial compression mode measured by parametric heating $\omega_c/(2\pi)$ is related to the radial trapping frequency $\omega_r/(2\pi)$ by the relation $\omega_c = \sqrt{10/3}\omega_r$ [Pethick and Shmidt, 2001] (see also [Freund, 2022]). Axial and radial trapping frequencies as a function of the microtrap power are shown in Fig. 1.11. For both recorded trapping frequencies, we fit the data by a function of the type $f(P) = A\sqrt{P - P_0}$, where P is the power, A is the prefactor, and P_0 is the eventual offset in the power recorded by the photodiode, which gives the following calibrations as a function of the power of the microtrap's beam

$$f_{ax}[Hz] = (497 \pm 15)[Hz \cdot W^{-1/2}]\sqrt{P[W] - (10.8 \pm 2.6) \times 10^{-3}[W]} \tag{1.9}$$

$$f_r[Hz] = (26900 \pm 700)[Hz \cdot W^{-1/2}]\sqrt{P[W] - (11.2 \pm 3.3) \times 10^{-3}[W]}. \tag{1.10}$$

The uncertainty in the fit is shown in Fig. 1.11 by the shaded area, which is calculated including the statistical error in the power. It is important to note that a finite P_0 offset in power is a direct consequence of the fact that the power calibration was performed in an environment where the background light was effectively negligible. Conversely, during these measurements, as with any other measurement when the experiment is fully operative, the light emitted by the second dimple trap beam is scattered and collected on the MT photodiode, resulting in the presence of background light that leads to a power offset of about 11 mW[18]. It should be noted that the measurement presented in this thesis exploits a calibration that excludes this offset, and therefore, the calibration of the frequency in the power is just given by $f(P) = A\sqrt{P}$, where A is the same appearing in Eq. 1.9 and 1.10 for axial and radial frequencies, respectively. In Fig. 1.11 a secondary axis is also present, which shows the trap depth calculated for a single-focused beam and considering an offset in the power of 11 mW.

The measured aspect ratio between radial and axial trapping frequencies is about 56:1, which is in good agreement with the one calculated taking into account the astigmatism coming from the dichroic mirror, which is 56.6(1.6).

Transport of Li atoms. The transport of Li atoms is characterized as a function of beam displacement, stage acceleration, and trap depth. The losses in the atom number due to the cloud motion are determined by comparing the atom number N at the displaced position with the atom number N_0 without displacement after keeping the atoms in the microtrap for the same time. Each measurement is performed with a non-interacting cloud and it is averaged over 10 repetitions.

Figure 1.12 (b) shows the characterization of the transport as a function of the displacement Δx of the stage for a cloud of 6×10^4 atoms prepared at a trap depth of 120 μK (corresponding to a laser beam power of 230 mW). Figure 1.12 (b, top) shows the trajectory of the center of mass of the cloud for a constant acceleration and deceleration of 1 mm/s^2 up to a maximum velocity of 1 mm/s, with the translation stage displacement varying between ± 3 mm along the direction of propagation of the beam. The slope extracted is 0.941(12), which reveals a small deviation from the perfect horizontal alignment of the beam. The corresponding losses in atom number, shown in Fig. 1.12 (b, bottom), increases with displacement. However, a displacement of the atoms of 230 μm, used for the mixing procedure described in Sec. 2.2, corresponds to a loss of less than 10%. Figure 1.12 (c) instead shows the transport efficiency as a function of a constant acceleration in the range allowed by the translation stage, which can reach up to 10 mm/s^2. Here we have prepared a thermal cloud of 8×10^4 atoms at a trap depth of 50 μK (corresponding to a laser beam power of 96.5 mW), fixing the displacement to 230 μm and the scattering length to $a_{12} \simeq -300\ \mathrm{a}_0$. The change in the acceleration does not affect the number of atoms left after the displacement of the stage. Indeed, at this trap depth, the dipole trap is not significantly altered by the force imposed on the atoms, regardless of the acceleration. The resulting potential is tilted but still confining. We calculated that for the

---

[18] Only recently, we implemented a notch filter to block the DT light

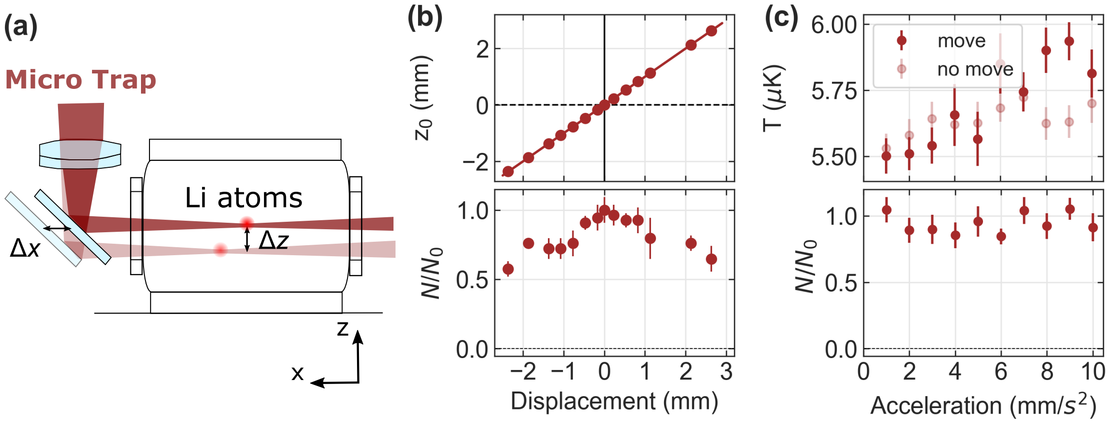

FIGURE 1.12: Transport of Li atoms trapped in the MT. (a) Sketch of the transport setup. The microtrap beam is focused by an achromatic doublet with a focal length of 25 cm and addressed through reflection by a dichroic mirror into the chamber of science. The dichroic mirror is mounted on the translational stage. A displacement of the stage of Δx corresponds to a vertical displacement of the focal position of the gaussian beam of the same quantity $\Delta z = \Delta x$. (b) Position of the center of mass of the cloud along the vertical direction z_0 and transport efficiency N/N_0 as a function of the displacement of the stage at a maximal acceleration of 10 mm/s^2 and a trap depth of 120 μK. (c) Temperature and transport efficiency over a round trip as a function of the acceleration of the stage, for a displacement of 230 μm and a power P = 96.5 mW and corresponding to a trap depth of U/k_B = 50 μK. The measurement in (b) has been performed at an offset magnetic field of 526 G, where $a \simeq 0\ a_0$, while the one in (c) was at 320 G, where $a \simeq -300\ \mathrm{a}_0$.

maximum acceleration allowed by the stage of 10 mm/s^2, the potential is always confining until the trap depth is deeper than 50 nK. However, we observed heating of 10% for an acceleration > 8 mm/s^2.

The atoms loss during the transport are due to vibrations transmitted to the laser beam, causing fluctuations in the central position of the trapping potential. When these vibrations match the trapping frequencies, they heat the cloud and lead to subsequent losses. Figure 1.13 (a) shows the transport efficiency as a function of the trap depth over a displacement of the cloud of 1.6 mm at an acceleration of 10 mm/s^2. The trap depth is varied between 50 μK and 120 μK, and the efficiency decreases for trap depths below 80 μK, corresponding to an axial trapping frequency of about 200 Hz. The corresponding position fluctuation spectrum is recorded and the single-sided power spectrum is calculated as $S(\nu) = 2\mathrm{FFT}(\nu)\mathrm{FFT}^*(\nu)/\mathcal{N}$, where $\mathcal{N}$ is the number of data points and $\mathrm{FFT}(\nu)$ is the Fast Fourier Transform of the position fluctuations of the translation stage [Freund, 2022]. The results are averaged over 10 repetitions and a rolling average is taken over 8 Hz. As radial frequencies, which are on the order of several kHz, are insensitive to mechanical vibrations, the analysis focuses on the axial trapping frequencies. The spectrum recorded during the motion was compared to the spectrum obtained for no motion, taken on the same time scale, i.e. 600 ms. Following Savard *et al.* [1997], the energy-doubling time $T = \langle x^2 \rangle / (\pi^2 \nu^2 S(\nu))$, for trapping frequency ν and spectrum $S(\nu)$, can be

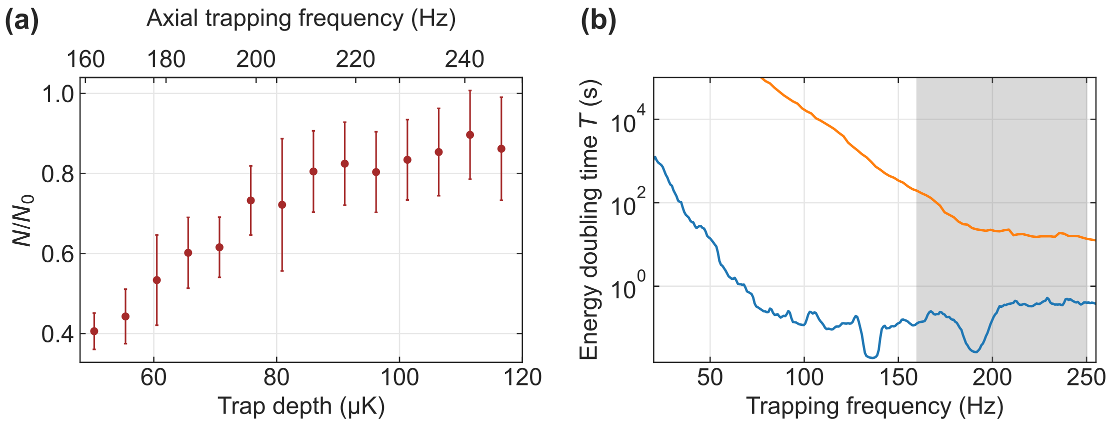

FIGURE 1.13: Transport efficiency as a function of the trap depth. (a) Transport efficiency for a non-interacting sample over a displacement of 1.6 mm at an acceleration of 10 mm/s^2. The efficiency N/N_0 is expressed as the ratio between the number of atoms before and after the displacement. (b) Energy-doubling time T given by the position fluctuation spectrum as a function of the trapping frequencies, for the stage in motion (blue) and at rest (orange). The gray shaded area indicates the range of trapping frequencies corresponding to the interval of trap depth in (a). There is a broad minimum centered at around 190 Hz. For this reason we chose to transport the atoms once they are stored in a potential with a trap depth > 80 μK. These pictures are adapted from [Freund, 2022].

calculated as shown in Fig. 1.13 (b). Therefore, the energy-doubling time is compared to the efficiency of the transport over the range of frequencies corresponding to the range of trap depth 50 μK to 120 μK, corresponding to axial trapping frequencies between 160 Hz and 260 Hz. The energy-doubling time decreases by a factor of 10 in the range between 200 Hz and 70 Hz, while the efficiency drops to zero at a trap depth of 25 μK (115 Hz) and remains low down to 10 μK (70 Hz). The simultaneous decrease in transport efficiency and energy-doubling time at around 200 Hz can partially explain the losses during transport while keeping the atoms trapped at a trap depth lower than 80 μK. This observation motivated us to ramp up the power of the microtrap before transport in the mixing sequence presented in Sec. 2.2.

1.4 Feshbach magnetic field

Magnetic field stability is fundamental for the experiments performed in optical dipole traps where it is important to control and tune the interactions between the atoms close to Feshbach resonances (see Sec. 2.1.2). Homogeneity and long-time stability of our magnetic fields allowed in the past to perform high-resolution Feshbach-spectroscopy [Zhu *et al.*, 2019b,a; Gerken *et al.*, 2019] with a minimal step-size of 1 mG, enabling the detection of a splitting in the loss feature up to 20 mG in a ^{6}Li-^{133}Cs mixture and 6 mG in a spin polarized sample of ^{6}Li.

In the following, I focus on some important features of the Helmholtz Feshbach coils used to tune the interactions between Li and Cs atoms. In section 1.4.1 I will show a

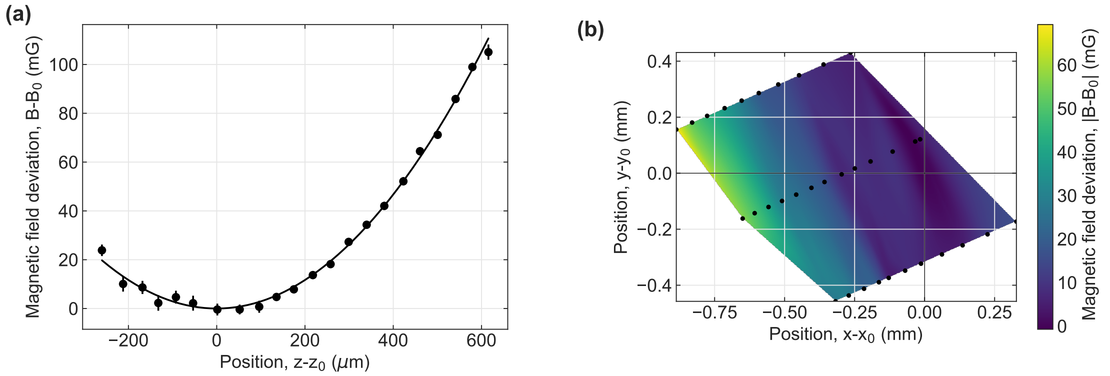

FIGURE 1.14: Tomography of the magnetic field produced by the Feshbach coils: (a) along the z-axis (direction of gravity), (b) in the horizontal xy plane. The magnetic field is measured by microwave spin flips on Cs atoms confined in the RT and it is given as the deviation from its minimum value $B_0 = 1074.95$ G. In (a) the solid line is a parabolic fit to the data that yields a curvature of 0.027 cm^{-2}. In (b) we used cubic interpolation to the black data points. The spatial magnetic field deviation is given relative to the saddle point (x_0, y_0). Both pictures are adapted from [Gerken, 2022].

tomographic measurement performed to map the residual magnetic field gradient of the Feshbach coils. I will then explain our magnetic field calibration procedure in section 1.4.2.

1.4.1 Magnetic field tomography

The placement of the coils in the re-entrant view-ports prevents the realization of a perfect Helmholtz configuration leading to a finite curvature of the magnetic field at the center of the chamber. In order to detect the magnetic field inhomogeneity along the z axis we adopted a tomographic approach. We prepare Cs atoms in the RT in $|F, m_F\rangle = |3, 3\rangle$ and perform microwave spectroscopy to the $|4, 4\rangle$ state by detuning the microwave frequencies such that atoms are selectively excited at different positions with pulses of 35 μs. We can then directly record the center position of the atom cloud from a gaussian fit for different microwave detunings and, by means of the Breit-Rabi formula, calculate the corresponding magnetic field. To have a complete tomography, we move the cloud by means of the piezo-mirror over a region of $\sim$1 mm.

The variation of the measured magnetic field from the bias field of B$_0$=1074.95 G is shown in Fig. 1.14 and can be reproduced by a parabolic function $B(z) - B_0 = B_0 c_z z^2$, where $c_z = 0.027$ cm^{-2} is the obtained coefficient for the curvature along z-direction. Each fit result is the average of 5 pixels (≈ 40 μm). We measure an uncertainty of fluctuations of 16 mG over a timescale of several hours. However, this systematic error is irrelevant for estimating the finite curvature of the coils. The obtained profile shows that for a displacement of a few hundreds μm from the center, the variation in the magnetic field amounts to just a few mG. For a typical experiment with a Li-Cs mixture cloud at 400 nK, we expect thermal cloud sizes of respectively $\sigma_{Li} = (140, 10, 10)$ μm and $\sigma_{Cs} = (70, 5, 6)$ μm. We can see that in the z-direction the magnetic field variation due to a residual magnetic field gradient is < 1 mG. We take as the upper limit the variation obtained for the Li cloud in the direction of its major elongation. This is estimated by considering that $B(x) - B_0 = B_0 c_x \sigma_{Li,x}^2$ with $c_x = c_z/2 = 0.0134\ \mathrm{cm}^{-2}$ and a large bias field of 1000 G. For a typical size of $\sigma_{Li,x} \sim 150\ \mu$m we achieve an uncertainty of 3 mG.

1.4.2 Calibration of the magnetic fields

I discuss here the procedure of calibration of the magnetic field. This is performed by driving radio-frequency spectroscopy on Li hyperfine states. For these measurements, we prepare a spin-polarized Li sample in spin state $|1/2, 1/2\rangle \rightarrow |1/2, -1/2\rangle$ by applying a rectangular radio-frequency pulse. The remaining number of Li atoms in state $|1/2, 1/2\rangle$ is recorded and fitted with a proper line-shape function. We obtain the magnetic field strength by comparison to the Breit-Rabi energy difference. The typical statistical error in the determination of the resonance frequency is at the 1 Hz level, corresponding to a magnetic field accuracy of less than 1 mG (see also [Häfner, 2017]). By repeating the measurements for different values of the control parameter, we have a calibration given by a linear function between the magnetic field and the control parameter. This procedure leads to a maximal uncertainty of 9 mG [Ulmanis, 2015]. In the work by [Ulmanis, 2015], the total systematic error in the magnetic field determination was also estimated. Here, residual magnetic field gradient, long-term stability, length of the experimental sequence and calibration were considered as the main sources of systematic error. By assuming all these uncertainties uncorrelated and by adding them up quadratically, a total systematic error that amounts to 16 mG was obtained. Such a good magnetic field stability permitted to have high resolution in atom-loss spectroscopy [Zhu *et al.*, 2019b,a; Gerken *et al.*, 2019].

1.5 Detection tools

To obtain information on the physical properties of ultracold gases we use spectroscopic methods [Vale and Zwierlein, 2021] and absorption imaging [Ketterle *et al.*, 1999]. In Sec. 1.5.1, I introduce the setup used for radiofrequency and microwave spectroscopy, as well as the energy state investigated in the experiments. In Sec. 1.5.2, I give an overview of absorption imaging for our double species experiment.

1.5.1 Radio-frequency and microwave spectroscopy

In the context of this thesis, spectroscopic techniques such as radio-frequency and microwave spectroscopy are mainly used either to probe the polaron energy or as a tool to calibrate the magnetic fields. Radio-frequency spectroscopy of Li atoms was intended to address Li impurities in a Bose-Einstein condensate by quenching Li impurities from the non-interacting Li$|1\rangle \oplus$Cs$|1\rangle$ state to the interacting Li$|2\rangle \oplus$Cs$|1\rangle$ state at around 888.6 G. Similarly, Raman spectroscopy, the setup and characterization of which are described in the context of Fermi polarons in Sec.3.2.2, has been implemented to probe Cs impurities

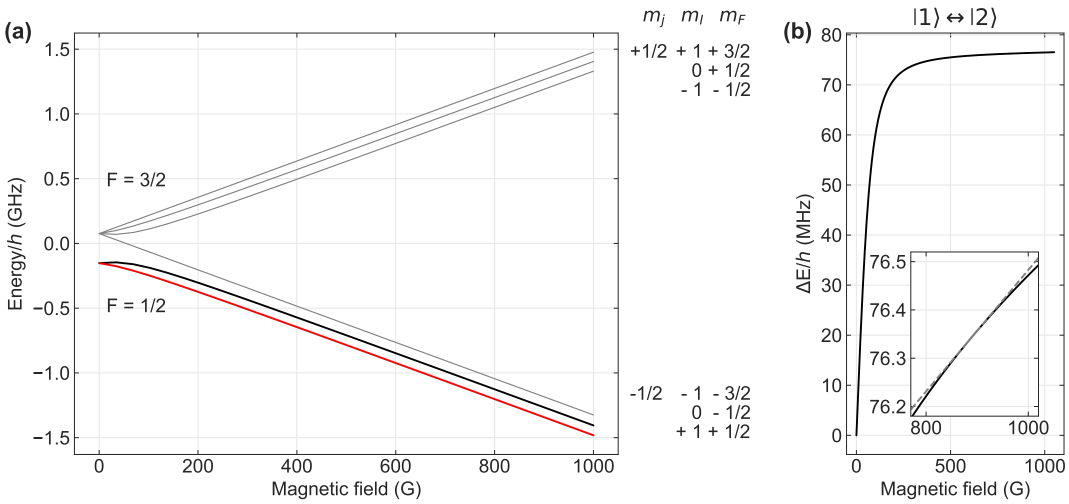

FIGURE 1.15: (a) Energy levels for the hyperfine states of ^{6}Li in its electronic ground state as a function of the magnetic fields. Energy for the state $|1/2, 1/2\rangle \equiv \mathrm{Li}|1\rangle$ is highlighted in red, while for $|1/2, -1/2\rangle \equiv \mathrm{Li}|2\rangle$ is in black. (b) Energy difference between the states $|1/2, 1/2\rangle$ and $|1/2, -1/2\rangle$. The inset is a zoom on the region between 800 G and 1000 G. The dashed line is a linear fit of the energy difference in the range between 880 and 900 G, which gives a difference in the magnetic moments of $h \times (1.256 \pm 0.002)$ kHz/G and provides a rule of thumb for which 1 kHz corresponds to 800 mG. In all plots, the energy is expressed in units of h.

in a Li-Fermi sea by driving transitions from the interacting $\mathrm{Li}|2\rangle \oplus \mathrm{Cs}|1\rangle$ state to the non-interacting $\mathrm{Li}|2\rangle \oplus \mathrm{Cs}|2\rangle$ state at around 888.6 G. On the other hand, both radio-frequency on Li atoms between $\mathrm{Li}|1\rangle \leftrightarrow \mathrm{Li}|2\rangle$ and microwave on Cs atoms between $\mathrm{Cs}|1\rangle \leftrightarrow \mathrm{Cs}|4, +4\rangle$ are used for the magnetic field calibration, as already described in Sec. 1.4.1 and Sec. 1.4.2 respectively.

Breit-Rabi diagrams for ^{6}Li and ^{133}Cs. The Zeeman effect results in the splitting of the energy levels of the atomic hyperfine states with total angular momentum F, according to their projection m_F along the quantization axis. This phenomenon is exemplified in the Breit-Rabi diagrams for ^{6}Li and ^{133}Cs atoms in their electronic ground states, shown in Fig. 1.15 and Fig. 1.16. In this thesis, we identify atomic states by their total angular momentum F and projection m_F at zero magnetic field, expressed as $|F, m_F\rangle$. The Zeeman effect allows tuning the energy difference between various hyperfine and electronic levels.

We use Li atoms prepared in the Zeeman states $|1/2, 1/2\rangle$ or $|1/2, -1/2\rangle$, as described in Fig. 1.15 (a). In this thesis, we identify these two states as

$$\mathrm{Li}\,|1\rangle = |F = 1/2, m_F = 1/2\rangle\,, \tag{1.11}$$

$$\mathrm{Li}\,|2\rangle = |F = 1/2, m_F = -1/2\rangle\,. \tag{1.12}$$

In the region between 880 and 900 G, the difference in the magnetic moments between these two states is $h \times (1.256 \pm 0.002)$ kHz/G and provides a rule of thumb for which 1

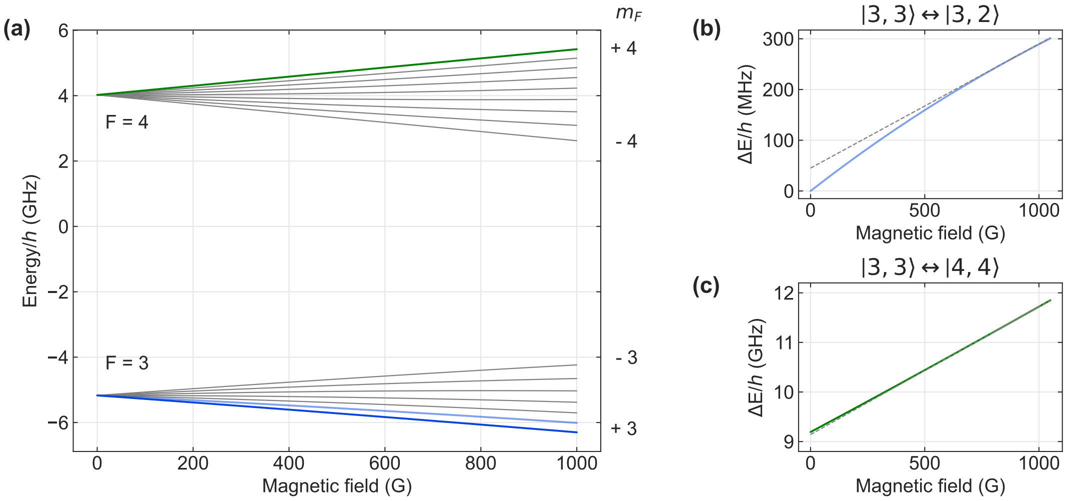

FIGURE 1.16: (a) Energy levels for the hyperfine states of ^{133}Cs in its electronic ground state as a function of the magnetic fields. The highlighted curves represent the states $|3, +3\rangle$, in blue, $|3, +2\rangle$, in light blue, and $|4, +4\rangle$, in green. (b) and (c): Energy difference between respectively, $|3, +3\rangle$ with $|3, +2\rangle$, and $|3, +3\rangle$ with $|4, +4\rangle$. In (b), the dashed line is a linear fit of energy difference in a range between 880 and 900 G, which gives a difference in the magnetic moments of $h\times(244.8 \pm 0.1)$ kHz/G. This provides us a rule of thumb for which 1 kHz corresponds to 4 mG. In (c), considering a range between 800 and 1000 G, the fit gives a difference in the magnetic moment of $h\times(2.578 \pm 0.001)$ MHz/G: here, 1 kHz corresponds to 0.4 mG. In all plots, the energy is expressed in units of h.

kHz corresponds to 800 mG (see Fig. 1.15 (b)).

The energy states that we consider for Cs, as shown in Fig. 1.16 (a), are the ground state $|3, +3\rangle$, where we prepare our mixture, the first excited state $|3, +2\rangle$, which we use as the "non-interacting" state for the Fermi polaron protocol experiment, and the state $|4, +4\rangle$, which we use to calibrate the magnetic fields. In particular, in this thesis the two lowest states of the hyperfine ground state are named as

$$\mathrm{Cs}\,|1\rangle = |F = 3, m_F = 3\rangle\,, \tag{1.13}$$

$$\mathrm{Cs}\,|2\rangle = |F = 3, m_F = 2\rangle\,. \tag{1.14}$$

The difference in magnetic moments in the range between 880 and 900 G, that is between $|3, +3\rangle$ and $|3, +2\rangle$ is $h\times(244.8 \pm 0.1)$ kHz/G (see Fig. 1.16 (b)). This gives us a rule of thumb that 1 kHz corresponds to 4 mG. In the range between 800 and 1000 G, the difference in magnetic moment between $|3, +3\rangle$ and $|4, +4\rangle$ is $h\times(2.578 \pm 0.001)$ MHz/G: here 1 kHz corresponds to 0.4 mG (see Fig. 1.16 (c)).

Radio-frequency spectroscopy setup. The current radio-frequency (RF) setup was designed to amplify the signal at 76 MHz, in order to drive fast transitions between the

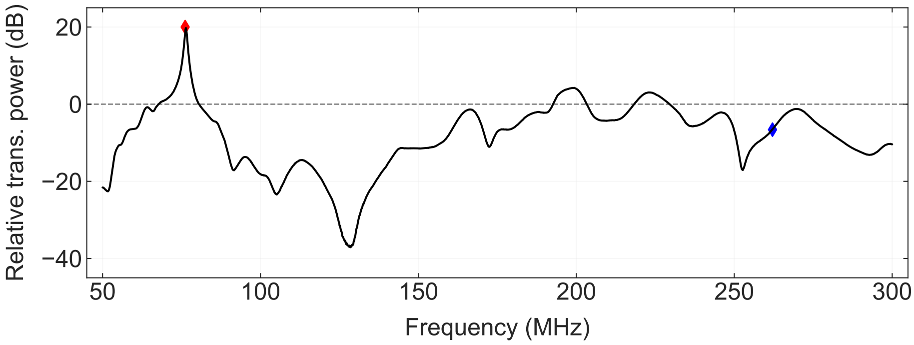

FIGURE 1.17: Measured transmitted relative power spectrum (in dB) of our RF-antenna at a power of -20 dBm. The antenna is impedance-matched at 76.426(9) MHz (red diamond). The blue diamond marks the transition energy for Cs between state $|3, +3\rangle$ and $|3, +2\rangle$ at 890 G. The ratio of powers transmitted at 76 MHz and 260 MHz is around -30 dB.

Zeeman states of Li $|1/2, 1/2\rangle$ or $|1/2, -1/2\rangle$ at magnetic fields around 890 G. A radio-frequency generator[19], which allows driving frequencies between 250 kHz and 3 GHz, produces a typical output frequency of 76 MHz. The signal is amplified[20] up to 100 W before being emitted by a double loop antenna, which is impedance-matched at 76.426(9) MHz and mounted inside the chamber of science in vacuum (see also Tran [2022]). Measured transmitted relative power spectrum (in dB) of our RF-antenna at a power of -20 dBm is shown in Fig. 1.17. Critical to this setup is the protection of the RF antenna inside the vacuum chamber, which is done via an interlock system that prevents overheating during operation. The pulse duration is controlled by an FPGA control system, with a Rb clock[21] serving as a 10 MHz reference oscillator for the frequency generator. The shape of the RF signal can be modified by combining the RF signal with an external pulse of an arbitrary waveform. This waveform can be, for example, a rectangular function, as shown in Fig. 1.18 (a), or a Blackman function, as shown in Fig. 1.18 (b). Blackman pulses effectively eliminate the sidelobes that are inherent to rectangular pulses. However, this results in a notable broadening of the width in the frequency domain when compared to the rectangular pulses. Details about the performance of our RF setup can be found in Filzinger [2018]

In order to drive transitions on the lowest Cs Zeeman states for Fermi polaron detection, we initially considered utilizing the existing RF antenna. However, as illustrated in Fig. 1.17, the ratio between the powers transmitted at 76 MHz and 260 MHz is approximately -30 dB. This would result in a reduction of the Rabi frequencies by a factor of approximately 30. We evaluated a series of options, which however resulted to be unfeasible. (i) Substitution of the electronic circuit impedance-matched for Cs was not possible, as the antenna was required to prepare Li atoms either $|1/2, 1/2\rangle$ or $|1/2, -1/2\rangle$

---

[19] Agilent E4421B

[20] Mini Circuits ZHL-100W-52+

[21] SRS FS 725

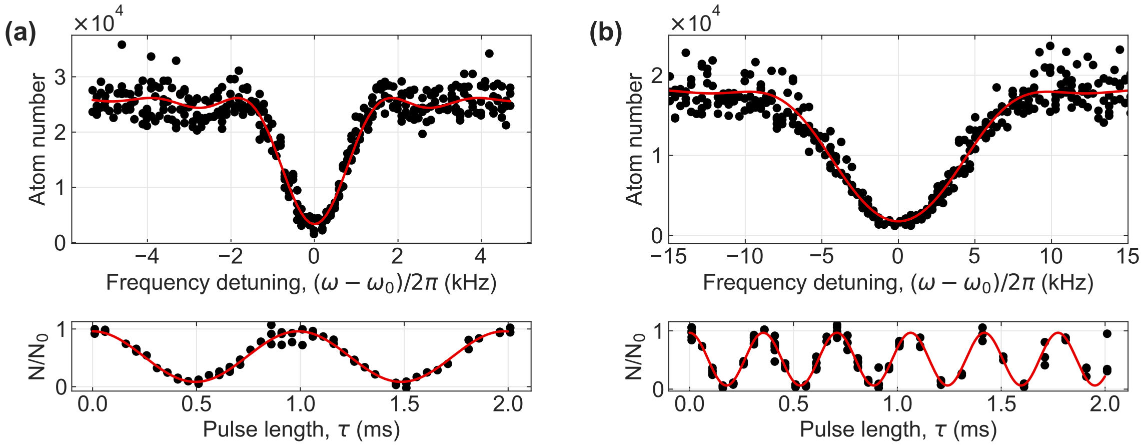

FIGURE 1.18: Radio-frequency energy spectra of the $|1/2, 1/2\rangle$ to $|1/2, -1/2\rangle$ transition of Li. (a) Spectrum taken with RF pulses of square temporal shape for -10 dBm and a $\pi-$pulse of 0.5 ms (top). Rabi oscillation at resonance $\Omega_0 = (1.010 \pm 0.005)$ kHz (bottom). (b) Spectrum taken with +10 dBm and a $\pi-$pulse of 0.18 ms (top). Rabi oscillation at resonance $\Omega_0 = (2.819 \pm 0.005)$ KHz (bottom). For the Blackman pulse the sidelobes are strongly suppressed.

on a routine basis during the experimental sequence. (ii) Implementation of a switchable circuit would have required a significant investment of resources that was not affordable in a reasonable timescale. (iii) Construction and placement of a new antenna outside was considered and initiated. The optimal placement for the antenna would have been at the top, but due to limited space, it was necessary to position it laterally, which resulted in a suboptimal coupling with the stainless steel chamber. Finally, we opted for an optical approach based on two-photon Raman spectroscopy, detailed in Sec. 3.2.2. This approach allowed us to overcome all these issues.

Microwave spectroscopy setup. For Cs atoms a microwave generator[22], which allows driving frequencies between 8 kHz and 12.7 GHz, produces a typical output frequency of 9.2 GHz, which is amplified[23] before being emitted with a horn[24]. As for radio-frequency, the pulse duration is controlled by an FPGA control system, and a Rb clock serves as 10 MHz reference oscillator to the frequency generator. This setup is implemented to drive transitions between $F = 3 \leftrightarrow F = 4$. A detailed description of the MW setup was reported in [Tran, 2022] and investigation of Cs atoms were described in [Gerken, 2022].

1.5.2 Double-species absorption imaging

Absorption imaging is the technique we use for extracting information on the atomic clouds, such as atom number, density distributions, and temperature [Ketterle *et al.*, 1999]. A resonant light beam, tuned to specific fine-structure splitting transitions (see

---

[22] Rohde & Schwarz SMA100B
[23] Mini Circuits ZVE-3W-183+
[24] Tactron WR90

Fig. 1.3), illuminates the atoms. They absorb the light depending on their spatial distribution, creating a shadow of the atomic cloud that is recorded by a CCD camera positioned behind them. For each species, we take three different images: (i) with atoms, displaying an intensity distribution $I_{abs}(x,y)$; (ii) with laser light only, $I_{div}(x,y)$; and (iii) five averaged pictures with neither atoms nor light, capturing only readout and thermal noise, denoted as I_{bg}. The transmission of the light through the atomic cloud is calculated using the Beer-Lambert law:

$$T(x,y) = \frac{I_{abs}(x,y) - I_{bg}(x,y)}{I_{div}(x,y) - I_{bg}(x,y)} = e^{-\sigma_{abs}\int n(x,y,z)dz} \tag{1.15}$$

where $n(x,y,z)$ is the density distribution and σ_{abs} is the absorption cross-section[25]. The column density, obtained by integrating the density distribution along the direction of light propagation, is given by

$$n(x,y) = \int n(x,y,z)dz = -\frac{1}{\sigma_{abs}}\log(T(x,y)) = -\frac{1}{\sigma_{abs}}OD(x,y) \tag{1.16}$$

where $OD(x,y)$ is the optical density, defined as $OD(x,y) = -\log(T(x,y))$. By fitting the column density with a two-dimensional Gaussian distribution, we extract both the total atom number and the $1/e^2$ cloud radii. Specifically, we use time of flight (TOF) expansion to measure temperatures and initial cloud sizes. By measuring the ballistic expansion of the cloud after switching off the trapping potential and assuming that the velocity distribution of the thermal cloud follows a Maxwell-Boltzmann distribution, the evolution of the cloud size with respect to the time of flight follows

$$\sigma_{x,y,z}(t_{\mathrm{TOF}}) = \sqrt{\sigma^2_{x,y,z}(t_{\mathrm{TOF}} = 0) + \frac{k_B T}{m}t^2_{\mathrm{TOF}}}, \tag{1.17}$$

where m is the atomic mass. The initial sizes and temperature T are extracted as free parameters. We can assume that the expansion is purely ballistic if $\omega^2_{x,y,z}t^2_{\mathrm{TOF}} \gg 1$; in this case, the temperature T does not depend, to a good approximation, on the initial size of the cloud. Conversely, it is important to consider the initial sizes if $\omega^2_{x,y,z}t^2_{\mathrm{TOF}} \approx 1$. Alternatively to TOF measurements, the initial size can be obtained either by imaging the cloud *in situ*, which means just after that the trapping potential is switched off, or by calculating $\sigma_{x,y,z}(t_{\mathrm{TOF}} = 0) = \omega^{-1}_{x,y,z}\sqrt{\frac{k_B T}{m}}$, from an independent determination of the trapping frequencies $\omega_{x,y,z}$ and temperature T.

In circumstances where a global fit model is not feasible, or when it is useful to obtain detailed spatial information just locally, such as in the measurements in Sec. 3.2.2 and Sec. 3.3, the approach for the determination of the atom number is different. Instead of relying on a continuous model fit, we work directly with the discretized column density provided by the pixels of the CCD chip, with pixel sizes s_x and s_y. To determine the total atom number N, we sum the optical density OD values over all the pixels. This can be

---

[25] For negligible saturation ($I \ll I_{sat}$) and for near-resonant light $\sigma(z) \approx \sigma_0$.

expressed as [Ketterle and Zwierlein, 2008]

$$N = \int n(x,y)\,dx\,dy = \frac{s_x s_y}{M\sigma_{abs}} \sum_{\text{pixels}} OD(x,y), \tag{1.18}$$

where M is the optical magnification. Additionally, when dealing with relative quantities, such as the ratio of the atom number to a maximum value N/N_{max}, the calculation simplifies further. The ratio can be directly derived from the total optical density OD_{tot} to its maximum value OD_{max}

$$\frac{N}{N_{\text{max}}} = \frac{OD_{\text{tot}}}{OD_{\text{max}}} \tag{1.19}$$

as the pixel sizes s_x and s_y and the absorption cross-section σ_{abs}, which are constants, cancel out, it remains a dimensionless ratio that is easy to calculate. This simplification is particularly advantageous when evaluating relative changes or variations in atom numbers without the need for an absolute calibration of each imaging parameter.

Imaging at low and high magnetic fields. For both species, we need to image the cloud at zero magnetic fields, for example after the MOT and sub-Doppler cooling schemes, and at high magnetic fields once the atoms are trapped in the dipole traps, typically between 800 G and 1000 G. At high magnetic fields, we perform spin-state selective imaging, as the imaging frequencies depend on the Zeeman splitting. This method requires independent diode laser sources, which are stabilized by an offset lock to the low-field lasers [Schünemann *et al.*, 1999]. The detailed setup description is presented in [Schoenhals, 2013] for Cs and [Heck, 2012] for Li, respectively.

For Cs atoms, the imaging scheme consists of two beams, one for "imaging", whose frequency is adjusted to be resonant with the $F = 4 \to F' = 5$ transition, and another for "repumping", which is used to pump the atoms initially prepared in the $F = 3$ state to the $F = 4$ state. This scheme is valid for both low and high magnetic fields, but in the latter scenario the two beams come from two independent lasers. The detailed scheme can be found in [Schoenhals, 2013]. As discussed in Sec. 2.3.1, this scheme does not allow distinguishing between population of atoms initially prepared in the $|3,+3\rangle$ or $|4,+4\rangle$ state.

For Li atoms, imaging at low magnetic fields involves the transition from the $F = 1/2$ ground state manifold to the unresolved $F' = 1/2, 3/2, 5/2$ excited manifold. As Li atoms decay back to the $F = 3/2$ hyperfine state, an additional repumping beam is used. After the imaging pulse is turned on, the repumping beam is switched on for a few hundred microseconds to optically pump the atoms back into the $F = 1/2$ manifold. At high magnetic field, the two hyperfine sub-levels are no longer degenerate, allowing selective imaging of different states by varying the frequency of the high-field imaging laser. Recent improvements on the setup of Li high-field imaging is presented in [Schürg, 2024]. Additionally, we use spin-selective spectroscopy to prepare Li atoms in a single spin state by applying a resonant light pulse (see Sec. 2.2).

Cameras: resolution and orientation. In our systems three CCD cameras are currently implemented: one to take pictures of the clouds along the horizontal direction, and two along the vertical direction. The camera for imaging along the horizontal plane is a Ximea MD028MU-SY CCD camera. Along the vertical direction there is an AVT Guppy F-038 NIR camera and an Andor Ikon-M 934 back-illuminated Deep Depletion CCD camera. The former is currently used just for checking the position of the clouds after MOT and sub-Doppler cooling schemes, whereas the latter is the camera we use for double-species imaging. This camera features a fast kinetic (FK) mode that allows imaging both species in the same experimental cycle in a time frame of ≈ 1.5 ms. This is achieved by imaging on a subset of pixels on the CCD chip. After capturing the first image, the charges are quickly shifted to an unused subset of pixels. This allows us to take a second image on the initial subset of pixels before reading out the chip. The coating BEX2-DD allows a similar quantum efficiency of about 80% [Renner, 2014] for both species. The resolution of our imaging setup (with an NA = 0.15) is below 2 μm [Filzinger, 2018] and enables us to resolve density distributions of both bosonic and fermionic degenerate quantum gases. A comprehensive description of the imaging setup can be found in [Renner, 2014; Eberhard, 2016; Häfner, 2017]. Detailed information on noise analysis is available in [Filzinger, 2018], while [Klaus, 2019; Rautenberg, 2021] discuss estimates of the resolvable atom numbers. This camera was used here for the first time to capture images of the two atomic clouds within the same experimental cycle. The measurements in this thesis, involving Li and Cs trapped together, were taken with the Andor camera in FK mode. Conversely, the characterization of the Li cloud was performed using the Ximea camera. A detailed numerical simulation of the imaging process involving all the possible noise sources of both Ximea and Andor cameras can be found in [Borchers, 2023].

Chapter 2

A Li Fermi Sea with Cs impurities

The heteronuclear Fermi-Bose system formed by light fermionic ^{6}Li and heavy bosonic ^{133}Cs atoms is the combination with the largest mass ratio among all the stable alkali isotopes. The large mass imbalance combined with the suitable scenario of Feshbach resonances at high magnetic fields [Repp *et al.*, 2013; Tung *et al.*, 2013; Pires *et al.*, 2014a] gives access to the physically relevant limit of heavy particles coupled to a degenerate Fermi Sea, a non-trivial paradigm of many-body systems. Nevertheless, the large mass difference and species dependent polarizability pose several experimental challenges for slowing, cooling and trapping the two species together. Therefore, the development of an efficient experimental sequence to produce two-component mass-imbalanced quantum gases deserves particular attention.

In this chapter I present the experimental scheme implemented for the realization of low-density Cs samples prepared in the Cs ground state $|3,+3\rangle$ mixed with a degenerate Fermi gas prepared in the Li$|2\rangle$ state. Although some aspects of the mixing scheme were originally designed for the realization of a system of Li impurities immersed in a Cs-Bose Einstein condensate, the same scheme was then adapted for the complementary scenario aiming at the realization of Fermi polarons. In Sec. 2.1 I revise important quantities for trapped Bose and Fermi gases and for two-body elastic scattering at ultracold temperatures. I present Li-Cs Feshbach resonances for the scattering channels Li$|1\rangle\oplus|3,+3\rangle$ and Li$|2\rangle\oplus|3,+3\rangle$ and discuss challenges and implemented solutions for the realization of ultracold Li-Cs mixtures. In Sec. 2.2 I describe the experimental sequence for mixing Li and Cs atoms, following the individual steps. I first present the realization of the highly degenerate Fermi Sea, then the realization of the low-density Cs Bose gas, and finally the procedure for overlapping and mixing the two species using a bichromatic approach, where Li atoms are trapped in the tightly confining and mobile microtrap (MT) at the Cs tune-out wavelength, while Cs is trapped in the dimple trap (DT). In Sec. 2.3 I present the experimental results about the loss processes that occur in our mixed system, focusing on the one-body losses induced by light at the tune-out wavelength on Cs atoms and on the Li-Cs three-body losses. The loss spectroscopy measurements are performed near the Li-Cs Feshbach resonance at 888.6 G. In Sec. 2.4 I summarize the main results and briefly discuss possible improvements of the setup for Fermi polaron experiments.

2.1 Interacting Bose-Fermi Li-Cs mixtures

Before starting our journey on the route for preparing the Li-Cs mixture, I introduce important quantities for trapped Bose and Fermi gases (see Sec. 2.1.1) as well as fundamental concepts about scattering theory and Feshbach resonances (see Sec. 2.1.2). I explain how resonant scattering behavior in ultracold collisions leads to tunable interactions between atoms and I provide an overview of the interspecies Li-Cs Feshbach resonances for the scattering channels between Li, either in the ground state Li$|1\rangle$ or in the excited state Li$|2\rangle$, and Cs in the ground state $|3,+3\rangle$. In Sec. 2.1.3 I explain the main experimental challenges for the realization of ultracold degenerate Li-Cs mixtures and illustrate the solution implemented in the course of this work.

2.1.1 Bose and Fermi quantum gases in harmonic traps

All constituents of matter, either elementary or composite particles, can be divided into bosons and fermions, depending on whether their spin is integer or half-integer. Ultracold quantum gases are thus classified as either fermionic or bosonic, based on the spin of the atomic species used. According to the symmetrization and antisymmetrization postulate for bosons and fermions, respectively, the mean occupation number of a single-particle energy eigenstate with energy ϵ is given by [Goodstein, 1985]

$$f_{\pm}(\epsilon) = \frac{1}{e^{(\epsilon-\mu)/k_B T} \pm 1}, \tag{2.1}$$

where μ is the chemical potential fixed by the atom number N, and T is the temperature. In the thermal regime, when the atomic density is low or the temperature is high, i.e. $(\epsilon - \mu) \gg k_B T$, Eq. (2.1) approaches to the Maxwell-Boltzmann distribution $f(\epsilon) = e^{-(\epsilon-\mu)/k_B T}$, which is independent from the intrinsic nature of the particle. However, by lowering the temperature or increasing the atomic density the degenerate regime can be reached when the term $\pm$ 1 becomes relevant, leading to different energy distributions for bosons and fermions. Qualitatively, the occupation of low-energy states compared to a classical gas is expected to be enhanced for bosons, according to the $-$ term, and suppressed for fermions due to Pauli blocking, according to the $+$ term. The condition that marks the onset of quantum degeneracy is reached when the inter-particle spacing $n^{1/3}$ is comparable with the De Broglie wavelength

$$\lambda_{dB} = \sqrt{\frac{2\pi\hbar^2}{m k_B T}} \tag{2.2}$$

determined by the temperature T and the atomic mass m [Ketterle *et al.*, 1999]. The phase-space density $\rho = n\lambda_{dB}^3$, at this point, is on the order of unity and the individual wave functions start to overlap. Therefore, the particles exhibit collective phenomena. For a Fermi gas at $T = 0$, fermions fill up all the available states starting from the lowest energy level up to the Fermi energy $E_F = T_F k_B$. The Fermi temperature sets the temperature scale at which a Fermi gas deviates from the classical behaviour[1] [Ketterle and Zwierlein, 2008; Giorgini *et al.*, 2008]. On the other hand, a Bose gas, enters the degeneracy regime below a critical temperature T_C, when a macroscopic number of atoms occupy the ground state of the system leading to Bose-Einstein condensation (BEC) [Ketterle *et al.*, 1999; Pethick and Shmidt, 2001].

In this thesis we work with either thermal gases or non-interacting Fermi gases, trapped in optical dipole traps, which provide a confinement well described by harmonic potentials of the form

$$U(x,y,z) = \frac{1}{2}m(\omega_x^2 x^2 + \omega_y^2 y^2 + \omega_z^2 z^2), \tag{2.3}$$

where m is the mass of the particle, and $\omega_x, \omega_y, \omega_z$ are the trapping frequencies in three spatial directions. The harmonic approximation holds when the thermal energy $k_B T$ of an atomic cloud is much smaller than the potential depth U_0. Furthermore, in order to evaluate thermodynamic quantities in a harmonic potential, it is convenient to change from the representation of discrete energies to a continuous density of energy eigenstates. This is a good approximation when the thermal energy $k_B T$ of the system is much larger than the largest energy spacing in the harmonic potential, i.e., when $k_B T/\hbar \gg Max(\omega_x, \omega_y, \omega_z)$.

For finite temperature, the fugacity $q = \exp(\mu/(k_B T))$ parametrizes the degree of degeneracy of the gas and can be obtained numerically from

$$N = \int_0^\infty g(\epsilon) f(\epsilon) d\epsilon = \pm \frac{k_B^3 T^3 \mathrm{Li}_3(\pm q)}{\hbar^3 \bar{\omega}^3}, \tag{2.4}$$

where $Li_n(x)$ is the polylogarithmic function of n-th order and the ± is for either bosons or fermions, respectively. For a three-dimensional harmonic trapping potential, the density of energy states is $g(\epsilon) = \epsilon^2/(2\hbar^3\overline{\omega}^3)$, with $\overline{\omega} = (\omega_x\omega_y\omega_z)^{1/3}$ geometric mean trapping frequency. The three dimensional atomic density distribution $n(x,y,z)$ of a thermal cloud, centered at a position (x_0, y_0, z_0), is given by

$$n(x,y,z) = \frac{N}{(2\pi)^{3/2}\sigma_x\sigma_y\sigma_z} e^{-\left(\frac{(x-x_0)^2}{2\sigma_x^2} + \frac{(y-y_0)^2}{2\sigma_y^2} + \frac{(z-z_0)^2}{2\sigma_z^2}\right)}, \tag{2.5}$$

where the value $n_0 = n(x_0, y_0, z_0)$ denotes the peak density, and the cloud sizes are σ_x, σ_y and σ_z, where $\sigma_i = \sqrt{k_B T/(m\omega_i^2)}$ are the widths of the atomic clouds. For a Fermi gas, the Fermi energy is defined as the chemical potential at zero temperature, $E_F \equiv \mu(T=0)$ and it can be obtained from

$$N = \int_0^\infty g(\epsilon) f_+(\epsilon) d\epsilon \overset{T=0}{\equiv} \int_0^\infty g(\epsilon)\Theta(\epsilon - E_F) d\epsilon \tag{2.6}$$

being N the number of atoms for a given spin species and choosing the + term for the

---

[1] The effect is visible for $T/T_F < 0.6$ [Ketterle and Zwierlein, 2008].

energy distribution $f(\epsilon)$. The global Fermi energy in a three-dimensional harmonic potential is therefore $E_F = (6N)^{1/3}\hbar\bar{\omega}$. The local Fermi energy at position (x, y, z) in the trap can be defined as $\epsilon_F(\mathbf{r}) = \hbar^2(6\pi^2 n_{\mathrm{Li}}(\mathbf{r}))^{2/3}/(2m)$ [Ketterle and Zwierlein, 2008], which coincides with the relation for a uniform Fermi gas [Giorgini *et al.*, 2008]. The fugacity q is related to the Fermi energy by combining Eq. (2.6) with Eq. (2.4)

$$\frac{T}{T_{\mathrm{F}}} = [-6\mathrm{Li}_3(-q)]^{-1/3}. \tag{2.7}$$

To obtain the density distribution we combine Eq. (2.1) for fermions with Eq. (2.3) [Ketterle and Zwierlein, 2008; Giorgini *et al.*, 2008]

$$n(x, y, z) = \int d\mathbf{p} f(\mathbf{r}, \mathbf{p}) = -\Big(\frac{mk_BT}{2\pi\hbar^2}\Big)^{3/2}\mathrm{Li}_{3/2}\Big(-\exp\Big(\frac{\mu - U(x, y, z)}{k_BT}\Big)\Big) \tag{2.8}$$

For fermions, the density profile changes smoothly from the gaussian distribution for high temperatures to the zero temperature profile

$$n_F(x, y, z) = \frac{8}{\pi^2}\frac{N}{R_{Fx}R_{Fy}R_{Fz}} \times \Big[\max\Big(1 - \big(\frac{x^2}{R_{Fx}^2} + \frac{y^2}{R_{Fy}^2} + \frac{z^2}{R_{Fz}^2}\big)\Big)\Big]^{3/2} \tag{2.9}$$

with the Fermi radius $R_{Fi} = \sqrt{(2E_F)/(m\omega_i^2)}$. The profile of the degenerate Fermi gas has a rather flat top compared to the gaussian profile of a thermal cloud, as the occupancy of available phase-space cell saturates at unity.

2.1.2 Interactions in an ultracold Li-Cs mixture

The length scale on which interactions between neutral atoms take place is given by the short-range van der Waals potential, which scales as r^{-6} and has a finite range known as the van der Waals radius r_{vdW}. The temperature at which quantum degeneracy is reached is between 100 nK and 50 nK, λ_{dB} is about 1 μm. The range of interaction is given by the van der Waals radius $r_{\mathrm{vdW}}^{LiCs} = 45\ a_0$, $r_{\mathrm{vdW}}^{Cs} = 101\ a_0$ [Häfner, 2017], where $a_0 = 0.5292 \times 10^{-10}$ m is the Bohr radius. Those quantities satisfy the inequality $\lambda_{dB}, n^{1/3} \gg r_{vdW}$, meaning that the particles interact via two-body collisions.

Fundamentals of scattering theory. I will provide the fundamental concepts of scattering theory, following the review article by Dalibard [1999]. We consider a three-dimensional quantum gas characterized by a two-body interacting potential $V(\mathbf{r})$ that is radially symmetric short range and that decreases as $1/r^j$, $j > 1$. In the long distance term, the wave function, $\psi(\mathbf{r})$, that satisfies the Schrödinger equation

$$\Big[-\frac{\hbar^2}{2m}\nabla^2 + V(\mathbf{r})\Big]\psi(\mathbf{r}) = E\psi(\mathbf{r}), \tag{2.10}$$

where $\mathbf{r}$ is the relative coordinate and m is the reduced mass of the particle, can be written as a sum of an incoming plane-wave plus an outgoing spherical wave with k momentum along the axis of its initial motion

$$\psi_k(\mathbf{r}) \propto e^{ikz} + f(k,\theta)\frac{e^{ikr}}{r}. \tag{2.11}$$

where $f(k,\theta)$ is the the scattering amplitude. Since the relative distance between two particles $|r|$, given by $n^{1/3}$, is larger than r_{vdW}, the long range limit reflects the condition in ultracold gases quite well. All the relevant information are contained in the scattering amplitude which can be calculated expanding the wave-function $\psi(\mathbf{r})$ into the spherical-waves basis with angular momentum l. This expansion, inserted in the Schrödinger equation, leads to a radial equation that depends on l and that can be related to the centrifugal barrier inhibiting the scattering for $l > 0$ in the regime of small scattering energies. The centrifugal barrier for Li-Cs is on the order of 2 mK [Gerken, 2022] and thus collisions for lower temperatures can only occur due to isotropic s-wave scattering. The only effect of an elastic collision is a phase shift of δ_l for each spherical wave. In order to determine the scattering amplitude, it is necessary to take into account that it is not possible to distinguish between two scattering processes that differ only in terms of the permutation of the particles' positions

$$\frac{d\sigma_{indist}}{d\Omega} = |f(k,\theta) \pm f(k,\pi-\theta)|^2, \tag{2.12}$$

and the total cross-section is obtained by integrating it over the full solid angle

$$\sigma_{tot}(k) = \frac{4\pi}{k^2}\sum_{l=0}^{\infty}(2l+1)[1 \pm (-1)^l]\sin^2(\delta_l(k)). \tag{2.13}$$

The contribution to the total scattering cross-section is different from zero for polarized bosons (fermions), which corresponds to even (odd) values of l. At ultra-low temperatures, the De Broglie thermal wavelength, associated with the relative momentum k, far exceeds the van der Waals range of the interatomic potential. As such, similarly to a light wave imprinting on a scatterer much smaller than its wavelength, the resulting collision process is predominantly isotropic, i.e. s-wave (l=0). The scattering length in the limit of low energies is given by

$$a = -\lim_{k\to 0}\frac{\tan\delta_0(k)}{k}. \tag{2.14}$$

The s-wave cross-section for identical bosons is $\sigma(k) = 8\pi a^2/(1+k^2a^2)$, while for identical fermions is $\sigma(k) = 0$. Indeed, a Fermi gas interacting via s-wave scattering can only be realized with at least two different kinds of fermions which are then distinguishable. For distinguishable particles, $\sigma(k) = 4\pi a^2/(1+k^2a^2)$ and in the low energy limit $k \to 0$, $\sigma(k) = 4\pi a^2$. In the unitarity limit, when the scattering length exceeds the De Broglie wavelength $\lambda \sim k^{-1}$ and $k^2a^2 \gg 1$, the cross-section becomes independent of the scattering length, leading to $\sigma(k) = 4\pi/k^2$.

Moreover, for s-wave, the scattering properties are fully encoded in the s-wave scattering amplitude, which in turn can be expanded as

$$f(k) = -\frac{1}{ik + \frac{1}{a} - R^* k^2}. \tag{2.15}$$

The ultracold collisions are therefore characterized by two parameters which are the scattering length a and the effective range parameter R^*. While a depends on the presence of weakly bound (or virtual) molecular states near the energy threshold of the colliding atoms, R^* is essentially determined by the microscopic properties of the van der Waals interatomic potential [Petrov, 2012]. In particular, when the molecular state is above the scattering threshold, a is negative, corresponding to a net atom-atom attraction. On the other hand, the net interaction is repulsive when the molecular state is below the scattering threshold and thus a is positive.

The scattering processes are universal and can be described as a contact interaction [Ketterle and Zwierlein, 2008] with a pseudo-potential

$$V(\mathbf{r}) = g\delta(\mathbf{r}) \tag{2.16}$$

where $g = 4\pi\hbar^2 a/m$ is the interaction strength. The mean interaction energy in a sample with homogeneous density $n = N/V$ is given by

$$E_{int}(a) = gn = \frac{4\pi\hbar^2 n}{m} a \tag{2.17}$$

where the sign of the scattering length a leads to a different kind of mean-field interaction, i.e. attractive if a is positive, repulsive if a is negative.

Feshbach resonances. The scattering properties of a pair of atoms can be resonantly controlled by tuning the scattering length. A good introduction to Feshbach resonance is provided by Chin *et al.* [2010]. A magnetic Feshbach resonance occurs when the open scattering channel is brought into energy degeneracy, via the Zeeman effect, with a bound molecular state supported by a closed channel with a different magnetic moment. Since the two interaction potentials depend on the hyperfine states of the interacting particles, their magnetic momenta differ and the difference in their energy is given by $\Delta E = \delta\mu\Delta B$. Near the pole of the resonance B_0, the scattering length deviates from its background value a_{bg} and shows a strong dependence on the external magnetic field B, given by

$$a(B) = a_{bg}\left(1 - \frac{\Delta}{B - B_0}\right), \tag{2.18}$$

where Δ is the resonance width. In particular, the value and sign of $a(B)$ directly determine both the scattering cross-section of the atom pair and the strength of the interparticle interaction, i.e. attractive if $a(B) > 0$, repulsive otherwise. For large positive values of the scattering length, i.e. $a \gg R^*$, the binding energy E_b of the weakly bound

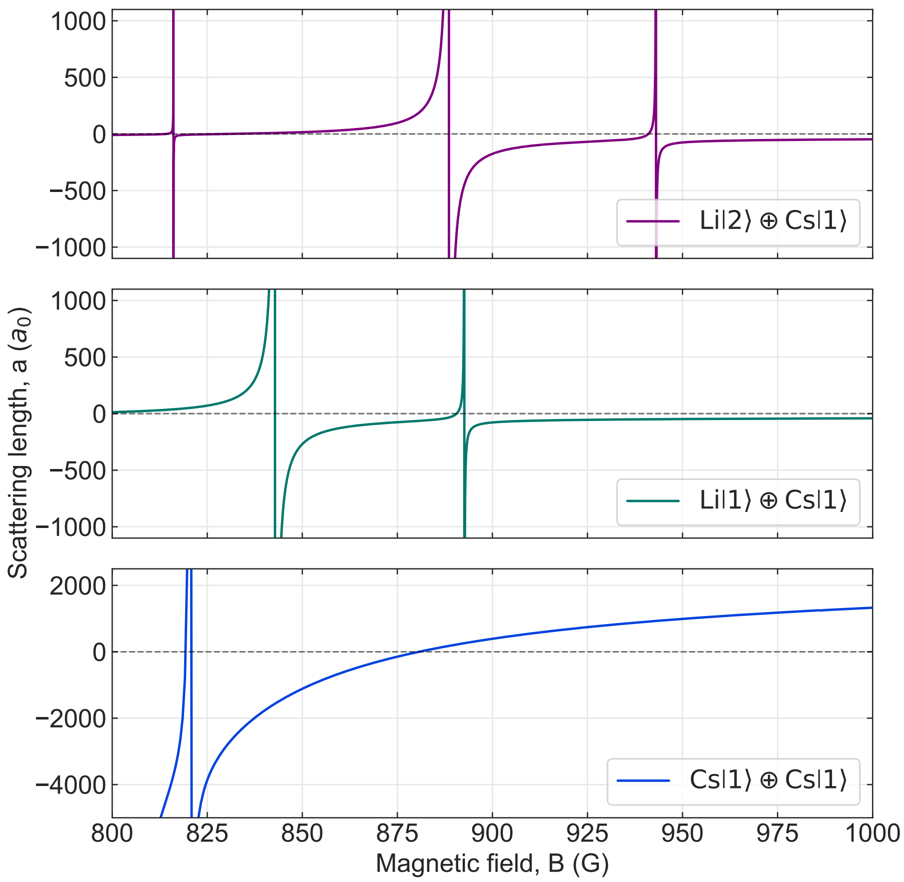

FIGURE 2.1: Interspecies scattering lengths a_{LiCs} for the channels Li$|2\rangle\oplus$Cs$|1\rangle$ (upper panel, purple line), Li$|1\rangle\oplus$Cs$|1\rangle$ (middle panel, green line) and intraspecies scattering length a_{Cs} for Cs atoms in the ground state Cs$|1\rangle\oplus$Cs$|1\rangle$ (lowest panel, blue line). The scattering lengths for Li-Cs have been calculated with parameters in Ulmanis *et al.* [2015], while those for Cs-Cs are taken from Berninger *et al.* [2013].

dimer takes the form

$$E_b = -\frac{\hbar^2}{2ma^2}. \tag{2.19}$$

For smaller a, the binding energy is linear with a slope proportional to the difference in magnetic moment $\delta\mu$. The regime where the binding energy has a quadratic dependence on the scattering length is considered *universal* because a is the only relevant length scale and is independent of microscopic details of the potential.

Feshbach resonances between Li and Cs $|3,3\rangle$. The scattering channels we experimentally take into account in this Chapter are

$$|\alpha\rangle = \mathrm{Li}\,|1/2,+1/2\rangle \oplus \mathrm{Cs}\,|3,3\rangle = \mathrm{Li}\,|1\rangle \oplus \mathrm{Cs}\,|1\rangle\,, \tag{2.20}$$

$$|\beta\rangle = \mathrm{Li}\,|1/2,-1/2\rangle \oplus \mathrm{Cs}\,|3,3\rangle = \mathrm{Li}\,|2\rangle \oplus \mathrm{Cs}\,|1\rangle\,, \tag{2.21}$$

where Li $|1\rangle$ = Li $|1/2, +1/2\rangle$, Li $|2\rangle$ = Li $|1/2, -1/2\rangle$ and Cs $|1\rangle$ = Cs $|3, 3\rangle$. The channels $|\alpha\rangle$ and $|\beta\rangle$ are characterized by a different projection of the total angular momentum m_f, equal to 7/2 and 5/2, respectively.

The Li-Cs s-wave scattering length for the channels $|\alpha\rangle$ and $|\beta\rangle$ as a function of the magnetic field is shown in Fig. 2.1. In the range between 800 G and 1000 G, the system offers a total of five interspecies Feshbach resonances. Two of these, at 889 G and 843 G, are intermediately broad with $s_{\mathrm{res}} \approx 0.7$ [Tung *et al.*, 2013], while the other three, at 893 G, 916 G and 943 G, are narrow resonances characterized by $s_{\mathrm{res}} \leq 0.03$ [Tung *et al.*, 2013]. These resonances have been mapped experimentally by atom-loss spectroscopy [Repp *et al.*, 2013; Tung *et al.*, 2013] and by radio-frequency association of weakly bound dimers [Ulmanis *et al.*, 2015]. A detailed comparison between different theoretical models for an accurate analysis of the Li-Cs Feshbach resonances has been presented by Pires *et al.* [2014a]. The Cs-Cs scattering length in this magnetic field region is dominated by a broad s-wave Feshbach resonance located at 787 G [Berninger *et al.*, 2013] and displays a zero-crossing at about 880 G.

The inter- and intra- species scattering lengths in the Li-Cs system offer access to several interesting regimes. Specifically, the two intermediately broad Li-Cs Feshbach resonances are characterized by a different sign and magnitude of the Cs-Cs scattering length a_{Cs}: while close to the 843 G resonance the intraspecies scattering length is large and negative $a_{\mathrm{Cs}} \approx -1500\, a_0$, the 889 G resonance is characterized by a small and positive intraspecies scattering length $a_{\mathrm{Cs}} \approx +190\, a_0$ [Berninger *et al.*, 2013]. Moreover, since the 889 G Li-Cs Feshbach resonance in channel $|\alpha\rangle$ is close to the zero-crossing in a_{Cs}, it offers the possibility to form a stable Cs BECs with slightly repulsive interactions, while the Li-Cs interactions can be tuned from weak to strong and from repulsive to attractive. The scattering channels and the Feshbach resonances taken into consideration for realizing the Fermi polaron scenario are described in Sec. 3.2.1.

2.1.3 Challenges for the realization of ultracold Li-Cs mixtures

The aim is to study interacting low-density thermal gases of bosonic Cs atoms mixed with a highly degenerate Fermi gas of Li atoms at magnetic fields close to the Li-Cs Feshbach resonance at 888.6 G in the channel Li $|2\rangle \oplus$ Cs $|1\rangle$ with a density ratio between the two samples of $n_{\mathrm{Cs}}/n_{\mathrm{Li}} \lesssim 0.1$. On the one hand, all previous experiments within our research group [Repp *et al.*, 2013; Zhu *et al.*, 2019b,a; Ulmanis *et al.*, 2016b,c; Häfner *et al.*, 2017] were performed under experimental conditions well below the degeneracy threshold for both species. On the other hand, experiments performed by Chin's group in Chicago on ^{6}Li -^{133}Cs [DeSalvo *et al.*, 2017, 2019; Patel *et al.*, 2023] have demonstrated the possibility of realizing double degeneracy mixtures, where the Cs Bose-Einstein condensates are embedded in the Li Fermi Sea. Recently, in Tung's group in Taiwan, Bose-Bose degenerate mixtures of ^{7}Li -^{133}Cs have also been realized [Chen *et al.*, 2023]. However, since we want to have Cs gas at low densities and degenerate Li-Fermi gases at high densities, the requirements for the optical trap geometry and the experimental preparation sequence are different from the aforementioned experiments. Therefore, we have realized a loading sequence based on a bichromatic approach that guarantees: (i) an independent control of the trap depth of the optical potential for each species, (ii) an external control of the differential gravitational sag, and (iii) a central symmetry, favorable for detection with high resolution imaging along the gravitational direction. It should be underlined that the approach used in this work is only one possible way to deal with the Li-Cs mixture, and it is a compromise between several aspects. In the following I discuss the individual steps from loading into the MOT to combining the optical traps, underlining the explicit main challenge for the Li-Cs mixture. Therefore, I will present the solutions implemented in the current mixing scheme.

Dual-species MOT loading: inelastic collisions. The trapping of Li and Cs atoms in a double species magneto-optical trap (MOT) is affected by light-assisted inelastic collisions that cause atomic losses for both species [Schlöder *et al.*, 1999; Kraft, 2006; Deiglmayr, 2009]. In particular, collisions with optically excited Cs atoms can lead to fine-structure changing collisions or radiative decay processes with ground state Li atoms [Weiner *et al.*, 1999; Schlöder *et al.*, 1999]. The dominant loss channel has been identified as inelastic collisions between excited Cs $6P_{3/2}$ state and ground state Li $2S_{1/2}$ atoms, while collisions between Li and ground state Cs atoms are dominated by the elastic channel.

To overcome inelastic light-assisted collisions in a MOT, we use a subsequent loading scheme, which prevents losses between the excited state of both Li and Cs atoms, while to overcome losses between excited Cs $6P_{3/2}$ state and ground state Li $2S_{1/2}$ atoms the two species are spatially separated. We first prepare a Li MOT, and then we sequentially load the atoms first into the DT and then into the MT. The MT is then displaced from the center in the vertical direction, enabling Cs atoms to be loaded into the MOT. The spatial separation of the two clouds, thus avoiding inelastic collisions.

Dipole trap loading: different temperatures. An efficient transfer of laser-cooled atoms into an optical dipole trap requires proper adaptation of the trap depth to the temperature of the atomic cloud during the trap loading process. Trap depths of typically $U \sim 6 - 10\, k_B T$ are required, which cannot be fulfilled for both species at the same time. In the most simple mixture experiments, the two atomic species are loaded from the MOT into a common magnetic trap or optical dipole trap, followed by evaporative cooling. This is possible because the mismatch in mass ratios, polarizabilities and magnetic moments allows for similar trap depths for both species. Some examples are given by mixtures of ^{6}Li-^{40}K [Spiegelhalder *et al.*, 2010], ^{6}Li-^{23}Na [Hadzibabic *et al.*, 2002], ^{6}Li-^{87}Rb [Silber *et al.*, 2005] or ^{40}K-^{87}Rb [Ospelkaus *et al.*, 2007]. In our case, Cs$|3, +3\rangle$ cannot be purely trapped magnetically and the mismatch between polarizabilities and mass ratio does not allow for pure optical trapping of both species at the same wavelength and with the same trap depth. Moreover, while Cs is routinely laser-cooled to temperatures of $T_{\mathrm{Cs}} \sim 1\ \mu$K, Li atoms are prepared at temperatures of $T_{\mathrm{Li}} \sim 42\ \mu$K after gray molasses cooling. Additionally, maintaining low densities for Cs is crucial to prevent significant three-body losses.

The individual requirements during the transfer process can be satisfied by implementing a sequential transfer scheme into spatially separated optical dipole traps, which are the dimple trap (DT) and the large volume reservoir trap (RT), respectively. These traps are well mode-matched to the individual species in terms of trap depth and trap volume. Cs atoms in the reservoir trap are prepared in the $|3,+3\rangle$ ground state, which requires a small magnetic field of a few G to maintain the spin polarization and to avoid anti-confining effects. Conversely, when loading Li atoms into the MT and performing grey molasses cooling, the latter is already significantly disturbed at magnetic fields above 1 G. This issue can therefore be avoided by loading Cs atoms into the reservoir trap only after grey molasses cooling is completed. After loading these species into their respective reservoirs, the RT for Cs and the DT for Li, they are sequentially transferred to the trapping potential desired for polaron experiments, which is the dimple trap for Cs and the MT for Li. Here, each species is individually evaporated to reach similar temperatures. The use of the highly confining MT allows reaching very high Fermi temperatures T_F and thus low T/T_F in a short evaporation time. Therefore, the microtrap trapping potential is well suited for the production of highly degenerate single-component Fermi gases. Furthermore, the Cs tune-out wavelength allows the two traps to overlap without the trapping potential for Li affecting the one for Cs.

Dual species overlap: large differential gravitational sag. In previous experiments, Li and Cs were trapped both in the dimple trap at 450 nK being still in a thermal regime [Pires, 2014]. The challenge in further decreasing the temperature of Li-Cs mixture in a single wavelength optical dipole trap arises from the significantly different gravitational potentials due to the mass imbalance between Li and Cs. Pure optical monochromatic trapping is indeed possible only as long as the dipole potential dominates over the gravitational potential, which prevents performing further forced evaporation. At the wavelength of the DT, the difference in the atomic polarizability of a factor of $\alpha_{\mathrm{Cs}}/\alpha_{\mathrm{Li}} \sim 4$, results in the same factor in the potential depths such that $U_{dip}^{Cs} \approx 4U_{dip}^{Li}$. Considering a harmonic trap confinement, the gravitational sag is given by

$$z_0 \propto g/\omega_z^2 \propto m/\alpha, \tag{2.22}$$

where g is the gravitational acceleration, ω_z is the trapping frequency along the vertical direction, m is the atomic mass and α the atomic polarizability. For a mass imbalance of 22 then $z_0^{\mathrm{Cs}}/z_0^{\mathrm{Li}} = \frac{m_{\mathrm{Cs}}}{m_{\mathrm{Li}}}\frac{\alpha_{\mathrm{Li}}}{\alpha_{\mathrm{Cs}}} \sim 5$. In our case the highly mass-imbalanced Li-Cs mixture entirely separates at temperatures below 100 nK [Ulmanis *et al.*, 2016c]. The solution adopted for mixtures at 100 nK, was to use species-selective trapping [LeBlanc and Thywissen, 2007], imposing a bichromatic trapping at a wavelength of 921.1 nm, where the polarizability for Cs is twelve times greater than the one for Li. Even if this allows increasing the trapping potential, thus restoring the confinement against gravity for Cs atoms, the estimated spatial overlap between the two clouds is still only about 45% and the differential gravitational sag is 16 μm [Ulmanis *et al.*, 2016c]. This differential sag is too large to assure a sufficient overlap once we consider degenerate samples, for which the Fermi radius along the vertical direction is $< 10\ \mu$m (see Freund [2022]).

The use of a movable microtrap enables us to displace the trapped Li atoms along the vertical direction and to compensate an arbitrary differential gravitational sag. Thanks to the use of the tune-out wavelength of 880 nm the process takes place without affecting the Cs trapping potential, i.e. trapping frequencies and density.

2.2 Production of a Li Fermi Sea with Cs impurities

The best way to understand the experiment is to experience it from the perspective of the atoms. Following this approach, I will discuss in detail the individual preparation of the two species as implemented for the combined sequence depicted in Fig. 2.2. We use a subsequent approach where we first prepare the Li sample in about 6 s and store it away from the crossing of the DT beams. Then we start the preparation of Cs, evaporating it up to a temperature similar to that of Li. Finally, we overlap the two clouds together. The production of a Li Fermi Sea trapped in the MT will be described in Sec. 2.2.1 and of a dilute thermal gas of Cs atoms trapped in the DT in Sec. 2.2.2. In Sec. 2.2.3 I will explain the overlap procedure and the final experimental parameters that we obtain for our Li-Cs mixture.

2.2.1 Production of a Li Fermi Sea

The experimental preparation of a Li Fermi Sea trapped in the microtrap is divided into several steps: (i) laser cooling and trapping in the dimple trap, which plays the role of a reservoir for Li atoms, (ii) loading into a tightly confined and movable dipole trap (the microtrap), (iii) evaporative cooling in the microtrap at 320 G, (iv) compression, transport and storage, and (v) spin preparation. Step (i) is similar to the procedure described in previous works by Gerken [2022] and Tran [2022]. The other steps are rather specific to the sequence presented here and aim to have a sequence for mixing Li with Cs following the criteria discussed in Sec. 2.1.3. Figure 2.3 shows the phase-space density as a function of Li atom number for different stages of laser and evaporative cooling. This figure of merit provides a guideline for the route described in the following.

Laser cooling and trapping into the Dimple Trap. The experimental sequence for producing a quantum degenerate ^{6}Li gas starts with loading a MOT of 7×10^7 atoms in 2 s, at a temperature of about 1.5 mK. After this loading, we use the curvature coils to compress the cloud. Further cooling takes place in the compressed MOT configuration (cMOT), where we collect 5×10^7 atoms at a temperature of 300 μK. While the cMOT is still on, the spatially modulated dipole trap beams are turned on 1.5 ms before shutting off the MOT lights. After the cMOT, an efficient sub-Doppler scheme based on gray molasses cooling, which exploits the $\mathcal{D}_1$ line of Li, is implemented. As the cooling of the grey molasses reduces the temperature of the atoms in free space by a factor of 8, the DT, originally designed to be loaded directly from the cMOT, is adapted to have a trap depth and volume

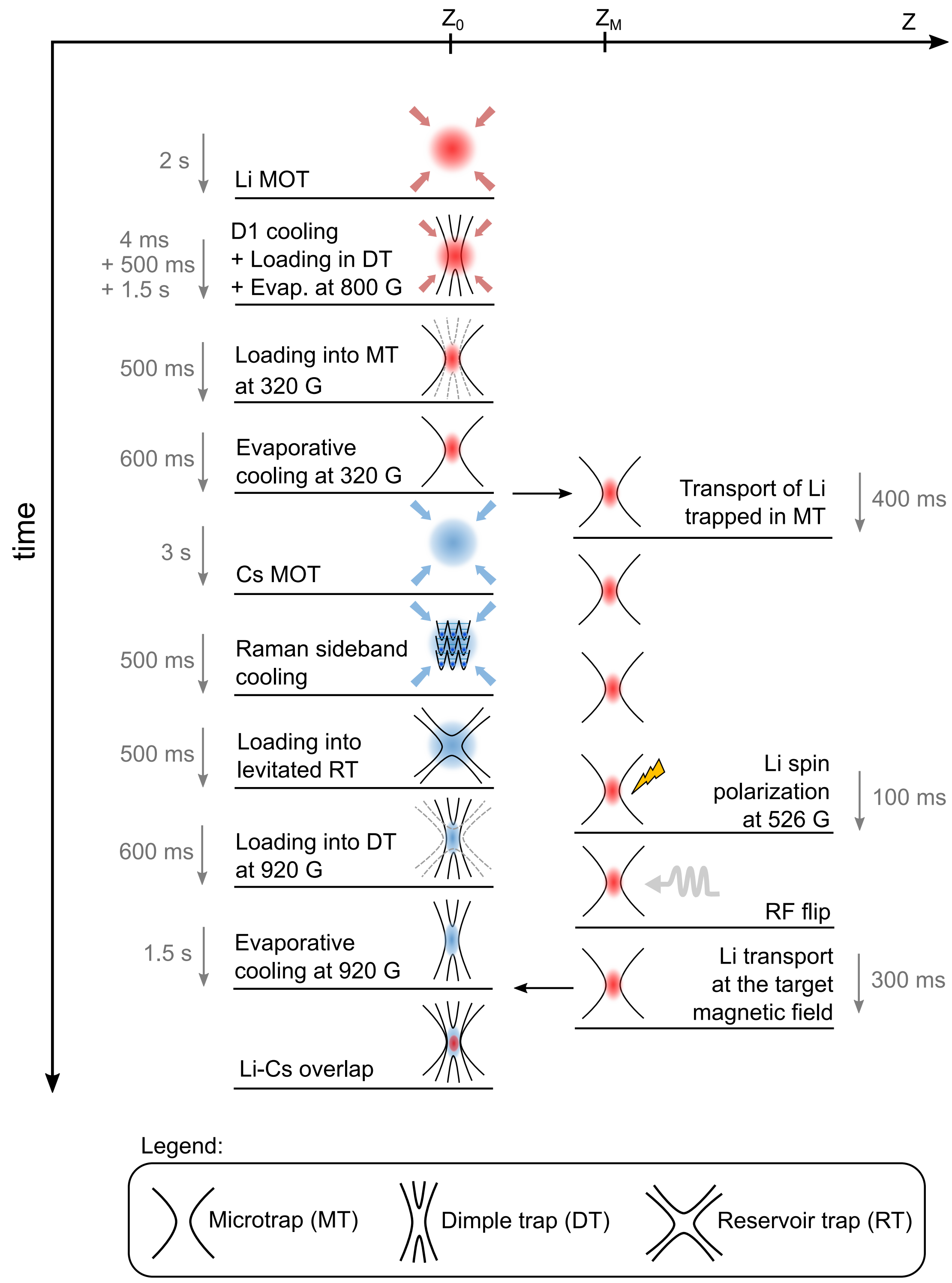

FIGURE 2.2: Schematic of the experimental sequence for the preparation of a Li-Cs mixture. Time is shown along the *vertical* axis, while the displacement of the traps along the vertical (gravity) z-direction is shown along the *horizontal* axis: z_0 corresponds to the position defined by the crossing point of the DT beams, which is centered on the center of the Feshbach coils, as determined by Feshbach tomography (see Sec. 1.4.1); z_M is the position where we store the Li cloud trapped in the MT during the preparation of the Cs cloud, as determined experimentally (see Sec. 2.2.1). A detailed description is given in the text along the entire Sec. 2.2.

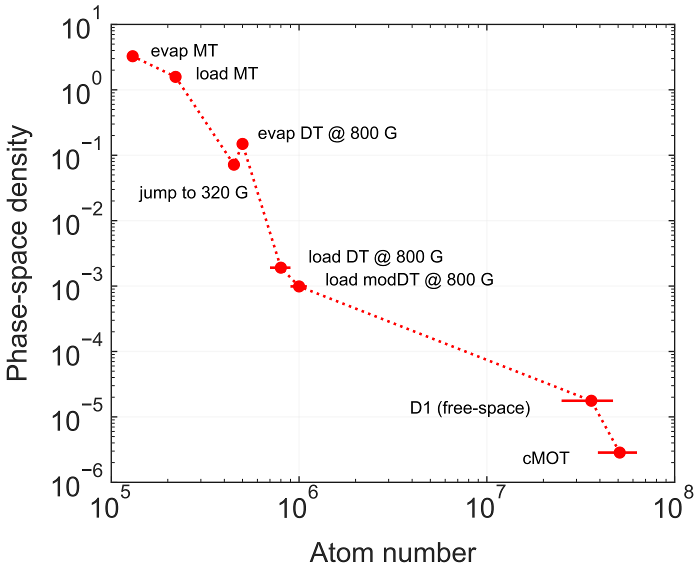

FIGURE 2.3: Phase-space density as a function of the atom number for different stage of laser and evaporative cooling.

corresponding to the temperature and volume occupied by the cloud after $\mathcal{D}_1$ cooling. The performance of our $\mathcal{D}_1$ cooling scheme has been quantified in Neiczer [2018] and the detailed loading procedure into the DT has been discussed in Gerken [2022]. We optimize the power of the $\mathcal{D}_1$ cooling beams and their detuning in order to maximize the loading into the DT. With this procedure, by measuring the performance of $\mathcal{D}_1$ cooling in free space, we achieve a temperature of $T = 60\ \mu$K for about the 70% of the atoms collected in the cMOT[2]. After a typical 4 ms long pulse of $\mathcal{D}_1$ cooling, we turn on the repumping beams for a few hundred microseconds to ensure half of the atoms in the Li$|2\rangle$ state and half in Li$|1\rangle$. We jump to a high magnetic field of 800 G close to the Feshbach resonance at 832 G between the Li$|1\rangle$and Li$|2\rangle$ states to ensure fast thermalization. The timescales associated with elastic two-body collisions for a scattering length of 1×10^4 a$_0$ are about 0.5 ms for typical densities of 4.5×10^{11} cm^{-3}. As the high laser powers of the dimple trap reach 110 W per beam, the two beams separate within tens of milliseconds due to thermal lensing effects of the AOM [Heck, 2012; Simonelli *et al.*, 2019]. Therefore, a first evaporation is performed by ramping down the power to 32 W per beam in 500 ms before the beams separate. We obtain a balanced mixture of Li$|1\rangle\oplus$Li$|2\rangle$ states, with 1×10^6 atoms in each spin state, at a temperature of 30 μK with typical sizes of (30, 260) μm. The number of atoms finally trapped by turning off the modulation is 8×10^5 at trapping frequencies of (4×10^3, 240) Hz and with sizes of (30, 150) μm. For densities of 6.4×10^{12} cm^{-3} we obtain a two-body collisional time of 0.25 ms. At this point the phase-space density is $\rho \approx 6 \times 10^{-3}$ and $T/T_F \approx$4. We consider these parameters to be the starting condition for evaporative cooling, which depends on the mixing scheme procedure for Li and Cs.

---

[2] The lowest temperature that can be reached is $\sim$ 42 μK; the minimum in temperature does not correspond to the maximum number of atoms collected [Gerken, 2016; Burchianti *et al.*, 2014].

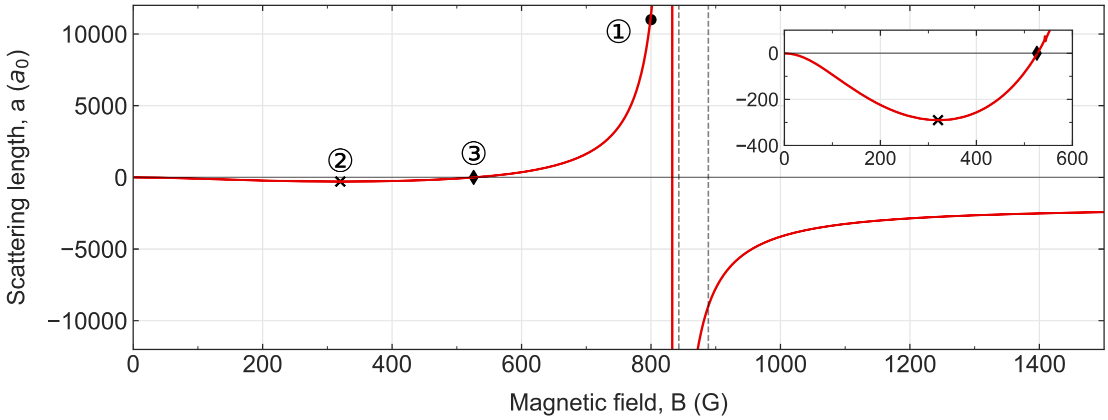

FIGURE 2.4: Li-Li scattering length for a Li$|1\rangle\oplus$Li$|2\rangle$ mixture. The magnetic fields used for the preparation of Li in the DT are marked in black: 800 G (dot), 320 G (cross), 526 G (diamond). The dashed lines correspond to the positions of the intermediate Li-Cs Feshbach resonances, at 843 G for the Li$|1\rangle\oplus$Cs$|1\rangle$mixture, and 888.6 G for Li$|2\rangle\oplus$Cs$|1\rangle$, respectively. The broad s-wave Feshbach resonance is centered at around 834 G. The inset shows an enlargement of the magnetic field region below 600 G. Data are taken from Zürn *et al.* [2013].

Loading into a tightly confining and movable dipole trap. The aim here is to produce single-component degenerate Fermi gases trapped in the MT and mix them with Cs. Therefore, we need to go to magnetic fields where the scattering length is zero in order to selectively prepare the atoms in a single spin state by applying a light pulse. Loading the MT from the DT at 800 G would cause the sample to become degenerate immediately due to the very high densities. To reduce the losses due to molecule formation when jumping to 526 G, corresponding to a_{12} is zero (see Fig. 2.4), we prepare the weakly interacting Fermi gas at 320 G [Lompe, 2011; Burchianti *et al.*, 2014], where no weakly bound dimer state exists. However, the forced evaporation at 320 G is much slower than at 800 G, as the scattering cross-section is at least a factor of 25 times smaller, and therefore it is beneficial to start the evaporative cooling at 320 G with the cloud as cold as possible. The fraction of atoms N_{atom} that can form molecules N_{mol} is given by $N_{mol}/N_{atom} = \rho \exp\left(E_b/k_B T\right)$, where ρ is the phase-space density of free atoms and $E_b = -\hbar^2/(ma^2)$ is the molecule binding energy [Jochim, 2004]. Thus, we evaporate in the dimple trap until $k_B T > E_b$, i.e. before the temperature becomes so low that the sample begins to contain a significant fraction of molecules we stop the evaporation and jump to a magnetic field of $B = 320$ G, while atoms are still trapped in the DT, as shown in Fig. 2.5 (a). The evaporation at 800 G is done by reducing the laser intensities in three successive linear ramps, decreasing the power from 32 W to 2 W in 2.5 s. This results in samples of 5×10^5 atoms at a temperature of 3.5 μK. The trapping frequencies are reduced to $(\omega_r, \omega_{ax})/2\pi$ =(1.3×10^3, 75) Hz and the calculated trap depth is $\approx$ 40 μK; typical densities are of 7.9×10^{12} cm^{-3}. The T/T_F here estimated is on the order of 1 and the $\rho = 0.4$. The jump to 320 G causes a slight heating of the atoms to 5.5 μK while decreasing the atom number of only 10%, which results in a peak density of 3.4×10^{12} cm^{-3}, a phase-space density of $\rho = 0.1$ and a degeneracy parameter of $T/T_F = 1.6$. By adiabatically switching on the MT, the temperature

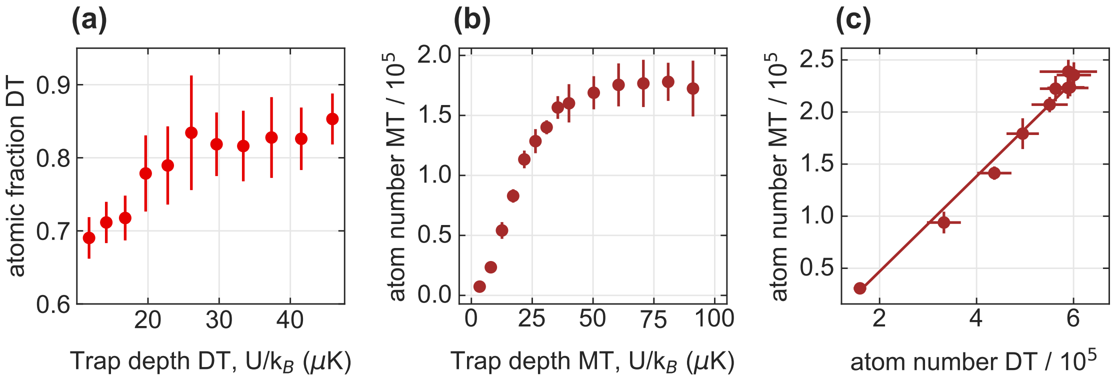

FIGURE 2.5: Loading procedure of Li atoms from the dimple (DT) to the microtrap (MT). (a) Atomic fraction of atoms after the jump between 800 G and 320 G as a function of the trap depth of the DT. (b) Atom number loaded into the MT as a function of the trap depth of the MT. (c) Efficiency of the loading from the DT to the MT. The solid line is a fit and has a slope of (0.46 ± 0.03), which means that the atom number loaded in the MT is half of the atoms trapped in the DT.

remains nearly unchanged compared to the temperature in the initial DT volume, but the Fermi energy increases proportionally to the depth of the optical trap [Viverit *et al.*, 2001]. We maximize the atom number loaded into the MT and choose a trap depth of $\approx 40\ \mu$K as shown in Fig. 2.5 (b, c). We collect up to 2×10^5 atoms and a temperature of 4 μK. This results in a decrease of the degeneracy parameter by a factor of 4 corresponding to a $T/T_F = 0.4$. The trapping frequencies $(\omega_r, \omega_{ax})/2\pi =(8.3\times10^3, 154)$ Hz are and densities of 2×10^{13} cm^{-3}. We measure a one-body $1/e$ lifetime of $\tau = (38.0 \pm 0.9)$ s as in Fig. 2.6 by holding a thermalized Li Fermi gas at the zero-crossing of the scattering length at 526 G. This corresponds to a one-body loss rate of $\Gamma = (0.0270 \pm 0.0009)$ s^{-1}. Such a lifetime is much longer then the ≈ 6 s that are needed to prepare Cs, and therefore the one-body losses do not limit the Li final atom number for the mixing with Cs.

Evaporative cooling at 320 G. The mixture of atoms in the Li$|1\rangle$ and Li$|2\rangle$ states is evaporated at 300 G, where the scattering length of $a_{12} \simeq -290$ a$_0$ promotes the evaporation efficiency. Typical initial trap parameters are similar to the measurement presented here and they are: $N_i = 1.2\times10^5$ (for each spin state), $\omega_{i,r}/2\pi = 8.3(2)$ kHz and $\omega_{i,ax}/2\pi = 154(5)$ Hz, $T_i = 3.7(2)\ \mu$K, $U_i = 36.8(6)\ \mu$K, $P_i = 95.6(6)$ mW, and $T/T_F = 0.37(4)$ as calculated from T_i, N_i and $\omega_{i,(\mathrm{r,ax})}$. To increase the level of degeneracy of the system we follow the Boltzmann equation model proposed in O'Hara *et al.* [2001] for evaporation in optical traps, which holds for fermionic gases far from unitarity[3]. This model leads to scaling laws for the atom number and for other relevant quantities and it follows from energy conservation with the assumption that the truncation parameter $\eta = U/k_B T$, where U is the trap depth and T is the temperature of the sample, remains constant during the process by lowering the power of the optical trap. The ramp we implemented for forced evaporation follows the theoretical curve derived in O'Hara *et al.*

---

[3] In Luo *et al.* [2006] the case of evaporation at unitarity is treated.

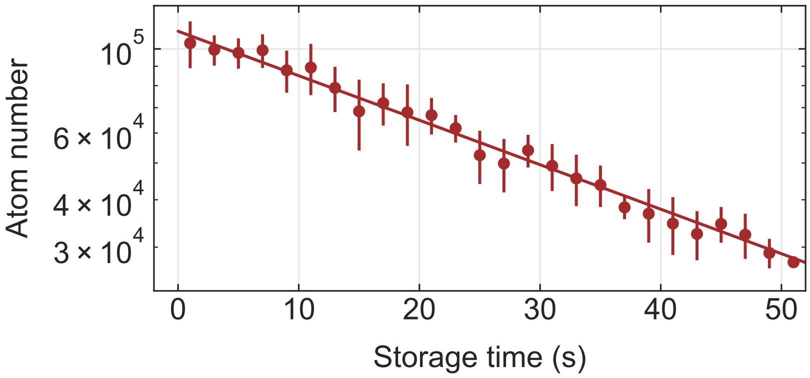

FIGURE 2.6: Atom number of a thermalized cloud of Li atoms stored in the MT at a trap depth of 40 μK at 526 G, where $a_{12} = 0$. From an exponential fit to the data a $1/e$ lifetime of $\tau = (38.0 \pm 0.9)$ s is found.

[2001] for the trap depth

$$U(t) = U_0(t)(1 + t/\tau)^{-2(\eta' - 3)/\eta'}, \tag{2.23}$$

which assumes a constant truncation parameter η for the whole evaporation process. The coefficient η' is related to η as $\eta' = \eta + (\eta - 5)/(\eta - 4)$. We use a time constant of $\tau = 300$ ms, which is experimentally optimized for obtaining the maximum atom number, and $\eta' = 10.8$, obtained for a truncation parameter of $\eta = 10$. The power was adjusted to follow the theoretical curve in Eq. (2.23). To characterize the performance of the evaporation at 320 G, we performed TOF absorption imaging for different power jumping to 526 G, which corresponds to the zero crossing for a Li$|1\rangle \oplus$Li$|2\rangle$ mixture. Figure 2.7 summarizes the main results of the forced evaporation. The cloud was fitted with a bidimensional Fermi distribution and the temperature was extracted as a free parameter from a ballistic expansion. The atom number was averaged over different TOF expansions. The degeneracy parameter T/T_F is extracted in two different ways: (i) by fitting the density profiles with a bidimensional finite-temperature Fermi distribution (see the gray diamonds in Fig. 2.7 (b)), and (ii) from trapping frequencies taken from a calibration (see Fig. 1.11) and atom number as $T_F = \hbar\bar{\omega}(6N)^{1/3}/k_B$, with $\bar{\omega} = (\omega_r^2 \omega_{ax})^{1/3}$ (see the brown dots in Fig. 2.7 (b)). The trap depth has been calculated assuming a single focused gaussian beam in the presence of the gravitational potential, even though gravity is negligible compared to the optical potential, even at low MT powers.

The trap depth of the MT is reduced by an order of magnitude in less than 2 s and an efficient cooling of the cloud is observed down to a trap depth of 3 μK, corresponding to evaporation times of 1.4 s and to a power $P = 8.0(4)$ mW. At this point, $N = 7.7 \times 10^4$ atoms in each spin state remained trapped at a temperature of $T = 0.16(1)$ μK, corresponding to a $T/T_F = 0.07(1)$. Here, we measure trapping frequencies of $\omega_r/2\pi = 2.4(1)$ kHz and $\omega_{ax}/2\pi = 44(2)$ Hz. By fitting a bidimensional Fermi distribution we obtain a $T/T_F = 0.09(4)$, which is consistent with the value calculated from atom number and

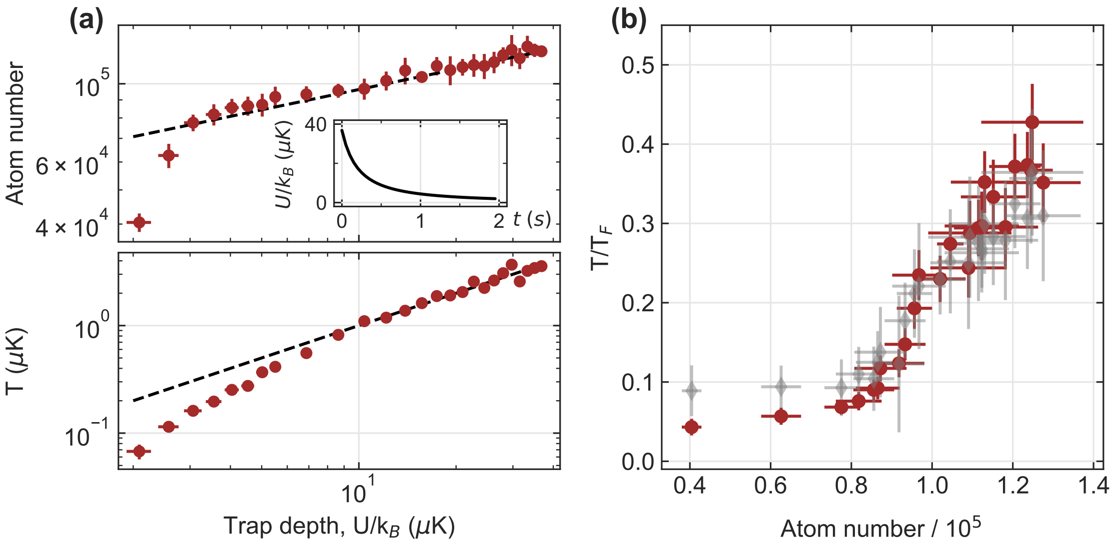

FIGURE 2.7: Forced evaporation of Li atoms at 320 G. (a) Atom number (top) and temperature (bottom) as a function of the trap depth at different points of the forced evaporative cooling. The dashed lines represent the scaling law $N = N_0(U/U_0)^{3/(2(\eta'-3))}$ [O'Hara *et al.*, 2001], with $\eta' = 10.8$ and $\eta \equiv U/k_BT = 10$ (top), and $T = 0.1 \times U/k_B$ (bottom), respectively. The trap depth spans one order of magnitude, between 4 and 40 μK in a time of 2 s as shown in the inset. (b) Degeneracy parameter T/T_F as a function of the atom number, for the same measurement. The degeneracy parameter is extracted in two different ways: fitting the density profiles with a bidimensional finite-temperature Fermi distribution (gray diamonds), and calculating $T_F = \hbar\bar{\omega}(6N)^{1/3}/k_B$ as described in the text (brown dots). The error bars in (a) and (b) include statistical errors (from up to 10 independent measurements). A systematic error of 10% is also considered for the T/T_F extracted by fitting the Fermi distribution (gray diamonds).

trapping frequencies. This is the trap depth that we set as target for our evaporation scheme. Indeed, for trap depths lower than 3 μK, the evaporation efficiency breaks down. We compare our measurement of atom number over trap depth with the predictions provided by the scaling laws inferred from the Boltzmann equation model [O'Hara *et al.*, 2001]. Contrary to other experiments, such as [Burchianti *et al.*, 2014; Gross *et al.*, 2016], even if we start the evaporation from a gas which is already degenerate, the scaling laws are in reasonable agreement with the Boltzmann model, and the Fermi statistic, which becomes relevant for $T/T_F < 0.6$, does not severely suppress the efficiency of evaporative cooling, in agreement with [O'Hara *et al.*, 2001].

Compression, transport and storage. Transport after preparation of the Li cloud is mainly necessary to avoid losses induced by photon scattering from the MT once the Cs atoms are prepared in their lowest ground state[4]. The minimum displacement of the

---

[4] The displacement of the Li cloud during the Cs MOT was taken as one of the criteria for redesigning the trapping scheme to avoid inelastic collisions. Contrary to expectations, we have experimentally observed that Li atoms trapped in the MT do not show any loss feature when superimposed to the Cs MOT. This effect was not deepened further, but it seems that the MT light creates a dark spot for the Cs atoms trapped in the MOT, shielding the Li atoms trapped in the MT from Cs. Therefore, inelastic interspecies collisions are suppressed.

MT necessary to avoid losses on Cs atoms was experimentally measured to be 230 μm. This value was optimized looking at the number of remaining Cs atoms in the presence of the MT and roughly corresponds to the size of the Cs cloud loaded in the levitated RT. However, we have found that the efficiency of the transport is higher for deeper trap depths, because at low trapping frequencies the noise related to beam pointing causes heating and subsequent loss of Li from the trap (see Sec. 1.3.2 and Fig. 1.13). We therefore set the trap depth for transport to maximize the number of atoms remaining in the trap afterward. To do this, we need to adiabatically compress the cloud. The idea is to increase the trap depth while keeping the entropy and the ratio of T/T_F constant [Ketterle *et al.*, 1999; Walraven, 2019], so that the process is reversible. Since collisions help to keep the cloud thermalized, we compress the cloud containing the sample at 320 G. The fraction of atoms is independent from the ramp time for $t_{ramp} > 10$ ms, which is a factor of 70 larger than the collisional time. We ramp up the MT power in 100 ms from a trap depth of ≈ 3 μK to 76 μK. Assuming the process is adiabatic, T/T_F should be conserved and the temperature should increase as $\overline{\omega_f}/\overline{\omega_i} \propto \sqrt{U_f/U_i}$, corresponding to an increase of $\approx 20\%$. This should also result in an analogous decrease in temperature the power is ramped down to the lowest value reached after evaporative cooling. Our aim was to perform this process in such a way that T/T_F does not change over the entire storage time. However, we found that the process is not adiabatic due to several reasons. First, during the preparation of Cs atoms, the number of Li atoms stored in the MT is reduced by a factor of $\Gamma\Delta t$, where $\Gamma = (0.0270 \pm 0.0009)$ s^{-1} is the one-body loss rate and Δt is the waiting time. Consequently, T$/T_F$ is reduced by a factor of $(N_f/N_i)^{-1/3}$. A storage time of 6 s results in a 15 % reduction of the atom number, which implies that $N_f/N_i \approx 0.85$. The corresponding change in T/T_F is of $\approx 5\%$, which is negligible. Second, during the spin cleaning process, the cloud is heated by about 10%, while the number of atoms per spin state remains the same. Therefore, the change in T$/T_F$ is $\approx 10\%$. Third, during the displacement of the trapped atoms at a trap depth of 76 μK, we lose about 20% of them for each trip, becoming 40% considering going back and forth. Therefore, T$/T_F$ is reduced by $\approx 20\%$. However, the main contribution is given by magnetic fields jumping, which increases the temperature by about a factor of 3. At the end of the whole procedure we have a Li temperature of about 0.6(2) μK and an atom number of 4×10^4. Then, we adjust the final trap depth to limit the atom loss.

Spin preparation. We prepare a spin-polarized Li sample by applying a $\mathcal{D}_2$ resonant light pulse on the Li$|2\rangle$ state. Spin cleaning is performed during the preparation of Cs atoms, while atoms are stored in the MT, displaced from the Cs cloud by 230 μm, as shown in Fig. 2.10, (A). The removal is done by setting a magnetic field of 526 G, which corresponds to a non-interacting Li$|1\rangle\oplus$Li$|2\rangle$ mixture. The pulse length is adjusted experimentally to 60 μs. The Li$|1\rangle$ spin state remains trapped, but the temperature increase is about 10%, as photon scattering heats the atoms.

It should be noted that we remove the Li$|2\rangle$ state independently from the desired final state. In fact, during the preparation of Cs in the RT, by changing both the magnetic field offset and the gradient, the Li population becomes unbalanced with 30% of the atoms in the $\mathrm{Li}|2\rangle$ state and 70% in the $\mathrm{Li}|1\rangle$ state. We then eliminate the state containing the minority of the atoms. Afterwards, by using a radio-frequency sweep, we transfer the population from the $\mathrm{Li}|1\rangle$ state to the $\mathrm{Li}|2\rangle$ state and obtain a mixture of $\mathrm{Li}|2\rangle \oplus \mathrm{Cs}|1\rangle$. This is done at 900 G with the two clouds still spatially separated and once the process of Cs evaporation in the DT is completed (see Sec. 2.2.2).

2.2.2 Production of a dilute Cs Bose gas

The experimental sequence employed to create a dilute Cs sample for mixing with the Li Fermi Sea is described below. Our efforts to design and implement an optimal sequence for the realization of a Bose-Einstein condensate are described in Tran [2022] and will not be repeated here. After the finalization of that work, due to the emptying of the Cs in the oven, we worked with very poor Cs conditions and a very low atom number. For the preparation of bosonic Cs ultracold gases, we follow some of the steps designed for the aforementioned optimal sequence, but add important criteria such as (i) retaining as much Cs as possible in such unfavorable situation and (ii) adapting the final Cs temperature in the DT to match the Li temperature in the MT.

Cs experimental preparation in a nutshell. Each experimental cycle starts by loading the Cs MOT for a typical duration of 3 s, followed by a 30 ms long compression phase. Subsequently, a sub-Doppler cooling scheme is applied [Drewsen *et al.*, 1994], resulting in a sample of 2.5×10^6 atoms where temperatures on the order of 10 μK are reached[5]. At this point, the RT is turned on at a power of 25 W per beam. While the dipole trap is on, Cs atoms are prepared by means of the degenerate Raman-sideband cooling (DRSC) [Vuletic *et al.*, 1998; Kerman *et al.*, 2000; Treutlein *et al.*, 2001] in the lowest hyperfine state $|F = 3, m_F = 3\rangle$ of Cs, where two-body losses are suppressed by applying a 1.5 ms long DRSC pulse [Tran, 2022]. The magnetic fields as well as the beam powers of the Raman lattice and polarizer, are ramped down in order to achieve temperatures of less than 1 μK and a spin polarization of 85%. In order to facilitate the efficient transfer of Cs atoms into the RT after DRSC, it is necessary to apply a magnetic field gradient in order to prevent the atoms from a free fall under the influence of gravity. Furthermore, a magnetic field offset must be employed in order to compensate for anti-trapping in the xy plane [Tran, 2022]. To achieve fast turn-on times, the voltage applied to the coils, is first maximized and then limited, as described in detail in Rautenberg [2021] and Tran [2022]. This process is applied to a magnetic field of 200 G[6] and a corresponding levitation gradient of 30 G/cm. Typical samples of 8×10^5 spin-polarized atoms are finally loaded into the RT at a temperature of 1 μK and with atomic peak-densities of 8×10^{10} cm^{-3}.

---

[5] The measurements shown in Fig. 1.5 have been performed before the emptying of the Cs oven.

[6] The choice of this magnetic field is motivated, on the one hand, by the fact that this was the magnetic field necessary to compensate for anti-trapping in the case of larger reservoir trap beam waist, used for a certain period, and on the other hand, to make smoother the jump to 526 G.

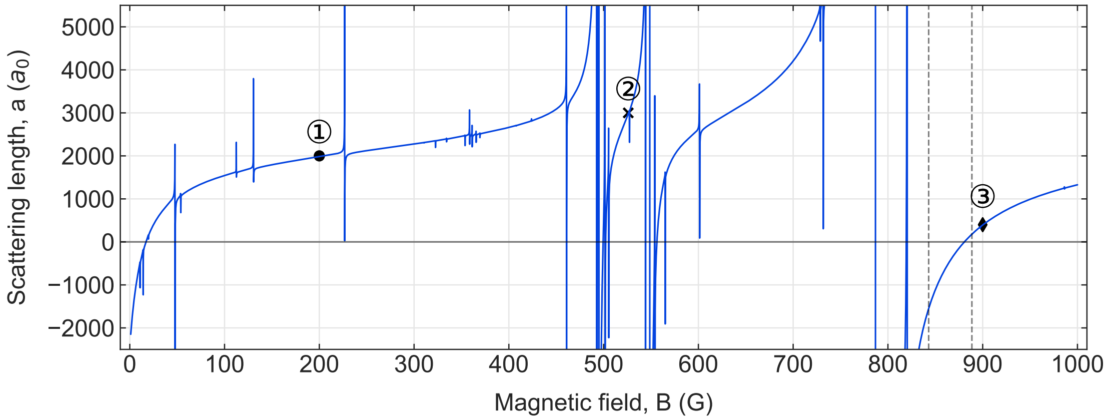

FIGURE 2.8: Cs-Cs scattering length in the $|3,+3\rangle$ state as a function of the applied magnetic field offset (including s-, d- and g-wave resonances). The magnetic fields used for the preparation of Cs in the DT are marked in black: 200 G, corresponding to $a_{\mathrm{Cs}} \approx 2000\ a_0$ (dot); 526 G, corresponding to $a_{\mathrm{Cs}} \approx 3000\ a_0$ (cross), 900 G, corresponding to $a_{\mathrm{Cs}} \approx 300\ a_0$ (diamond). The dashed lines correspond to the positions of the intermediate Li-Cs Feshbach resonances, at 843 G and 888.6 G, respectively. The three broad s-wave Feshbach resonances are centered around -12 G, 549 G and 787 G. Data are taken from Berninger *et al.* [2013].

Once the RT has been loaded, and before reaching the target magnetic field between 800 G and 100 G, it is essential to jump to 526 G (see Fig. 2.8 and Fig. 2.10 (A)), which corresponds to the zero crossing for the scattering length a_{12} in the channel Li$|1\rangle \oplus$Li$|2\rangle$. At this point, a resonant light pulse provided by the imaging beam (see Sec. 1.5.2) selectively excites the Li$|2\rangle$ state, without affecting Cs. In order to limit Cs losses, we reach 526 G, corresponding to $a_{\mathrm{Cs}} \approx 3000\ a_0$, as smoothly as possible. Therefore, we first jump to $\approx$ 511 G, which has a scattering length $a_{\mathrm{Cs}} \approx 2000\ a_0$, similar to that at 200 G, and then we ramp up the magnetic field to the target value of 526 G. This process is subject to periodic optimization to prevent the voltage of the coils from exceeding a predefined threshold. Nevertheless, in this step, we register a loss in the atom number of 50%. We then jump to $\approx$ 900 G, which corresponds to a scattering length of 400 a_0, to take advantage of the three-body loss minimum[7], and set a corresponding magnetic field gradient for levitation of 27.7 G/cm. We wait 100 ms for the coils to reach this value and for the sample to thermalized. Even when we reach this magnetic field as quickly as possible, we observe atomic losses of 80%, with respect to the previous step, and a temperature increase by a factor of 2.5. The dimple trap is then ramped up to 230 mW in 300 ms, corresponding to a trap depth of 16 μK, followed by the ramping down of the reservoir trap in another 300 ms. We load into the DT a sample of 1×10^5 atoms at a temperature of 2.5 μK, resulting in atomic peak-densities of 2×10^{11} cm^{-3}.

From here on, we start forced evaporation to lower Cs temperature in order to match the temperature of Li atoms. A first evaporation is performed by lowering the magnetic field gradient from 27.7 G/cm to 0 G/cm in 200 ms, which corresponds to a tilting of

---

[7] There is a Cs three-body loss minimum at 893 G, corresponding to a_{CsCs} =270 a_0 [Kraemer *et al.*, 2006; Berninger *et al.*, 2011].

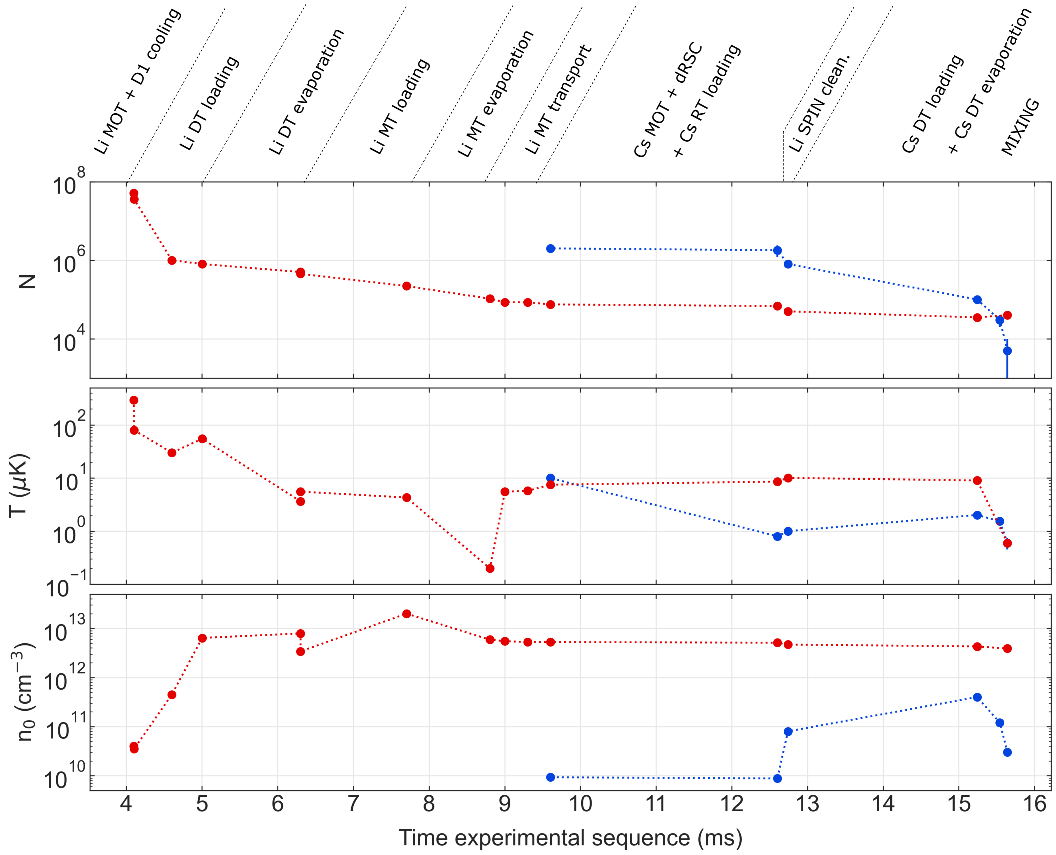

FIGURE 2.9: Relevant quantities for both Li (red) and Cs (blue) during the complete experimental sequence from loading of Li MOT to mixing of the two species. From top to bottom: atom number, temperature and peak atomic densities. On top, the different experimental steps as for the corresponding timing diagram in Fig. 2.10.

the trap in the z-direction and provides a trap depth of 6 μK and trapping frequencies of $\omega_{x,y,z}/2\pi$ = (10, 143, 166) Hz. During this process, the power of the MT (for Li) is also slightly adjusted in order to compensate for the removal of the artificial gradient. We obtain 3×10^4 atoms at a temperature of 1 μK, resulting in atomic peak-densities of 2.3×10^{11} cm^{-3}. The power of the DT laser is then reduced with a linear ramp from 230 mW to 150 mW, which corresponds to a trap depth of U = 3 μK in 1 s. Here, we estimated the trapping frequencies to be $\omega_{x,y,z}/2\pi$ = (8, 112, 121) Hz. We reach 6.5×10^3 atoms at a temperature of 300 nK, resulting in atomic peak-densities of 4×10^{10} cm^{-3}. Then, we jump to the target magnetic field, after which we move the MT back, starting the process of overlapping and consequently mixing the two species.

2.2.3 Production of a Li-Cs mixture

Figure 2.9 shows the characteristic quantities during the whole experimental procedure, reporting the typical atom number, temperatures and densities for both Li and Cs at different stages of the experimental sequence up to the production of individual ultracold samples, as summarized in Fig. 2.2 and described in detail in Sec. 2.2.2 and Sec. 2.2.1.

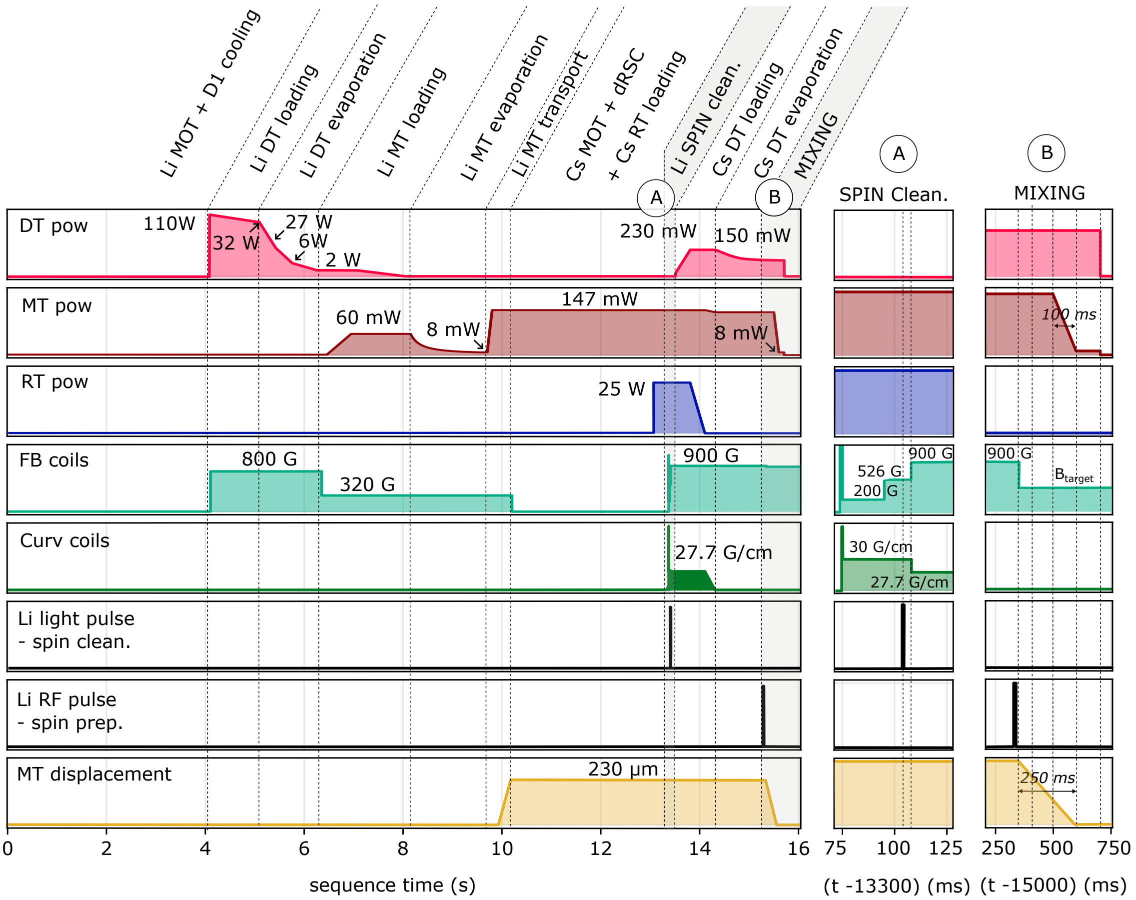

FIGURE 2.10: Timing diagrams for the sequential trapping of Li and Cs atoms and subsequent mixing. Parameters are described in the main text. The sequence time is in real scale. The diagrams for the magnetic fields corresponds to commands given to the coils. Panel (A) shows a zoom on the spin cleaning sequence in order to prepare Li spin polarized sample. Panel (B) show a zoom on the mixing procedure.

Figure 2.10 shows the timing diagram for sequential trapping of Li and Cs atoms and subsequent mixing.

Compensation of the gravitational sag. The compensation of the differential gravitational sag is done by mechanically shifting the position of the Li cloud with respect to the Cs cloud by moving the MT beam (see Sec. 1.3.2). First, the position of the focus of the MT is chosen to be optimal for loading Li atoms from the DT (see Sec. 2.2.1). Then, as described in Sec. 2.2.2, we load Cs atoms into the DT while levitating them against gravity by a magnetic field gradient provided by the curvature coils. For mixing Li with Cs, we remove the magnetic field gradient such that Cs is purely optically trapped and therefore, it is pulled down. To achieve the overlap between the two species, it is necessary to move the Li cloud trapped in the MT downwards by a distance equal to the gravitational sag of Cs. For a harmonic confinement, the gravitational sag of Cs trapped in DT can be calculated as

$$z_0 = \frac{\epsilon_0 c \pi}{4\alpha_p} \frac{w_0^4}{2P} (\mu B_g - mg) \tag{2.24}$$

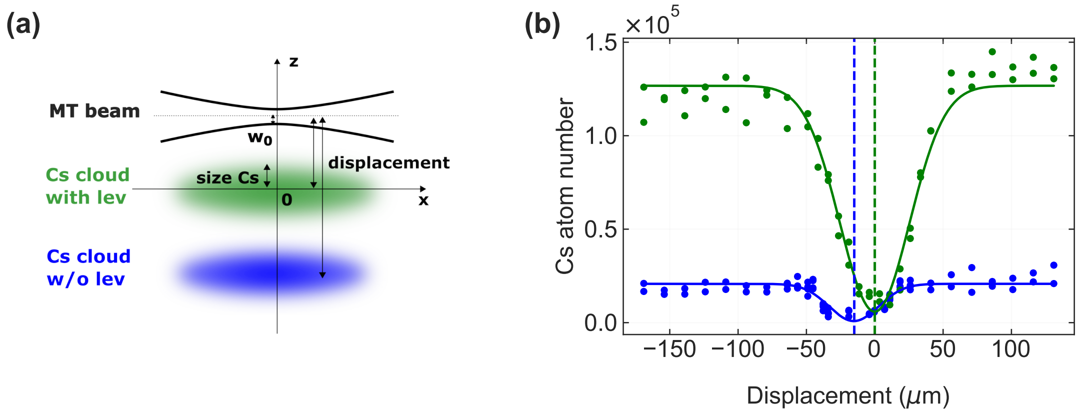

FIGURE 2.11: Measurement of the gravitational sag. (a) Sketch of the procedure. (b) Loss measurement on Cs atoms induced by photon scattering at the tune-out wavelength as a function of the displacement of the MT set by the translation stage. The Cs cloud is prepared in the DT at 900 G, with a magnetic field gradient of 27.7 G/cm providing levitation (in green) and without levitation (in blue). The solid lines represent a Gaussian fit to the data and the vertical dashed lines indicate the position of the minima. The difference between the two minima gives the gravitational sag of Cs Δz_0 = (15.0±1.8) μm. The zero of the x-axis corresponds to the position where the gravitational sag is compensated.

where α_p, w_0, P are the polarizability, beam waist and power of the DT, respectively, while μ is the magnetic moment for Cs atoms at a given magnetic field offset, B_g is the magnetic field gradient for levitating Cs and m is its mass. To levitate the Cs cloud prepared in the DT with a magnetic field offset of 900 G and a power of 200 mW, a magnetic field gradient of 27.7 G/cm is required. With such a levitation, the trap depth is 16 μK and the vertical size of the cloud is σ_z^{Cs} = (37.7±0.3) μm. By decreasing the magnetic field gradient, the trap depth is reduced to 6 μK and the size to (25.0±0.5) μm. In order to know the correction of the stage after switching off the magnetic field gradient, we perform a kind of tomographic measurement. Indeed, the differential gravitational sag is measured by loss tomography on Cs atoms induced by photon scattering at the tune-out wavelength (see section 2.3.1). The MT beam (without Li) is used as a probe and its height from the horizontal plane, defined by the crossed DT beams, is varied in a range larger than the size of the Cs cloud. The power of the beam is experimentally adjusted to maximize the losses without saturating the signal. We change the focal position of the MT beam by moving the translation stage. We measure the remaining atom number as a function of the displacement of the stage, and the position where the losses are maximized is set as the target where to move the MT. A typical measurement is shown in Fig. 2.11. The power of the MT is here set to 147 mW and the loss rate is about 5.21 s^{-1} (see Sec. 2.3.2). The signal is reproduced by a Gaussian function of (25±1) μm with and (18±1) μm without levitation. The difference between the center position of the Gaussian functions, is Δz_0 = (15.0±1.8) μm and represents the effective differential gravitational sag between Li and Cs at 900 G. This results is comparable to the Cs gravitational sag expected from Eq. (2.24), which is about 10 μm. This result differs of approximately 20% with the sag

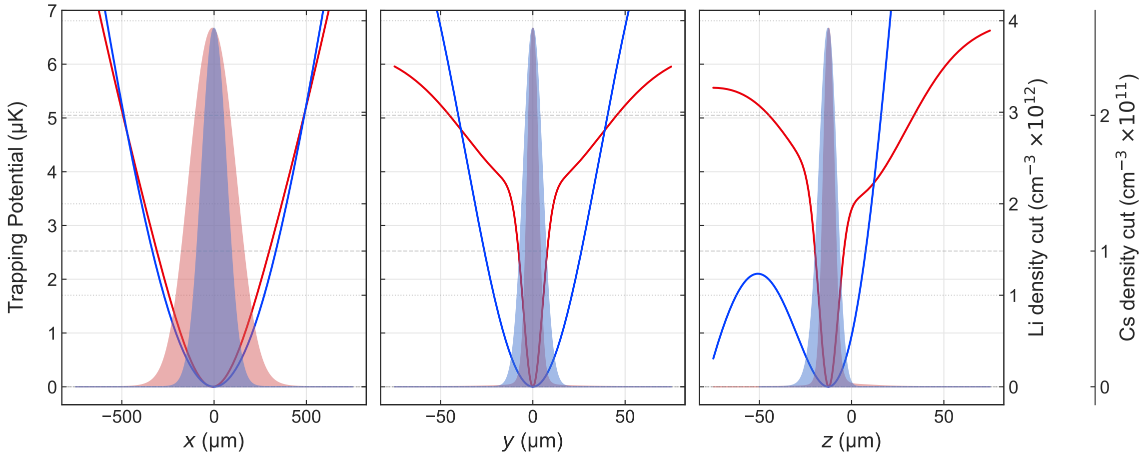

FIGURE 2.12: Trapping potentials and density distributions for Li (red) and Cs (blue) in a purely optical bichromatic trap, in the final preparation step. Li is essentially trapped by the microtrap in y and z directions and by the dimple trap in the x-direction, whereas Cs is only confined by the larger trapping potential provided by the dimple trap. Cuts of the density profiles at the peak density are shown. They are calculated for typically measured atom numbers of $N_{\mathrm{Li}} = 4\times10^4$, $N_{\mathrm{Cs}} = 6.5\times10^3$, $P_{MT} = 8$ mW, $P_{DT} = 150$ mW and magnetic field offset of $B = 900$ G. The gravitational sag is set to zero, as it is compensated by moving the MT with the translational stage. For Li, we consider here a Fermi distribution at finite temperature.

calculated from the full potential, which leads to a gravitational sag of 13 μm. This procedure, in combination with in-situ absorption imaging from top, is regularly performed before mixing the two species in order to compensate for the Cs gravitational sag and center Li on the Cs cloud.

Overlap and final properties of the mixture. The final procedure of overlap between the two species is illustrated in Fig. 2.10 (B). To prevent high intensities and excessive scattering, we ramp down the trap while moving it back. The linear ramp back takes approximately 100 ms. Since returning over a distance of 230 μm with an acceleration of 10 mm/s^2 takes approximately 250 ms, we start to ramp down the power 150 ms after the stage is triggered. The Li cloud has a vertical size of 10 μm, while the Cs cloud has a size of 25 μm. They start to overlap when their centers of mass are 35 μm apart. Considering the accelerated motion of the Li cloud with an acceleration of 10 mm/s^2, this distance is covered in a time of 17 ms. Therefore we have to consider that the sample starts to interact before that they are perfectly overlapped. In the case of the experiment in Sec. 3.3 we wait an additional 100 ms after the end of the ramp down due to the uncertainty in the position of the stage.

Waiting 20 ms, at 900 G, after we reach the target power for the MT, we end up with a mixture of $N_{\mathrm{Li}} = 4\times10^4$, $N_{\mathrm{Cs}} = 6.5\times10^3$ in a bichromatic trapping configuration. Here, the microtrap, at a laser power of $\sim$ 8 mW provides a trapping potential for Li only, which results in a trap depth of $\approx$ 3 μK and trapping frequencies of $\omega_{\mathrm{Li}}/2\pi$ = (44, 2.4$\times10^3$,

2.4×10^3) Hz. The dimple trap, instead, provides trapping mainly for Cs, with trapping frequencies of $\omega_{\mathrm{Cs}}/2\pi$ = (80, 112, 121) Hz. For Li atoms, the DT trap creates a much shallower trap and the atoms remain mainly sucked into the deeper potential provided by the microtrap. We measured separately $T_{\mathrm{Li}} \simeq T_{\mathrm{Cs}} = 560$ nK[8]. Typical peak densities are $\mathrm{n}_{0,Li,F} = 4.0\times10^{12}$ cm^{-3}, $n_{0,Cs} = 5.4\times10^{10}$ cm^{-3} with an estimated $T/T_F = 0.36$. The ratio of the densities is smaller about 1% as desired for impurity physics. The trapping potentials and the density distributions for both Li and Cs are shown in Fig. 2.12. The gravitational sag is set to zero, as it is compensated by moving the MT with the translational stage. The Li spatial density distribution looks completely embedded in the thermal Cs along y and z direction of confinement. We define the volume of spatial overlap between the two clouds as the volume of the overlap normalized to the peak densities of the Cs cloud $n_{0,\mathrm{Cs}}$ and Li cloud $n_{0,\mathrm{Li}}$

$$\frac{V_{overlap}}{V_{\mathrm{Cs}}} = \frac{1}{V_{\mathrm{Cs}}} \underbrace{\int \mathrm{d}^3r\, \frac{n_{\mathrm{Li}}(\mathbf{r})\, n_{\mathrm{Cs}}(\mathbf{r})}{n_{0,\mathrm{Li}} n_{0,\mathrm{Cs}}}}_{V_{overlap}} . \tag{2.25}$$

Assuming thermal distributions for both clouds $V_{overlap} = 0.03 \times V_{\mathrm{Cs}} = 0.7 \times V_{\mathrm{Li}}$. The overlap between the two clouds is confirmed by the signature of interspecies interaction detected as three-body Li-Cs losses near the Feshbach resonance at 888.6 G shown in Sec. 2.3.2. Another independent indication of the overlap between the two clouds is given by the measurements performed in Sec. 2.3.1 by the estimate of the overlap between the MT laser beam and the Cs cloud.

Considerations about thermalization. The collisional rate is given by [Mosk *et al.*, 2001; Ivanov *et al.*, 2011]

$$\tau_{coll}^{-1} = \xi \bar{v} \sigma_{\mathrm{LiCs}} \bar{n}, \tag{2.26}$$

where $\bar{n} = (N_{\mathrm{Li}}^{-1} + N_{\mathrm{Cs}}^{-1}) \int \mathrm{d}^3r\; n_{\mathrm{Li}}(\mathbf{r})\; n_{\mathrm{Cs}}(\mathbf{r})$ is the overlap density [Silber *et al.*, 2005; Ivanov *et al.*, 2011], $\bar{v} = \sqrt{\frac{8k_B}{\pi}(\frac{T_{\mathrm{Li}}}{m_{\mathrm{Li}}} + \frac{T_{\mathrm{Cs}}}{m_{\mathrm{Cs}}})}$ is the mean thermal velocity, σ_{LiCs} is the s-wave scattering cross-section and $\xi = 4m_{red}/M = 4m_{\mathrm{Li}}m_{\mathrm{Cs}}/(m_{\mathrm{Li}} + m_{\mathrm{Cs}})^2$ is the mass-mismatch factor that corrects for unequal mass collisions, which for Li-Cs is $\xi \simeq 0.17$. We include an energy dependence to s-wave cross-section $\sigma_{\mathrm{LiCs}} = (4\pi a_{\mathrm{LiCs}}^2)/(1 + k^2 a_{\mathrm{LiCs}}^2)$, where $\hbar k = m_{red}\bar{v}$ is the mean relative thermal momentum with $m_{red} = m_{\mathrm{Li}}m_{\mathrm{Cs}}/(m_{\mathrm{Li}} + m_{\mathrm{Cs}})$ the reduced mass for Li-Cs. Assuming for both $n_{\mathrm{Li}}(\mathbf{r})$ and $n_{\mathrm{Cs}}(\mathbf{r})$ two gaussian distributions as in Eq. (2.5) with $x_0^{\mathrm{Li,Cs}} = y_0^{\mathrm{Li,Cs}} = 0$, the overlap density can be simplified to

$$\bar{n} = (N_{\mathrm{Li}}^{-1} + N_{\mathrm{Cs}}^{-1}) \cdot \frac{N_{\mathrm{Li}} N_{\mathrm{Cs}}}{(2\pi)^{3/2}} \exp\left(\frac{\Delta z^2}{2(\sigma_{z,\mathrm{Li}}^2 + \sigma_{z,\mathrm{Cs}}^2)}\right) \prod_{i=x,y,z} \frac{1}{\sqrt{(\sigma_{i,\mathrm{Li}}^2 + \sigma_{i,\mathrm{Cs}}^2)}}, \tag{2.27}$$

---

[8] It should be noted that the measured Cs temperature is higher by a factor of 3 than that expected by considering a thermalization factor between 6 and 10 for the calculated trapping potential. The values of the sizes obtained from the ballistic expansion of the TOF measurements are also higher than those expected from the calculated density distributions. Cs is already interacting with the MT light and heating up.

where $\sigma_i = \sqrt{k_B T/(m\omega_i^2)}$ are the widths of the atomic clouds and $\Delta z = z_0^{\mathrm{Li}} - z_0^{\mathrm{Cs}}$ is the difference between the centers of the Li and Cs distributions and provides the differential gravitational sag of the two species. The overlap density, calculated for the parameters reported at the beginning of the previous paragraph, is $\overline{n} = 2.8\times10^{11}$ cm^{-3}, while $\int d^3r\ n_{\mathrm{Li}}(\mathbf{r})\ n_{\mathrm{Cs}}(\mathbf{r})$ = 1.6×10^{15} cm^{-3}. The inter-component thermalization time, which characterizes the variation of the temperature difference $\Delta T = T_{\mathrm{Li}} - T_{\mathrm{Cs}}$ is given by [Mosk *et al.*, 2001; Mudrich *et al.*, 2002]

$$-\frac{1}{\Delta T}\frac{d(\Delta T)}{dt} = \tau_{th}^{-1} = \frac{1}{\alpha}\tau_{coll}^{-1}, \tag{2.28}$$

where α is the average number of collisions needed for thermalization. For harmonic traps $\alpha \sim 3$ [Wu and Foot, 1996; Arndt *et al.*, 1997; Delannoy *et al.*, 2001; Mosk *et al.*, 2001; Mudrich *et al.*, 2002]. If the offset magnetic field is set to 900 G, corresponding to $\mathrm{a_{LiCs}} = -175\ \mathrm{a_0}$, the expected collision rate between the two species is $\tau_{coll}^{-1} \sim 2.3$ s^{-1}. This rate corresponds to $\tau_{coll} \sim 440$ ms and $\tau_{th} \sim 1.3$ s is the expected thermalization time. If instead the mixture is prepared directly at unitarity, i.e. at 888.7 G (as for the measurements in Sec. 2.3.2 and Sec. 3.3.1) then $\tau_{coll}^{-1} \sim 1.4\ \times10^3$ s^{-1}, leading to $\tau_{coll} \sim$ 0.7 ms and $\tau_{th} \sim 2$ ms. By replacing $n_{\mathrm{Li}}(\mathbf{r})$ with a Fermi distribution (see Eq. (2.8)), the overlap density needs to be evaluated numerically. We performed this calculation by considering a pure harmonic potential (see Eq. 2.3) with trapping frequencies $\omega_{\mathrm{Li}}/2\pi$ = (44, 2.4×10^3, 2.4×10^3) Hz provided by the MT only and with a chemical potential of $\mu = k_B \times 1.35\ \mu$K. The resulting collisional rates are reduced by 10% compared to the rates calculated assuming thermal density distributions for both clouds.

2.3 Loss processes in a Li-Cs mixture

In order to gain experimental access to the creation of Fermi polarons, it is important to understand the losses that occur in our mixed system. In a $\mathrm{Li}|2\rangle\oplus\mathrm{Cs}|1\rangle$ mixture, losses mainly include the one-body losses, in particular induced by light at the tune-out wavelength on Cs atoms as well as Li-Cs three-body losses [Ulmanis, 2015]. In Sec. 2.3.1 we investigate the effect of the one-body losses induced by the MT at the tune-out wavelength and in Sec. 2.3.2 we observe a clear signature of interspecies interactions, manifested in the three-body loss close to the Li-Cs Feshbach resonance at 888.6 G. In addition, by measuring both types of losses, we qualitatively test the overlap between the atomic clouds.

2.3.1 Light-induced Cs loss at the tune-out wavelength

The use of a dipole trap for trapping Li atoms tuned at the Cs tune-out wavelength [Arora *et al.*, 2011; Jiang *et al.*, 2020; Ratkata *et al.*, 2021] (see also Sec. 1.3) facilitates the independent control over the two species when the two clouds are spatially overlapped, as it prevents imposing any additional confinement on the Cs atoms [LeBlanc and Thywissen, 2007]. Nevertheless, the Cs tune-out wavelength is in between the D_1 and D_2 line and this leads to relevant spontaneous photon scattering by Cs atoms, which increases

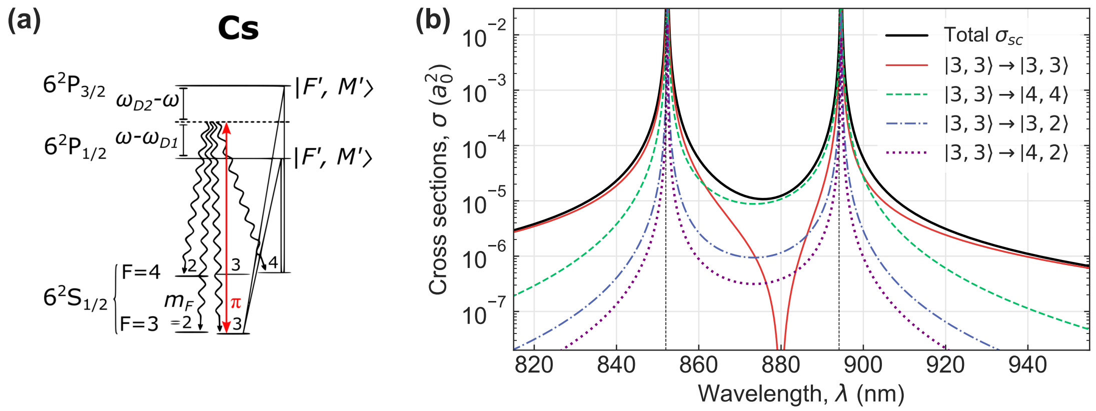

FIGURE 2.13: Spontaneous photon scattering by Cs atoms. (a) Energy levels of ^{133}Cs showing spontaneous transitions from linearly polarized light. The laser light at frequency ω is in red and lies in between $\mathcal{D}_1$ and $\mathcal{D}_2$ lines. The solid lines show the path for scattering process when laser detuning is larger than the excited-state hyperfine-structure splitting. This picture has been inspired by Cline *et al.* [1994]. (b) Scattering cross-sections for π-polarized light interacting with Cs atoms in the ground state as a function of the laser wavelength. The total scattering cross-section is indicated with a solid black line, Rayleigh scattering cross-section is the solid red line, and F-changing Raman scattering cross-section to $|F'', m_F''\rangle = |4,4\rangle$, $|3,2\rangle$ and $|4,2\rangle$states are the green dashed, violet dot-dashed and purple dot-lines, respectively. Both pictures have been adapted from [Welz, 2024].

the trap loss rates and might prevent state-selective experiments for Cs [Cline *et al.*, 1994; Kaplan *et al.*, 2005].

Spontaneous photon scattering. Spontaneous scattering is a two-photon process, in which an atom initially in a state $|F, m_F\rangle$ absorbs a photon from the trapping laser and goes to an intermediate state $|F', m_F'\rangle$ of some excited level. The atom then decays back to the ground state, to a final state $|F'', m_F''\rangle$. If the final state matches the initial state, specifically $F'' = F$ and $m_F'' = m_F$, the process is identified as Rayleigh scattering. Conversely, if the final state differs, i.e. $F'' \neq F$ or $m_F'' \neq m_F$, the process is known as Raman scattering, prevents the possibility to prepare the atoms in a well defined state and therefore has a negative impact on spectroscopic measurements. Following the considerations in Cline *et al.* [1994] and [Kaplan *et al.*, 2005] applied to Rubidium atoms, the probability amplitude for scattering between $|F, m_F\rangle$ and $|F'', m_F''\rangle$ via $|F', m_F'\rangle$ is proportional to $\langle F, m_F|\hat{d}_0|F', m_F'\rangle \langle F', m_F'|\hat{d}_q|F'', m_F''\rangle$ where d_q are the spherical components of the dipole moment operator q = 0 ,1 or -1 depending on the polarization of the absorbed and emitted photons. We consider here a linearly polarized laser and for the conservation of the angular momentum we have $m_F = m_F'$. Moreover, considering that the detuning from resonance is large enough such that no specific intermediate state is resolved, the rate of transition between $|F, m_F\rangle$ and $|F'', m_F''\rangle$ is given by the sum over all possible intermediate states as provided by the so called Kramers-Heisenberg formula [Cline *et al.*, 1994;

Loudon, 2000]

$$\Gamma_{|FM\rangle\rightarrow|F''m''_F\rangle}(\mathbf{r},\omega) = \frac{I(\mathbf{r})(\omega-\omega_{F''m''_F})^3}{\hbar^3\epsilon_0^2c^46\pi}\left|\sum_{q,J',F',m'_F}\frac{\langle F'',m''_F|\,\hat{d}_q\,|F',m'_F\rangle\,\langle F',m'_F|\,\hat{d}_0\,|F,m_F\rangle}{\omega_{J',F',m'_F}-\omega}\right|^2 \tag{2.29}$$

where ω is the frequency of the laser of the dipole trap and $I(\mathbf{r})$ is the gaussian intensity profile of the laser beam. Moreover, the sum over the contributions from all the final possible states $|F'',m''_F\rangle$ coincides with the total scattering rate as calculated from the imaginary part of the polarizability in Eq. (1.5)

$$\Gamma_{sc}(\mathbf{r},\omega) = \sum_{F'',m''_F}\Gamma_{|3,3\rangle\rightarrow|F'',m''_F\rangle}(\mathbf{r},\omega) \equiv \frac{1}{\hbar\epsilon_0 c}\Im m\{\alpha(\omega)\}I(\mathbf{r}) \tag{2.30}$$

Figure 2.13 (a) shows the transitions for Cs atom prepared in the $|3,+3\rangle$ state when it spontaneously scatters a photon from linearly polarized light at the tune-out wavelength. The intermediate states correspond to the $6^2\mathrm{P}_{1/2}$ and $6^2\mathrm{P}_{3/2}$ excited states, while the only possible final states are $|F'',m''_F\rangle = |3,3\rangle$, $|4,4\rangle$, $|3,2\rangle$ and $|4,2\rangle$ [Welz, 2024]. In Fig. 2.13 (b) the total scattering rate calculated from Eq. (1.7) and the spontaneous photon scattering rates calculated from Eq. (2.29) are shown as a function of the wavelength for linear polarization of the laser light. Both processes are expressed in terms of the scattering cross-section to be intensity independent. The total scattering cross-section $\sigma_{sc}(\omega)$ is then given by:

$$\sigma_{sc}(\omega) = \frac{\hbar\omega\Gamma_{sc}(\mathbf{r},\omega)}{I(\mathbf{r})}. \tag{2.31}$$

The dominant contribution to the spontaneous scattering cross-section at 880.25 nm is given by the spontaneous two-photon Raman scattering from the state $|3,+3\rangle$ to the state $|4,+4\rangle$, which is more than one order of magnitude larger than the contributions to the spontaneous scattering from the state $|3,+3\rangle$ to the states $|3,2\rangle$ and $|4,2\rangle$, respectively. The spontaneous Rayleigh cross-section is zero due to destructive interference between the transition probabilities over the $\mathcal{D}_1$ and $\mathcal{D}_2$ lines.

Cs losses at the tune-out wavelength. We study Cs losses of optically trapped atoms due to light scattering from the laser light at the tune-out wavelength. We prepare about $N = 2.5\times10^4$ atoms in the $|3,+3\rangle$ state at a temperature of $T = 1\ \mu$K and a magnetic field offset of 880 G, corresponding to the zero crossing of the $|3,+3\rangle\oplus|3,+3\rangle$ scattering length. We switch on the laser light at $\lambda_{MT} = 880.25$ nm for a variable amount of time and record the time evolution of the atom number for different laser power values as shown in Fig. 2.14 (a). In order to understand how the atomic population is distributed among the states $|3,+3\rangle$ and $|4,+4\rangle$ once the MT laser light is turned on, we write down a set of coupled differential equations which describe the evolution of the atomic densities $n_3(\mathbf{r})$ and $n_4(\mathbf{r})$, corresponding to the states $|3,+3\rangle$ and $|4,+4\rangle$, respectively (see also [Welz,

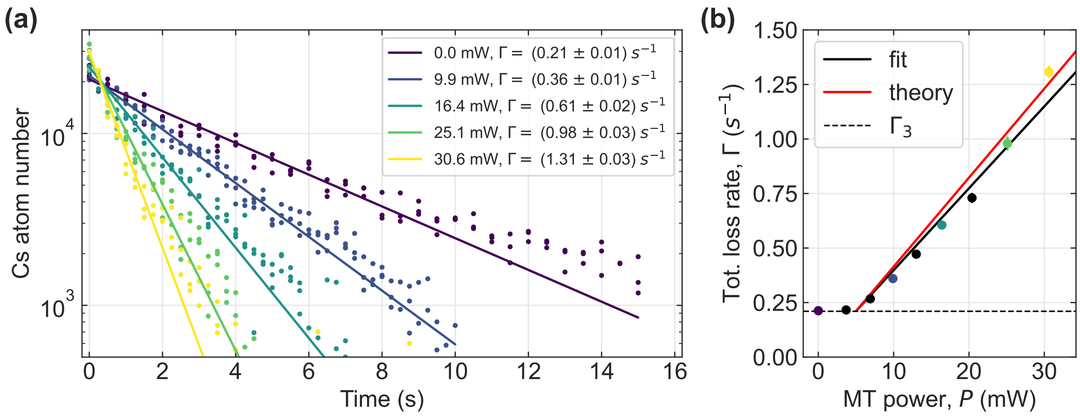

FIGURE 2.14: Cs light-induced loss at the tune-out wavelength. (a) Remaining number of Cs atoms trapped in the DT and prepared in the $|3, +3\rangle$ state as a function of the exposure time to light tuned at its tune-out wavelength (MT) for different MT powers. The solid lines are exponential fit to data with Γ as free parameter. (b) Loss rate Γ as a function of the MT power P. The colored dots correspond to the data shown in panel (a). The black solid line is a linear fit to the data with η_3 as free parameter as in Eq. (2.44); the red solid line reproduces the loss rate with η_3 as calculated by Eq. (2.37) for the measured sizes of the cloud. The black dashed line is the measured loss rate in absence of the MT light, $\Gamma_3 = (0.21 \pm 0.01)\ \mathrm{s}^{-1}$.

2024]):

$$\dot{n}_3(\mathbf{r}) = -\Gamma_{34}(\mathbf{r}) \cdot n_3(\mathbf{r}) + \Gamma_{43}(\mathbf{r}) \cdot n_4(\mathbf{r}) - \Gamma_3 \cdot n_3(\mathbf{r}) \tag{2.32}$$

$$\dot{n}_4(\mathbf{r}) = +\Gamma_{34}(\mathbf{r}) \cdot n_3(\mathbf{r}) - \Gamma_{43}(\mathbf{r}) \cdot n_4(\mathbf{r}) - \Gamma_4 \cdot n_4(\mathbf{r}), \tag{2.33}$$

where Γ_3 and Γ_4 are the one-body loss rates of Cs from the trap in the $|3, +3\rangle$ and $|4, +4\rangle$ in absence of the MT light; $\Gamma_{34}(\mathbf{r})$ and $\Gamma_{43}(\mathbf{r})$ are the scattering rates from the ground state $|3, +3\rangle$ to the excited state $|4, +4\rangle$ and viceversa at the frequency ω_{MT} of the MT, corresponding to the tune-out wavelength[9]. Here, $\Gamma_{34}(\mathbf{r}) \equiv \Gamma_{43}(\mathbf{r})$ and can be calculated using Eq. (2.29). The scattering cross-section for $\omega_{MT} = 2\pi c/\lambda_{MT}$ is $\sigma_{34} = \sigma_{43} = 1.09 \times 10^{-5}\ \mathrm{a}_0^2$. We spatially integrate Eq. (2.32) and Eq. (2.33) over the density distributions and arrive at the equivalent system of differential equations for the atom numbers N_3 and N_4 of the two spin states:

$$\dot{N}_3 = -\frac{\sigma_{34}}{\hbar\omega} \int_R I(\mathbf{r}) n_3(\mathbf{r}) d\mathbf{r} + \frac{\sigma_{43}}{\hbar\omega} \int_R I(\mathbf{r}) n_4(\mathbf{r}) d\mathbf{r} - \Gamma_3 \cdot N_3, \tag{2.34}$$

$$\dot{N}_4 = +\frac{\sigma_{34}}{\hbar\omega} \int_R I(\mathbf{r}) n_3(\mathbf{r}) d\mathbf{r} - \frac{\sigma_{43}}{\hbar\omega} \int_R I(\mathbf{r}) n_4(\mathbf{r}) d\mathbf{r} - \Gamma_4 \cdot N_4. \tag{2.35}$$

We define an average scattering rate $\overline{\Gamma}_{34}$ and $\overline{\Gamma}_{43}$, introducing the coefficients η_3 and η_4, which take into account the finite volume of overlap between the space occupied by the

---

[9] Two-body inelastic processes between the state $|3, +3\rangle$ and $|4, +4\rangle$ at 880 G are neglected. Indeed, we prepare on purpose a sample with half of the atoms in the state $|3, +3\rangle$ and half in the state $|4, +4\rangle$ without MT light and record the atoms in the $|4, +4\rangle$ state with and without atoms in the $|3, +3\rangle$. The $1/e$ lifetime extracted in the two cases is identical. Feshbach spectroscopy of several Cs scattering channels is reported in [Chin *et al.*, 2004] but only to magnetic fields up to 30 G.

gaussian beam, whose intensity distribution $I(\mathbf{r})$ is given by Eq. (1.8), and the gaussian density distribution $n(\mathbf{r})$ for a thermal Cs cloud, which is given by Eq. (2.5). The coefficient of overlap η between the Cs cloud and the MT beam is defined by

$$\int_R I(\mathbf{r})\, n(\mathbf{r})\, d\mathbf{r} \;=\; I_0 N_0 \eta \tag{2.36}$$

and obtained by substituting Eq. (1.8) and Eq. (2.5) in the right part of Eq. (2.36)

$$\eta = \underbrace{\frac{1}{R_{\mathrm{x}} R_{\mathrm{y}} R_{\mathrm{z}} \sqrt{\pi^3}}}_{V_{\mathrm{cloud}}^{-1}} \underbrace{\int_{-\infty}^{\infty} dx \frac{\exp\left(-x^2/R_{\mathrm{x}}^2\right)}{(2/(w_0^2(1+(x/x_R)^2)) + 1/R_{\mathrm{y}}^2)(1+x^2/x_{\mathrm{R}}^2)}}_{V_{\mathrm{overlap}}}, \tag{2.37}$$

where R_x, R_y, R_z are the sizes of the thermal Cs cloud, while w_0 and x_R are the beam waist and the Rayleigh length of the MT beam, respectively. If the cloud and beam are not centered one on top of each other, then, only in one of the functions under the integral, $\mathbf{r} \rightarrow \mathbf{r} - \mathbf{r}_0$, and the variable $\mathbf{r}_0$ needs to be introduced. The average scattering rate is then defined as

$$\overline{\Gamma}_{34}(P) = \frac{\sigma_{34}}{\hbar\omega} \eta_3 I_0(P) \quad \text{and} \quad \overline{\Gamma}_{43}(P) = \frac{\sigma_{43}}{\hbar\omega} \eta_4 I_0(P), \tag{2.38}$$

where $I_0(P) = 2P/\pi w_0^2$ is the peak intensity of the MT laser beam with power P. Therefore, Eq. (2.34) and Eq. (2.35) can be re-written as

$$\dot{N}_3(P) = -\overline{\Gamma}_{34}(P) \cdot N_3 + \overline{\Gamma}_{43}(P) \cdot N_4 - \Gamma_3 \cdot N_3, \tag{2.39}$$
$$\dot{N}_4(P) = +\overline{\Gamma}_{34}(P) \cdot N_3 - \overline{\Gamma}_{43}(P) \cdot N_4 - \Gamma_4 \cdot N_4. \tag{2.40}$$

The one-body loss rates Γ_3 and Γ_4, are taken from independent measurements in absence of the MT light, preparing intentionally the cloud in one of the two states. For the cloud prepared in $|3,+3\rangle$ we measure $\Gamma_3 = (0.21 \pm 0.01)\ \mathrm{s}^{-1}$, corresponding to timescales of $\Gamma_3^{-1} = (4.7 \pm 0.2)s$. For the cloud prepared in $|4,+4\rangle$, instead, we obtain much higher rates of $\Gamma_4 = (62.1 \pm 0.2)\ \mathrm{s}^{-1}$ and timescales of $\Gamma_4^{-1} = (16.1 \pm 0.05)$ ms. Depending on the relation between $\Gamma_4, \overline{\Gamma}_{43}$ and $\overline{\Gamma}_{34}$, one can distinguish between different regimes.

Regime $\Gamma_4 \ll \overline{\Gamma}_{43}, \overline{\Gamma}_{34}$: It can be demonstrated that assuming the population in the $|4,+4\rangle$ to be in equilibrium, such that $\dot{N}_4 = 0$, and the one-body losses from that state to be the slowest loss process in the system, the population which accumulates in the state $|4,+4\rangle$ due to spontaneous Raman scattering is negligible. Therefore, the evolution of the atom number follows a pure exponential decay and the total loss rate for atoms in the $|3,+3\rangle$ changes linearly as a function of the power. These conditions read as

$$\dot{N}_4(P) = 0 \longrightarrow N_4 = \frac{\overline{\Gamma}_{34}(P)}{\overline{\Gamma}_{43}(P) + \Gamma_4} N_3. \tag{2.41}$$

Inserting this result in Eq. (2.39) we obtain

$$\dot{N}_3(P) = \underbrace{-\Gamma_3 + \left(\frac{\overline{\Gamma}_{34}(P)}{1+\frac{\overline{\Gamma}_{43}(P)}{\Gamma_4}}\right)}_{\Gamma(P)} N_3 \longrightarrow N_3(t;P) = N_0 e^{-\Gamma(P)t}. \tag{2.42}$$

As $\overline{\Gamma}_{43} \approx \overline{\Gamma}_{34}$ and for $\Gamma_4 \gg \Gamma_{43}$, then $N_4 \sim 0$ and the total loss rate reduces to

$$\Gamma(P;\eta_3) = \Gamma_3 + \overline{\Gamma}_{34}(P;\eta_3) \tag{2.43}$$

$$= \Gamma_3 + \frac{\sigma_{34}}{\hbar\omega}\eta_3 \frac{2P}{\pi w_0^2} \tag{2.44}$$

where $\overline{\Gamma}_{34}(P)$ is defined in Eq. (2.38) and η_3 is taken as free parameter. Since it is challenging to determine a priori what is the MT power (intensity) for which the above condition holds, we measure the time evolution of the number of Cs atoms initially prepared in the $|3,+3\rangle$ for different MT powers, as shown in Fig. 2.14 (a). We experimentally determine that a good exponential fit is achieved up to powers of ≈ 30 mW. This is slightly above the typical power used for trapping Li when the two species are overlapped. Figure 2.14 (b) shows that the loss coefficient Γ increases linearly with power in the same range, as expected from Eq. (2.44). Due to an offset in the calibration of the MT power, the total loss rate up to 5 mW coincides with the background one-body loss. Beyond 5 mW, the loss rate increases linearly with the power, with an angular coefficient of ≈ 0.04 s^{-1} mW^{-1}, reaching a rate of 1.25 s^{-1} for 30 mW, which corresponds to a $1/e$ lifetime of 800 ms. The fit of the loss rate as a function of the power is done by fixing all the parameters except η_3, which is the coefficient of overlap as defined in Eq. (2.37). We determine experimentally $\eta_3^{exp} = (0.044 \pm 0.003)$. This result is in very good agreement with the calculated value $\eta_3^{th} = (0.051 \pm 0.002)$, as given by Eq. (2.37) considering the cloud and the beam centered on each other and for the measured size of the Cs cloud considered here, which are $R_{y,z} = 27.5(5)$ μm and $R_x = 257(4)$ μm. We can then define an effective scattering cross-section $\sigma_{34,eff} = \sigma_{34} \cdot \eta_3$, which results in $(4.796 \pm 0.014) \times 10^{-7}$ a_0^2, with η_3^{exp} found experimentally and $(5.51 \pm 0.18) \times 10^{-7}$ a_0^2, with η_3^{th} calculated from Eq. (2.37).

In order to draw conclusions about the consequences of such a loss rate to the Fermi polaron experiment, we need to compare the total one-body loss found here with the timescales involved in the polaron experiment. This means that the lifetime of the Cs atoms in the presence of the MT must be sufficiently larger than the pulse length τ_{pulse} and the Fermi time $\tau_F = E_F/h$ (see section 3.3), which are on the order of tens and a few microseconds, respectively. This requirement is satisfied by keeping the power of the MT lower than 30 mW when the two species are overlapped, resulting in a Cs lifetime of about 800 ms. In addition to the procedure of overlap described in 2.2.3, there are further times to consider, such as the time required to set a magnetic field and the waiting time for the stage to adjust to the target position, which can introduce a delay of up to 100 ms. However, these are technical times that can be optimized. On the basis of these considerations, the total one-body loss rates do not seem to be a limitation for the experiment.

It should be noted that the loss rate depends on the coefficient η, which quantifies the normalized volume of overlap between the atomic cloud and the light beam. On the one hand, with regard to a global observable such as the atom number in atom loss spectroscopy, the region to be considered is the entire Cs cloud. Raman spontaneous scattering is therefore not a limiting factor. On the other hand, for an observable related to a local quantity, such as the atomic density at a given local Fermi energy $E_F(\mathbf{r})$ (as in polaron spectroscopy), the region to consider must be reduced. The challenge is to define the region from which the signal comes. The timescales associated with Raman spontaneous scattering from the $|3,+3\rangle$ to the $|4,+4\rangle$ state mentioned above can then only be considered as an upper limit. The lower limit is instead given by a scenario where $V_{\text{overlap}} = V_{\text{cloud}}$, which means that $\eta = 1$ and therefore $\sigma_{34,eff} = \sigma_{34}$. The loss rate would be proportional to the power with an angular coefficient of $\approx 0.8\ \text{s}^{-1}\ \text{mW}^{-1}$. This would imply a Γ of 4 s^{-1} for 10 mW, 12 s^{-1} for 20 mW and 20 s^{-1} for 30 mW, corresponding to timescales of 260 ms, 90 ms and 50 ms respectively. These timescales could be problematic for polaron experiments.

Regime $\Gamma_4 \simeq \overline{\Gamma}_{34}, \overline{\Gamma}_{43}$: If the average scattering rates $\overline{\Gamma}_{34}$ and $\overline{\Gamma}_{43}$ become comparable to the loss rate Γ_4, then part of the atomic population is transferred from the $|3,+3\rangle$ to the $|4,+4\rangle$ state. In this scenario, the cloud is a mixture of the two states whose relative distribution changes over time and the total loss rate as a function of the power is not expected to be linear. This prevents state-selective experiments, as required for the Fermi polaron. In addition, two aspects complicate the study of this situation. First, the imaging scheme (see section 1.5.2) makes impossible to distinguish atoms in the $|3,+3\rangle$ state from those in the $|4,+4\rangle$ state [Schoenhals, 2013]. Indeed, we first pump the atoms from the $|3,+3\rangle$ to the $|m_J' = 1/2, m_I' = 7/2\rangle$ state. They decay into the $|4,+4\rangle$ and back to the $|3,+3\rangle$. Therefore, we repump them into the $|4,+4\rangle$ state and then we do imaging by using the transition $|4,+4\rangle \rightarrow |m_J' = 3/2, m_I' = 7/2\rangle$ of the excited $6^2\text{P}_{3/2}$ manifold. Second, the excited state $|4,+4\rangle$ has a different trap confinement than the $|3,+3\rangle$ state because it is magnetically antitrapping and therefore its effective trap depth depends crucially on the dimple trap being centered on the curvature of the magnetic field provided by the Feshbach coils along the axial direction (see section 1.4.1). If the Cs cloud is not at the center of the Feshbach coils, the losses increase and the exponential fit might not work [Welz, 2024].

2.3.2 Signatures of Li-Cs interactions

The best indication of spatial overlap between the Li and Cs cloud is provided by the observation of interspecies interactions, manifested in the three-body loss near the Feshbach resonance. With this aim, we perform loss spectroscopy measurements close to the Li-Cs Feshbach resonance at 888.6 G and record the corresponding time evolution of the number of Li and Cs atoms during the time of interaction. Additionally, the set of measurements presented here is performed in the presence of large MT photon scattering, manifesting essentially as Cs one-body loss. We would like to show that the time evolution of the number of Cs atoms in presence of such high one-body loss, still shows characteristic three-body loss decay. To this end, I compare the remaining number of Li and Cs atoms as a function of the interaction time with a theoretical model, taking into account one-body loss recorded by an independent measurement, and three-body loss calculated at unitarity.

The experimental preparation of the mixture of Cs$|3,+3\rangle \oplus$Li$|2\rangle$ follows the sequential bichromatic scheme described in Sec. 2.2. The power of the MT is set to 147 mW, corresponding to a trap depth of $\approx 76\ \ \mu$K. We prepare samples of 2.5×10^4 atoms of Cs and 2×10^4 atoms of Li at temperatures of $T \approx 1\ \ \mu$K and $\approx 4\ \ \mu$K, respectively. We calculated trapping frequencies of $(\omega_r^{Li}, \omega_{ax}^{Li}) = 2\pi \times (11 \times 10^3, 200)$ Hz for Li and $(\omega_r^{Cs}, \omega_{ax}^{Cs}) = 2\pi \times (140, 10)$ Hz for Cs. From the former ones a Fermi temperature of $T_F \approx 7\ \ \mu$K is calculated and results in a $T/T_F \sim 0.6$ and a peak density $n_0^{Li} = 1.8 \times 10^{13}$ cm^{-3} for Li and $n_0^{Cs} = 2.3 \times 10^{11}$ cm^{-3} for Cs. The initial sizes of both clouds, $(\sigma_r^{Li}, \sigma_{ax}^{Li}) = (12, 70)\ \mu$m and $(\sigma_r^{Cs}, \sigma_{ax}^{Cs}) = (22, 200)\ \mu$m, are extracted from a fit of TOF expansions obtained by independent measurements. At the Li-Cs Feshbach resonance, the interspecies scattering length $a_{\mathrm{LiCs}} \to \infty$, while the Cs intra-species scattering length is $a_{\mathrm{CsCs}} = 180\ \mathrm{a}_0$.

Loss spectroscopy. Feshbach spectroscopy is performed by ramping up the magnetic field to a desired value immediately after the translation stage brings the Li cloud into superposition with the Cs cloud, and then waiting 100 ms to allow the interacting system to evolve. The magnetic field is calibrated by RF spectroscopy on Li atoms as shown in Sec. 1.4.2 and Fig. 1.17 (a). The remaining atoms for both species are monitored in the same experimental cycle. High field absorption imaging is used to image selectively the states Li$|2\rangle$ and Cs $|3,+3\rangle$. The time delay between the two images is 1.5 ms (first Li and then Cs). The measurement shown in Fig. 2.15 was made with a step size of 550 mG between 880.22 G and 897.04 G. The loss signal is about 26% for Li atoms and about 40% for Cs atoms, which is consistent with the 1:2 ratio expected for Li-Cs-Cs losses. This is a clear signature of the resonance and it does not saturate the signal. We reproduce the loss feature with a Gaussian function and extract an FWHM of (2.35 ± 0.14) G on Li, and of (4.03 ± 0.16) G, on Cs. In the case of Cs, we add a slope to take into account losses due to Cs-Cs interactions.

Temporal evolution. To ensure that we understand the loss dynamics, even in this slightly complicated scenario with MT-induced Cs losses, we take a closer look at the atom numbers recorded as a function of interaction time. Therefore, the evolution of the atom numbers of Li and Cs over the interaction time is compared with a theoretical model which takes into account independent measurements of the one-body loss and the calculated value of the three-body loss at unitarity. The procedure is the following: (i)

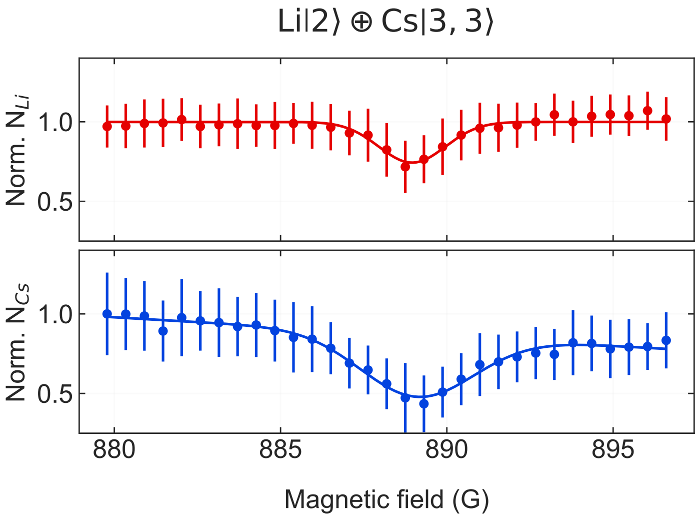

FIGURE 2.15: Loss spectra of the interspecies Li-Cs s-wave Feshbach resonance at 888.6 G on Li (red) and Cs (blue) in a Li-Cs mixture Li$|2\rangle \oplus$Cs$|3, +3\rangle$. The y axis shows the remaining atom number normalized to the atom number recorded at a magnetic field of 880 G. Each data point is the average of at least twenty independent measurements and the error bars represent the standard deviation.

writing the coupled differential equations for the density distributions of both species following the model in [Ulmanis, 2015]; (ii) performing a spatial integration of this equation to obtain an equation for the atom numbers, which is the observable we can measure [Ulmanis, 2015]; (iii) adding assumptions specific to the measurement presented here, which further simplify the model, and calculating the three-body loss rate at unitarity; (iv) comparing the result with the data.

The set of coupled differential equations which describes the time evolution of the atomic densities n_{Li} and n_{Cs} is given by [Ulmanis, 2015]

$$\dot{n}_{\mathrm{Cs}} = -L_1^{\mathrm{Cs}} n_{\mathrm{Cs}} - 2L_3 n_{\mathrm{Cs}}^2 n_{\mathrm{Li}} - L_3^{\mathrm{Cs}} n_{\mathrm{Cs}}^3, \tag{2.45}$$

$$\dot{n}_{\mathrm{Li}} = -L_1^{\mathrm{Li}} n_{\mathrm{Li}} - L_3 n_{\mathrm{Cs}}^2 n_{\mathrm{Li}}, \tag{2.46}$$

where $L_1^{\mathrm{Li,\,Cs}}$ are the one-body loss rates of Li and Cs atoms from the trap and L_3^{Cs} is the three-body recombination loss rate coefficient. The interspecies inelastic three-body losses due to Cs-Cs-Li collisions are described by the loss rate coefficient L_3. The factor of two that multiplies L_3 in the equation for Cs indicates that two Cs atoms and one Li atom are lost from the trap in each recombination process. Following the consideration in Ulmanis [2015], the inelastic Li-Li-Cs collisions are neglected, since this process is strongly suppressed due to Pauli blocking. We also neglect inelastic two-body collisions as we prepare the atoms in their respective ground state manifold[10]. Moreover, as we do not observe any temperature rise during the entire interaction time, we do not include

---

[10] For atoms polarized in the Li$|1\rangle \oplus$Cs$|1\rangle$ channel, this process is excluded; for the Li$|2\rangle \oplus$Cs$|1\rangle$ channel it is negligible [Tung *et al.*, 2013].

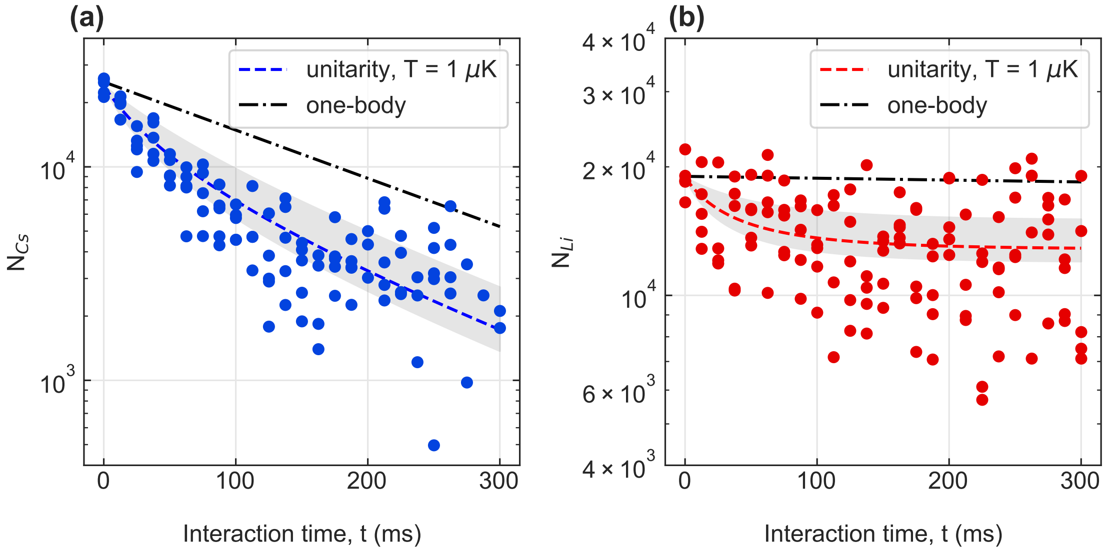

FIGURE 2.16: Temporal evolution of the remaining atom number of Cs (blue) and Li (red) in a Li-Cs mixture of Li$|2\rangle \oplus$Cs$|3,+3\rangle$ at the Li-Cs Feshbach resonance at 888.6 G (at unitarity). The dashed lines represent the solution of the differential equations in Eq. (2.51) and 2.52 for L_3=L_3^{un} at T = 1 μK and $L_1^{Cs} = 5.2\,\mathrm{s}^{-1}$. The black dot-dashed lines reproduce the exponential decay functions fitted to an independent measurement without Li (a) or Cs (b), respectively. The measured one-body loss rate for a pure Li gas corresponds to $L_1^{Li} = 0.0925\,\mathrm{s}^{-1}$ and for a pure Cs gas in presence of MT light at a power of 147 mW to $L_1^{Cs} = 5.2\,\mathrm{s}^{-1}$. The gray shaded area is given by a systematic error in the determination of the geometric conversion factor to L_3, which assumes an uncertainty of 20% in the Cs cloud size.

recombinational heating in our model.

The densities $n_{\mathrm{Li,Cs}}$ are not directly accessible in our experiment, but we can only record the total number of atoms $N_{\mathrm{Li,Cs}}$ as a function of the interaction time. We spatially integrate Eq. (2.45) and (2.46) over the density distributions and arrive at the equivalent system of differential equations [Ulmanis, 2015]

$$\dot{N}_{\mathrm{Li}} = -L_1^{\mathrm{Li}} N_{\mathrm{Li}} - K_3 N_{\mathrm{Li}} N_{\mathrm{Cs}}^2, \qquad (2.47)$$

$$\dot{N}_{\mathrm{Cs}} = -L_1^{\mathrm{Cs}} N_{\mathrm{Cs}} - 2K_3 N_{\mathrm{Li}} N_{\mathrm{Cs}}^2 - K_3^{\mathrm{Cs}} N_{\mathrm{Cs}}^3, \qquad (2.48)$$

where the loss rates K_3 and K_3^{Cs} are related to the three-body rates coefficients defined in Eq. (2.45) and (2.46) by constants of unit volume squared. For the specific measurement presented in Fig. 2.16[11], we assume gaussian density distributions for both species of the

---

[11] For the specific measurement presented here, we estimated a $T/T_F \approx 0.6$. The density distribution of a Fermi gas starts to change from a thermal distribution to a Thomas-Fermi profile at the fraction of $T/T_F = 0.6$ [Ketterle and Zwierlein, 2008] and therefore, we model the Li cloud with a thermal atomic density distribution.

atomic clouds and arrive at the following relations [Ulmanis, 2015]

$$L_3 = 8\pi^3 \exp\left(\frac{\Delta z^2}{2\sigma_{z,\mathrm{Li}}^2 + \sigma_{z,\mathrm{Cs}}^2}\right) K_3 \prod_{i=x,y,z} \sigma_{i,\mathrm{Cs}} \sqrt{2\sigma_{i,\mathrm{Li}}^2 + \sigma_{i,\mathrm{Cs}}^2}\,, \tag{2.49}$$

$$L_3^{\mathrm{Cs}} = 24\sqrt{3}\pi^3 K_3^{\mathrm{Cs}} \prod_{i=x,y,z} \sigma_{i,\mathrm{Cs}}^2\,, \tag{2.50}$$

where $\sigma_i = \sqrt{k_B T/(m\omega_i^2)}$ are the widths of the atomic clouds. The difference $\Delta z = z_0^{\mathrm{Li}} - z_0^{\mathrm{Cs}}$ between the centers of the Li and Cs distributions reduces the experimentally observable loss rate K_3 and provides the differential gravitational sag of the two species. The differential gravitational sag z_0 is zero, because before the measurement we center the focus of the microtrap on the center of the Cs cloud, which corresponds to the position where Cs losses in absence of Li are maximized (see Sec. 2.2.3). For the geometric correction factor given by Eq. (2.49) we consider the sizes determined as described at the beginning of this Sec. 2.3.2.

A typical evolution of the remaining number of Li and Cs atoms at the Li-Cs Feshbach resonance is shown in Fig. 2.16. For interpreting these measurements we neglect $K_3^{\mathrm{Cs}} N_{\mathrm{Cs}}^3$, $L_1^{Li} N_{\mathrm{Li}}$ and fix the value of L_1^{Cs}. These assumptions lead to the model described by

$$\dot{N}_{\mathrm{Li}} = -K_3 N_{\mathrm{Li}} N_{\mathrm{Cs}}^2, \tag{2.51}$$

$$\dot{N}_{\mathrm{Cs}} = -L_1^{\mathrm{Cs}} N_{\mathrm{Cs}} - 2K_3 N_{\mathrm{Li}} N_{\mathrm{Cs}}^2, \tag{2.52}$$

which is based on the following considerations. The one-body loss rates of Li and Cs are determined from independent measurements of each species in the absence of the other. For these measurements, the evolution of the atom number was reproduced by a pure exponential decay. The one-body loss rates for Cs, as explained in Sec. 2.3.1, result from two contributions: (i) the collisions with the background gas and the absorption of photons from the dimple trap; (ii) the spontaneous Raman scattering due to the MT light, which depends on the MT power (intensity). For the measurement shown here, the power of the MT was set to $P = 147$ mW and we measure a total loss rate $L_1^{\mathrm{Cs}} = (5.21 \pm 0.03)\ \mathrm{s}^{-1}$, corresponding to timescales of (190 ± 10) ms. In Fig. 2.16 (a) we can observe that the function calculated with the values extracted from the exponential fit without Li is well above the data measured in presence of Li[12]. For Li, we measure a one-body loss rate of $L_1^{\mathrm{Li}} = (0.0925 \pm 0.0008)\ \mathrm{s}^{-1}$, corresponding to timescales of (10.8 ± 0.1) s. The curve calculated with the values extracted from the exponential fit without Cs is shown in Fig. 2.16 (b)[13]. Considering a peak atomic density of $n_{\mathrm{Cs}} = 1 \times 10^{11}\ \mathrm{cm}^{-3}$ and the estimate for the three-body loss rate at unitarity at $T = 1\ \mu$K as in Eq. (2.53), we calculate $\dot{n}_{\mathrm{Li}}/n_{\mathrm{Li}} = L_3 n_{\mathrm{Cs}}^2 = 0.76\,\mathrm{s}^{-1}$, which is much larger compared to the one-body

---

[12] The data recorded without Li are omitted for the sake of clarity.

[13] The data recorded without Cs are omitted for the sake of clarity.

loss rate L_1^{Li}. Therefore, in Eq. (2.47), we neglect the term multiplied by L_1^{Li}. The three-body loss rate coefficient for Cs-Cs-Cs collisions at 888.6 G ($a_{\mathrm{CsCs}} = 180\,a_0$) is expected to be $L_3^{Cs} \approx 1 \times 10^{-28}$ cm^{6}s^{-1}, that is quite close to the three-body loss minimum at 893 G (a_{CsCs} =270 a$_0$)[14]. Considering a peak atomic density of $n_{\mathrm{Cs}} = 1 \times 10^{11}\,\mathrm{cm}^{-3}$, we obtain $\dot{n}_{\mathrm{Cs}}/n_{\mathrm{Cs}} = L_3^{\mathrm{Cs}} n_{\mathrm{Cs}}^2 \approx 1 \times 10^{-6}\,\mathrm{s}^{-1}$, which is negligible compared to the one-body loss rate L_1^{Cs} dominated by the photon scattering. Therefore, in Eq. (2.48) we neglect the term multiplied by K_3^{Cs}. The order of magnitude estimate at the unitarity limit for the three-body loss rate is given by [Ulmanis, 2015; Petrov and Werner, 2015]

$$L_3^{un} = \frac{4\pi^2\hbar^5}{\mu_3^3 (k_B T)^2} \tag{2.53}$$

where $\mu_3 = \sqrt{m_{\mathrm{Cs}}^2 m_{\mathrm{Li}}/(2m_{\mathrm{Cs}} + m_{\mathrm{Li}})} \simeq 0.15$ m$_{\mathrm{Cs}}$ is the three-body reduced mass. For a temperature of $T = 1\ \mu$K this gives $L_3^{un} = 7.6 \times 10^{-23}$ cm^{6}s^{-1}. It should be noted that Eq. (2.53) holds in thermal equilibrium, thus it is only used as an order of magnitude estimate for our situation, since Li and Cs clouds have different temperatures.

Figure 2.16 shows that the model described by Eq. (2.51) and Eq. (2.52) is on the right order of magnitude with respect to the data. The error in the determination of the number of Li atoms is dominated by shot-to-shot fluctuations[15] and therefore a good comparison between the data and the model is provided only for Cs. We have estimated a systematic error in the determination of K_3 related to the uncertainty in the determination of geometric conversion factor to the loss rate coefficient L_3 as in Eq. (2.49). The uncertainty comes from the determination of the Cs cloud sizes and carries a relative error of 20%, which has been estimated as the discrepancy in the Cs cloud size determined using different methods. We qualitatively understand the relevant contributions to the loss processes and the mixture is stable enough to unambiguously observe Li-Cs interactions. It is questionable whether the three-body loss would limit the observation of polarons. To evaluate this, it would be necessary to systematically extract the three-body loss coefficient from a thermalized sample for the desired temperatures and densities for the study of polaron many-body physics.

---

[14] Theoretically, $L_3 = 3\,C(a)\frac{\hbar}{m}a^4$ [Esry *et al.*, 1999; Bedaque *et al.*, 2000; Braaten and Hammer, 2001, 2006], where $C(a)$ is a log-period function which leads to loss minima (maxima) for a>0 (a<0) caused by phenomena related to Efimov physics. For Cs gases, these parameters are determined experimentally [Kraemer *et al.*, 2006; Berninger *et al.*, 2011] by fits to the experimental data.

[15] The measurement is randomized and takes about thirty minutes in total. We measured a periodic variation in the number of Li atoms up to 35% and in the vertical position of the center of mass of the Li cloud trapped in the MT of 2 μm over a period of about fifteen minutes. We found that these regular oscillations were related to a periodic increase in the temperature of the water that cools the coils and the DT laser of 2° C in the same period, associated with a problem with the water chiller.

2.4 Summary and outlook

We have successfully achieved a mixture of Li and Cs atoms $T/T_F \approx 0.3$, with a peak density ratio of Cs to Li of $n_{Cs}/n_{Li} \approx 0.01$. This is the first time our group has realized a mixture where one of the two species is in the degenerate regime. The use of a mobile, tightly focused dipole trap for Li at the tune-out wavelength of Cs enabled us to reach high degeneracy in a short amount of time. By adiabatically switching on the MT, the temperature remains nearly unchanged compared to the temperature in the initial DT volume, but the Fermi energy increases proportionally to the depth of the optical trap. This results to a decrease of the degeneracy parameter by a factor of 4. We load the MT with a $T/T_F = 0.4$ for an atom number of 2×10^5 atoms. The evolution of temperature and atom number during forced evaporation at 320 G aligns well with evaporation characterized by a truncation parameter of $\eta = 10$. This process allows us to achieve a $T/T_F < 0.1$ in less than 2 s.

The Cs gravitational sag in our final settings was measured to be (15.0±1.8) μm, which is larger than the radial size for Li atoms measured in this situation. The newly implemented bichromatic trapping scheme allowed us to maintain independent control over the two species and to fully compensate for the differential gravitational sag between Li and Cs. We perform loss spectroscopy on Li and Cs atoms and simultaneous imaging of the two species in the same experimental cycle, obtaining a loss signal with a Li-Cs ratio of 1:2, as expected for Li-Cs-Cs losses. The mixture is stable enough to observe the Li-Cs interactions close to the 888.6 G.

However, large losses of Cs atoms have been observed when the MT overlaps the Cs cloud. These losses are explained by spontaneous two-photon Raman scattering and are related to the proximity of the trap light to the Cs transitions. In the current setting, the lifetime of Cs atoms in the presence of the MT, considering an averaged scattering rate over the region of overlap between the beam and the cloud, is limited to between a few hundred milliseconds and a few seconds. This timescale is on the same order of magnitude as the estimated thermalization timescale at $a_{Li,Cs} = -175\ a_0$, but much larger than the timescales at unitarity, which are on the order of a few hundred microseconds. However, the local scattering rate relevant for polaron experiments is in the order of tens to hundreds of milliseconds. Even if this still guarantees thermalization at unitarity, these timescales are too short compared to the technical times we need for them to overlap. In addition, it remains to be verified whether three-body losses would limit the observation of the polaron, since in general they can severely limit the stability of Bose-Fermi mixtures, especially as the boson density increases. Unfortunately, due to the depletion of the Cs source and the consequent low reliability and stability of the Cs cloud state, which makes the Cs conditions difficult to manage and reproduce, we did not have the opportunity to perform systematic measurements to extract the three-body loss in the final cloud configuration.

Following the essential replacement of the Cs atom source, it is crucial to gain a comprehensive understanding of three-body losses as well as of the temperature evolution of the mixture. To increase the time that Li and Cs atoms can be trapped together and to allow thermalization between the two species, we plan to shift the wavelength of the movable Li trap away from the Cs tune-out wavelength at about 880 nm. Some possible alternative trapping schemes are outlined in Sec. 3.4.1. Once the mixture will be not limited by trap effects, sympathetic cooling can be used to create a well thermalized sample at moderate interspecies interactions. Afterwards, three-body inelastic collisions between Cs atoms in presence of a Li Fermi Sea can be reliably studied. Recent experiments on Bose-Fermi mixtures have observed a strong suppression of the losses [Patel *et al.*, 2023; Chen *et al.*, 2022; Yan *et al.*, 2020]. This observation may be related to a study made in our group [Enss *et al.*, 2020] (see also section 3.1.3 and Appendix B), where we discuss how a finite density of fermions provides a repulsive barrier between bosons that can prevent them from coming too close to each other. This repulsive interaction suggests a large suppression of losses and an enhanced stability near resonance, which may explain the recent observations mentioned above. The experimental investigation of the atomic losses that occur in our specific mixture setting would be relevant to understand if three-body loss times are longer than the timescales that are relevant for the observation of the Fermi polaron. Moreover, a quantitative evaluation of the three-body losses would allow extracting the spatial overlap, which can be used as an observable to reveal the phase separation between the two clouds in a deeply degenerate regime, as a function of the interspecies repulsive scattering length [Lous *et al.*, 2018]. These measurements would be relevant to map the collisional properties of the mixture for higher Cs densities.

Improvements on how we perform thermometry of the Fermi gas is also necessary. On the one hand, we need to understand the source of discrepancy that occurs for the determination of the degeneracy parameter either via fitting Fermi distributions or through indirect calculations from independent determinations of atom number, temperature, and trapping frequencies. While measurements taken with the Ximea camera show a very good agreement between these two methods, as demonstrated by Fig. 2.7, a significant discrepancy has been revealed in many cases when using the Andor camera. Many parameters can enter into the game such as, for example, atom number fluctuations, signal to noise ratio for very low Ti:Sa power and imaging processing. A preliminary study of comparison about imaging processing in Ximea and Andor camera for Li thermometry is carried out in Borchers [2023]. A general requirement that we would like to fulfill is to improve and implement the monitoring of different experimental parameters that can influence thermometry, as trap powers, atom number in MOTs over time and beam pointing. Also high field imaging for both Li and Cs needs to be reconsidered, and will be done starting from the work of Schürg [2024]. On the other hand, more advanced methods of thermometry could be implemented. For example, thermal expansion of the non-condensed Cs cloud could be used as a thermometer for the Li Fermi Sea. Alternatively, one can deduce the temperature of the mixture from either the condensed fraction of a Cs BEC [Lous *et al.*, 2017] or even the Fermi polaron peak shift, as recently demonstrated [Yan *et al.*, 2024b].

Chapter 3

Heavy Fermi polarons

What happens when a single impurity, infinitely heavy, is immersed into a Fermi Sea? This question was the starting point for Anderson's work on studying perturbations of many-body phenomena [Anderson, 1967]. The answer is that, in the thermodynamic limit, even a single potential, regardless of the nature of the impurity (i.e. boson, fermion or deep potential), significantly perturbs the Fermi Sea, resulting in a state that is completely orthogonal to the initial one.

However, if the boundary of an infinitely heavy impurity is released and a finite mass imbalance between the impurity and the fermionic medium is restored, we encounter the problem of a single mobile particle interacting with many. While there is no general solution for the problem of many particles interacting among each other, known as many-body-problem, a special exception regards the problem of many interacting fermions, known as Landau's Fermi liquid theory [Mahan, 2000]. This theory introduces the paradigmatic case of a single impurity dressed by interactions with the surrounding medium, which is described as a quasi-particle. As the bath under consideration consists of fermions, the dressed quasi-particle is named Fermi polaron. This is one of the simplest examples of the many-body problem and it shows strong similarities with famous condensed matter problems, such as the Kondo effect [Mahan, 2000], the X-rays singularities in metals [Nozières and De Dominicis, 1969], the mobility of ions [Prokof'ev, 1995] and ^{4}He [Arias de Saavedra *et al.*, 1994] in ^{3}He. Additionally, the Fermi polaron plays a significant role in the physics of semiconductors [Sidler *et al.*, 2017; Muir *et al.*, 2022] and in the study of neutron matter [Nakano *et al.*, 2020; Vidaña, 2021; Forbes *et al.*, 2014].

Ultracold atoms are an appealing platform for the investigation of Fermi polaron physics, as low densities and high degree of degeneracy ensure that all the interesting many-body processes occur on the experimentally accessible microsecond timescale, in contrast to the attosecond timescales typical of condensed matter systems. The preparation of both impurity and bath particles in a well-defined quantum states is enabled by the combination of the control over interatomic interactions, exploiting Feshbach resonances, with advanced spectroscopic techniques. In the last decade, several experiments based on ultracold atom platforms have allowed deeper understanding in fundamental many-body phenomena related to Fermi polarons [Massignan *et al.*, 2014; Schmidt *et al.*, 2018; Scazza *et al.*, 2022]. The possibility to control the relevant experimental parameters, such as interaction, temperature and impurity concentration, has allowed for the characterization of the Fermi-polaron properties in strongly interacting regimes in three- [Schirotzek *et al.*, 2009; Kohstall *et al.*, 2012] and two-dimensional environment [Koschorreck *et al.*, 2012; Zhang *et al.*, 2012]. Moreover, not only attractive polaron ground-state but also the repulsive first excited-state was prepared and investigated [Scazza *et al.*, 2017; Darkwah Oppong *et al.*, 2019]. Later on, different configurations have allowed for studios of the temperature dependence [Yan *et al.*, 2019], polaron formation dynamics [Cetina *et al.*, 2015, 2016], polaron-to-molecule transition [Ness *et al.*, 2020] and mediated interactions [Baroni *et al.*, 2024a]. With the introduction of an asymmetry in the mass between the atomic impurity and the quantum medium, the impurity problem changes qualitatively and new phenomena that do not occur in single species experiments, as most of the experiments listed above, appear [Baroni *et al.*, 2024b].

This chapter focuses on the study of a low-density Cs gas interacting with a fermionic spin-polarized Li degenerate gas. The large mass imbalance between Li and Cs allows for the study of the behavior of very heavy impurities coupled to a Fermi Sea. The Fermi polaron is theoretically introduced in the context of ultracold atoms in Sec. 3.1 with a focus on the infinitely heavy impurity limit. Then, the main ingredients required for probing the Fermi polarons in Li-Cs mixtures are discussed in Sec. 3.2. The properties of the scattering channels involved are discussed in Sec. 3.2.1, while the spectroscopic scheme for Cs impurities is outlined in Sec. 3.2.2. The first attempt to observe the attractive Fermi polaron is shown in Sec. 3.3. Necessary changes to the experimental apparatus are proposed in order to realize the Fermi polaron and prospects for future experiments are discussed in Sec. 3.4.

Collaborations with external groups from different fields of expertise have been established to identify a suitable protocol for realizing the Fermi polaron in a Li-Cs mixture. To this end, we have collaborated with Moritz Drescher and Tilman Enss from the University of Heidelberg on the topic of Fermi polarons at finite temperature for the case of an infinitely heavy impurity. Drescher has performed the calculation of the polaron spectra via Functional Determinant Approach (FDA) shown in Sec. 3.1.2. We have gained knowledge regarding Cs intraspecies scattering properties which are presented in Sec. 3.2.1 thanks to Matthew Frye and Jeremy Hutson from the University of Durham. Additionally, for the same Sec. 3.2.1, we have consulted with Chris Greene from Purdue University (US) as well as Arthur Christianen and Richard Schmidt from the University of Heidelberg to extract properties of Li-Cs interactions with the first excited state of Cs, from Multichannel Quantum Defect Theory (frame transformation) (MQDT-FT) and coupled channel (cc) calculations, respectively. Moreover, we have taken inspiration for our Raman spectroscopy setup from the scheme developed in the Li-K experiment of Rudi Grimm's group at the University of Innsbruck.

3.1 Fermi polaron in the heavy-mass impurity limit

The mass of the impurity in the Fermi polaron picture plays an important role, and in the case of heavy impurities a few peculiarities have to be taken into account. On the one hand, in the single polaron picture, this scenario is close to the fully solvable problem of an infinitely heavy fixed impurity in a Fermi sea. This problem has an analytical solution at $T = 0$ [Fumi, 1955; Combescot *et al.*, 2007] and a numerical but exact solution at finite temperature [Liu *et al.*, 2020]. Furthermore, the system exhibits the so-called orthogonality catastrophe, where the real time overlap between the interacting and non-interacting state approaches zero and shows universal power law singularities [Schmidt *et al.*, 2018]. On the other hand, in the context of interacting impurities, the scattering phase shift and the induced scattering length between two infinitely heavy impurities in a Fermi sea can be calculated exactly. These results show that in the strong coupling regime close to the resonant Bose-Fermi interaction the fermionic medium mitigates the collapse between interacting bosons [Enss *et al.*, 2020] in comparison with the case of a pure bosonic medium.

In this section I will provide a theoretical overview to heavy Fermi polarons, focusing on three aspects: (i) calculation of the polaron energy (attractive ground state) for a Li-Cs mixture compared to the case of an infinitely heavy impurity, at $T = 0$, see Sec. 3.1.1; (ii) discussion of the properties of the energy spectra obtained at finite temperature by FDA in the limit of an infinitely heavy impurity, for the relevant experimental *ejection* and *injection* protocols, see Sec. 3.1.2; (iii) discussion of the scattering properties of two heavy Fermi polarons, see Sec. 3.1.3.

3.1.1 One single heavy impurity in a Fermi Sea

We consider the general problem of a single atom with mass m_I in a bath consisting of a fully polarized Fermi sea of N_b atoms with mass m_b and atomic density $n_b = k_F^3/(6\pi^2)$, where k_F is the Fermi wave vector defining the Fermi energy $E_F = \hbar^2 k_F^2/2m_b$. The interaction between the two atomic species is characterized by an s-wave scattering length a_{Ib}, the value of which can be detuned via a broad Feshbach resonance from positive to negative values of the interaction parameter $1/(k_F a_{Ib})$. We also assume that the interatomic distance between the particles of the bath is much larger than the effective range of the interspecies interaction. The total Hamiltonian is given by [Scazza *et al.*, 2022]

$$\hat{H} = \underbrace{\sum_{\mathbf{k}} (\epsilon_{\mathbf{k}}^{bath} - \mu_b) \hat{f}_{\mathbf{k}}^\dagger \hat{f}_{\mathbf{k}}}_{\hat{H}_{\text{bath}}} + \underbrace{\sum_{\mathbf{k}} \epsilon_{\mathbf{k}} \hat{c}_{\mathbf{k}}^\dagger \hat{c}_{\mathbf{k}}}_{\hat{H}_{\text{imp}}} + \underbrace{\sum_{\mathbf{k},\mathbf{q}} V(\mathbf{q}) \hat{\rho}_{\mathbf{q}} \hat{c}_{\mathbf{k}+\mathbf{q}}^\dagger \hat{c}_{\mathbf{k}}}_{\hat{H}_{\text{int}}} \tag{3.1}$$

where the Hamiltonian $\hat{H}_{\text{bath}}$ governs the bath, $\hat{H}_{\text{imp}}$ is the non-interacting impurity, μ_b is the chemical potential and $\hat{H}_{\text{int}}$ the impurity-bath interactions. The single particle dispersion relation in the bath is given by $\epsilon_{\mathbf{k}}^{bath} = \hbar^2 k^2/2m_b$ with wave vector $\mathbf{k}$, and the creation operator $\hat{f}_{\mathbf{k}}^\dagger$ obeys the usual fermionic commutation rules. The impurity energy is given by $\epsilon_{\mathbf{k}} = \hbar^2 k^2/2m_I$ and $\hat{c}_{\mathbf{k}}^\dagger$ is the impurity creation operator. The potential $V(\mathbf{q})$

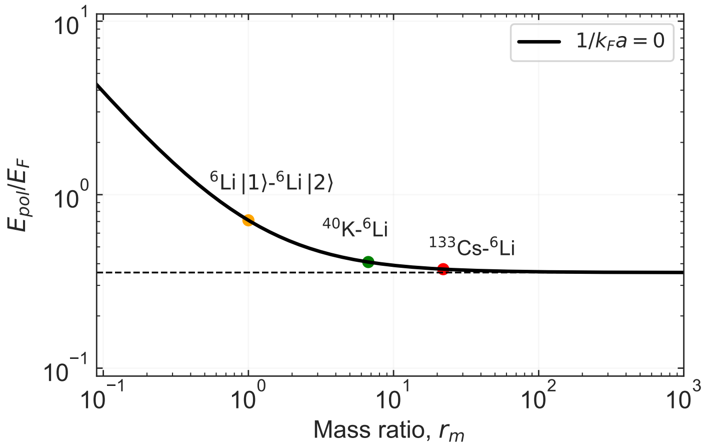

FIGURE 3.1: Polaron energy E_{pol} as a function of the mass ratio $r_m = m_I/m_b$ at unitarity $1/(k_F a) = 0$ and $T = 0$. The scattered points mark the energy for mass ratios corresponding to specific atomic mixture: in red ^{133}Cs-^{6}Li with $r_m = 22$, in green ^{40}K-^{6}Li with $r_m = 6.7$ and in orange ^{6}Li prepared in different hyperfine states with $r_m = 1$. The horizontal dashed line is the result for $r_m = \infty$. The polaron energy is expressed in unit of Fermi energy E_F.

can be a generic finite-range potential and $\hat{\rho}_{\mathbf{q}} = \sum_{\mathbf{k}} \hat{f}^{\dagger}_{\mathbf{k}-\mathbf{q}} \hat{f}_{\mathbf{k}}$ is the bath density operator. We consider here short-range contact-interactions, and whether it is attractive or repulsive, the low energy s-wave scattering amplitude between the impurity and the bath has the universal form $f(\mathbf{k}) = -1/(a_{Ib}^{-1} + ik)$. This allows us to use pseudo-potentials for the impurity-bath interactions.

The most comprehensive theoretical treatment of the impurity-bath system at strong interactions is provided by the T-matrix approach [Combescot *et al.*, 2007]. All the quasi-particle properties are encoded in the retarded impurity Green's function that can be expressed in terms of the "self-energy" $\Sigma(\mathbf{p}, \omega)$, where the dispersion relation for the impurity is given by $\omega - \epsilon_{\mathbf{k}} + \mu_I - \Sigma(\mathbf{p}, \omega) = 0$ and $\mu_I = \Sigma(0, 0)$. Since in our situation the single impurity does not perturb the Fermi sea in the thermodynamic limit, the so-called "ladder-approximation" can be applied and the obtained polaron energy shift is in good agreement with the ground state that is found via the variational wave function approach based on the Chevy ansatz [Chevy, 2006], shown in the next paragraph. Both methods are also in good agreement with quantum Monte Carlo simulations [Lobo *et al.*, 2006] and with the results found in several experiments [Schirotzek *et al.*, 2009; Scazza *et al.*, 2017; Yan *et al.*, 2019]. All these methods agree that even at unitarity the effect of interactions is fairly weak and can be well described by using single particle-hole excitations.

In the following paragraphs I compare the energy shift as calculated from the variational approach [Chevy, 2006], for the finite mass ratio of the Li-Cs mixture, with the energy calculated analytically for an infinitely heavy impurity [Fumi, 1955], at $T = 0$.

Then, I will explain peculiar properties of heavy impurities, such as the polaron-to-molecule transition and the fate of the quasi-particle weight, following the description in [Combescot *et al.*, 2007]. But first, to introduce why Li-Cs is a special case compared to other mixtures already used to study polarons, and why it can serve as a test-bed for systems with infinitely heavy impurities, I will make use of Fig. 3.1. This shows the polaron energy E_{pol} as a function of the mass ratio at unitarity, $1/(k_F a_{Ib}) = 0$. The energy is calculated by the T-matrix approximation [Combescot *et al.*, 2007] in the limit of a large chemical potential ratio between impurity and bath $\rho = \mu_I/\mu_b$. In such a case the expression for the self-energy is simplified, the chemical potential for the impurity is equal to the polaron energy E_{pol}. This results in an analytical formula that links $\rho = |E_{pol}|/E_F$ to $1/(k_F a_{Ib})$ as [Combescot *et al.*, 2007]

$$\frac{1}{k_F a_{Ib}} = \sqrt{\frac{\rho r_m}{1+r_m}} - \frac{2}{3\pi}\frac{1+r_m}{\rho r_m}, \tag{3.2}$$

where $r_m = m_I/m_b$ is the mass ratio. At unitarity, i.e. $1/(k_F a_{Ib}) = 0$, it reduces to

$$\frac{|E_{pol}|}{E_F} = \left(\frac{2}{3\pi}\right)^{2/3}\left(\frac{1+r_m}{r_m}\right). \tag{3.3}$$

For large $r_m \to \infty$, this energy ratio saturates to $(2/(3\pi))^{2/3}$. The relative difference between the $^{133}Cs{-}^{6}\mathrm{Li}$, with $r_m = 22$, and the infinite heavy impurity is less than 5%, while for example, already for $^{40}K{-}^{6}\mathrm{Li}$ [Kohstall *et al.*, 2012], with $r_m = 6.7$, is about 15%. It is an indication that the Li-Cs does not differ much from the case of an infinite heavy impurity. However, this is an approximation of the T-matrix approach, and the analytical formula is valid only for unitarity. In the next section, I will calculate the energy as a function of the interaction parameter, using the variational approach without further approximations.

Energy ground state for a Cs impurity in a Li Fermi Sea with the variational approach. In order to calculate the polaron energy for the Li-Cs mass ratio as a function of the interaction parameter $1/(k_F a)$ without constraints on the ratio of the chemical potentials, I have followed the variational approach proposed by Chevy [2006]. This assumes that the ground state of the system is described by

$$|\psi\rangle = \Phi_0 \hat{c}^\dagger_{\mathbf{p}} |\mathrm{FS}\rangle + \sum_{\mathbf{q}<k_F}^{\mathbf{k}>k_F} \Phi_{\mathbf{q},\mathbf{k}} \hat{c}^\dagger_{\mathbf{p}+\mathbf{q}-\mathbf{k}} \hat{f}^\dagger_{\mathbf{k}} \hat{f}_{\mathbf{q}} |\mathrm{FS}\rangle, \tag{3.4}$$

where $|\psi\rangle$ is given by the sum of two terms: (i) non-interacting Fermi sea $|\mathrm{FS}\rangle$ plus a free impurity with momentum $\mathbf{p}$, (ii) Fermi Sea dressed by single-particle excitations and composed by particle-hole pairs with momentum $\mathbf{k}$ and $\mathbf{q}$, respectively, plus an impurity with momentum recoil $\mathbf{p}+\mathbf{q}-\mathbf{k}$. This assumption is known as *Chevy ansatz*. The quasi-particle weight, which describes the overlap between the interacting and the non-interacting state is here defined as

$$Z := \Phi_0^2 = |\langle \mathrm{FS}|\psi\rangle|^2, \tag{3.5}$$

and therefore, $\Phi_0 = \sqrt{Z}$. For $\mathbf{p} = \mathbf{0}$, the change of energy E corresponds to the polaron energy E_{pol}. In order to find the ground state one can minimize the expectation value of the total energy with respect to the coefficients Φ_0 and $\Phi_{\mathbf{q},\mathbf{k}}$ and obtain the implicit equation

$$E_{pol} = \sum_{q<k_F} \frac{1}{\sum_{k>k_F}\left(\frac{1}{\epsilon_{\mathbf{k}}+\epsilon_{\mathbf{q}-\mathbf{k}}-\epsilon_{\mathbf{q}}-E_{pol}} - \frac{1}{2\epsilon_{\mathbf{k}}}\right) - \sum_{k<k_F}\frac{1}{2\epsilon_{\mathbf{k}}}} \tag{3.6}$$

where $\epsilon_{\mathbf{q}}$ is the energy of the hole with mass m_b, $\epsilon_{\mathbf{k}}$ is the energy of the impurity with mass m_I, $\epsilon_{\mathbf{q}-\mathbf{k}}$ is the energy acquired by the impurity to satisfy momentum conservation. The term $\sum_k \frac{1}{2\epsilon_{\mathbf{k}}}$ is given by the Lippman-Schwinger equation [Chevy, 2006]

$$\frac{1}{g_b} = \frac{m_{red}}{4\pi\hbar^2 a_{Ib}} - \frac{1}{V}\sum_k \frac{1}{2\epsilon_{\mathbf{k}}}, \tag{3.7}$$

which relates the s-wave scattering length a_{Ib} between the impurity and the bath to g_b, which is the bare coupling constant characterizing interparticle interactions, where $m_{red} = m_I m_b/(m_I + m_b)$ is the reduced mass of the system. This equation represents a normalization that serves to regularize the singular behaviour for which the terms with $\phi_{\mathbf{k},q} \sim 1/k^2$ would diverge for $k \to \infty$ [Chevy, 2006]. Eq. 3.6 can be re-written by replacing $\sum_{\mathbf{k}} \to \int d\mathbf{k}/(2\pi)^3$ and with the adimensional parameters $\epsilon' = 2m_{red}E_{pol}/k_F^2$ and $\rho = (m_I - m_b)/(m_I + m_B)$, where the latter is related to the impurity to bath ratio by $r_m = (1+\rho)/(1-\rho)$. I computed and solved numerically this equation for different values of the scattering parameter $1/(k_F a_{Ib})$ in the range $-3 < 1/(k_F a_{Ib}) < 2$, fixing the mass ratio r_m to 22, 1 and ∞. The results are plotted in Fig. 3.2. It is evident that the result for the Li-Cs case corresponding to $r_m = 22$ shows a very good agreement with the result obtained for $r_m = \infty$[1]. The absolute energy difference between the Li-Cs case with respect to the system with equal mass is $\sim 0.1 \times E_F$ for $1/(k_F a_{Ib}) \ll 1$, while it is much larger than $1 \times E_F$ for $1/(k_F a_{Ib}) \gg 1$. It should be noted that for $1/(k_F a) = 0$, E_{pol}/E_F is -0.607 for equal mass systems ($r_m = 1$), -0.448 for the Li-Cs case ($r_m = 22$) and -0.466 for the infinitely heavy impurity ($r_m \to \infty$). The results for $r_m = 1$ and $r_m = \infty$ were also used as a benchmark to validate the accuracy of my numerical methods. These specific cases were chosen also because the corresponding curves are presented in [Combescot et al., 2007], and my results are in complete agreement with those reported there.

---

[1] This result is true for both computing methods, i.e. the variational approach, as obtained here, and the exact calculation, which is detailed in the next paragraph.

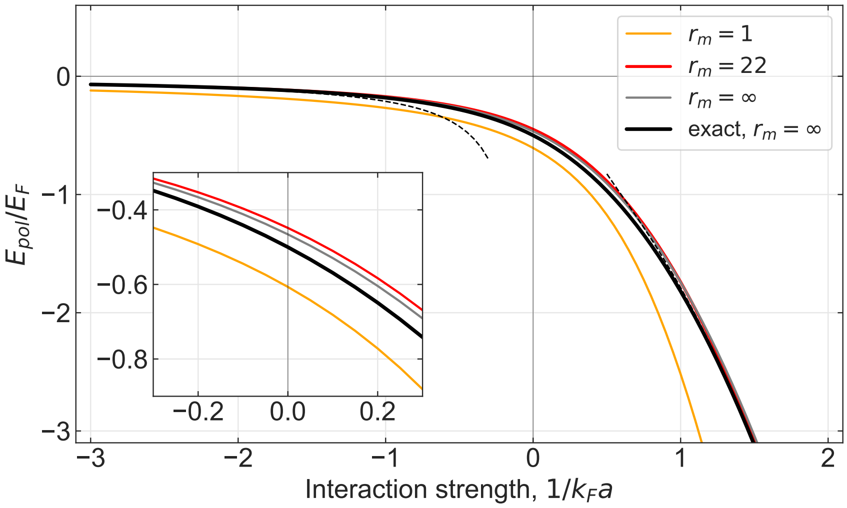

FIGURE 3.2: Polaron energy E_{pol} as a function of the interaction parameter $1/(k_Fa)$ for different mass ratios $r_m = m_I/m_b$ at $T = 0$. Numerical results for $r_m = 1$ (orange), 22 (red), ∞ (gray) obtained by the variational approach are shown. The thick black line shows the exact result obtained with Eq. 3.12 for $r_m = \infty$. The dashed black lines show the asymptotic behaviour for $a \to 0^-$ and for $a \to 0^+$. The inset contains an enlargement in the region close to unitarity: the exact result for $r_m = \infty$ is -0.5, which is quite close to the numerical result of -0.448 for the Cs-Li mass ratio obtained by the variational approach. The polaron energy is expressed in unit of Fermi energy E_F.

Energy ground state of an infinitely heavy impurity. In the case of an infinitely heavy impurity $\hat{H}_{\text{imp}} = 0$, the Hamiltonian of Eq. 3.1 reduces to

$$\hat{H} = \hat{H}_{\text{bath}} + \hat{H}_{\text{int}} \tag{3.8}$$

and leads to the problem of a fixed impurity in a Fermi sea, where we remove the degree of freedom associated with $\hat{c}^\dagger_{\mathbf{k}}$. The interaction Hamiltonian $\hat{H}_{\text{int}}$ is described by the Fano-Anderson model [Schmidt *et al.*, 2018; Liu *et al.*, 2020] and reads as

$$\hat{H}_{\text{int}} = \epsilon_d \hat{d}^\dagger \hat{d} + \frac{g}{\sqrt{V}} \sum_{\mathbf{q}} (\hat{d}^\dagger \hat{f}_{\mathbf{q}} + \hat{f}^\dagger_{\mathbf{q}} \hat{d}) \tag{3.9}$$

where $\hat{d} = \sum_{\mathbf{k}} \hat{d}_{\mathbf{k}}$ is a fermionic operator, ϵ_d is the energy detuning from the bare closed-channel which mediates the interaction between the atoms, g is the strength of the inter-channel coupling and V is the volume of quantization.

However, the $T = 0$ ground state energy is known from the Fumi's theorem [Fumi, 1955] and can be calculated analytically. Specifically, we consider here the attractive ground state of the system. One has to consider the impurity at the center of a sphere of radius R which by definition encloses the Fermi sea [Combescot *et al.*, 2007; Schmidt *et al.*, 2018]. For s-wave interactions, the general solution of the two-particle problem is proportional to $\sin(k_jr + \delta_0(k_j))$ with $k_jr + \delta_0(k_j) = j\pi$ where $j \leq n$ is an integer and

$n = k_F R/\pi$. The s-wave scattering phase shift in the presence of the impurity is given by $\tan \delta_0(k) = -k a_{Ib}$ and it vanishes in the absence of the impurity. The total energy E of the system can be written as the sum of the energy of the unperturbed system plus the energy shift E_{pol} induced by the impurity and expressed as

$$E_{pol} = \int_0^{E_F} \delta_0\Big(k(E)\Big) \frac{dE}{\pi}. \tag{3.10}$$

The calculation is done by finding the change in the energy due to a change in the scattering length, and it leads to

$$E_{pol} = -\frac{k_F^2}{2m} \cdot \frac{1}{\pi} \left(\left(1 + \frac{1}{(k_F a_{Ib})^2}\right) \arctan\left(k_F a_{Ib}\right) - \frac{1}{k_F a_{Ib}} \right) \tag{3.11}$$

where $E_F = \frac{k_F^2}{2m}$, which holds only for $a < 0$. The analytic extension is given by

$$E_{pol}/E_F = -\frac{1}{\pi}\left(\left(1 + y^2\right) \left(\frac{\pi}{2} + \arctan y\right) + y \right), \tag{3.12}$$

where $y = 1/(k_F a_{Ib})$. This result is shown in Fig. 3.2 for comparison with the results obtained by the variational approach via the Chevy ansatz. This formula interpolates between the weak attractive coupling limit $E_{pol,-}/E_F = \frac{2}{3\pi} \cdot y^{-1}$ for $a_{Ib} \to 0^-$ and weak repulsive coupling limit $E_{pol,+}/E_F = -y^2 + \frac{2}{3\pi} \cdot y^{-1} - 1$ for $a_{Ib} \to 0^+$. At unitarity it reaches the value $E_{pol}/E_F = -0.5$, which is in very good agreement with the values of -0.448 for Li-Cs and -0.466 for the infinitely heavy impurity calculated numerically from the Chevy ansatz. Furthermore, one can notice that the result obtained for $r_m = \infty$ using Chevy differs from that obtained through the exact calculation. This discrepancy highlights the limitations of this variational approximation, in the specific case of $r_m = \infty$. We can conclude, then, that the ground state energy of a Li Fermi sea coupled to a heavy Cs impurity (as obtained by the variational approach) is in very good approximation with the energy calculated for an infinitely heavy impurity immersed in a Fermi sea.

Polaron to molecule transition. While for $y \ll -1$ the physics is dominated by the mean-field interaction, which scales as $1/y$, for $y \gg 1$ a molecular state is energetically favored with respect to the many-body polaronic state. The reason is that the quasiparticle weight vanishes beyond a critical interaction parameter. The value of the interaction parameter $1/(k_F a_c)$ at the crossing between the polaron ground state and the molecule differs from one mixture to another, as it depends on the mass ratio and the resonance width [Trefzger and Castin, 2012; Massignan *et al.*, 2014]. The crossing value $1/(k_F a_c)$ increases for a given mass ratio by increasing the resonance width, while, for a given resonance, it changes from positive to negative by increasing the mass ratio. For equal masses of impurity and bath, at $T = 0$ and $k_F R^* = 0$, this has been calculated to occur at $1/(k_f a_c) = 0.9$ [Punk *et al.*, 2009; Schmidt and Enss, 2011], where a_c is the critical scattering length. However, a recent work based on ejection Raman spectroscopy on a mass-balanced system revealed that for finite temperature there is no phase transition but rather a smooth crossover [Ness *et al.*, 2020]. For an impurity of infinite mass, no crossing between the two states is expected even at zero temperature due to the vanishing quasi-particle weight. In Sec. 3.4.2 I will discuss possible spectroscopic schemes that would enable us to investigate the polaron to molecule transition in the Li-Cs system.

The fate of the quasi-particle weight. An important property that emerges in the limit of a static impurity is that the quasi-particle weight Z vanishes. The many-body wave function of the Fermi sea, when the impurity is present, is orthogonal to the wave function without the impurity. In other words, the overlap between the wave functions of the non-interacting and interacting ground state of the isolated system becomes zero. This phenomenon is known with the name of "orthogonality-catastrophe" [Anderson, 1967]. For a mobile impurity, it follows from momentum conservation that the particle can generate only particle-hole excitations with a recoil energy up to $\sim 2\hbar^2 k_F^2/2M$, where $M = m_I + m_b$, which limits the available phase-space for scattering. For the case of a static impurity, the quasi-particle picture breaks down since a static impurity can excite an infinite number of low energy particle-hole excitations causing a complete shake-up of the Fermi sea.

This phenomenon occurs at zero temperature and in the thermodynamic limit of $N_b \to \infty$. As ultracold atoms are systems constituted by a finite number of particles, the quasi-particle weight is still finite even if $\ll 1$. Indeed $Z \approx N_b^{-2\sin^2 \delta_F/\pi^2}$, with δ_F the scattering phase shift [Anderson, 1967]. At unitarity, where $\sin^2 \delta_F = 1$ and this effect is most pronounced, for a typical sample of 1×10^4 atoms, one expects $Z \approx 0.15$ still. However, after the quench of the impurity between the non-interacting and the interacting state, the system will take a finite amount of time to become orthogonal. The orthogonality catastrophe manifests itself not only in ground state properties, which might be challenging to detect, but also in non-equilibrium dynamics. The dynamical evolution of the system can be measured by interferometric Ramsey-like spectroscopic schemes. At long times compared to the Fermi timescale, the coherence of the state that describes the system, i.e. the real-time overlap of the interacting and non-interacting state, is expected to show a universal power-law decay behaviour [Knap *et al.*, 2012; Schmidt *et al.*, 2018]. In Sec. 3.4.2 I will discuss possible spectroscopic schemes to reveal signatures of this universal behaviour in the Li-Cs system.

3.1.2 Ejection and injection spectral functions at finite temperature

Up to now we just looked at the case at zero temperature. However, finite temperature effects reduce the polaron energy shift. Moreover, it was found experimentally that the polaron peak for equal mass systems survives until $T/T_F \approx 0.75$ [Yan *et al.*, 2019]. This effect is expected to be more severe for systems with heavier impurities. For a weak coupling the physics is dominated by the mean-field interaction, which scales with the inverse of the reduced mass. Similarly, the bound molecule energy also scales with the inverse of the reduced mass. Therefore, we expect that the highest temperature at which

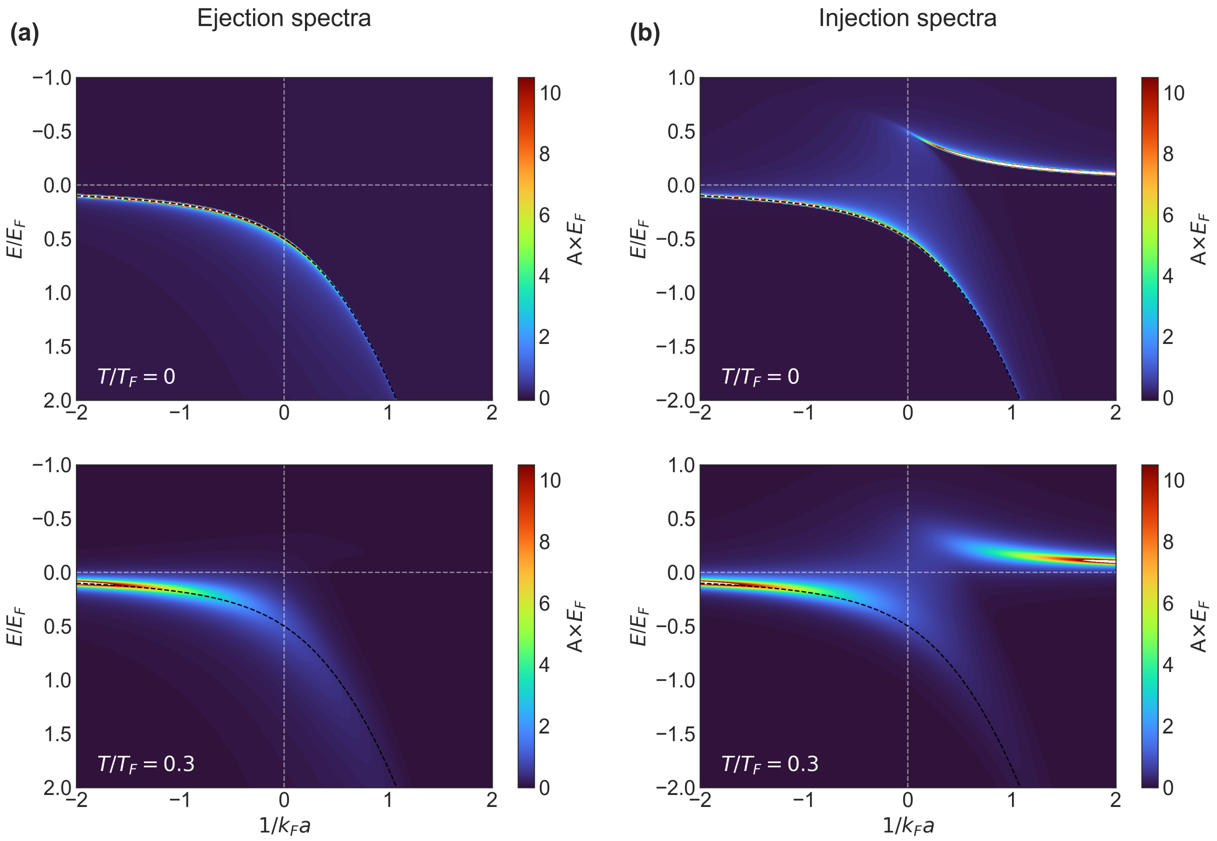

FIGURE 3.3: Energy spectra as a function of the interaction parameter $1/(k_F a)$ at finite temperature for an infinitely heavy impurity calculated by FDA. (a) Ejection and (b) injection spectra are shown. For both protocols, spectra for $T/T_F = 0$ (upper row) and for $T/T_F = 0.3$ (lower row) are shown. The black dashed line shows the energy obtained from Eq. 3.12 at $T = 0$. The color map displays the response amplitude A in unit of $1/E_F$ up to a value of $A \times E_F = 10$, with E_F the Fermi energy. These graphs are based on calculations by Moritz Drescher (permission granted) [Drescher *et al.*, 2024].

one can resolve the polaron shift is lower for higher mass-ratio [Liu *et al.*, 2020; Hu and Liu, 2022].

Due to the lack of recoil, in the case of an infinitely heavy impurity, the polaron energy can be calculated exactly even at finite temperature [Liu *et al.*, 2020]. The calculation of the energy spectral functions is performed by using a method called Functional Determinant Approach (FDA) [Levitov and Lesovik, 1993; Knap *et al.*, 2012; Schmidt *et al.*, 2018; Liu *et al.*, 2020], which explicitly incorporates the dependency on the temperature. The numerical results discussed in this section are obtained by Moritz Drescher, who collaborated with us on the polaron project for the theoretical part. The FDA method used for these calculation is explained in Drescher *et al.* [2024]. The energy spectral functions shown in the following have been obtained by considering a delta function as probe and the single channel limit, $k_F R^* = 0$, for two different relevant experimental protocols.

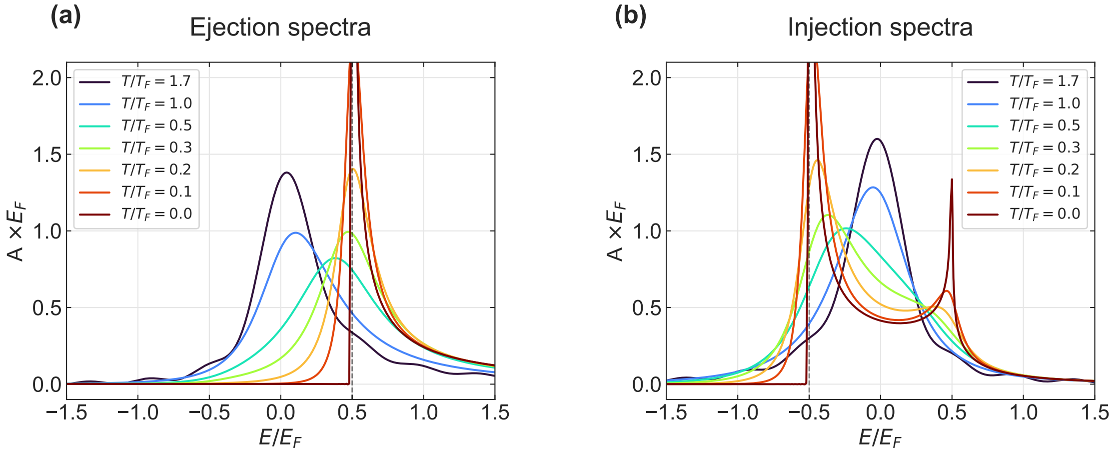

FIGURE 3.4: Ejection (a) and injection (b) energy spectral function for an infinite mass impurity at unitarity for different temperatures. On the y-axis the response amplitude A in unit of $1/E_F$ is displayed, with E_F is the Fermi energy. These graphs are based on calculations by Moritz Drescher (permission granted) [Drescher *et al.*, 2024].

There exist two different kinds of protocol that one can implement for creating a polaron: *injection*, where the impurity is merged into a bath from an initially non-interacting state, and the *ejection*, where the impurity is ejected from a state where it is initially interacting with the surrounding bath. These two methods lead to different spectral functions: the *injection* method excites the impurities into a continuum of states, whereas the *ejection* probes the ground state energy of the impurities. The two protocols are connected by a simple mapping based on a balance condition in the thermal equilibrium [Liu *et al.*, 2020].

Figure 3.3 shows the full exact ejection and injection energy spectral functions in dependence of the interaction parameter for two cases: zero temperature, $T/T_F = 0$, and finite temperature, $T/T_F = 0.3$. The response amplitude is given by A and it is expressed in unit of E_F^{-1}. The injection spectrum shows two energy branches, the attractive ground state and the metastable repulsive first-excited state. Conversely, the ejection spectrum captures the attractive ground state only. It is evident that an increase in temperature results in a broadening of the spectral response. For negative and large interaction parameter values the polaron peak is more narrow than at unitarity and shows a smaller shift from the bare transition. On the other hand, for positive and large interaction parameter values the polaron peak is more shallow than at unitarity, even if the shift would become larger. The exact solution in Eq. 3.12 is in good agreement with the FDA calculations for both zero and finite temperature.

The energy spectral functions at unitarity for different values of T/T_F, ranging from 0 to 1.7, are shown in Fig. 3.4. At low temperatures, the injection spectrum contains two peaks, associated respectively to the attractive and the repulsive polaron branch, whereas ejection exhibits only the peak relative to the attractive ground state of the system. The ejection spectrum at $T = 0$ shows the typical Fermi edge-singularity at $0.5 \times E_F$ expected for an infinite mass impurity. For $T/T_F > 0.6$ both cases display a single narrow peak

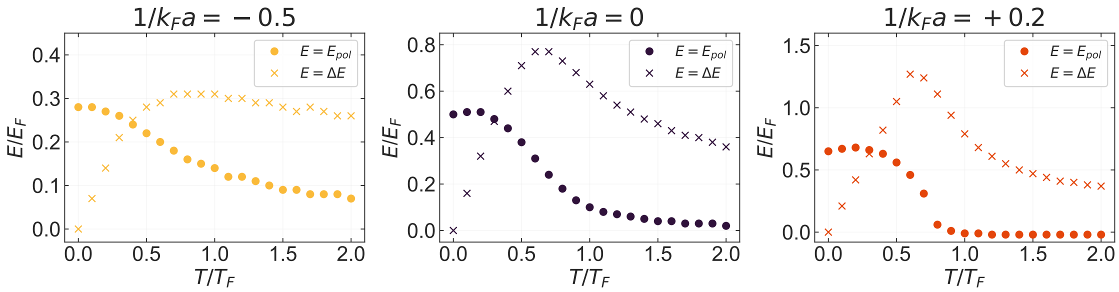

FIGURE 3.5: Temperature dependence of the ejection energy spectrum peak position E_{pol} and full width at half maximum ΔE for an infinitely heavy impurity at different interaction parameters $1/(k_F a)$ = -0.5, 0 and +0.2, respectively. These graphs are adapted from calculations by Moritz Drescher (permission granted) [Drescher *et al.*, 2024].

centered at $E = 0$, which indicates the complete disappearance of the polaron peak.

The temperature at which the polaron shift results comparable to the spectral width can be set as an upper limit for the temperature at which the polaron peak can be resolved with respect to the usual bare transition. Figure 3.5 shows the temperature dependence of the polaron peak E_{pol} and the full width at half maximum ΔE at a positive, a negative and the zero value of the interaction parameter, for the ejection energy spectrum. For the three different scenarios, the two quantities cross at a temperature ratio of $T/T_F \approx 0.3$. We can also extract further information. First, for $T/T_F \ll 1$, the polaron peak as a function of the temperature moves to slightly higher energies due to the strong asymmetry of the spectrum caused by the presence of the characteristic power-law singularity for a static impurity. This results in an initial upward shift of the peak. For $T/T_F > 1$ the peak approaches zero. Second, the broadening ΔE for $T/T_F \ll 1$ shows a characteristic linear dependence $\Delta E \sim T$, whereas at high temperature it recalls the behaviour of $\Delta E \sim T^{-1/2}$ of equal mass systems [Liu *et al.*, 2020].

It is to notice that the results presented in this section show a good agreement with analogous calculations in Liu *et al.* [2020]. I will use the ejection spectra described here to interpret the experimental results shown in Sec. 3.3 and discussed in Sec 3.3.2.

3.1.3 Two heavy bosons in a Fermi Sea

As mentioned in Sec. 2.4, three-body recombination at the strongly interacting regime could prevent the observation of the polaron. However, in a recent work carried out in our group [Enss *et al.*, 2020], which dealt with the study of scattering properties of two heavy bosons in a Fermi Sea, it emerged the capability of dilute Bose gas of stabilizing Bose-Fermi mixtures, close to strongly interacting regime, against three-body losses. Being this topic of critical importance in the context of this thesis work, I will qualitatively discuss such an interesting result in this paragraph. The complete article can be found in Appendix B, and is also discussed in Tran [2022].

A fermionic medium, composed by a non-interacting Fermi sea plus two heavy impurities, obeys to the Pauli blocking principle. The induced interaction between the bosons

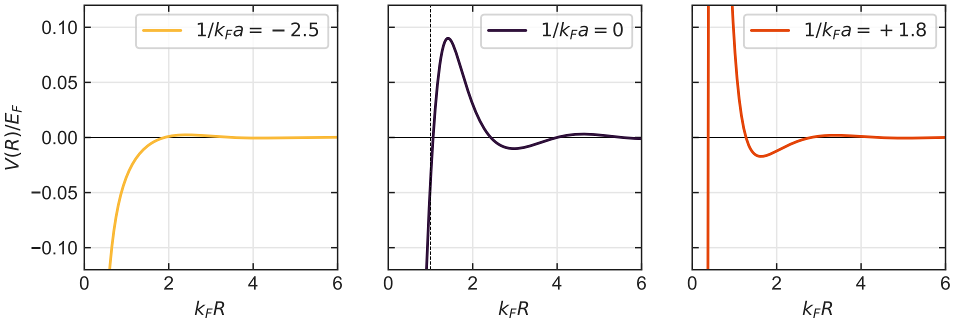

FIGURE 3.6: Effective potential induced between two Cs atoms in a Li Fermi Sea as a function of their inter-particle distance R for negative, resonant and positive scattering lengths a between Li and Cs atoms (from left to right). The picture is adapted from our joint publication [Enss *et al.*, 2020].

must flip sign approximately on the length scale defined by the particle-fermion spacing in the medium, which on the order of $1/k_F$. As a result, the induced interaction $V(R)$ between the bosons can also become repulsive, as shown in Fig. 3.6. In general, one potential issue with a Bose gas is that bosons may form tightly bound molecules and become unavailable to the system due to three-body recombination. Conversely, if there is a repulsive potential between two heavy impurities mediated by the presence of the Fermi sea, this can enhance the stability of the mixture.

The induced potential $V(R)$ can be inserted into the Schrödinger equation to understand the scattering properties of these two heavy impurities. We found that in the strong coupling regime near resonant Bose-Fermi interaction, the induced boson scattering length a_{ind} can even change sign and become repulsive, as shown in Fig. 3.7. Resonances appear at the positions where the Efimov states cross the scattering continuum and the induced scattering length between bosons exhibits a repulsive behavior near to the scattering resonance between the impurity and the medium. Specifically, while the interaction is attractive for $|1/k_Fa| > 2$, as in a pure bosonic medium, near the interspecies scattering resonance, the two impurities repel each other. Therefore, the fermionic medium seems to mitigate the collapse between bosons, which is a qualitatively different behavior compared to a pure Bose gas and points towards stabilizing a Bose-Fermi mixture.

Interestingly, this repulsive interaction, which suggests a large suppression of losses and an enhanced stability near resonance, may explain the recent observations in Chen *et al.* [2022]. A similar behaviour has also been observed by studying the sound propagation in a Li-Cs double degenerate mixture, where a Bose-Einstein condensate is confined in the center of a degenerate Fermi gas [Patel *et al.*, 2023]. Remarkably, they found that the sound propagation close to the interspecies scattering Efimov resonance becomes stable for all interspecies scattering lengths greater than the scattering length associated to the Efimov state.

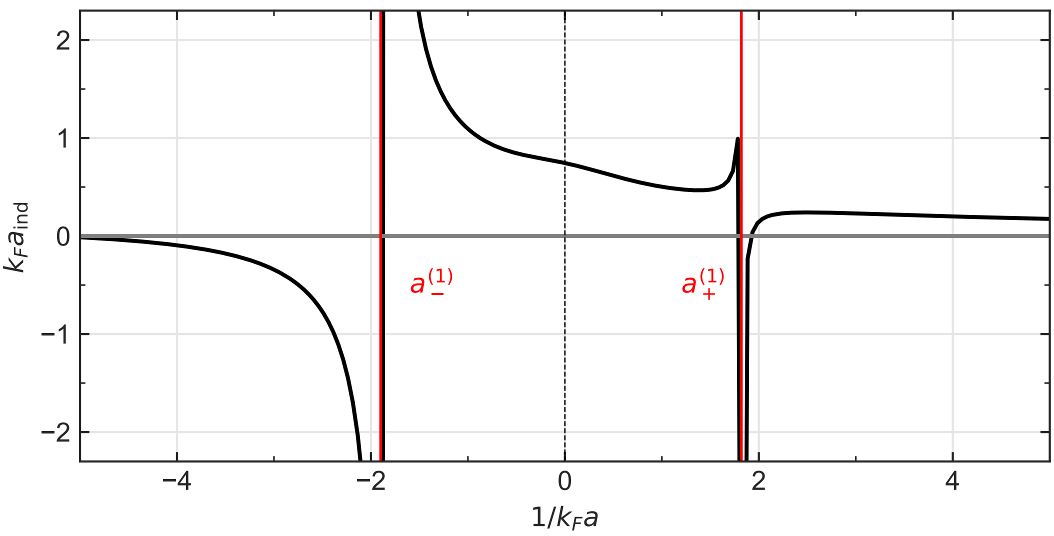

FIGURE 3.7: Induced scattering length a_{ind} between two Cs atoms in a Li Fermi sea as a function of the Li-Cs scattering length a. The exact solution of the Schrödinger equation shows resonances at the positions where the Efimov states cross the scattering continuum, $a_-^{(1)}$ and a_+^{1}, marked in red, and exhibits a repulsive behavior near to the scattering resonance between the impurity and the medium. The picture is adapted from our joint publication [Enss *et al.*, 2020].

3.2 Implementation for Li-Cs mixtures

Our system consists of a small Cs density sample, which plays the role of the impurity, interacting with a polarized Fermi Sea of Li atoms, which plays the role of the bath. In order to probe the Fermi-polaron scenario in a Li-Cs mixture, two ingredients are needed: (i) the ability to tune the magnetic field strength in the vicinity of favorable interspecies Feshbach resonances, (ii) the ability to probe the energy of the impurity as a function of this interaction parameter, which is generally done by an energy-selective transfer of the impurity from a non-interacting state to an interacting one or viceversa.

General concepts about tunable interactions and Feshbach resonances involving the Cs $|3,3\rangle$ have been already introduced in Sec. 2.1.2. I will introduce here the properties of the intra- and inter-species scattering channels which involve Cs $|3,2\rangle$ in Sec. 3.2.1. This is useful in order to understand if timescales associated with two-body inelastic collisions could limit our experiment. The newly implemented Raman spectroscopic scheme on Cs impurities, conceived to transfer atomic population between Cs $|3,3\rangle$ and Cs $|3,2\rangle$, is outlined in Sec. 3.2.2.

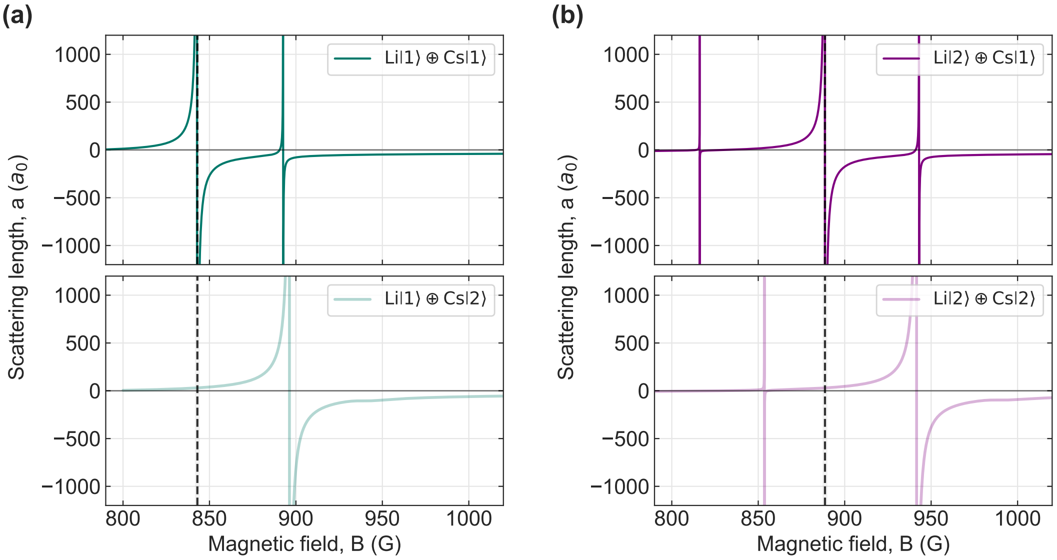

FIGURE 3.8: Scattering length in the Li-Cs scattering channels involving (a) Li$|1\rangle$ (in green) and (b) Li$|2\rangle$ (in purple) as a function of the magnetic field. The scattering lengths for the scattering channels Li$|1\rangle\oplus$Cs$|1\rangle$ and Li$|2\rangle\oplus$Cs$|1\rangle$ (upper row) have been plotted with parameters reported in Ulmanis *et al.* [2015]. For Li$|1\rangle\oplus$Cs$|2\rangle$ (a, down) we use data from MQDT-FT calculations at 1μK provided by Chris Greene (permission granted). For Li$|2\rangle\oplus$Cs$|2\rangle$ (b, down) we use numerical data provided by Arthur Christianen (permission granted) and extracted from cc-calculations at 1μK using the potential found in Pires *et al.* [2014a]. The black dashed lines indicate the more favorable Feshbach resonances for probing the Fermi polaron. A region of ±1 G from the pole of the resonance, which corresponds to $\sim 1/(k_F a) \pm 1.5$ for a typical Fermi energy of $E_F = h \cdot 50$ kHz, is the most favorable for probing the Fermi polaron. The scattering length is given in units of the Bohr radius a_0.

3.2.1 Scattering channels involving Cs $|3,2\rangle$

The most common approach to detect the polaron energy shift is to spectroscopically address the internal energy states of the minority species[2]. Conceptually, the first step is to choose the spin component for the Fermi Sea, either Li$|1\rangle$ or Li$|2\rangle$, and then select one pair of Cs states which allows driving transitions from interacting to non-interacting Li-Cs states. The natural choice is to use Cs ground state Cs $|3,3\rangle$ = Cs$|1\rangle$ and its first excited Zeeman state Cs $|3,2\rangle$ = Cs$|2\rangle$ since for both states the interactions with Li have been already experimentally observed and mapped out [Repp, 2013].

In addition to the scattering channels $|\alpha\rangle$ and $|\beta\rangle$ presented in Chapter 2, we take here into consideration also the channels

$$|\delta\rangle = \text{Li}\,|1/2,-1/2\rangle \oplus \text{Cs}\,|3,2\rangle = \text{Li}\,|2\rangle \oplus \text{Cs}\,|2\rangle\,, \tag{3.13}$$

$$|\gamma\rangle = \text{Li}\,|1/2,+1/2\rangle \oplus \text{Cs}\,|3,2\rangle = \text{Li}\,|1\rangle \oplus \text{Cs}\,|2\rangle \tag{3.14}$$

---

[2] The few experimental attempts done to probe the bath instead of the impurity have yielded a very small signature of the polaron peak [Schirotzek *et al.*, 2009].

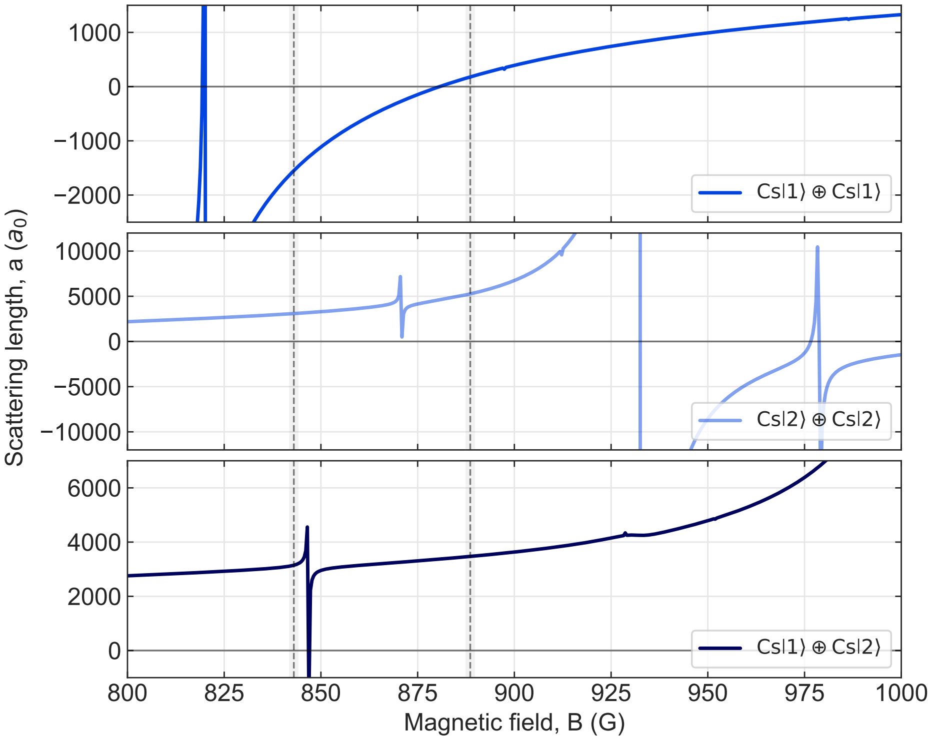

FIGURE 3.9: Scattering length for the Cs-Cs scattering channels, as a function of the magnetic field. Data relative to the channel Cs$|1\rangle \oplus$Cs$|1\rangle$ and Cs$|2\rangle \oplus$Cs$|2\rangle$ are taken from [Frye *et al.*, 2019] and data relative to the channel Cs$|1\rangle \oplus$Cs$|2\rangle$ come from numerical data provided by Matthew Frye and Jeremy Hutson (permission granted). The black dashed lines indicate the Li-Cs Feshbach resonances at 843 G and 888.6 G. The tiny gray shaded areas mark regions favorable for probing the Fermi polaron.

which are characterized by projections of the total angular momentum m_f, equal to 3/2 and 5/2, respectively. The only drawback is that those scattering channels can undergo two-body inelastic collisions since the resonant state is comparably coupled to both the incident channel and inelastic channel. In order to understand the behaviour of the scattering length and of the inelastic rate coefficient as a function of the magnetic field between 800 G and 1000 G it is necessary to look at the theoretical models in Pires *et al.* [2014a]. Regarding the Cs-Cs system, we refer instead to the work of Frye *et al.* [2019] based on potentials reported in Berninger *et al.* [2013].

Scattering lengths. The interspecies s-wave scattering length for the Li-Cs system are shown in Fig. 3.8. Data relative to the scattering channels Li$|1\rangle \oplus$Cs$|2\rangle$ come from MQDT-FT calculations at 1 μK by Chris Greene, while for the channel Li$|2\rangle \oplus$Cs$|2\rangle$ they come from cc-calculations performed by Arthur Christianen using the potential reported in [Pires *et al.*, 2014a]. The scattering lengths for Li-Cs, involving the Cs$|1\rangle$ state, have been already shown in Sec. 2.1.2 and were calculated with experimental parameters found in Ulmanis *et al.* [2015]. Corresponding to the two intermediate broad resonances at 843 G and 888.6 G, the scattering lengths in the Li$|1\rangle \oplus$Cs$|2\rangle$ and Li$|2\rangle \oplus$Cs$|2\rangle$ states are small and positive, $a \simeq 30\ a_0$. for a typical Fermi energy of $E_F = h \cdot 50$ kHz, a region of ±1 G around the pole of the resonance, corresponding to a range $\pm 1.5 \times (k_F a)^{-1}$, is the most favorable for probing the polaron.

In Repp *et al.* [2013], in the range between 800 G and 1000 G, a Feshbach resonance at 896.6(7) G with an FWHM of 10(2) G was experimentally found for the Li$|1\rangle \oplus$Cs$|2\rangle$. In the same work, Feshbach resonances for the Li$|2\rangle \oplus$Cs$|2\rangle$ scattering channel have been detected at 835.85(1) G and 943.5(1) G with an experimental FWHM of 0.15(3) G and 15(3) G, respectively. The theoretical curves in Fig. 3.8, show that the scattering length for Li$|1\rangle \oplus$Cs$|2\rangle$ is small and positive until 896.6(7) G and becomes small and negative after the resonance. Similarly, for Li$|2\rangle \oplus$Cs$|2\rangle$ the scattering length is small and positive up to the Feshbach resonance at 943.5(1) G and becomes small and negative after that[3].

The intraspecies s-wave scattering length for Cs-Cs system are shown in Fig. 3.9. For Cs-Cs, data for the channels Cs$|1\rangle \oplus$Cs$|1\rangle$ and Cs$|2\rangle \oplus$Cs$|2\rangle$ are taken from [Frye *et al.*, 2019] and data for the channel Cs$|1\rangle \oplus$Cs$|2\rangle$ comes from numerical data provided by Matthew Frye and Jeremy Hutson. All these data are based on coupled channel calculations at 1 nK. Here, the scattering lengths for the channel Cs$|1\rangle \oplus$Cs$|1\rangle$ at 888.6 G are relatively small and repulsive, whereas at 843 G they are large and attractive; for the channel Cs$|2\rangle \oplus$Cs$|1\rangle$ as for the Cs$|2\rangle \oplus$Cs$|2\rangle$ they are instead also large but repulsive.

Two-body collisional properties. The inter- and intraspecies scattering channels that involve the Cs$|2\rangle$ state can decay through two-body inelastic collisions. When inelastic scattering is possible, the scattering length $a(k)$ becomes complex, $a(k) = \alpha(k) + i\beta(k)$ and the rate coefficients of elastic and inelastic collisions are given by the diagonal elements of the scattering matrix $S_{ll}(k) = e^{2i\delta_l(k)}$, where δ_l is the scattering phase shift. Suppose we consider only s-waves (with $l = 0$) and additional open channels besides the low energy incident channel, denoted channel 0. The incident kinetic energy in channel 0 is $\Delta E_0 = E - E_0 = \frac{\hbar^2 k_0^2}{2\mu}$, where E is the total energy of the system and μ is the reduced mass. For example, if there are two channels, the inelastic scattering probability to transition from channel 0 to channel 1 is given by $|S_{10}|^2$. Generalizing the problem to N channels, the inelastic scattering probability is given by the sum of all the individual probabilities to go into one of these N states $\sum_{i\neq 0}^{N} |S_{i,0}|^2$. The elastic and inelastic scattering cross-section $\sigma_{el,in}$ are given by [Balakrishnan *et al.*, 1997; Idziaszek and Julienne, 2010]

$$\sigma_{el}(k_0) = \frac{\pi}{k_0^2} \cdot |1 - S_{i,i}|^2 \tag{3.15}$$

$$\sigma_{in}(k_0) = \frac{\pi}{k_0^2} \cdot (1 - |S_{i,i}|^2) \tag{3.16}$$

---

[3] Unfortunately, using Li$|2\rangle \oplus$Cs$|2\rangle$ and Li$|1\rangle \oplus$Cs$|2\rangle$ as "interacting channels" around 896.6(7) G and 943.5(1) G, respectively, is not favourable because of Li-Cs inelastic scattering rates that are three orders of magnitude higher than at 843 G and 888.6 G.

where k_0 is the wavevector of the incoming channel. At low energy, $S_{i,i}$ is parameterized in terms of the energy-dependent complex scattering length $a(k_0)$, such that

$$a(k_0) = \frac{1}{ik_0}\left(\frac{1 - S_{i,i}}{1 + S_{i,i}}\right). \tag{3.17}$$

The cross-sections can then be written exactly in terms of the scattering length as [Hutson, 2007; Cvitaš *et al.*, 2007]

$$\sigma_{el}(k_0) = \frac{4\pi|a|^2}{1 + k_0^2|a|^2 + 2k_0\beta} \xrightarrow{k_0 \to 0} 4\pi a^2 \tag{3.18}$$

$$\sigma_{in}(k_0) = \frac{4\pi\beta}{k_0(1 + k_0^2|a|^2 + 2k_0\beta)} \xrightarrow{k_0 \to 0} \frac{4\pi}{k_0}\beta. \tag{3.19}$$

Similarly, considering that we have an equivalent formula given by the inelastic scattering cross-section, σ_{in} can also be calculated as follows[4]

$$\begin{aligned} \sigma_{in} &= \frac{\pi}{k_0^2} \cdot \sum_{i \neq 0}^{N} |S_{i,0}|^2 \\ &= \frac{\pi}{k_0^2} \cdot \Big(1 - \exp(-4k_0|\beta|)\Big). \end{aligned} \tag{3.20}$$

Following [Bohn and Julienne, 1997], the rate coefficients, for elastic k_{el} and inelastic k_{inel} collisions, are given by the thermal averages

$$k_{el,in} = \langle v_i \sigma_{el,in}(E) \rangle \tag{3.21}$$

where $v_i = \hbar k_i / m_{red}$ is the relative incident velocity of the colliding atoms related to their relative kinetic energy $E = \hbar^2 k_i^2 / 2m_{red}$ with reduced mass m_{red}. For sub-mK temperatures, the s-wave collisions dominate. The average, at these temperatures, reduces to the evaluation of $v_i \sigma(E)$ at a single scattering energy $E = k_B T$ corresponding to the trap temperature T. This leads to

$$k_{el,in}(E) = \sqrt{\frac{2E}{m_{red}}} \cdot \sigma_{in,el}(E). \tag{3.22}$$

For s-wave it is important to notice that $k_{el}(k_0) \propto k_0 a^2$ while $k_{in}(k_0) \propto a$. This means that the inelastic scattering rate is independent from k_0, whereas the elastic scattering depends linearly on k_0, which scales as $\sqrt{T}$. The two-body elastic and inelastic collisional rate depends on the atomic density n_0 and it is defined as

$$\tau_{el,in}^{-1} = k_{el,in} \cdot n_0 \tag{3.23}$$

---

[4] Handwritten lecture notes by Chris Greene.

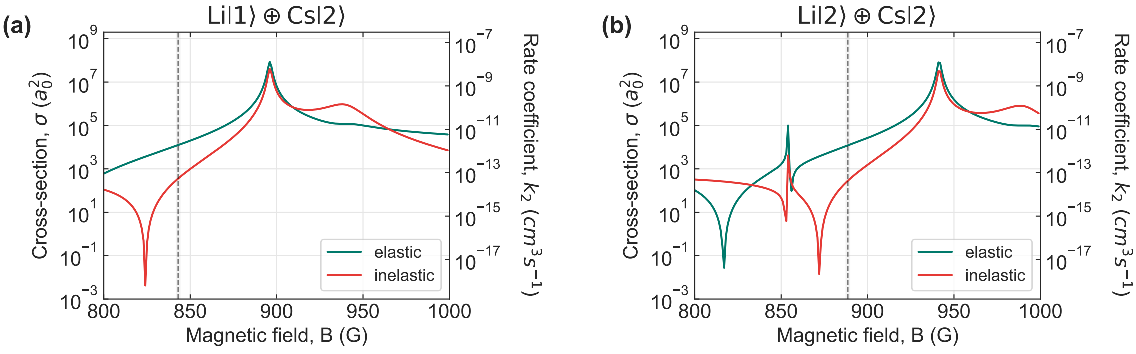

FIGURE 3.10: Elastic (green) and inelastic (red) cross-section and rate coefficient for the inelastic scattering channels (a) Li$|1\rangle \oplus$Cs$|2\rangle$ and (b) Li$|2\rangle \oplus$Cs$|2\rangle$ as a function of the magnetic field. The cross-section shown here is adapted from data obtained by Arthur Christianen (permission granted) from cc-calculations for a temperature of 1 μK. The black dashed lines indicate the Li-Cs Feshbach resonances at 843 G and 888.6 G. The cross-section is given in atomic units of a_0^2.

where $\tau_{el,in}$ gives the timescales associated with two-body scattering processes. The elastic collision rate is proportional to the thermalization time, while for inelastic collisions it is the time at which two-body losses occur.

Interspecies collisional properties between Li-Cs for Li$|1\rangle \oplus$Cs$|2\rangle$ and Li$|2\rangle \oplus$Cs$|2\rangle$ are shown in Fig. 3.10 and summarized in Tab. 3.1. Figure 3.10 shows the elastic and inelastic cross-sections and rate coefficients as a function of the magnetic field between 800 G and 1000 G. The cross-sections have been obtained by cc-calculations performed at 1 μK by Arthur Christianen and based on potentials accurately determined by Pires *et al.* [2014a]. The rate coefficients have been calculated using Eq. 3.22 at the single relative kinetic energy of $E/k_B = 1\ \mu$K. The dashed black lines mark the positions of Li-Cs Feshbach resonances at 843 G for Li$|1\rangle \oplus$Cs$|2\rangle$ and at 888.6 G for Li$|2\rangle \oplus$Cs$|2\rangle$, respectively. These magnetic fields are both close to the absolute minima, respectively at 817 G and 872 G, thanks to which, our scattering cross-sections remain quite low, as reported in Tab. 3.1. The maxima in the inelastic cross-section correspond to the poles of the Feshbach resonances. For typical densities of the Li Fermi Sea of $n_{0,Li} = 1 \times 10^{12}$ cm^{-3}, loss coefficients of 5.3×10^{-2} s^{-1} and 4.2×10^{-2} s^{-1} are calculated at 843 G and 888.6 G, respectively. Both scenarios lead to a loss timescale $\simeq$ 20 s, which is not a limiting factor for our experiment. A ratio of approximately 40 between elastic and inelastic cross-sections allows for a clear separation of the timescales associated with elastic and inelastic collisions.

The same quantities have been studied for Cs intraspecies interactions. As Cs plays the role of the impurity, we consider atomic densities much lower than for Li. These quantities for Cs$|2\rangle \oplus$Cs$|2\rangle$ and Cs$|1\rangle \oplus$Cs$|2\rangle$ are shown in Fig. 3.11 and summarized in Tab. 3.1. The rate coefficient k_{in} has been obtained from cc-calculations at 1 nK from [Frye *et al.*, 2019] for Cs$|2\rangle \oplus$Cs$|2\rangle$ and from private exchanges with Matthew Frye and Jeremy Hutson for Cs$|1\rangle \oplus$Cs$|2\rangle$. The inelastic scattering cross-sections have been calculated from

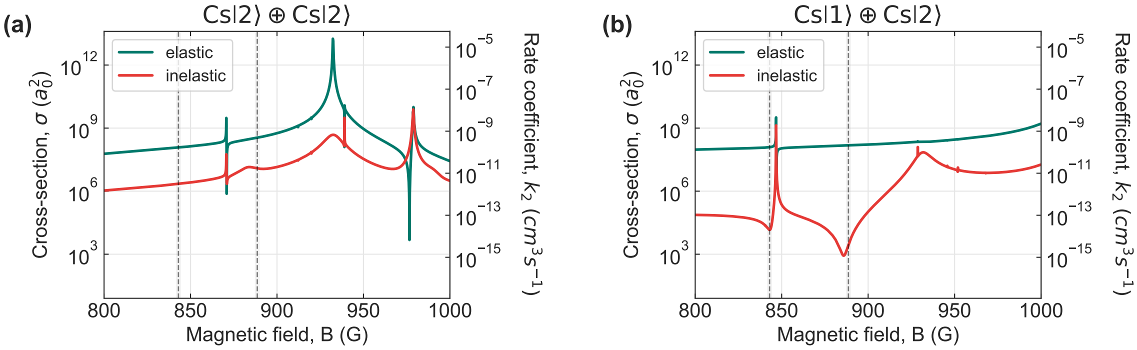

FIGURE 3.11: Elastic (green) and inelastic (red) cross-section and rate coefficient for the Cs-Cs scattering channels Cs$|2\rangle\oplus$Cs$|2\rangle$ and Cs$|1\rangle\oplus$Cs$|2\rangle$ in dependence of the magnetic field. Both sets of data have been obtained by coupled-channel calculation for a temperature of 1 nK. Graphs for the channel Cs$|2\rangle\oplus$Cs$|2\rangle$ are adapted from data in [Frye *et al.*, 2019] and for Cs$|1\rangle\oplus$Cs$|2\rangle$ are adapted from data provided by Matthew Frye and Jeremy Hutson (permission granted). The black dashed lines indicate the Li-Cs Feshbach resonances at 843 G and 888.6 G.

k_{in} obtained by the inverse of Eq. 3.22. The elastic cross-sections and rate coefficients have been calculated with Eq. 3.18, considering E/k_B=1 nK, for consistency with the data relative to a and k_{in}.

- For the scattering channel Cs$|2\rangle\oplus$Cs$|2\rangle$ there is no pronounced minimum close to the Li-Cs Feshbach resonances. For densities of $n_{0,Cs} = 1 \times 10^{10}$ cm^{-3}, we expect inelastic collisional rates of 3.1×10^{-2} s^{-1} at 843 G and 1.7×10^{-1} s^{-1} at 888.6 G, which lead to timescales of $\sim$ 30 s and $\sim$ 6 s, respectively. Those timescales are not expected to limit the experimental protocol for probing the polaron energy.
- For the scattering channel Cs$|1\rangle\oplus$Cs$|2\rangle$ the decrease in the inelastic scattering around 886 G represents an interference minimum. This phenomenon arises from two different pathways: the direct inelastic scattering from the incoming channel to the loss channel, and the inelastic scattering that occurs through an intermediate resonant state, which is responsible for the pronounced decay resonance near 930 G. These pathways can interfere, leading to destructive interference on one side of the resonance, which in turn suppresses the loss. The same effect causes the smaller dip near 845 G associated with the narrower 850 G resonance. For Cs densities of $n_{0,Cs} = 1 \times 10^{10}$ cm^{-3} this leads to inelastic collisional rates of 2.0×10^{-4} s^{-1} at 843 G and 4.8×10^{-5} s^{-1} at 888.6 G, corresponding respectively to timescales of $\sim$ 5×10^3 s and 2×10^4 s. These values are long enough to not limit our experiment.

For both scattering channels, and both magnetic fields of interest, the ratio between elastic and inelastic cross-section assures a good separation of the timescales. It is important to note that even for s-wave approximation, where k_{in} is expected to be independent of k_0, the scattering length for Cs is generally quite sensitive to temperature, and hence the timescales shown here are expected to be the upper limit, as they are calculated for 1 nK.

B (G)	channels	$\sigma_{in}(a_0^2)$	$k_{2,in}$ (cm^3 s^{-1})	σ_{el}/σ_{in}
843.0	Li$\|1\rangle\oplus$Cs$\|2\rangle$	3.7×10^2	5.3×10^{-14}	3.5×10^1
	Cs$\|2\rangle\oplus$Cs$\|2\rangle$	2.2×10^6	3.1×10^{-12}	5.3×10^1
	Cs$\|1\rangle\oplus$Cs$\|2\rangle$	1.4×10^4	2.0×10^{-14}	8.6×10^3
888.6	Li$\|2\rangle\oplus$Cs$\|2\rangle$	2.9×10^2	4.2×10^{-14}	4.2×10^1
	Cs$\|2\rangle\oplus$Cs$\|2\rangle$	1.2×10^7	1.7×10^{-11}	2.9×10^1
	Cs$\|1\rangle\oplus$Cs$\|2\rangle$	3.5×10^3	4.8×10^{-15}	4.4×10^4

TABLE 3.1: Inelastic cross-section and rate coefficient in different scattering channels at 843.0 G and 888.6 G at a relative kinetic energy of $E/k_B = 1\ \mu$K for Li-Cs and 1 nK for Cs-Cs. The last column gives the ratio between the elastic and inelastic cross-section corresponding to the good to bad collisional-rate ratio.

Consequences for the choice of spectroscopic protocols. Firstly, in order to prevent undesirable atom loss, it is necessary to maintain the densities of Cs at a sufficiently low level. Secondly, it is advantageous to select a spectroscopic protocol that allows the initial inter-species scattering state, for the chosen magnetic field, to remain as collisionally stable as possible. Thirdly, if the final state is strongly interacting and involves inelastic scattering, spin exchange collisions may occur, which could invalidate the protocol for probing a specific state. Moreover, given the aforementioned timescales and mixing scheme, and considering that these timescales are quite sensitive to temperatures and densities, we have chosen the *ejection* spectroscopy around the Feshbach resonance at 888.6 G as the most suitable protocol for our current experimental setup. The states that we take in consideration are then:

$$|\beta\rangle = \mathrm{Li}\,|2\rangle \oplus \mathrm{Cs}\,|1\rangle\,, \tag{3.24}$$

$$|\delta\rangle = \mathrm{Li}\,|2\rangle \oplus \mathrm{Cs}\,|2\rangle\,, \tag{3.25}$$

where $|\beta\rangle$ plays the role of the interacting state, while $|\delta\rangle$ is the non interacting state. We are going to prepare the system in the state $|\beta\rangle$ and then eject the impurities into the state $|\delta\rangle$.

3.2.2 Raman spectroscopy on Cs atoms

The most well-established technique for probing quasi-particles in ultracold atoms is radiofrequency (RF) spectroscopy [Vale and Zwierlein, 2021]. This technique involves two internal hyperfine states of the impurity atoms that are coupled by an oscillating RF field. The two coupled impurity states are chosen such that they feature different interaction parameters $1/(k_F a)$ with the surrounding medium and, especially, one of them has to be at most weakly interacting.

Similarly to RF spectroscopy, two-photon Raman spectroscopy can also be used to identify the coherent response of polarons and determine some of their key properties [Ness *et al.*, 2020]. Raman spectroscopy allows for local addressability of the atomic cloud and for finite momentum-transfer [Veeravalli *et al.*, 2008; Shkedrov *et al.*, 2020]. Indeed, in the Raman process the momentum change compared to the atomic momentum is not negligible and the transition rate depends on the atomic velocity. This opens up the possibility of investigating momentum-dependent phenomena [Ness *et al.*, 2020; Diessel *et al.*, 2024] that cannot be studied with RF.

After some effort in adapting our existing RF setup to the Cs transition frequencies as shown in Sec. 1.5.1, we abandoned this approach because it turned out to be not feasible due to bad coupling of the RF fields into our steel vacuum chamber. Inspired by the work of Rudi Grimm in Innsbruck and in collaboration with his group[5], we moved to an optical approach where the use of two co-propagating laser beams enables us to drive two-photon Raman transitions between the two lowest Cs hyperfine states.

Stimulated Raman transitions on Cs hyperfine states. The two-photon Raman process couples two states to each other through an intermediate excited state. The schematic that describes the situation for the specific application to Cs is depicted in Fig. 3.12 (a). Here, Cs$|1\rangle$ and Cs$|2\rangle$ states are coupled to each other through an intermediate excited state $|e\rangle$ of the excited manifold $6^2\mathrm{P}_{3/2}$, corresponding to the $\mathcal{D}_2$-Line. Each of the two states is coupled to the excited state $|e\rangle$ with a Rabi coupling $\Omega_{1,2}$. Each of these optical fields is detuned from the excited state by a factor Δ much larger than the excited state linewidth $\gamma_{\mathcal{D}_2}$ [Steck, 2023]. While a large Δ reduces the effective two-photon coupling, it ensures that detrimental single-photon scattering with the excited state are avoided and that the population can be coherently transferred from the state Cs$|1\rangle$ to the state Cs$|2\rangle$. The two optical fields are characterized by a different frequency $\omega_{1,2}$ and a different polarization, which is linear and circular, leading to π and σ^+ polarized light, respectively. These two optical fields can also have different wave vectors $\mathbf{k_{1,2}}$, but here we consider the case with zero momentum transfer, $\Delta\mathbf{k} = \mathbf{k_2} - \mathbf{k_1} = 0$, which is realized by two co-propagating laser beams. For typical magnetic field offsets, between 880 G and 890 G, the energy difference ω_0 between the two states Cs$|1\rangle$ and Cs$|2\rangle$ falls in the range that goes from $\omega_0 = 2\pi \times 262.5$ MHz to 262.9 MHz with 245 kHz/G, as in Fig. 1.16.

To calculate the effective Rabi frequency of the two-photon Raman process only a few states of the excited manifold $6^2\mathrm{P}_{3/2}$ are relevant, as depicted in Figure 3.12. These are labeled as $|m_j, m_I\rangle = |-1/2, 7/2\rangle$, $|1/2, 5/2\rangle$, $|3/2, 3/2\rangle$. At typical magnetic fields of 890 G, the manifold $6^2\mathrm{P}_{3/2}$ is already in the Paschen-Back regime and these states are labeled with m_j and m_I, according to the magnetic quantum number associated with the total electronic and nuclear angular momentum, $\mathbf{J}$ and $\mathbf{I}$, respectively. All other states are assumed to be so far from the resonance that any additional contributions can be neglected. Since the detuning is of the same order of magnitude of the hyperfine splitting, the contribution of each hyperfine state must be considered individually. Thus, the Rabi frequencies $\Omega_{i,e}$ for the coupling between the ground state $|i\rangle$ and the excited state $|e\rangle$ are

---

[5] Private exchanges with Erich Dobler and Cosetta Baroni.

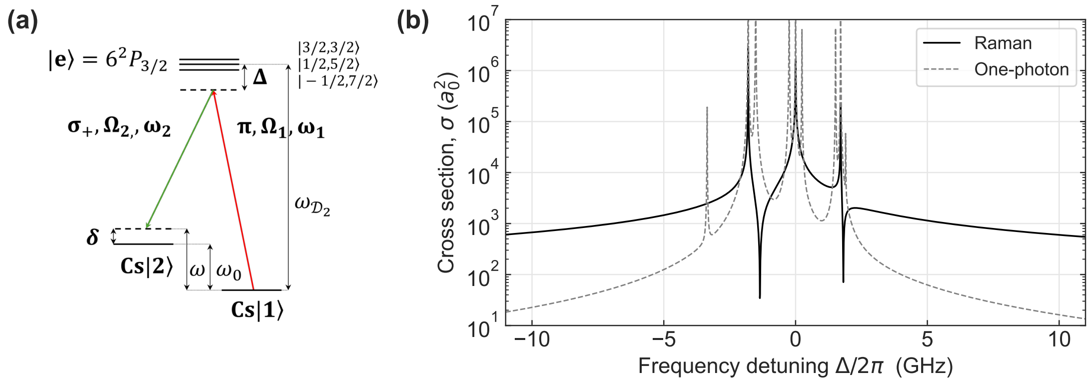

FIGURE 3.12: Two-photon Raman transitions on Cs atoms. In (a), a schematic of the energy levels involved in the Raman scheme is shown. The optical fields, with frequencies ω_1 and ω_2 are detuned to the $\mathcal{D}_2$ transition of Cs by the detuning Δ, while the frequency difference between two differently polarized optical fields resolves the energy difference $\omega = \omega_0 + \delta$ of the two lowest Cs Zeeman states. In (b), the Raman scattering cross-section as a function of the detuning Δ is shown. The resonances in the two-photon Raman cross-section (black solid line) correspond to the Cs$|1\rangle$ $\rightarrow$ $|{-1/2,7/2}\rangle$, $|1/2,5/2\rangle$, $|3/2,3/2\rangle$ transitions. The one-photon scattering cross-section (gray dashed line) exhibits resonances corresponding to π and σ_+ polarized light. Picture (b) is adapted from [Welz, 2024].

calculated individually

$$\hbar\Omega_{1,e} = \mathcal{E}_1 \langle 1|e\hat{r}_\pi|e\rangle = \sum_{F=3,4\ F'=2,3,4,5} \mathcal{E}_1 \langle 1|F,3\rangle \langle F,3|e\hat{r}_\pi|F',3\rangle \langle F',3|e\rangle \tag{3.26}$$

$$\hbar\Omega_{2,e} = \mathcal{E}_2 \langle 2|e\hat{r}_+|e\rangle = \sum_{F=3,4\ F'=2,3,4,5} \mathcal{E}_2 \langle 2|F,2\rangle \langle F,2|e\hat{r}_+|F',3\rangle \langle F',3|e\rangle \tag{3.27}$$

where branching ratios of the transitions are calculated with the definition of $\langle F, M|e\,\hat{r}_q|F', M'\rangle$ in [Steck, 2023], with the Wigner 6-j symbol and the Wigner 3-j symbol as it was defined in [Loudon, 2000]. For details on this calculation I address the reader to [Welz, 2024].

When $|\delta|, \gamma_{\mathcal{D}_2} \ll |\Delta|$, an effective Rabi frequency can be defined for the Cs$|1\rangle$ to Cs$|2\rangle$ transition via the excited state $|e\rangle$, and it depends on the relative detuning Δ to the state $|e\rangle$ as [Foot, 2005]:

$$\Omega_{\mathrm{R}}(\Delta) = \frac{\Omega_{1,e}\Omega_{2,e}}{2\Delta}, \tag{3.28}$$

with $\Omega_{1,e}$ and $\Omega_{2,e}$ the coupling strengths of the $|1\rangle$ and $|2\rangle$ states to $|e\rangle$. Assuming that both optical fields have the same intensity $I_1 = I_2 = I$ with $I = \frac{1}{2}\epsilon_0 c|\mathcal{E}|^2$, the Eq. 3.28 can be written as

$$\Omega_{\mathrm{R}}(I, \Delta) = \frac{\hbar^2 \langle 1|e\hat{r}_\pi|e\rangle \langle e|e\hat{r}_+|2\rangle}{\Delta\epsilon_0 c} I. \tag{3.29}$$

The effective two-photon Rabi frequency, named Raman frequency, is given by the coherent sum of the individual frequencies Ω_{R} as [Steck, 2024]:

$$\Omega_{\mathrm{R}}(I,\Delta) = \left| \sum_{|e\rangle = |\frac{3}{2},\frac{3}{2}\rangle, |\frac{1}{2},\frac{5}{2}\rangle, |-\frac{1}{2},\frac{7}{2}\rangle} \Omega_{\mathrm{R}}(I,\Delta) \right|. \tag{3.30}$$

To express the two-photon Raman coupling with an expression independent from the intensity and to compare it with the one-photon cross-section, one can proceed similarly to the one-photon scattering [Foot, 2005]. This procedure consists in dividing the Rabi frequency for the photon flux $I/\hbar\omega$

$$\sigma_{\mathrm{Raman}}(\Delta) = \frac{\Omega_{\mathrm{R}}(\Delta)\hbar\omega_{\mathcal{D}_2}}{2\pi I}. \tag{3.31}$$

Here, we assume that both optical fields ω_1, ω_2 have approximately the same frequency, because $\omega_{\mathcal{D}_2} \gg \omega_0$ [Steck, 2023]. The two photon Raman cross-section as function of the detuning Δ for an offset magnetic field of 890 G is shown in Fig. 3.12 (b). The interference minima come from adding coherently one to each other the contributions coming from pairs of different states. For comparison, the dashed line takes into account the one-photon scattering, calculated as in Welz [2024]. The behaviour of the one-photon scattering shows that for a detuning Δ larger than approximately $2\pi \cdot 2.5$ GHz, the one-photon scattering is negligible compared to the Raman process, since it is at least one order of magnitude smaller. For 10 GHz detuning and a total intensity of 10 $\mathrm{mW/mm^2}$, we should get a Rabi Frequency of $\Omega_R = 2\pi \times 51$ kHz. It should be noted that as the hyperfine coupling for Cs at about 890 G is still larger than the Zeeman term, in turns the Raman coupling is large compared to other atoms. For instance, in the case of ^{41}K, at 335 G (position of the ^{6}Li- ^{41}K Feshbach resonance), the Raman coupling is a factor of three smaller then what we expect here, since K is already in the Paschen-Back regime and therefore the hyperfine coupling is much weaker.

Optical setup with co-propagating beams. The optical setup for the preparation of the Raman light is divided into two parts that are illustrated in Fig. 3.13[6]. We use a Sacher laser-Tec150[7] tunable in the range 830-870 nm with an accuracy of 0.122 nm per 26 V with piezo actuator. At 852.3 nm, the output power is > 80 mW after the internal optical isolator and > 50 mW after the fiber. On the laser table, the laser light is coupled into a polarization-maintaining fiber and collimated with a collimator with a focal length of 4 mm (Schäfter-Kirchhoff, 60FC-4-A4-02). It is then split by a polarization beam splitter (PBS) into two branches whose intensity ratio can be adjusted. The reflected beam is sent to a wavemeter to monitor the wavelength over time, while the transmitted beam goes to a first AOM, which is used to switch on and off the laser transmission. The beam is then divided again in two branches by another PBS such that the transmitted beam passes through a double-pass AOM which detunes the laser frequency

---

[6] Further details on the developments of this setup will be provided in the PhD thesis by Tobias Krom.

[7] Then it has replaced for the measurements presented in Sec. 3.3.1 with a Sacher VBG-0852-080-BFY.

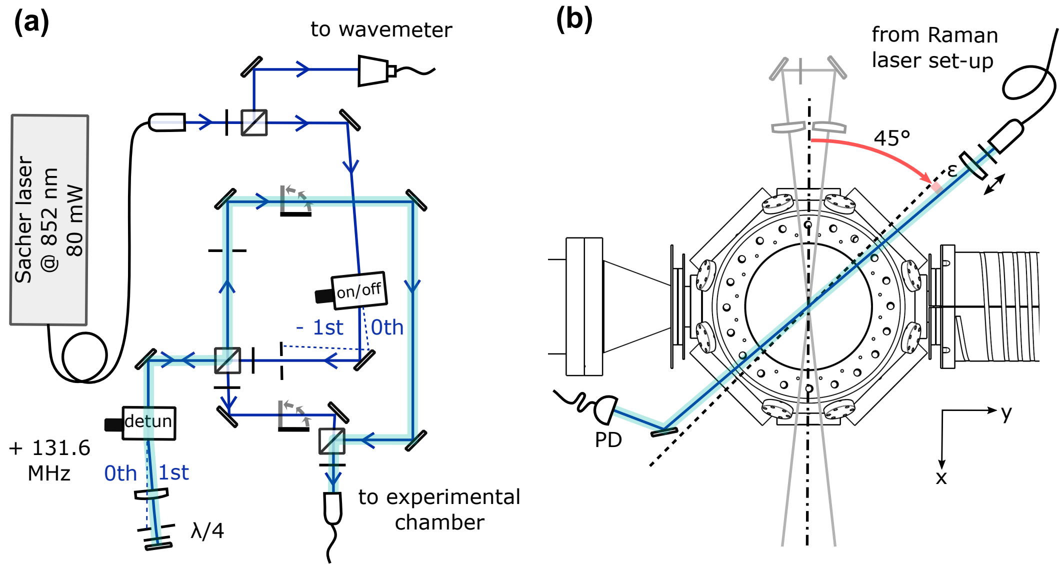

FIGURE 3.13: Optical setup for the preparation of the beams for Raman spectroscopy: (a) on the laser table and (b) on the experimental chamber table. On the laser table, the laser is switched on by a first AOM and split in two by a polarizing beam splitter. The transmitted beam passes through a double-pass AOM which detunes the laser frequency of $\delta/2\pi \sim 2 \times f_{AOM}$. The two branches are combined together with a polarizing beam splitter and then coupled into a polarization-maintaining optical fiber. In the experimental chamber table, the light is focused into the chamber of science through a lens which is mounted on a manual translational stage to adjust the position of the beam on the atoms.

by $\delta/2\pi \sim 2 \times f_{AOM} \sim 2 \times 131.3$ MHz. The double-pass AOM is connected to the microwave frequency generator and amplified by a mini-circuit amplifier. The two branches are then combined together again by a third PBS and coupled into a polarizing optical fiber 10 m long (Thorlabs P3-780PM-FC-10), which brings the light to the experimental table. In this way we obtained two beams with orthogonal polarization and different frequencies (one detuned from the other by $2 \times f_{AOM}$). Once there, the light is focused into the science chamber through a lens mounted on a manual translational stage to adjust the position of the beam on the atoms. The power of the laser is monitored behind the science chamber. The two beams are linear polarized and orthogonal each other.As their polarization is then orthogonal to the magnetic field we obtain π and σ_+ light, respectively (see Fig. 3.12). The largest beam diameter we can reach with the current setup is roughly up to 1 mm and the maximal power per beam is 5 mW.

Performance: energy spectrum and Rabi frequencies. In order to benchmark the performance of our Raman setup, we have performed both spectroscopic and Rabi oscillation measurements of the $\mathrm{Cs}|1\rangle$ to $\mathrm{Cs}|2\rangle$ transition. After sending a square Raman pulse on the Cs sample prepared in the $\mathrm{Cs}|1\rangle$ state, the population starts oscillating between the states $\mathrm{Cs}|1\rangle$ and $\mathrm{Cs}|2\rangle$ with the generalized Rabi frequency $\Omega = \sqrt{\Omega_R^2 + \delta^2}$. The fractional population in $\mathrm{Cs}|1\rangle$ ρ_{11} can be written as a function of both the detuning δ and

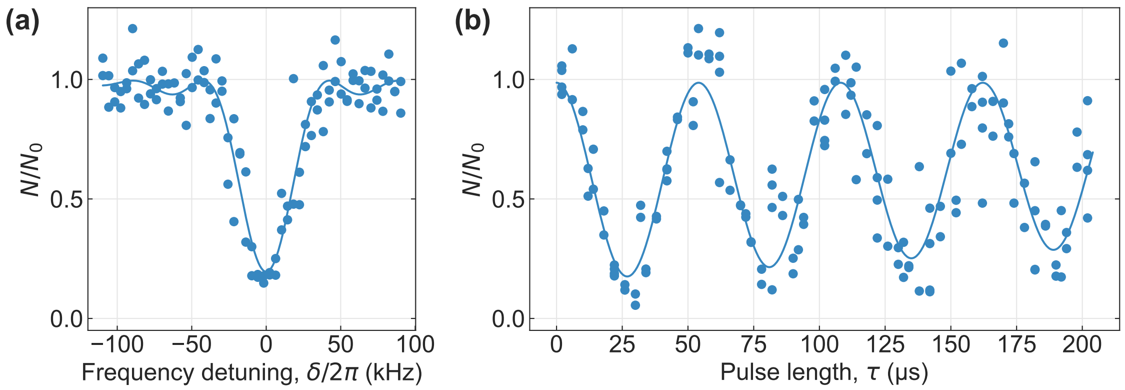

FIGURE 3.14: Two-photon Raman transitions on Cs. The graph (a) shows a scan of the frequency difference for a fixed pulse length, which corresponds to a π-pulse. In (b) the coherent Rabi oscillations for the case $\omega = \omega_0$ is shown. The dots are the experimental data points, while the lines are the respective fit, which are described in the text.

laser-atom interaction time, or pulse length, τ as in [Linskens *et al.*, 1996]

$$\rho_{11}(\delta, \tau) = 1 - \frac{\Omega_R}{\sqrt{\Omega_R^2 + \delta^2}} \sin^2 \left(\frac{\sqrt{\Omega_R^2 + \delta^2}}{2} \tau \right). \tag{3.32}$$

It holds that $\rho_{11} + \rho_{22} = 1$ and $\rho_e = 0$. The factor in front of the sinusoidal function is the excitation amplitude, which depends on the two photon Rabi frequency Ω_R and determines the maximum degree of excitation. In the case of δ =0, i.e. pure two-photon resonance, Eq. 3.32 reduces to

$$\rho_{11}(\tau) = 1 - \sin^2 (\Omega_R \tau / 2). \tag{3.33}$$

Moreover, for a two-photon transition, $\Omega_R \tau \propto P/w_0$, with P being the total power of the beam and w_0 its beam waist, whereas for a one-photon transition $\Omega \tau \propto \sqrt{P}$ [Linskens *et al.*, 1996].

A spectroscopic measurement of the Cs$|1\rangle$ and Cs$|2\rangle$ transition in a dilute Cs Bose gas at $B_0 = 891$ G is displayed in Fig. 3.14 (a), obtained by measuring the fraction of Cs atoms remaining in the initially occupied Cs$|1\rangle$ state. For this measurement the power for each of the two beams is about 3 mW, the beam diameter is 870 μm and the detuning Δ is 20 GHz. We fit the data to the sinc-shape line in Eq. 3.32, with $\tau = 22$ μs, as a function of $\delta = \omega - \omega_0$. The resulting sinc-shaped line is centered at $\omega_0/2\pi = (263.2097 \pm 0.0007)$ MHz and is observed after a square pulse with a Raman beam intensity of 8 mW/mm^{-2}. The FWHM of the function is given by $\Delta_{FWHM} = 2 \times (16.1 \pm 0.5)$ kHz, which defines our spectral resolution in probing the polaron peak.

We have also performed Rabi oscillation measurements at the resonance ω_0. One illustrative result is displayed in Fig. 3.14 (b), where it is visible a quite coherent sinusoidal evolution of the state population. In this measurement, a small damping is observed over the time scales of the evolution. Therefore, we fit the data adding a damping rate Γ in Eq. 3.32 as follow[8] [Linskens *et al.*, 1996]:

$$\rho_{11}(\tau) = 1 - \frac{\Omega_R}{\sqrt{\Omega_R^2 + \delta^2}} \sin^2\left(\frac{\sqrt{\Omega_R^2 + \delta^2}}{2}\tau\right) \cdot e^{-\Gamma\tau}. \tag{3.34}$$

We find a Rabi frequency of $\Omega_R/2\pi = (15.6 \pm 0.9)$ kHz, which is on the same order of magnitude as the predicted one. This result corresponds to a π-pulse duration of $\tau_{\pi-pulse} = (32.1 \pm 1.8)\ \mu$s, which is one order of magnitude greater than the typical Fermi time of our system $\tau_F \approx 2\ \mu$s, thus fulfilling one of the main design goals required for the polaron experiment, as in Sec. 3.3. The non-negligible residual detuning $\delta/2\pi = (10 \pm 1)$ kHz and the small decay rate $\Gamma = (0.9 \pm 0.5)\ \mathrm{ms}^{-1}$, are probably given by both light-intensity and magnetic-field fluctuations. An accurate analysis of the possible sources of noise in our Raman setup is currently in progress (see the last paragraph of this section).

Local addressability of Raman spectroscopy. One of the advantages of Raman spectroscopy is that the atomic sample can be addressed locally with great precision. This is possible thanks to the control of the pointing and beam waist size that one can have on the laser beam. This feature, when combined with in-situ imaging of the cloud along the gravity direction, allows for the study of the local properties of the sample. However, in such a situation, the extraction of the typical properties of the cloud requires a local analysis of the pictures. This is due to the finite size of the optical gaussian Raman beam, which can be tuned to be either larger or smaller than the size of the atomic cloud. A global gaussian fit is only possible if the size of the Raman beam σ_R is larger or comparable to the size of the Cs cloud σ_{Cs}. An example of the consequences of this is given in Fig. 3.15. The plots illustrate the integrated optical density, normalized to its peak value, resulting in a one-dimensional column along the longitudinal direction of the cloud. This quantity is displayed over time by varying the pulse length τ of the two-photon Raman beams. In the case $\sigma_R \ll \sigma_{Cs}$, the optical density is completely perturbed by the Raman beam with respect to the case $\sigma_R \sim \sigma_{Cs}$. This kind of measurement demonstrated also that we can achieve Rabi frequencies up to 65.1(2) kHz, which have bean measured at the centre of the cloud.

The local analysis behind this kind of images is conducted as follows[9]: (i) A small portion of the absorption picture is selected, typically a box measuring approximately

---

[8] This model was chosen to interpret the change in contrast over time by trying to give a physical interpretation to the coefficient before the sinc function. Since magnetic field instability could have affected the measurement, the detuning could have changed and determined the change in contrast. A more sophisticated modeling of the process should be based on a deeper investigation of the processes that limit the reproducibility of Raman oscillation, as discussed at the end of this paragraph.

[9] The script for the local analysis of the images has been developed by Tobias Krom and Michael Rautenberg.

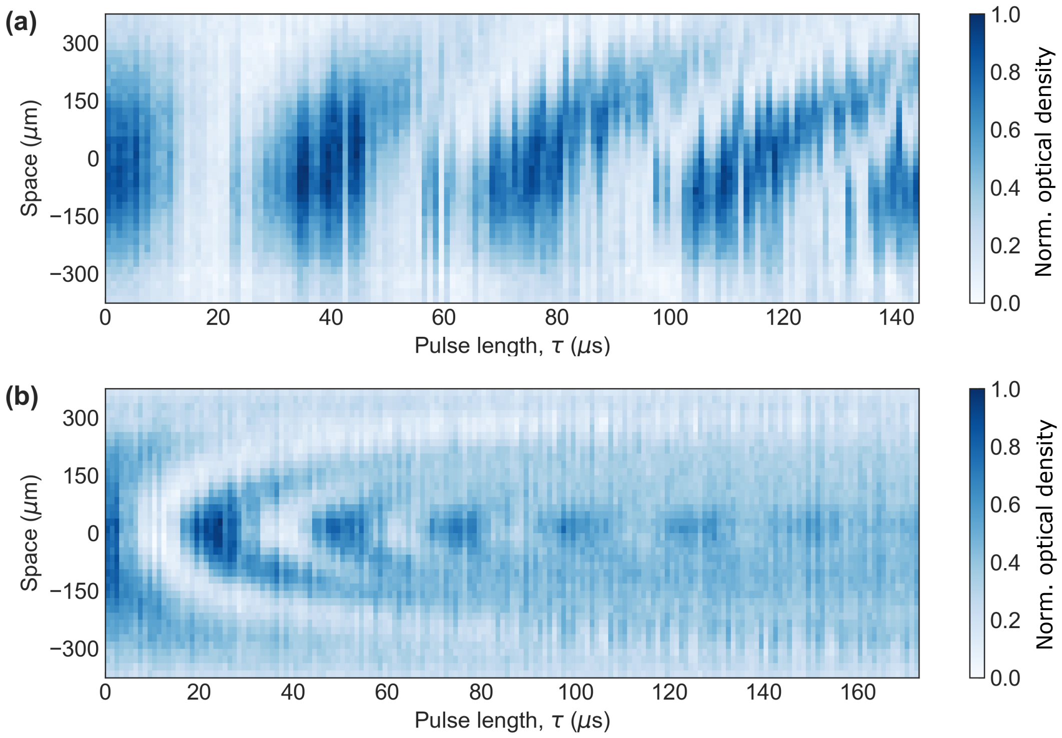

FIGURE 3.15: Effect of the finite size of the Raman beam on the spatially resolved Rabi oscillations. The plots show the integrated optical density, resulting in a one-dimensional column along the longitudinal direction of the cloud, displayed over time by varying the pulse length τ of the two-photon Raman beams. Examples of the optical density map are given for two different situations: (a) the size of the Raman beam σ_R is comparable to the size of the Cs cloud σ_{Cs}, (b) $\sigma_R \ll \sigma_{Cs}$.

800 μm × 70 μm, centered on the cloud's center and tilted at the same angle as the cloud. (ii) This box is divided into strips along the axial direction. Typically, there are 40 stripes with a width of 20 μm each. The sum over pixels is carried out along the short direction, resulting in a column density along the longitudinal direction of the cloud of 40 boxes 800 μm long. It is however to mention that by doing absorption imaging one naturally integrates over one direction. The optical density in Fig. 3.15 is displayed over time. This methodology allows for the extraction of local Rabi oscillations. The same procedure is employed for the extraction of the spectra (optical density over frequency).

Stability and reproducibility of Rabi oscillations. Our observations revealed fluctuations in the magnetic fields on a daily basis, accompanied by variations in the decay rates of Rabi oscillations. It is crucial to acknowledge that ongoing efforts are being made to enhance the stability and reliability of Rabi oscillations at low frequencies, which are essential for achieving a precise spectral response. A preliminary study can be found in Welz [2024]. Here, I will just summarize our findings, which however still require to be further studied.

- To rule out the possibility that a 50 Hz noise is caused by the power supply, the experimental cycles were synchronized to a 50 Hz signal. This ensured that each cycle commenced at the same moment in time as the signal. Consequently, magnetic-field fluctuations were consistent across each cycle and added the same noise, regardless of the length of the Raman pulse. However, to ensure that the phase evolution is continuous and the Rabi oscillations are coherent, the magnetic field should be stable on the order of ~ 10 mG.

- The measured one-photon cross-sections do not align with the predicted values. The observed damping is believed to arise from light fields resonantly interacting with the atoms. This light source could be identified in the noise floor of the laser, which is several decibels less intense than the peak of the laser's spectrum.
- When tuning the linearly and circularly polarized laser beam to match the one- and two-photon detuning, it is also necessary to consider the Stark shifts that the couplings induce to the levels [Steck, 2024]. The resulting two-photon Stark-shift for our mixture is given by $\Delta\delta_{\text{Stark}} = -2\pi \cdot 12.1\ \text{kHz}/(\text{kW}/\text{m}^2) \cdot \Delta I$, where ΔI is the mean intensity fluctuation in a certain time period. For typical fluctuations ΔI of $1.7\ \text{kW}\,\text{m}^{-2}$, the frequency variation induced by the Stark shifts is $\Delta\delta_{\text{Stark}} = -2\pi \cdot 20.6$ kHz [Welz, 2024]. It is evident that intensity fluctuations play a critical role in maintaining the stability of the measurements as even a minor variation can result in the two-photon transition becoming out of resonance.

3.3 Ejection spectroscopy on Cs atoms in a Li-Fermi Sea

We performed Raman spectroscopy on a dilute Cs sample interacting with a polarized Fermi Sea of Li atoms. The basic measurement procedure is shown in Fig. 3.16. We initially prepare the mixture in the interacting channel in the unitarity regime close to 888.6 G Li-Cs Feshbach resonance between Li$|2\rangle$ and Cs$|1\rangle$. Signatures of the polaron are expected to be frequency (energy) shifted from the bare atomic transition of the Cs impurities. The spectral response of Cs impurities is studied by spectroscopically probing the energy of the two lowest Zeeman states Cs$|1\rangle$ and Cs$|2\rangle$ via Raman spectroscopy. The two Raman beams transfer the atoms from the state Cs$|1\rangle$ to the state Cs$|2\rangle$ which is initially unoccupied. The measurements are performed by recording the atoms left in the Cs$|1\rangle$ state after the quench as a function of the detuning $\delta = \omega - \omega_0$, where $\omega = \omega_1 - \omega_2$ and ω_0 corresponds to the bare transition energy between states Cs$|1\rangle$ and Cs$|2\rangle$.

To observe the polaron, the following hierarchy of timescales should be fulfilled:

$$\tau_{loss} \gg \tau_{pulse} \gg \tau_{pol}, \tag{3.35}$$

where τ_{loss} is the lifetime of the gas in the trap, τ_{pulse} is the pulse length of the Raman spectroscopy, and τ_{pol} is the timescale of the polaron. The polaron is expected to exhibit an energy shift E_{pol} relative to the free-free transition E_0, which is determined by the Fermi energy E_F. Therefore, the timescale is given by $\tau_{pol} \sim \hbar/E_F$. Due to the Fourier limit, the pulse length must significantly exceed the polaron's timescale as discussed in Sec. 3.2.2.

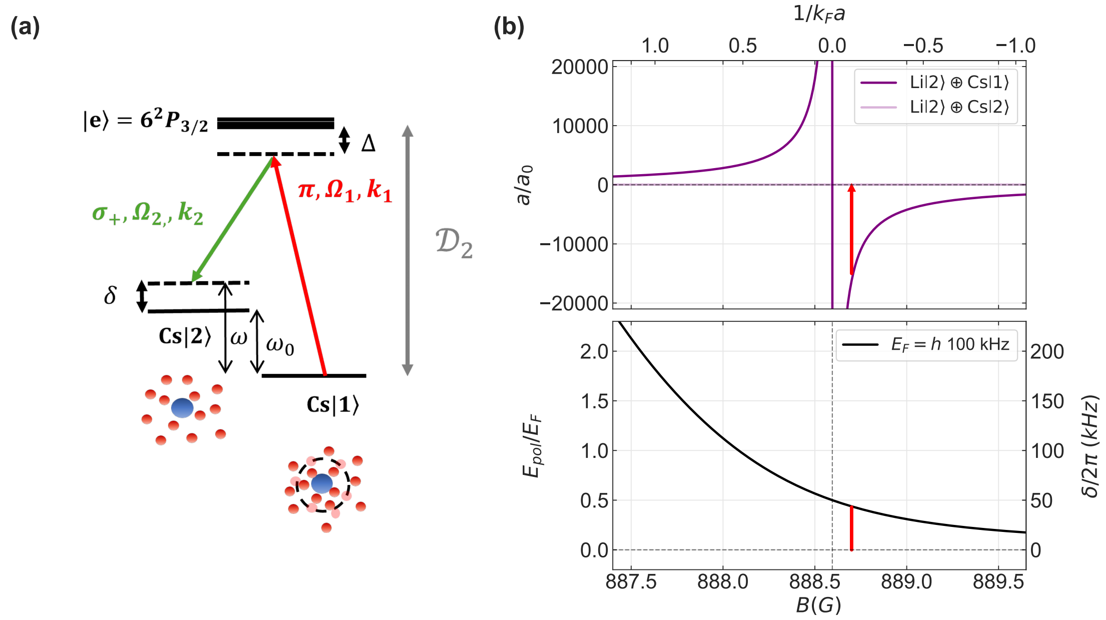

FIGURE 3.16: Sketch of the basic measurement procedure of a two-photon Raman ejection spectroscopy on Cs atoms in presence of a Li Fermi Sea close to the Li-Cs Feshbach resonance at 888.6 G. In (a) a schematic of the energy levels involved in the Raman scheme is shown. The energy difference in absence of a surrounding bath is $\hbar\omega_0$. The two-photon Raman pulse transfers the atoms from the Cs$|1\rangle$ state to the initially unoccupied Cs$|2\rangle$ state. In presence of the Li Fermi Sea, the atoms in the Cs$|1\rangle$ state strongly couple to the surrounding bath forming a polaron. By varying the frequency ω and recording the number of atoms left in the Cs$|1\rangle$ after the quench, it is possible to determine the polaron energy shift $E_{pol} = \hbar\delta$. In (b) the scattering length in the interacting channel Li$|2\rangle\oplus$Cs$|1\rangle$ and in the non-interacting channel Li$|2\rangle\oplus$Cs$|2\rangle$ (upper row) is shown together with the energy shift that is approximately expected for a Fermi energy of $E_F \sim h\times$ 100 kHz corresponding to the channel Li$|2\rangle\oplus$Cs$|1\rangle$ (lower row).

We estimated τ_{loss} by the shortest timescales defined by one-, two-, and three-body losses. Inter- and intraspecies three-body losses define the timescales $1/(L_3 n_{Cs}^2)$, $1/(L_3 n_{Cs} n_{Li})$, and $1/(L_3^{Cs} n_{Cs}^2)$ with Cs in the ground state, Cs$|1\rangle$. We consider the magnetic field and temperature-dependent three-body loss rate obtained in Sec. 2.3.2. Moreover, since the final state of the ejection scheme is the Cs$|2\rangle$ state, the two-body timescales $1/(k_{2,in}^{LiCs} n_{Li})$, $1/(k_{2,in}^{Cs_{2,2}} n_{Cs})$, and $1/(k_{2,in}^{Cs_{1,2}} n_{Cs})$ discussed in Sec. 3.2.1 should also be considered. It is important to note that all timescales associated with three- and two-body losses depend strongly on the magnetic field and atomic densities of both species. However, the lifetime of the gas in the trap is dominated, for most of the experimental settings, by light-induced losses by the tune-out trap as obtained in Sec. 2.3.1.

In Sec. 3.3.1 I will show typical results obtained for the ejection spectroscopy protocol on a Li-Cs mixture and in Sec. 3.3.2 I will discuss the limitations of our system.

3.3.1 Energy spectrum and Rabi oscillations

In the following I will present the experimental preparation, the typical analysis and the results obtained for the ejection spectroscopy protocol on a Li-Cs mixture.

Experimental preparation. For the specific measurement shown here, we prepared an ultracold mixture of 2×10^4 Li atoms in the state $\mathrm{Li}|2\rangle$ and 1×10^4 Cs atoms in the state $\mathrm{Cs}|1\rangle$ at a temperature of 1.5 μK. We estimate atomic peak densities of $n_{0,Li} = 1.4 \times 10^{13}\,\mathrm{cm}^{-3}$ and $n_{0,Cs} = 1.0 \times 10^{11}\,\mathrm{cm}^{-3}$ from which we obtain the Fermi wavevector $k_F^{-1} \simeq 1700\,\mathrm{a}_0$ and a Fermi energy of $E_F = h \times 100$ kHz. From the polylogarithmic fit of the Li cloud we extract a global $T/T_F \approx 0.3$[10]. Furthermore, the impurity density is almost two orders of magnitude smaller than that of the fermions $n_{Cs}/n_{Li} \approx 0.01$, which allows neglecting interactions between them at such low impurity concentrations. We choose a magnetic field of 888.7 G, which is slightly above the Feshbach resonance position corresponding to an interspecies scattering length of $a_{\mathrm{LiCs}} \approx -13000\,\mathrm{a}_0$. We obtain the dimensionless interaction parameter $1/(k_F a_{\mathrm{LiCs}}) \approx -0.13$. For this scattering length and atomic densities we estimate a lifetime of $\tau_{loss} \approx 600$ ms and expect a polaron energy of roughly $E_{pol} \approx 0.5 \times E_F = h \times 50$ kHz (see Fig. 3.16). Thus, we set the pulse length to $\tau_{pulse} = 34.0\,\mu$s, which corresponds to a π-pulse on the bare atomic transition that fulfills the relation $\tau_{loss} > \tau_{pulse} > \tau_{pol} \approx 20\,\mu$s.

In order to find the correct parameters, we first probe Rabi oscillations on resonance by applying Raman laser pulses at fixed frequency but variable pulse length to identify the Rabi frequency relevant to our scheme. Once the bare impurity regime has been mapped out, we perform Rabi-type spectroscopy on Cs in presence of the Li clouds and at the chosen magnetic field offset. In this setting, we apply Raman laser pulses with a fixed duration corresponding to a Rabi π pulse and vary the frequency detuning between the two laser beams to identify the polaron regime. The measurements were configured to ensure comparability between the scenario with and without Li. Therefore, for each frequency, the first experimental run included Li, followed by a subsequent run without Li.

We perform double absorption imaging at 890 G on both $\mathrm{Li}|2\rangle$ and $\mathrm{Cs}|1\rangle$[11] along the gravity direction. Therefore, we take a picture of $\mathrm{Li}|2\rangle$ and $\mathrm{Cs}|1\rangle$ during the same experimental cycle with a time delay of 1.5 ms: the first is Li, whose imaging is done in-situ; the second is Cs, which acquires a small time of flight.

---

[10] The local T/T_F is expected to be higher than this, but hard to access for our system (as explained later). Moreover, as mentioned at the end of Sec.2.4, for recent sets of measurement taken with the Andor camera, as those presented here, we found later on a discrepancy with respect to the global T/T_F extracted from trapping frequencies. For the presented measurement this would be rather on the order of 0.6, which would lead to a Fermi energy of 45 kHz and then to an expected polaron shift of 22.5 kHz.

[11] Our imaging scheme, as explained in Sec. 1.5.2, does not allow doing imaging of the $\mathrm{Cs}|2\rangle$.

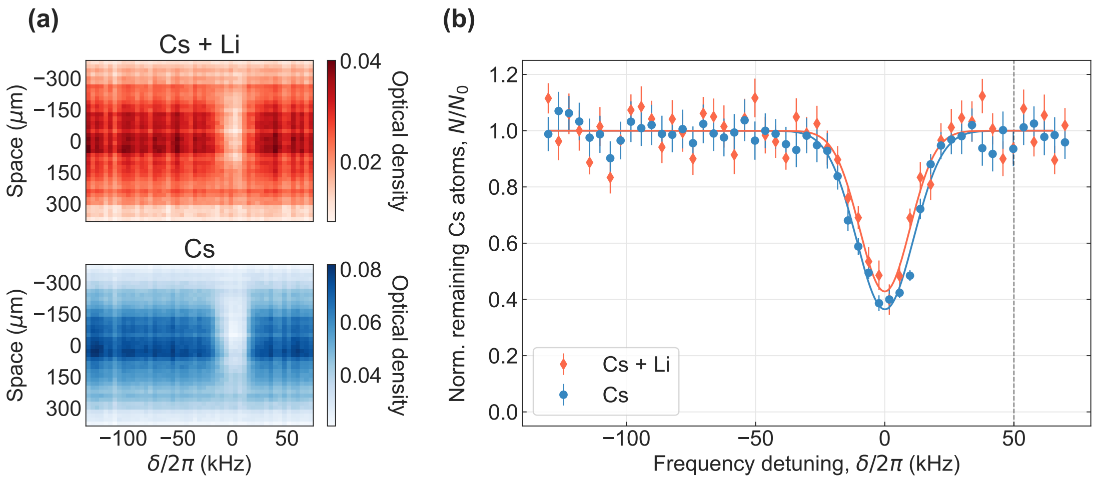

FIGURE 3.17: Population of Cs atoms remaining in Cs$|1\rangle$ after a π-pulse of length $\tau_{pulse} = 34.0\ \mu$s via Raman spectroscopy at unitarity, with B = 888.7 G. (a) Colour maps of the optical density (OD) of the Cs cloud, resolved in space as a function of the detuning $\delta = \omega - \omega_0$. Measurement with Cs superimposed to a Li Fermi sea at a $T/T_F \approx 0.3$ (top, red); measurement with a gas of pure Cs (bottom, blue). (b) Normalized remaining fraction of Cs atoms in the Cs$|1\rangle$ state, embedded in a Li Fermi Sea (red) or in a gas of pure Cs (blue). These data are the results of averaging in a region of $\pm 50\ \mu$m around the center of the cloud. The bare energy is given by $\omega_0 = 2\pi \times 262.6303(4)$ MHz, which is extracted by a gaussian fit to the data from a gas of pure Cs. The dashed line at 50 kHz marks the position at which we would have expected to observe the polaron peak.

Local analysis due to limited Li-Cs overlap. Absorption imaging is performed along the gravity direction, therefore integrating the signal in one of the three spatial directions. A local analysis is necessary for two reasons. First, since our sample is harmonically trapped, its spatial density distribution is not homogeneous. Hence, since the interatomic interactions is Li density-dependent, the spectral response is not constant across the cloud. Indeed, the Li-Cs interactions are parameterized by using the interaction parameter $1/(k_F a_{LiCs})$, which depends on the Li atomic density and on the magnetic field. Second, as already shown in Fig. 3.15, the gaussian shape of the Raman beams identifies a finite region of overlap with the Cs cloud, and the spectral response is not constant along the cloud in the region of the probe.

In order to reduce both effects we extract the spectroscopy signal only from the central part of the integrated density. We use typical box of sizes of $\sim 200\ \mu$m $\times$ $20\ \mu$m. These sizes are adapted depending on the size of the Raman beam and the relative position of the Li cloud. We then sum over the shortest direction ending up in one column of optical density along the axial direction of the cloud. We display this optical density column over the variable we are scanning (either time or frequency).

Energy spectrum. We obtain energy spectra by recording the population of the Cs atoms in the initially occupied and interacting Cs$|1\rangle$ state as a function of the frequency difference of the Raman beams. We apply a local density analysis as described in the previous paragraph. Moreover, since we cannot do imaging on the state where the impurities are transferred to and calculate the transfer ratio, we measure Cs$|1\rangle$ with and without Li atoms in two subsequent experimental runs. This is equivalent to having a measurement for both interacting and non-interacting samples [12]. Since the absolute total atom number is largely different due to not negligible three-body losses in the unitarity regime, the normalization N_0 of each measurement refers to the average over a certain range of frequencies far from the bare transition, where the transfer to other states is negligible. Therefore, from now on we will always consider the normalized atom number N/N_0. The obtained spectra are shown in Fig. 3.17. At the frequency $E_0/h = 262.6303(4)$ MHz of the Cs spin-flip transition, we transfer the Cs atoms from the interacting state Cs$|1\rangle$ to the non-interacting state Cs$|2\rangle$. Thus, we observe a minimum in the fractional population of the Cs$|1\rangle$ state at a frequency that corresponds to the bare transition recorded in absence of the Li Fermi Sea. We do not notice any depletion of the population in the state Cs$|1\rangle$ close to the expected polaron energy $E_{\text{pol}} \approx 0.5 \times E_F = h \times 50$ kHz. By using a gaussian fit, we determine a shift of (56.0 ± 0.9) Hz with respect to the bare transition. The reduction of 10% in width and amplitude of the normalized atom number calculated from the two fitted functions might be a signature of a small depletion of the bare transition in favour of populating another state. Experiments performed at different magnetic fields, i.e. different scattering length a_{LiCs}, pulse-length τ_{pulse}, Raman frequency Ω_R of the two-photon pulse and different global temperatures, did not reveal any clear signatures of polarons so far. However, some of these experiments show a reduction in width and amplitude of the signal at the bare transition frequency similarly to the one presented here. Thus, it remains an open question why the Fermi polaron was not observed in the Li-Cs system. I discuss possible reasons in Sec. 3.3.2 and suggest several prospects towards its observation in Sec. 3.4.

Rabi oscillations. Despite energy spectra and Rabi oscillation measurement providing similar information, the latter method is typically more resistant to noise. If the reduction of the signal observed in Fig. 3.17 is due to the presence of the polaron, then we would expect to observe a change in the Rabi frequency. Since the Rabi polaron energy differs from the bare Rabi frequency, if the polaron is there, we would have expected to measure frequencies different from the bare and to observe a reduction in the contrast of the oscillations. We drive Rabi oscillations on the two Cs impurity states in presence of the fermionic medium. The experimental conditions are similar to those of the previous measurement. We set a detuning between the Raman beams corresponding to the bare transition frequency ω_0 between Cs$|1\rangle$ and Cs$|2\rangle$, and then vary the pulse length. As before, to ensure comparability between the measurement with and without Li, we conduct each experimental routine with Li first, followed by the same routine without Li for each scan parameter. The obtained Rabi oscillations for a typical measurement of this kind are presented in Fig. 3.18 and the analysis procedure is similar to the one described for spectroscopic measurements. The fractional residual atoms are fitted with a function

---

[12] It is valid in the assumption that the final state is completely non-interacting, which is true in our case where $a_{LiCs2} \sim 30a_0$.

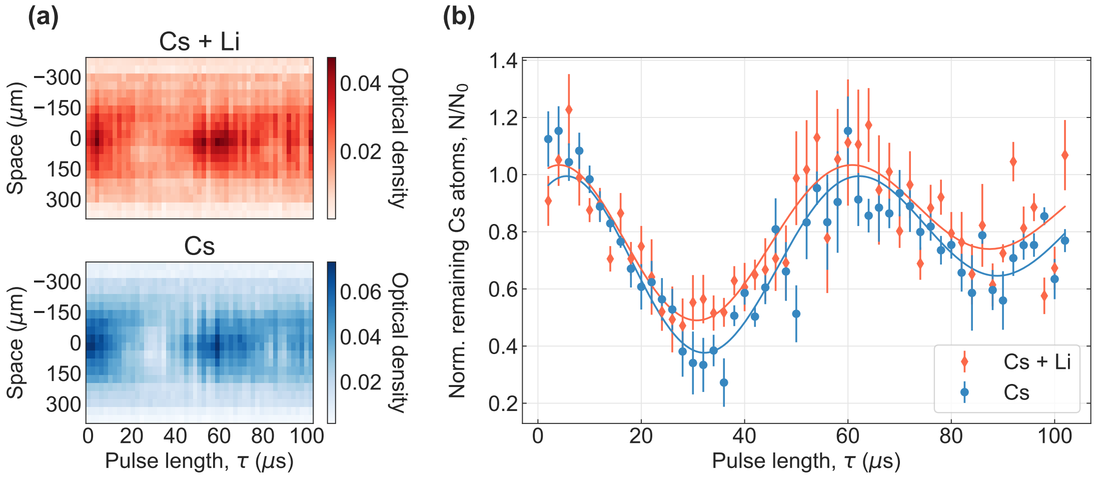

FIGURE 3.18: Time evolution of the remaining Cs atoms fraction in the Cs$|1\rangle$ in presence of Li$|2\rangle$, at unitarity, with $B = 888.7$ G at the bare frequency ω_0. (a) Colour maps of the evolution in the optical density of the Cs cloud, resolved in space over time: on top, it is shown the measurement with Cs superimposed to a Li Fermi sea at a $T/T_F \approx 0.3$, while on the bottom, a gas of pure Cs. (b) Normalized remaining fraction of Cs atoms in the Cs$|1\rangle$ state, embedded in a Li Fermi Sea (red) or in a gas of pure Cs (blue). These data are the results of the average in a region of $\pm$ 50 μm around the center of the cloud.

given by Eq. 3.34, at which we add a small time offset in the pulse length. The measured Rabi frequency results to be (12.5 ± 1.6) kHz with Li and (14.4 ± 1.3) kHz without. The remaining detuning has been estimated to be (12.4 ± 1.4) kHz with and (10.1 ± 1.7) kHz without Li. The decay rate is for both about 10 ms^{-1} and the time offset of around 5 μs. The contrast between the excitation amplitudes is about 0.87. It should be noted that in the data analysis process, averaging over a smaller region centered on the Cs cloud provides more signal coming from the region of interaction with Li, but it is also more noisy.

Even if we did not reveal any signatures of the polaron, this approach is particularly interesting. The coherent drive of Rabi oscillations between the two impurity states is a powerful tool for probing the quasi-particle weight Z. The weight Z is directly related to the Rabi frequency Ω normalized to the bare Rabi frequency [Kohstall *et al.*, 2012] and $\sqrt{Z}$ essentially quantifies the wavefunction overlap between the polaron state and the bare non-interacting impurity. Hence, $Z \simeq (\Omega_p^2 + \Gamma^2)/\Omega_0^2$ as long as $\Gamma \leq \sqrt{Z}\Omega_0$, where Γ is the decay rate [Kohstall *et al.*, 2012; Adlong *et al.*, 2020], and it reduces to $Z \approx \Omega_p^2/\Omega_0^2$ for very small Γ. This method has been proven both theoretically [Parish and Levinsen, 2016; Adlong *et al.*, 2020, 2021] and experimentally for the mixtures of ^{40}K-^{6}Li [Kohstall *et al.*, 2012], of two different spin states of ^{6}Li [Scazza *et al.*, 2017] and of two different spin states of ^{173}Yb [Darkwah Oppong *et al.*, 2019].

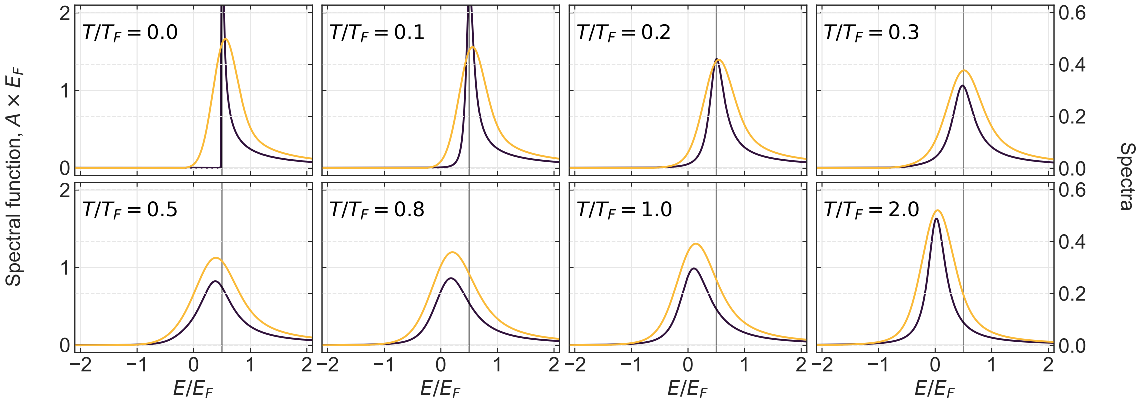

FIGURE 3.19: Ejection spectral function at unitarity for different T/T_F (in dark blue) and spectra (in yellow) obtained considering the convolution of the ejection spectral function with a gaussian probe with a finite width of $\Delta E = 0.2 \times E_F$. The ejection spectra are obtained as in Sec. 3.1.2. The solid vertical line at $E/E_F = 0.5$ marks the positions of the polaron peak in the limit of $T = 0$. These graphs are adapted from data obtained with FDA calculations provided by Moritz Drescher (permission granted) [Drescher *et al.*, 2024].

3.3.2 Limitations for finite temperature and overlap

In comparison to the observations for the mixtures of ^{40}K-^{6}Li [Kohstall *et al.*, 2012] and of different hyperfine spin states of ^{6}Li [Schirotzek *et al.*, 2009; Scazza *et al.*, 2017], we expect a smaller polaron energy shift due to the large mass imbalance between the impurity and the fermionic medium, as explained in Sec. 3.1.1. Moreover, in those experiments, the size of the atomic cloud of the minority species along the direction of imaging is much smaller compared to the size of the cloud of the bath. In our case, instead, the size of the Cs cloud along the direction of imaging is approximately two times as big as the size of the Li cloud and therefore a large part of the detected signal comes from Cs atoms, which are not interacting with Li atoms. Those atoms, when addressed by the spectroscopic pulse, undergo the bare transition and populate the bare state.

Another crucial point concerns the temperature of the Li cloud and the detection of the signal. A study of the temperature dependence of the polaron for an equal mass system in a homogeneous confinement shows that the polaron peak survives until $T/T_F \approx 0.75$ [Yan *et al.*, 2019]. However, in the case of a large mass imbalance, we expect the highest temperature at which one can resolve the polaron energy to shift at much lower values [Hu and Liu, 2022; Liu *et al.*, 2020]. In addition, the harmonic confinement always requires a local analysis in all three dimensions. As the size of the Cs cloud along the imaging direction is twice that of the Li cloud, a local analysis in two-dimension, as we currently do, is not enough since the signal along the direction of imaging is naturally integrated. Since the Fermi temperature T_F depends on the Li spatial density distribution $n_{Li}(r)$, being not able to determine the local Fermi temperature leads to an averaged polaron peak. Another evident limitation is given by the pulse length used for the spectroscopy. We tried to use longer pulses, but we did not manage to reach the full contrast in the Rabi oscillations, even without Li atoms. To aid our understanding, I will discuss these aforementioned arguments using a qualitative model divided in three steps.

1. As a first step, we perform a convolution between the discretized energy ejection spectrum $A(E_i)$, as obtained by FDA in Sec. 3.1.2, and a gaussian probe $g(E_i - E_0) = e^{-(E_i-E_0)^2/(2\Delta E^2)}/\Delta E\sqrt{2\pi}$ with a finite energy width of $\Delta E = 0.2 \times E_F$ as follows
$$(A * g)(E_0) = \sum_i^N A(E_i) g(E_i - E_0) \Delta E_{step} \tag{3.36}$$
with a finite step-size ΔE_{step} set by the discretization of the FDA data, and E_i such that $i = [1, N]$. This gives the experimentally relevant energy-averaged spectra for different T/T_F, which are shown in Fig. 3.19. We observe a nearly constant broadening of the response regardless of the temperature ratio T/T_F.

2. In a second step, we add the hypothesis of partial spatial overlap between the two clouds along the imaging direction by introducing the following simplified model. We consider that only half of the population in the initially occupied Cs$|1\rangle$ state can interact with Li atoms and form a polaron. Therefore, half of the population contributes to the polaron energy shift, while the other half will undergo the standard bare transition. The total energy spectra are given by the sum of these two individual contributions, one centered on the bare energy transition and the other centered on the expected polaron energy. The energy spectra for different T/T_F are shown in Fig. 3.20. We observe that the polaron peak does not emerge clearly for any global T/T_F here shown. The contribution of the bare transition and the large broadening of our probe are already sufficient to prevent the observation of the polaron peak. For the particular case of $T/T_F = 0.3$ one could detect the polaron contribution from the tail of the signal. This situation becomes even worst by decreasing the pulse length or reducing the amount of Cs atoms interacting with Li.

3. However, a third step is necessary to reproduce our real situation. Indeed, as previously mentioned, atoms are trapped in a harmonic confinement and therefore the T_F, which is given by $T_F = \hbar^2(6\pi^2 n_{Li}(r))^{2/3}/(2mk_B)$, depends locally on the atomic density $n_{Li}(r)$, which is not constant along the direction of imaging. What we measure is a signal that is integrated over several different T_F, which leads to smearing the polaron peak. It is therefore necessary to calculate the total energy spectra by weighting each local spectral function with the contribution associated with the local T_F. However, this would simply contribute to a worsening of the signal expected from the second step.

Although the polaron signal may have been washed out in this complex scenario, pressure broadening in the spectroscopic response due to thermal collisions with Li atoms could still be observed [Baranger, 1958a,b]. The reason why we do not observe this phenomenon is likely due to two factors. Firstly, our signal is not Fourier limited. Secondly,

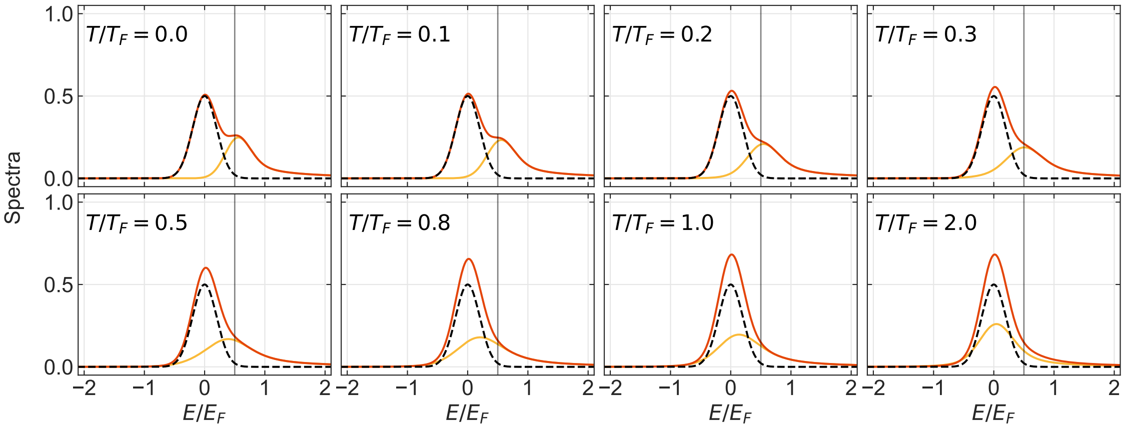

FIGURE 3.20: Total energy spectra at unitarity for different T/T_F for Cs population distributed 50:50 between the bare (black-dashed line) and the polaron state (yellow solid line). The probability distribution to undergo a polaron transition is obtained by considering a gaussian probe with a finite width of $\Delta E = 0.2 \times E_F$ as shown in Fig. 3.19. In red, the total probability resulting from the sum of the yellow and black-dashed curve. These graphs are adapted from data obtained with FDA calculations provided by Moritz Drescher (permission granted) [Drescher *et al.*, 2024].

the large mass ratio between Cs and Li atoms results in Cs experiencing a very small recoil energy, making this source of broadening negligible.

A further relevant constraint is given by the Cs losses induced by the microtrap light, discussed in detail in Sec. 2.3.1. The timescale associated with spin exchange processes from Cs$|3, +3\rangle$ to Cs$|4, +4\rangle$ averaged over the volume of overlap between the microtrap potential and the Cs cloud are large compared to the typical timescale for the polaron experiment discussed in Sec. 3.3. Nevertheless, the local losses at the center of the microtrap occur much faster and could empty the Cs$|1\rangle$ state before the Cs and Li clouds are fully overlapped (see Sec. 2.2).

In conclusion, there could be multiple reasons why the Fermi polaron was not observed. The most probable ones are related to a not optimal detection of the signal, such as spectroscopic pulse too short or signal coming from a Cs atoms non-interacting with Li, and to light induced Cs losses at the Cs tune-out wavelength. However, a more effective thermometry would also aid in understanding if our limitation is rather an incorrect determination of the global T/T_F of the cloud in such a scheme. Therefore, changes to our experimental setup and procedure are necessary to observe the Fermi polaron.

3.4 Towards the Fermi polaron in Li-Cs mixtures

In Sec. 3.4.1 several changes in the experimental setup are proposed. Afterwards, in Sec. 3.4.2, further directions of few- and many-body physics in the Li-Cs system are presented.

3.4.1 Upgrade of the experimental setup

The Fermi polaron has not been observed in our experiment so far and, therefore, we suggest the following improvements in order to experimentally study the Fermi polaron.

Local detection of Cs atoms interacting with Li: upgrade of the imaging scheme. In order to gain experimental access to the polaron signal, we plan to upgrade our imaging scheme. Conventional imaging techniques allow for spatial selection of a certain target area just in two spatial directions, while data relative to the third spatial direction cannot be directly acquired or post-selected. To circumvent this limitation, we propose to implement a thin light sheet, propagating perpendicularly to the imaging direction. The frequency of this light sheet is tuned to be resonant with the transition on which we optically pump Cs atoms from their ground state to an excited state for subsequent imaging. The implementation of an optical sheet of only a few μm thickness, will allow us to probe selectively the impurities in the central region of the Cs cloud, where the surrounding medium's density is relatively constant and defines a unique Fermi temperature.

Coherent Rabi oscillations: upgrade the spectroscopy scheme. For achieving coherent Rabi oscillations using Raman spectroscopy, we need to prioritize the stabilization of the magnetic field offset and laser intensities, especially on timescales of $\sim 100\ \mu$s. It is important to establish whether the limitations described in Sec. 3.2.2 and Sec. 3.3 arise solely from magnetic field or laser intensity fluctuations, or if there are other factors not considered yet which constrain the coherence of the Rabi oscillations. This extensive investigation is necessary to refine the methods for reliably driving Rabi oscillations in our experiment.

Spatial overlap and reduced Cs losses: implementation of alternative trapping schemes. Two schemes are suitable for ensuring a very dilute Cs cloud confined at the center of a degenerate spin-polarized Li Fermi Sea while avoiding undesired losses caused at the Cs tune-out wavelength.

A first approach proposes a monochromatic confinement for both species, mimicking the scheme used previously in our experiment to create mixtures of non-degenerate gases at temperatures as low as 200 nK, as reported in Repp *et al.* [2013], Pires *et al.* [2014b], Ulmanis *et al.* [2016b] and Zhu *et al.* [2019b]. The single optical trapping potential at 1070 nm would naturally create smaller sizes for the Cs cloud than for Li. However, pure optical trapping would not allow compensating for the differential gravitational sag between the two species, in particular at temperatures where Li is deeply degenerate. To overcome this issue, it is necessary to combine optical and magnetic trapping using a magnetic field gradient. The implementation of a setup to produce anti-levitation magnetic fields for both species is reported in Freund [2019] and a measurement which shows the effective possibility to create negative gradients can be found in Appendix A. This scheme creates a gradient that pushes both Li and Cs down along the direction of gravity, with a more pronounced effect for Li. This would enable us to fully overlap Li and Cs in the same optical potential independently from the temperature of the mixture.

The second approach, instead, involves the usage of a bichromatic trapping scheme similar to the one implemented in this thesis work. In order to increase the time for which Li and Cs atoms can be trapped together, and to allow both thermalization and sympathetic cooling between the two species, we propose to shift the wavelength of the movable Li trap away from the Cs tune-out wavelength, while maintaining the concept of a movable Li trap. The broadly tunable Ti:Sa laser wavelengths should be tuned to around 700 nm. As Li has a much higher polarizability than Cs at those wavelengths, we can use very low power, resulting in a negligible repulsive potential for Cs. A high power single mode and highly stable laser would be used as source for the final Cs trap. This would consist of two 30 μm beams crossing at an angle of 90°. The size of the trapping beams for Cs is chosen to ensure spatial overlap of Li and Cs down to temperatures of a few hundreds of nK.

3.4.2 Future polaron experiments

Besides mapping the energy polaron spectrum as a function of the interaction parameter and of the temperature, the Li-Cs system is well-suited for investigating many-body phenomena of broader interest because it naturally simulates an immobile pinhead surrounded by light particles. I will give here an overview on possible future experiments that we could realize thanks to the experimental upgrade described in Sec. 3.4.1 and after a first signature of the Fermi polaron will be observed in our mixture.

Polaron to molecule transition at finite temperature in the heavy mass limit. The polaron to molecule transition remains still largely experimentally unexplored, particularly in mixtures with heavy impurities. Similarly to the study conducted by Ness *et al.* [2020], mentioned in Sec. 3.2.2, ejection Raman spectroscopy can be used to distinguish between the polaronic and the molecular contributions to the energy spectra. Mapping out the polaron energy and the quasi-particle weight of the polaron over both the interaction parameter, the temperature and the degree of degeneracy expressed as T/T_F in a Li-Cs mixture would provide a comprehensive overview of the critical behaviour in the heavy impurity limit. For example, for interaction parameters larger than the critical value $1/(k_F a_c)$, one could extract the temperature at which the dressed dimer and polaron begin to separate. However, as shown in Fig. 3.21, ejection spectroscopy allows only for detection of the ground state.

Probing the full excitation spectrum of a dressed dimer. A dressed dimer at interaction parameters below the critical value, i.e. when it corresponds to the first excited state of the system, has not yet been observed experimentally. Diessel *et al.* [2024] proposes a novel protocol to create a dressed dimer (named "molaron") on demand and to probe its full excitation spectrum. This scheme employs Raman injection spectroscopy and requires driving transitions between a bound-state (pre-formed tightly-bound dimer) and

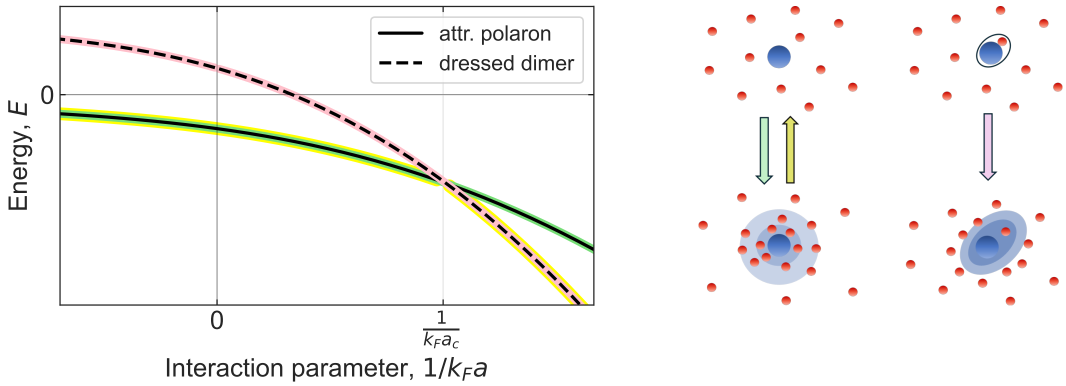

FIGURE 3.21: Scheme for probing the polaron (solid line) to molecule (dashed line) transition. The different colors indicate the kind of spectroscopy that can be used to probe either the polaron or the dressed dimer. Injection spectroscopy (green) allows for probing the polaron. Ejection spectroscopy (yellow) allows the detection of the full ground state, which corresponds to the polaron for $(k_F a)^{-1} < (k_F a_c)^{-1}$ and to the dressed dimer for $(k_F a)^{-1} > (k_F a_c)^{-1}$. The protocol proposed in [Diessel *et al.*, 2024], which proposes the injection of a tightly bound dimer in a dressed dimer (pink), would allow probing the full excitation spectrum of a dressed dimer, even for $(k_F a)^{-1} < (k_F a_c)^{-1}$ where neither of the other two protocols can work. This picture is inspired by [Diessel *et al.*, 2024].

another bound-state (dressed dimer), as shown in Fig. 3.21. This scenario necessitates using two interspecies Feshbach resonances where the initial dimer state has sufficient spectroscopic overlap with the final dressed dimer state. One resonance is used to create the dimer, and the other to inject the dimer into the dressed state.

Unfortunately, using two hyperfine states of Cs might be problematic since the pairs of Li-Cs Feshbach resonances available with Cs in different hyperfine states would not work. This is due to either insufficient overlap or inelastic spin decay in the final state, which would broaden the lines and cover the interesting many-body phenomena[13].

An alternative might be to use the hyperfine transitions between the hyperfine states of Li. The experimental procedure would consist of starting with the mixture of $\mathrm{Li}|2\rangle$ and $\mathrm{Cs}|1\rangle$ and use the Feshbach resonance at 888.6 G for preparing the tightly-bound dimer. Then, transfer all free Li atoms remaining into $\mathrm{Li}|1\rangle$. If this is done ideally, it would lead to a bath of $\mathrm{Li}|1\rangle$ plus dimers. Subsequently, jump to 843 G, where the bath is strongly interacting with $\mathrm{Cs}|1\rangle$ and transfer the tightly-bound dimer to the dressed-dimer state with the Raman protocol. In our existing setup this could be done with a

---

[13] We had taken into account the possibility to use the Feshbach resonance at 943.3 G between $\mathrm{Li}|2\rangle \oplus \mathrm{Cs}|1\rangle$ for pre-forming the molecule and the one at 941.6 G between $\mathrm{Li}|2\rangle \oplus \mathrm{Cs}|2\rangle$ for injecting the dimer into a dressed dimer. The resonance at 943.3 G is characterized by $s_{\mathrm{res}} \leq 0.03$ [Tung *et al.*, 2013] while the one at 941.6 G is open-channel dominated (from private exchanges with Arthur Christianen). The calculated overlap is small but sufficient (from private exchanges with Arthur Christianen). However, at such magnetic fields, even at low densities, if Cs is the impurity and it is not in the hyperfine ground state, spin changing collisions with Li are possible, because the splittings for Cs are larger than the splitting for Li. If one excites the hyperfine state of Cs, it is more favourable to change the spin of Li to an excited state so that Cs can go back to the ground state.

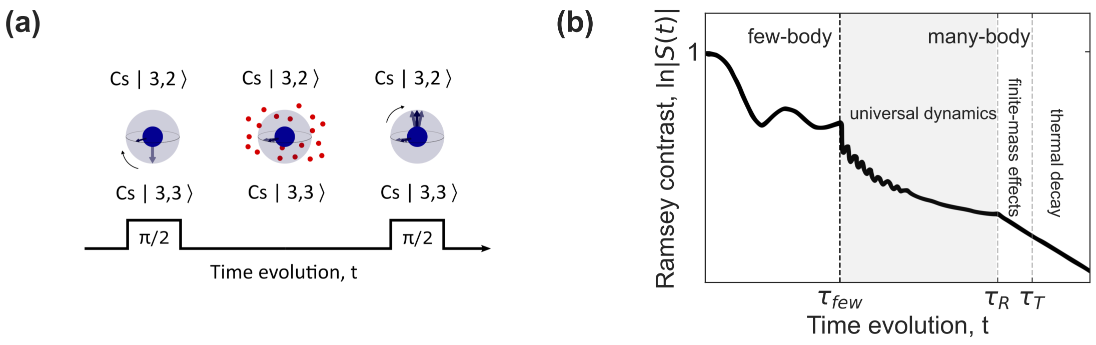

FIGURE 3.22: Scheme for probing the Anderson orthogonality catastrophe via a Ramsey interferometry protocol. (a) Sketch of the Ramsey protocol on Cs atoms. (b) Graphical illustration of the expected evolution of the Ramsey contrast $S(t)$. Picture (a) is inspired by [Cetina *et al.*, 2016] and (b) by [Schmidt *et al.*, 2018].

detuned transition of Li. In this scenario, for our current apparatus, a feasible experiment would consist of performing spectroscopy with zero momentum transfer. We could then replace the Raman protocol with RF-spectroscopy on the two lowest hyperfine states of Li. This would allow detecting the signal of the dressed dimer. As we want to detect the dimer, the flip of the majority species should bring a larger contribution compared to what we expect for the bath flip protocol with simple polarons.

Signatures of orthogonality catastrophe in the heavy mass limit. Following previous works [Cetina *et al.*, 2016, 2015], we expect Ramsey-type spectroscopy to be an experimentally relevant protocol to observe signatures of the orthogonality catastrophe, introduced in Sec. 3.1.1. Indeed, the evolution of the Ramsey contrast $S(t) = \langle e^{i\hat{H}_0 t} e^{-i\hat{H}t} \rangle$ is directly related to the real-time overlap between the many-body state with and without the impurity, governed respectively by the Hamiltonians $\hat{H}_0$ and $\hat{H}$ [Schmidt *et al.*, 2018].

The implementation of such a protocol consist of applying a first $\pi/2$ pulse to create a coherent superposition of interacting and non-interacting Cs states, let the impurities evolve for a variable interaction time, and probe the resulting state with a second $\pi/2$ pulse by measuring the variation of the atomic population.

The evolution of the Ramsey contrast can be divided into two regimes. For short evolution times $t \leq \tau_{few} \approx \tau_F$ few-body physics dominates, whereas, for longer times, with $t > \tau_F$, many-body correlations build up and polarons are formed. The universal power-law scaling of the Ramsey contrast is expected to be observable for timescales $\tau_F \leq t < \tau_R, \tau_T$. The time scale given by $\tau_R = \frac{9}{16} m_I / m_b \times \tau_F$ takes into account finite recoil effects and gives an estimate of the evolution time at which finite mass corrections become relevant [Cetina *et al.*, 2016]. The K-Li mass ratio of ~ 6.7 of the system used in Cetina *et al.* [2016] limits the time window for observing the universal dynamics associated with the Anderson orthogonality catastrophe to $\sim 4\tau_F$ [Cetina *et al.*, 2015, 2016]. Conversely, the Cs-Li of our system would allow accessing the power-law scaling behaviour in a larger time window, up to $\sim 12\tau_F$. However, the timescale on which thermal decay becomes relevant is given by $\tau_T = \tau_F \times (T/T_F)^{-1}$ and it is independent from the mass ratio. To prevent that thermal fluctuations hide most of the many-body correlations accessible in our large time window, the degree of degeneracy of our Li bath must satisfy $T/T_F \sim 0.07$. The idea would be then to use Ramsey spectroscopy protocols based on our newly implemented Raman transfer scheme described in Sec. 3.2.2.

From this experiment we expect to understand how a large but finite mass impurity at ultracold, but still finite, temperatures modifies polaron formation. It would be interesting to study how the Ramsey spectra change as a function of the temperature, the degree of degeneracy of the bath, the concentration of the impurity. This would allow exploring the emergence and disappearance of the universal scaling in dependence of these parameters.

It should be noted that the expected universal power law ω^α could also be extracted from the tail of the impurity energy spectrum [Knap *et al.*, 2012]. However, this approach is less robust than the interferometric approach described above.

Alternatively, Adlong *et al.* [2021] proposes to look for signatures of the orthogonality catastrophe in the Rabi oscillations driven by standard RF spectroscopy. In particular, if the Rabi coupling Ω_0 is large enough to overcome thermal effects, but still small enough to not completely smear the power law, the orthogonality catastrophe scaling α dictates the frequency of the Rabi oscillations. This condition, given as $2T < \Omega_0 < E_F$, can be easily fulfilled by our experimental parameters. In fact, the use of our Raman spectroscopy scheme would allow for a wide tunability of the Rabi frequencies.

Heavy polarons in BCS Fermi superfluids. The twin scenario of heavy polarons in a Fermi Sea is the case of heavy polarons in a Fermi superfluid, which can be realized by replacing the bath of a spin-polarized degenerate Fermi gas with a two-component Fermi gas involving intra-species interactions tuned in the BCS regime. This scenario is easily achievable in our mixture since BCS Fermi superfluid can be routinely prepared on the BCS side of the $\mathrm{Li}|1\rangle \oplus \mathrm{Li}|2\rangle$ Feshbach resonance at 832 G, and the Li-Cs interspecies interactions can be tuned near 843 G as well as near 888.6 G. The interacting superfluids would prevent the orthogonality catastrophe in such a system and would allow measuring the background superfluid excitation spectrum and the pairing gap [Wang *et al.*, 2022]. Moreover, the pairing gap would protect the polaron against thermal fluctuations, preserving clear polaron features in response functions even at finite temperature such that $k_B T$ is comparable to the energy associated with the pairing gap.

Conclusion

In this work we have realized a mixture composed of a Fermi Sea and heavy impurities and developed an experimental protocol for the detection of Fermi polarons. The system studied consists of a low-density sample of ^{133}Cs atoms, in the role of the impurities, and of a spin-polarized Fermi Sea of ^{6}Li atoms, in the role of quantum medium. We aimed to spectroscopically probe heavy thermal Cs impurities coupled to the Li Fermi Sea while tuning the interspecies interactions for mapping out the polaron energy spectrum and, thus, acquiring knowledge on many-body physics in systems with large mass imbalance.

For this purpose, we have extended and improved our experimental apparatus. On the one hand, a large effort has been devoted to the design and implementation of a bichromatic trapping scheme that allows compensating the differential gravitational sag, ensuring a good spatial overlap at arbitrary temperatures and independent manipulation of temperatures and densities of Li and Cs clouds. For this purpose, a tightly confining mobile trap for Li atoms at the Cs tune-out wavelength was designed, built up, tested and implemented in the main experiment. On the other hand, to probe the energy of the Cs impurities, we have built an optical setup to perform Raman spectroscopy on the two lowest Cs Zeeman states, which are $|3, +3\rangle = \mathrm{Cs}|1\rangle$ and $|3, +2\rangle = \mathrm{Cs}|2\rangle$. The detuning required to address these two states at the desired magnetic fields is about 263 MHz and we achieved typical Rabi frequencies of 15.6(9) kHz. This setup, together with the already existing spectroscopic tools, such as a radio-frequency antenna and a microwave horn, allows a versatile preparation and probing of the Li-Cs mixture in different states. Moreover, the combination of these spectroscopic techniques with high-resolution absorption imaging in fast kinetic mode, which allows the acquisition of images of both atomic clouds within the same experimental cycle, gives us complete access to the properties of the mixture. In addition, we have characterized existing features of the experimental apparatus, such as the performance of the double-species Zeeman slower and the homogeneity of the Feshbach coils. While the performance of the Zeeman slower plays a key role for loading Li and Cs clouds in their respective magneto-optical traps (MOTs), the homogeneity of the magnetic fields is an important prerequisite for controlling and tuning the intra- and inter-species scattering lengths via magnetic Feshbach resonances.

Strengthened by the upgrade of the experimental apparatus, we have realized, for the first time in our experiment, a mixture composed of a dilute thermal Cs gas and a degenerate Li Fermi Sea. For the mixing procedure, we have adopted a sub-sequential loading scheme where we first prepare Li and then Cs. Specifically, we load the Li MOT, perform

$\mathcal{D}_1$ cooling, load the atoms into the dimple trap, and then transfer them into the microtrap. This last step results in a decrease of T/T_F by a factor of 4. The evolution of temperature and atomic number during forced evaporation at 320 G agrees well with evaporation characterized by a truncation parameter of $\eta = 10$, and we obtain $T/T_F \lesssim 0.1$ with 8×10^4 atoms in less than 2 s. We then adiabatically compress, displace and store the Li cloud 230 μm away from the intersection of the dimple trap beams while loading the Cs MOT. After different sub-Doppler cooling stages, we load Cs into the reservoir trap, levitate the cloud with a finite magnetic field gradient and offset, and then jump to 526 G where we select the desired Li spin state. Finally, we apply a magnetic field of 900 G and then, after transferring the Cs atoms into the dimple trap, we remove the magnetic field gradient and evaporate, decreasing the laser power to reach a temperature similar to that of Li. Then, we spatially combine the two clouds while decreasing the microtrap power. Following this route, we obtained mixtures of Li$|2\rangle$ and Cs$|1\rangle$ where the peak density ratio of Cs to Li is $n_{\mathrm{Cs}}/n_{\mathrm{Li}} \approx 0.01$ and the Fermi Sea is characterized by a $T/T_F \approx 0.3$. A clear signature of the interaction between the two species was observed by performing Feshbach loss-spectroscopy near the Li-Cs Feshbach resonance at 888.6 G and recording a loss signal with a typical 1 : 2 ratio expected for Li-Cs-Cs three-body collisions.

After realizing the Li-Cs mixture and have observed the signature of interspecies interactions, we have focused on probing the energy spectrum of *heavy Fermi polarons* on ^{133}Cs atomic impurities immersed in the Fermi Sea of ^{6}Li atoms. We have estimated from theory the expected polaron shift as a function of the interaction strength at both zero and finite temperatures. For zero temperature, following [Combescot *et al.*, 2007], we have calculated the ground state of the polaron spectrum using the Chevy variational approach [Chevy, 2006] and then applied it to a finite impurity-bath mass ratio of $m_I/m_b = 22$. This has been compared to the analytical result for the case of an infinitely heavy impurity $m_I/m_b = \infty$. The results are in agreement, indicating that the limit of an infinitely heavy impurity remains accurate for the Li-Cs mixture. For finite temperatures, numerical predictions of the polaron spectral function calculated using the functional determinant approach [Drescher *et al.*, 2024] for an infinitely heavy impurity revealed that a $T/T_F \lesssim 0.3$ is required to distinguish the polaron from the bare transition. Experimentally, we have implemented an ejection spectroscopy protocol on Cs impurities near the Feshbach resonance at 888.6 G, corresponding to the Li$|2\rangle \oplus$Cs$|1\rangle$ scattering channel. This protocol consists of preparing the impurities in the Cs$|1\rangle$ state, which is initially interacting with the Li$|2\rangle$ state, and then transfer them to the state Cs$|2\rangle$, which is instead weakly interacting with Li$|2\rangle$. This method should allow probing the ground state of the system. Since this scattering channel, as well as the channels Cs$|2\rangle \oplus$Cs$|2\rangle$ and Cs$|1\rangle \oplus$Cs$|2\rangle$ can undergo two-body inelastic collisions, we must keep the Cs densities low, and possibly below 1×10^{11} cm^{-3}. The spectral response of Cs impurities is studied by probing the energy difference of the two lowest Zeeman states Cs$|1\rangle$ and Cs$|2\rangle$ via Raman spectroscopy. The two Raman beams transfer the atoms from the state Cs$|1\rangle$ to the state Cs$|2\rangle$ via a π-pulse. The number of atoms left in the Cs$|1\rangle$ state is recorded after the quench as a function of the detuning. The spectroscopic signal in the presence of the Fermi Sea is then compared with the signal obtained in its absence. Even though, we have studied the Li-Cs mixture for different temperatures and different interaction strengths, we have not observed any signal of the polaron.

Therefore, we reassessed some features of the experiment. On the one hand, the inhomogeneous density distribution of the Li and Cs atoms poses complications in the detection of the polaron signal. Indeed, Cs impurities experience the effect of the density variation of the Li bath $n_{\mathrm{Li}}(x,y,z)$, which in turn leads to a spatial variation of the polaron energy $E_{pol} \propto n_{\mathrm{Li}}(x,y,z)$. This results in a broadening of the energy spectrum around the polaron energy $E_0 + E_{pol}$, which makes the polaron feature not distinguishable from the noise. On the other hand, the Cs tune-out trap prevents the realization of state-selective experiments with the Cs ground state due to spontaneous two-photon Raman scattering, which results in significant Cs atom losses. To ensure thermalization occurs faster than light-induced losses, the species are overlapped at a magnetic field with high interspecies scattering lengths, i.e. at unitarity. Here, we have experimentally observed that light induced losses do not prevent interspecies interactions, which manifest in three-body losses close to the Feshbach resonance. However, locally, light-induced losses are expected to be much more severe than on average and, thus, to hinder the detection of polarons. Furthermore, the low reproducibility of the Raman spectroscopic signal and of its Rabi oscillations limits significantly the reproducibility of the polaron experiment.

In consideration of the aforementioned limitations associated with the current experimental setup, a series of modifications can be implemented. First, for improving the detection of the polaron, we propose to implement an optical light sheet of a few μm thickness that would permit the selective probing of the impurities in the central region of the Cs cloud, where the surrounding medium's density is relatively constant and defines a unique Fermi temperature. Second, in order to avoid the breakdown of the coherence of the prepared Cs state induced by spontaneous two-photon Raman scattering, we plan to shift the wavelength of the movable Li trap away from the Cs tune-out wavelength. This choice is also favorable to increase the time for which Li and Cs atoms can be trapped together and to allow sympathetic cooling between the two species at moderate interspecies scattering lengths. It would be advantageous to choose a trapping potential that ensures the confinement of the Cs cloud in the Li-Fermi Sea at a wavelength where dissipative effects are negligible. A common solution to both issues, which are the detection of the polaron and the loss of coherence of the prepared Cs state, would consist of using a bichromatic trapping scheme similar to the one implemented in this thesis work but shifting the wavelength of the tunable Ti:Sa laser to around 700 nm, where it creates a a repulsive potential for Cs atoms and an attractive potential for Li atoms. At the same time, the gravitational sag can be overcome by positioning the microtrap slightly below the dimple trap, pushing up the Cs atoms, while pulling down Li atoms. Another solution would be to use the existing dimple trap as the final trapping potential for both species, retrieving a very old scheme used in our experiment. However, this old scheme would be improved by using a magnetic gradient to push both species downward such that it compensates for the differential gravitational sag, by using a different evaporation scheme for Li atoms and relying on sympathetic cooling between the species. Both schemes are suitable for ensuring a dilute Cs cloud confined at the center of a degenerate spin-polarized Li Fermi Sea while avoiding undesired losses caused at the Cs tune-out wavelength. An additional important point is the necessity to achieve coherent and reproducible Rabi oscillations for Cs via Raman spectroscopy. It is important to determine whether the limitations are solely due to magnetic or laser intensity fluctuations, or there are other factors not considered yet that limit the coherence of the Rabi oscillations.

These upgrades should allow the detection and characterization of the properties of the Fermi polaron in the Li-Cs system. The first experiment should be devoted to map the energy polaron spectrum using zero-momentum transfer Raman spectroscopy on Cs impurities. More advanced spectroscopic protocols should then be applied to study the dynamics of heavy impurities in the context of the Anderson orthogonality catastrophe, both via Ramsey spectroscopy [Schmidt *et al.*, 2018; Cetina *et al.*, 2015, 2016] and via recording Rabi oscillations [Adlong *et al.*, 2021]. Thanks to the capability of the Raman setup to drive fast Rabi cycles, experiments on driven oscillations similar to Vivanco *et al.* [2023] are also a possible direction of study. Additionally, minimal changes to the existing Raman setup are needed to upgrade it for finite momentum transfer [Veeravalli *et al.*, 2008; Shkedrov *et al.*, 2020], which would open up to study momentum-dependent phenomena. For example, ejection Raman spectroscopy can be used to distinguish between the polaronic and the molecular contributions to the energy spectra [Ness *et al.*, 2020]. Raman injection spectroscopy would allow instead creating a dressed dimer and probing its full excitation spectrum [Diessel *et al.*, 2024]. Furthermore, replacing the Fermi Sea with a Fermi superfluid would also lead to the emergence of interesting phenomena: in such a system, the interacting superfluids would prevent the orthogonality catastrophe and allow the measurement of the background superfluid excitation spectrum and the pairing gap [Wang *et al.*, 2022]. Finally, after the necessary replacement of the Cs source, it should be possible to increase the density of the Cs-Bose gas and to produce again Cs Bose Einstein condensates [Tran, 2022]. This could be exploited to go beyond the Fermi polaron scenario and explore the Bose polaron scenario and its connection to Efimov physics [Levinsen *et al.*, 2015]. In addition, other relevant topics that could be studied in degenerate Fermi-Bose mixtures are for example the phase-diagram [Duda *et al.*, 2023], collective excitations [DeSalvo *et al.*, 2019; Patel *et al.*, 2023; Yan *et al.*, 2024a], and droplet formation [Rakshit *et al.*, 2019a,b].

In conclusion, in this thesis work we have laid the ground for an unique and versatile experimental setup capable of producing a degenerate Li Fermi gas mixed to a Cs thermal Bose gas, which can be used for the exploration of polaron physics in the heavy mass impurity limit.

Appendix A

Compensation of the differential gravitational sag: an alternative approach

In this Appendix, I describe a strategy to compensate for the differential gravitational sag of Li-Cs that is alternative to the use of species-selective trapping or to mechanical translation of one cloud with respect to the other. The proposal is to use monochromatic trapping of the two species by the dimple trap with a magnetic field gradient oriented in the same direction as the gravitational potential. In this combination of potentials, the differential gravitational sag is independent from the power of the dipole trap and, in theory, this system allows the complete overlap of Li and Cs cloud in the same optical dipole trap, independently from the temperature reached by the mixture at thermal equilibrium. During the course of this thesis a setup to produce *anti-levitation* magnetic fields for both species was implemented. This magnetic field is provided by the Curvature Coils, shown in Fig. 1.2 (c), which consist of a pair of coils with two layers and two windings each, placed inside the Feshbach coils [Pires, 2014]. An H-bridge was implemented and connected to this coils to allow switching the polarity of the magnetic field gradient. The gradient pushes both Li and Cs *down*, resulting in an artificial sag more pronounced for Li atoms than for Cs. The description of the setup, of its characterization and of the building of the H-bridge can be found in Freund [2019]. Here, I summarize the main expectations from the calculation of the total potential of this trapping scheme and show a measurement about the effective possibility to shift it, by using as a probe the MT light-induced loss on Cs atoms.

The differential gravitational sag is given by a combination of the different magnetic moments, polarizabilities and masses between Li and Cs (see Freund [2019]). The main results are summarized in Fig. A.1. The gravitational sag has been extracted by: (i) minimizing the full trapping potential, (ii) considering a harmonic approximation for optical trapping potential and linear approximation for the Breit-Rabi formula as given by Eq. 2.24. We computed the gradient necessary to cancel the differential gravitational sag for Li and Cs at different magnetic field offsets and we found that for offset values $B_0 > 100$ G, the expected magnetic field gradient is - 8 G/cm, for both mixtures of Li$|1\rangle\oplus$Cs$|1\rangle$ and Li$|2\rangle\oplus$Cs$|1\rangle$.

Experimentally, we show in Fig. A.2 that we can push the atoms down for negative magnetic field gradients. This does not prove that we can hold both of them together in such a combined potential, but that at least the gradient works as expected.

We proceeded by extracting the gravitational sag from measurements of light-induced Cs loss at the tune-out wavelength as a function of the displacement of the MT. In this measurement the MT beam is used as a probe and we vary its height from the horizontal plane defined by the crossed DT beams. We change the focal position of the MT beam up and down, along a diagonal, by moving the translation stage horizontally as described in Sec. 2.2.3. The gravitational sag was measured as a function of the magnetic field gradient as follow. The peak position of the Gaussian fit allowed for the extraction of the absolute gravitational sag.

For a levitated DT trap at a laser power of 300 mW, we prepared an atom number of $N = 2.5 \times 10^4$, which decreases by reducing the gradient until reaching $N = 3 \times 10^3$. The offset magnetic field is 880 G. The area of the scan is limited to $\pm 3 \times \sigma_r$ where σ_r is the radial Gaussian size of the Cs cloud. The magnetic gradient calibration is given by $B_g(I) = I \times (0.238 \pm 0.004)$ G cm^{-1}A^{-1}, where I is the current in the Curvature Coils [Freund, 2019]. As this measurement was only intended to be a proof of principle, it was only done for a few magnetic fields: $B_g = 0$ G/cm, which means pure optical trapping; $B_g = -8$ G/cm, which is the value where we expected to have compensation of the gravitational sag; $B_g = +27$ G/cm, which is the value for fully levitating Cs atoms at 880 G; $B_g = -15$ G/cm, which is for anti-levitation even steeper than the one required. A linear fit to the data gives a slope of (0.29 ± 0.08) cm^2/G with an offset of (-8.4 ± 1.6) μm, which corresponds to the gravitational sag without any additional magnetic gradient. This is compared to the gravitational sag as a function of magnetic field gradient obtained by minimizing the full trapping potential, as well as to the sag calculated using the harmonic approximation for the optical trapping potential and a linear approximation for the Breit-Rabi formula. The former has a slope of 0.24 cm^2/G and an offset of -6.6 μm.

Finally, Fig. A.3 shows how the gravitational sag changes as a function of the laser power, for a fixed magnetic field gradient of $B_g = -8$ G/cm and an offset magnetic field of B_0 = 880 G. For reference, we also computed and plotted the trap depth as a function of DT laser power and the profile of the total trapping potential along the vertical direction.

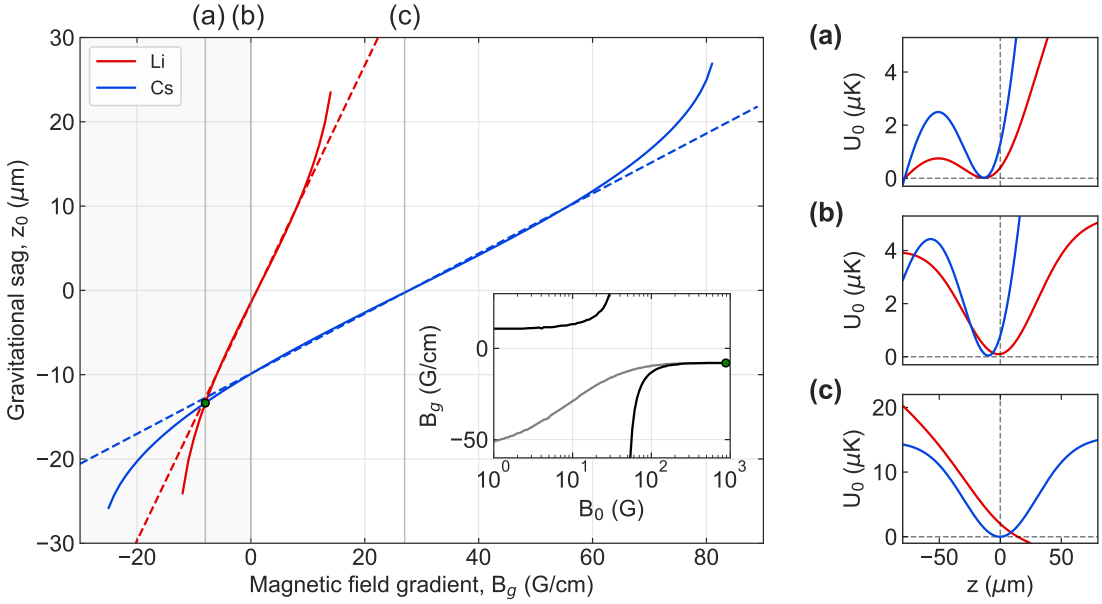

FIGURE A.1: Gravitational sag z_0 for Li$|1/2,-1/2\rangle$(red) and Cs$|3,+3\rangle$(blue) optically trapped at B_0 = 880 G with a laser power of 200 mW as a function of the magnetic field gradient B_g. The solid lines represent the gravitational sag extracted by minimizing the full trapping potential. The dashed lines, instead, are obtained considering the harmonic approximation for the optical trapping potential and a linear approximation for the Breit-Rabi formula. The gray shaded area represents the range of magnetic field gradient values accessible with the newly implemented H-bridge for the Curvature Coils. The differential gravitational sag Δz_{sag} is null at the crossing of the absolute gravitational sag z_0 for Li and Cs, which is marked by a green point. The plots on the right hand side show the trapping potential for Li (red) and Cs (blue) corresponding to the magnetic field gradients indicated by the gray vertical lines in the main plot: (a) B_g = - 8 G/cm, differential sag between the two species is null and $z_0^{Li,Cs}$ = 12.5 μm, (b) B_g = 0 G/cm, magnetic field gradient is null and Δz_{sag} = 10 μm: here the gravitational sag for Li almost vanishes z_0^{Li} $\sim$ 0 μm; (c) B_g = + 27 G/cm, gradient necessary for fully levitating Cs z_0^{Cs} $\sim$ 0 μm. The inset shows how the magnetic field gradient required for canceling the differential sag between Li and Cs changes following the offset magnetic field B_0. This dependence is shown in the inset for Cs$|3,+3\rangle$with Li$|1/2,-1/2\rangle$(black) or with Li$|1/2,1/2\rangle$(gray). Here, the green point marks the value of B_0 for the other plots shown within this figure.

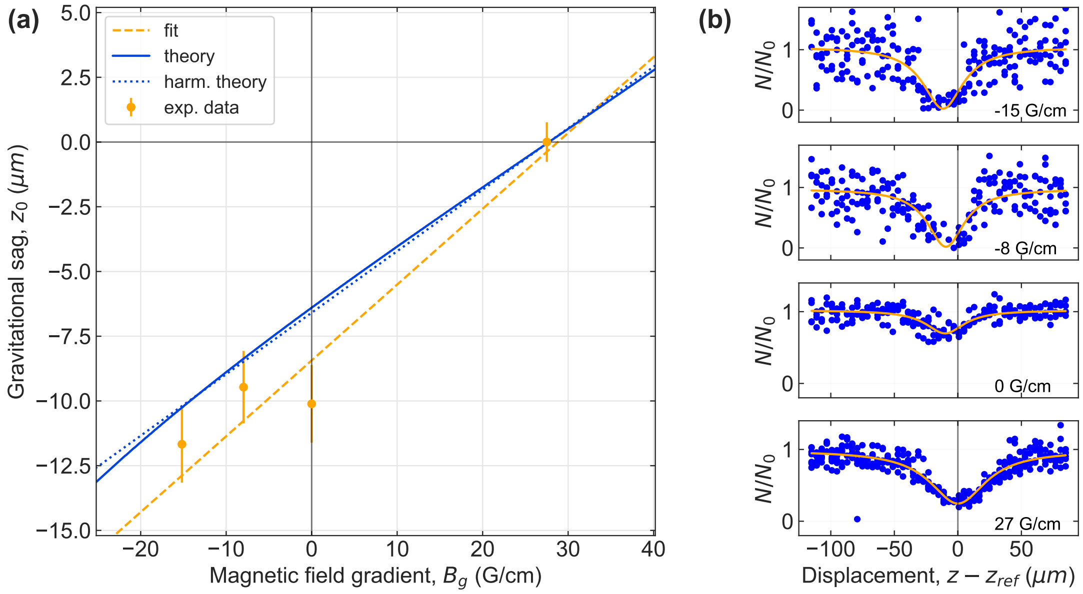

FIGURE A.2: Measurements of the (absolute) gravitational sag for Cs optically trapped in the DT at B_0 = 880 G with a power of 300 mW. (a) Gravitational sag as a function of the magnetic field gradient of the DT: the dots are the experimental data points extracted as shown in (b); the orange dashed line is a linear fit to the data; the blue-solid line is the gravitational sag obtained by minimizing the full trapping potential; the blue dashed line, is obtained considering the harmonic approximation for the optical trapping potential and a linear approximation for the Breit-Rabi formula. (b) Light-induced Cs loss at the tune-out wavelength in dependence of the position of the MT with respect to the Cs cloud. The peak position of the Gaussian fit (orange solid line) allows extracting the absolute gravitational sag.

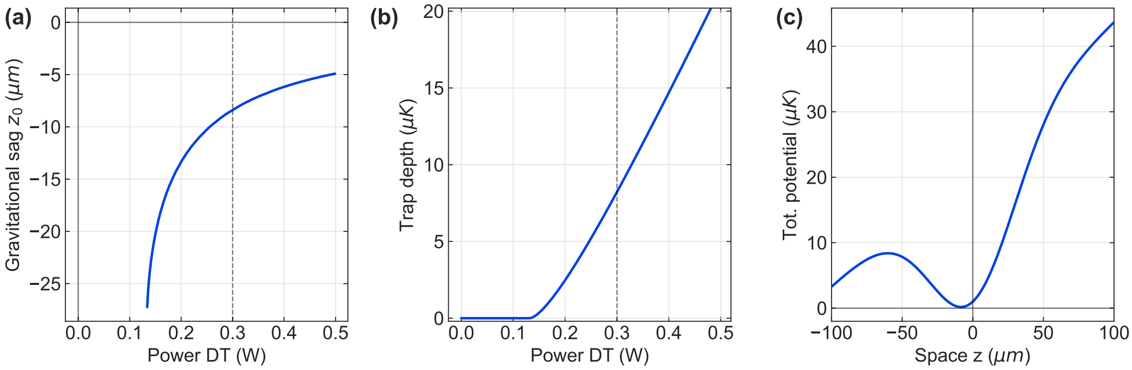

FIGURE A.3: Properties of Cs trapping potential for the magnetic field gradient $B_g = -8$ G/cm. The offset magnetic field is B_0 = 880 G and Cs is trapped in the DT. Gravitational sag z_0 (a) and trap depth (b) in dependence of the power of the DT. In (c) the trapping potential for Cs at 300 mW along the z-direction is shown.

Appendix B

Scattering of two heavy Fermi polarons

In this appendix the following publication is attached:

Scattering of two heavy Fermi polarons: Resonances and quasibound states
T. Enss, B. Tran, M. Rautenberg, M. Gerken, E. Lippi, M. Drescher, B. Zhu, M. Weidemüller, and Manfred Salmhofer
Physical Review A **102**, 063321 (2020)

PHYSICAL REVIEW A **102**, 063321 (2020)

Scattering of two heavy Fermi polarons: Resonances and quasibound states

Tilman Enss,[1] Binh Tran,[2] Michael Rautenberg,[2] Manuel Gerken,[2] Eleonora Lippi,[2] Moritz Drescher,[1]
Bing Zhu,[2,3] Matthias Weidemüller,[2] and Manfred Salmhofer[1]
[1]*Institut für Theoretische Physik, Universität Heidelberg, 69120 Heidelberg, Germany*
[2]*Physikalisches Institut, Universität Heidelberg, 69120 Heidelberg, Germany*
[3]*Hefei National Laboratory for Physical Sciences at the Microscale and Department of Modern Physics, and CAS Center for Excellence and Synergetic Innovation Center in Quantum Information and Quantum Physics, University of Science and Technology of China, Hefei 230026, China*

(Received 7 September 2020; accepted 24 November 2020; published 17 December 2020)

Impurities in a Fermi sea, or Fermi polarons, experience a Casimir interaction induced by quantum fluctuations of the medium. When there is short-range attraction between impurities and fermions, also the induced interaction between two impurities is strongly attractive at short distance and oscillates in space for larger distances. We theoretically investigate the scattering properties and compute the scattering phase shifts and scattering lengths between two heavy impurities in an ideal Fermi gas at zero temperature. While the induced interaction between impurities is weakly attractive for weak impurity-medium interactions, we find that impurities strongly and attractively interacting with the medium exhibit resonances in the induced scattering with a sign change of the induced scattering length and even strong repulsion. These resonances occur whenever a three-body Efimov bound state appears at the continuum threshold. At energies above the continuum threshold, we find that the Efimov state in medium can turn into a quasibound state with a finite decay width.

DOI: 10.1103/PhysRevA.102.063321

I. INTRODUCTION

The interaction of impurity particles in a medium is studied across physical disciplines. Specifically, the Casimir interaction between two impurities arises from fluctuations of the medium, or even the vacuum, subject to the boundary conditions imposed by the impurities [1]. Current applications range from neutron stars [2] and the quark-gluon plasma [3] to ultracold atoms [4,5]. Recent advances in experiments with ultracold atomic gases allow exploring mobile impurities in a fermionic medium, or Fermi polarons, in the regime of strong attraction [6–12] and precisely measuring their spectral properties. These experiments are performed not on a single impurity but on a dilute gas of impurities. The induced interaction between impurities is typically weak [13–16], but it can play an important role when the impurity-medium interaction becomes strong. Indeed, for large scattering length it can lead to Efimov three-body bound states [17–19] that are crucial for interpreting impurity spectra [20].

The interaction between localized spins in an electron gas is a classic result of condensed matter physics: by the Pauli principle, the induced Ruderman-Kittel-Kasuya-Yosida (RKKY) interaction oscillates in space and changes sign whenever the distance between the spins grows by about an electron spacing, or Fermi wavelength [21–23]. For larger objects in a Fermi sea, this can be understood by semiclassical methods [24]. More recently, these studies have been extended to the case of impurity atoms in a Fermi gas, or Fermi polarons [25–27]. When the impurity is tuned to strong attraction with the Fermi sea, it can form a bound state with one of the fermions [26,28,29]. These, in turn, lead to an enhanced attraction between two impurities at short distance [4,5,30] and even to bipolaron bound states between two impurities in a Fermi sea [5,31–34]. The Efimov bound states between two impurities and one fermion are characterized by discrete scaling relations [18,35]. In the medium, the scaling relations are modified by the Fermi wavelength as an additional length scale [5,31,33,34] and lead to shifts in the bipolaron resonance positions. Because they satisfy a new scaling relation, we refer to them as in-medium Efimov resonances. In the limit of a dense medium the induced interaction diminishes proportional to the Fermi wavelength and eventually vanishes [30].

In this work, we study the scattering properties of two heavy impurities in an ideal Fermi gas, as shown in Fig. 1. Based on the Casimir interaction potential [4], we compute the scattering phase shift and the induced scattering length between impurities and find that they scatter resonantly whenever an Efimov bound state appears at the continuum threshold. Moreover, for positive scattering length a repulsive barrier arises in the impurity potential, and remarkably the in-medium Efimov state can live on behind the barrier as a quasibound state at positive energies. In the following, we start by reviewing the Casimir interaction potential in Sec. II. In Section III we solve the Schrödinger equation for two impurities in this potential to find the scattering properties, and we discuss our results also for the experimentally relevant case of cesium-lithium mixtures [36,37] before concluding in Sec. IV.

II. CASIMIR INTERACTION

The interaction of two heavy impurities (mass M) in an ideal Fermi gas of light particles (mass m) is well described in the Born-Oppenheimer approximation. By the separation of

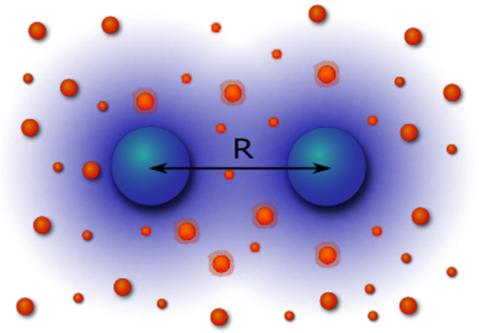

FIG. 1. Two heavy impurities (large blue dots) at distance R in a Fermi sea of light fermions (small red dots).

time scales, the impurities can be considered as a static scattering potential for the fermions and—in the case of a contact potential—provide only a boundary condition for the fermion wavefunctions. This approximation becomes exact in the limit of infinitely heavy impurities, where the problem reduces to potential scattering, and remains accurate at large mass ratio $M/m \gg 1$, for instance in a quantum gas mixtures of bosonic ^{133}Cs and fermionic ^{6}Li atoms. In this section we present the derivation of the interaction $V(R)$ induced between the two heavy impurities (of arbitrary statistics) by the presence of the Fermi sea, following Nishida [4].

Consider two infinitely heavy impurities at distance R with positions $\boldsymbol{R}_{1,2} = \pm\boldsymbol{R}/2$. The impurities have a short-range attractive interaction with the fermions, which we model by a zero-range Fermi pseudopotential. The action of the potential is equivalent to imposing the Bethe-Peierls boundary condition on the fermion wavefunction near an impurity at position $\boldsymbol{R}_i$,

$$\psi(\boldsymbol{x} \to \boldsymbol{R}_i) \propto \frac{1}{|\boldsymbol{x} - \boldsymbol{R}_i|} - \frac{1}{a} + O(|\boldsymbol{x} - \boldsymbol{R}_i|). \tag{1}$$

Here, a denotes the impurity-fermion scattering length that fully characterizes the contact interaction. The fermion wavefunctions solve the free Schrödinger equation, subject to the boundary conditions (1) at both $\boldsymbol{R}_1$ and $\boldsymbol{R}_2$. There are potentially two bound states at negative energies $E_\pm = -\kappa_\pm^2/2m < 0$, where the inverse length scale of the bound states $\kappa_\pm > 0$ is given by

$$\kappa_\pm = \frac{1}{a} + \frac{1}{R} W(\pm e^{-R/a}) \tag{2}$$

in terms of the Lambert W function that solves $x = W(x)e^{W(x)}$. Since real solutions exist for $x \in (-1/e, \infty)$, the bound state $\kappa_\pm > 0$ appears for distances $R/a > \mp 1$: while κ_- exists only for positive scattering length and $R > a > 0$, κ_+ exists both for $a < 0$ at small separation $R < |a|$ and for $a > 0$ at arbitrary R. Hence, a fermion attracted to two impurities forms a κ_+ bound state much more *easily* than one attracted only to a single impurity, and this will have dramatic consequences for the scattering properties between two impurities.

Besides the bound states, there is a continuum of fermion scattering states at positive energy $E = k^2/2m > 0$. For each mode $\boldsymbol{k}$, the fermion wavefunction $\sin(kr + \delta_\pm)$ at large distance r from both impurities acquires an s-wave phase shift with respect to the free wavefunction without impurities, which is given by

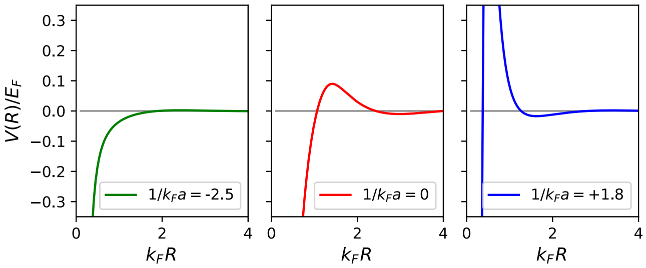

FIG. 2. Induced interaction potential $V(R)$ between two heavy impurities for negative, unitary, and positive interspecies scattering length a (from left to right). Data shown for Cs-Li mass ratio $M/m = 22.17$.

$$\tan\delta_\pm(k) = -\frac{kR \pm \sin(kR)}{R/a \pm \cos(kR)} \tag{3}$$

for the (anti)symmetric solution, where $0 \leqslant \delta_\pm(k) < \pi$. In the thermodynamic limit, the total energy change with and without impurities can be expressed as

$$\Delta E(R) = -\frac{\kappa_+^2 + \kappa_-^2}{2m} - \int_0^{k_F} dk\, k \frac{\delta_+(k) + \delta_-(k)}{\pi m}. \tag{4}$$

At large separation the impurities no longer interact, and the energy change approaches

$$\Delta E(R \to \infty) \to 2\mu, \tag{5}$$

or twice the single-polaron energy (chemical potential)

$$\mu = -\varepsilon_F \frac{k_F a + [1 + (k_F a)^2][\pi/2 + \arctan(1/k_F a)]}{\pi (k_F a)^2} \tag{6}$$

in terms of the Fermi energy $\varepsilon_F = k_F^2/2m$. The resulting Casimir interaction relative to the chemical potential,

$$V(R) = \Delta E(R) - 2\mu, \tag{7}$$

is shown in Fig. 2. For short distance it is strongly attractive as $-c^2/2mR^2$ from the bound-state contribution κ_+, where $c = W(1) \approx 0.567\,143$ solves $c = e^{-c}$; this effect is already present for a single fermion and gives rise to the Efimov effect [17–19]. In the fermionic medium, the Pauli principle requires that the induced interaction changes sign after an average spacing between the fermions, similar to the RKKY interaction in solids [21–23]. The strong attraction is thus canceled at larger distances by the contribution from the Fermi sea and crosses over near $k_F R \simeq 1$ into an oscillating decay $\cos(2k_F R)/R^3$ at large distance. Specifically at unitarity, the bound-state contribution $-c^2/2mR^2$ is present for *all* R and is canceled by the Fermi-sea contribution $2\mu + c^2/2mR^2 - \cos(2k_F R)/2\pi m k_F R^3 + O((k_F R)^{-4})$. For positive scattering length, a substantial repulsive barrier develops that will be able to capture a quasibound state, as we discuss in the next section.

III. SCATTERING BETWEEN IMPURITIES

Given the induced potential $V(R)$ between the impurities, we now generalize the approach of Ref. [4] to bosonic or distinguishable impurities and compute their scattering properties in the s-wave channel. We still work in the Born-Oppenheimer approximation where the heavy impurities move slowly, while the Fermi sea of light particles adjusts almost instantaneously to their positions and produces the potential. The stationary states of the impurities are then described by the Schrödinger equation

$$\left[-\frac{\nabla_{\boldsymbol{R}}^2}{M}+V(R)+2\mu-E\right]\Psi(\boldsymbol{R})=0 \tag{8}$$

in the central potential $V(R)$. The scattering properties are encoded in the scattering phase shifts $\delta_\ell^{\text{ind}}(k)$ induced by the medium in the ℓ partial wave component. We compute the s-wave phase shift by integrating the variable phase equation [38]

$$k\partial_R\delta_{\ell=0}^{\text{ind}}(k,R)=-MV(R)\sin\left[kR+\delta_{\ell=0}^{\text{ind}}(k,R)\right]^2. \tag{9}$$

Usually, one imposes the boundary condition $\delta_{\ell=0}^{\text{ind}}(k,R=0)=0$ at $R=0$ and integrates up to large R, where one reads off the phase shift $\delta_{\ell=0}^{\text{ind}}(k)=\delta_{\ell=0}^{\text{ind}}(k,R\to\infty)$.

A. Efimov resonances

The short-range singularity of the induced potential $V(R\to 0)=-\alpha/R^2$ leads to a Hamiltonian that is bounded from below only for weak attraction $\alpha<1/4$; for larger α there are an infinite number of Efimov bound states [18]. In our case $\alpha=(M/2m)c^2$ is always above 1/4 in the Born-Oppenheimer limit $M\gg m$, so the potential needs a regularization, which is physically provided by the repulsive core of the van der Waals potential between impurities [34]. We mimic the actual potential by a hard sphere of radius R_0, where the initial condition reads $\delta_{\ell=0}^{\text{ind}}(k,R_0)=-kR_0$, and integrate $R=R_0,\dots,\infty$ using a standard ordinary differential equation solver (DOP853). The cutoff radius R_0 is tuned to match the size of the lowest Efimov state in the real potential and is therefore directly related to the three-body parameter (3BP) which incorporates the relevant short-range physics [18,39]. As a specific example, in the Cs-Li system the heteronuclear Feshbach resonance at 889 G has $a_-^{(1)}=-2130a_B$ [40], which is reproduced by the induced potential with $R_0=220a_B$. For a typical fermion density of $n=10^{13}\ \text{cm}^{-3}$ in current experiments [10,15] we thus obtain $k_FR_0=0.1$ and we use this value in our plots to make quantitative predictions.

The bound-state spectrum for Eq. (8) is shown in Fig. 3 for the example of ^{133}Cs impurities in a ^{6}Li Fermi sea. One observes that the medium facilitates binding for weak attraction (shifting the onset to the left), but the repulsive barrier inhibits binding compared to the vacuum case for strong attraction [33].

B. Induced scattering length

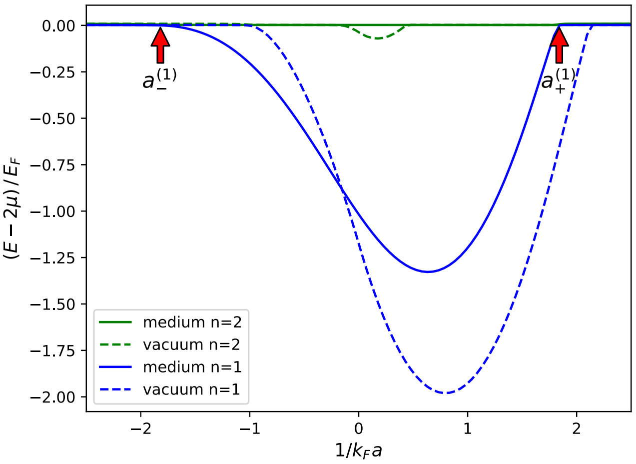

FIG. 3. Energy spectrum of Cs-Cs-Li Efimov states vs impurity-fermion scattering. The energies are given relative to the scattering continuum 2μ. Shown are the first [$n=1$, blue (lower) lines] and second [$n=2$, green (upper) lines] Efimov states, both in vacuum (dashed) and in medium (solid), with cutoff radius $R_0=0.1k_F^{-1}$. The Efimov bound states merge with the continuum at scattering lengths $a_\pm^{(n)}$, as indicated by the arrows for the first in-medium Efimov state. In vacuum, length units are $10R_0$ and energy units $1/2m(10R_0)^2$.

For a given cutoff radius R_0 and the corresponding Efimov spectrum, we compute the resulting s-wave scattering phase shifts $\delta_{\ell=0}^{\text{ind}}(k)$ that are shown in Fig. 4. In the limit of small k one can read off the induced impurity-impurity scattering length a_{ind} shown in the figure and the effective range r_{e} from the effective range expansion

$$k\cot\left[\delta_{\ell=0}^{\text{ind}}(k)\right]=-\frac{1}{a_{\text{ind}}}+\frac{r_{\text{e}}}{2}k^2+O(k^4). \tag{10}$$

Equivalently, the scattering length can be obtained from the variable phase equation (9) directly in the $k\to 0$ limit,

$$\partial_R a_{\text{ind}}(R)=-MV(R)[R-a_{\text{ind}}(R)]^2, \tag{11}$$

with initial condition $a_{\text{ind}}(R_0)=R_0$ and the final result $a_{\text{ind}}=a_{\text{ind}}(R\to\infty)$. The Efimov bound states lead to resonances in the induced scattering length [41], which are understood analytically from the solution of Eq. (11) for the $-\alpha/R^2$ potential with $\alpha>1/4$ for distances $R_0,\dots,R$,

$$a_{\text{ind}}(R)=R\left[1-\frac{1}{2\alpha}+\frac{s_0}{\alpha}\tan\left(\arctan\frac{1}{2s_0}-s_0\ln\frac{R}{R_0}\right)\right] \tag{12}$$

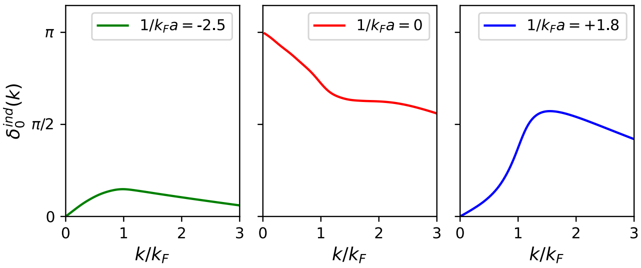

FIG. 4. Induced scattering phase shift $\delta_0^{\text{ind}}(k)$ for the potentials in Fig. 2. The initial slope near $k=0$ determines the induced scattering lengths $k_Fa_{\text{ind}}=-0.8$, $+0.7$, and -1.0 from left to right. On the $a>0$ side the phase shift steeply rises above $\pi/2$ indicating a quasibound state. Data shown for Cs-Li mass ratio $M/m=22.17$.

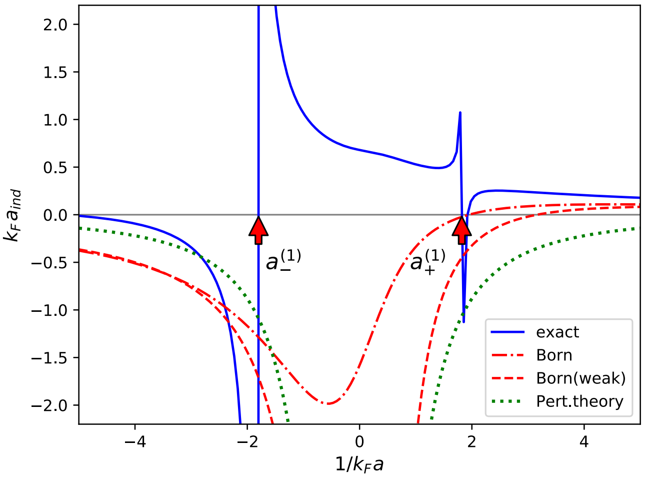

FIG. 5. Induced interaction between two heavy impurities: induced scattering length a_{ind} vs impurity-fermion interaction. From top to bottom: exact solution of Schrödinger equation (11) with cutoff $k_F R_0 = 0.1$ (blue solid line), Born approximation (13) (red dash-dotted line), analytical weak-coupling Born approximation (15) (red dashed line), and second-order perturbation theory (16) (green dotted line). The exact a_{ind} diverges at the in-medium Efimov resonances $a_\pm^{(1)}$ indicated by the arrows. Data shown for Cs-Li mass ratio $M/m = 22.17$.

with $s_0 = \sqrt{\alpha - 1/4} > 0$ [42]. This solution is valid for distances $R_0 < R \ll |a|, k_F^{-1}$ and shows that the continuous scale invariance of the $1/R^2$ potential is broken down to a discrete scaling symmetry. The solution repeats itself whenever $s_0 \ln(R/R_0)$ is a multiple of π and hence is log-periodic in R with a length scale factor of $l = \exp(\pi/s_0)$. For the case of ^{133}Cs impurities in ^{6}Li, the scale factor is $l \approx 5.6$ in the Born-Oppenheimer approximation, close to the experimentally observed value of $l \approx 4.9$ [35]. For larger distance $R \gtrsim k_F^{-1}$ the $-\alpha/R^2$ form of the potential is cut off by the Fermi sea, and no Efimov bound states of size larger than k_F^{-1} occur.

The full potential $V(R)$ in Eqs. (4) and (7) is computed numerically and agrees with known analytical limits for small or large distance and weak or strong coupling [4]. The induced scattering length for the full potential is shown in Fig. 5 for $k_F R_0 = 0.1$ (blue solid line). In this case, a_{ind} exhibits two scattering resonances at $a = a_\pm^{(1)}$, where a bound state crosses the continuum threshold. For smaller R_0, the potential admits more bound states and associated resonances at $a = a_\pm^{(n)}$ with $n > 1$ (for comparison see Fig. 2(b) in Ref. [33]). In the interval $1/a_-^{(n)} < 1/a < 1/a_+^{(n)}$ the induced potential admits n Efimov bound states, and the phase shift starts at $\delta_{\ell=0}^{\text{ind}}(k \to 0) = n\pi$ in accordance with Levinson's theorem, as shown for $n = 1$ in the central panel of Fig. 4.

The resonances of $a_{\text{ind}}(a)$ occur whenever an Efimov bound state crosses the continuum threshold. This can be seen in the energy spectrum in Fig. 3: for $1/a > 1/a_-^{(n)}$ the potential is deep enough to admit the nth bound state, but for even stronger attraction this bound state eventually merges again with the scattering continuum at $1/a = 1/a_+^{(n)}$. Note that the resonance positions $a_\pm^{(n)}(k_F)$ in medium depend on the density and differ from the vacuum values $a_\pm^{(n)}(0)$, as discussed in Refs. [31,33,34].

For the singular potential $V(R)$, the exact induced scattering length a_{ind} can differ drastically from the one obtained in Born approximation,

$$a_{\text{ind}}^{\text{Born}} = \int_0^\infty dR\, R^2 M V(R). \tag{13}$$

Here, the asymptotics at short distance $[1/R^2]$ and at large distance $[\cos(2k_F R)/R^3]$ are integrable and no cutoff R_0 is needed. The resulting scattering length is shown in Fig. 5 (red dash-dotted line); as might be expected for a singular potential, it does not approximate the exact solution well even for weak coupling.

It is instructive to compare the induced scattering length to the exact result in the weakly attractive limit $1/k_F a \lesssim -1$. In this case, the full induced potential is given analytically for all R as the sum of the singular attractive potential from the bound state and the regular oscillating potential from the Fermi sea,

$$V_{\text{weak}}(R) = -\frac{\Theta(|a| - R)}{2mR^2}\left(W(e^{R/|a|}) - \frac{R}{|a|}\right)^2 + \frac{a^2}{2m}\,\frac{2k_F R\cos(2k_F R) - \sin(2k_F R)}{2\pi R^4} + O((k_F a)^3). \tag{14}$$

For weak coupling, we find an analytical expression for the induced scattering length in Born approximation with $R_0 = 0$ (red dashed line in Fig. 5),

$$a_{\text{weak}}^{\text{Born}} = \frac{M}{2m}\left(\gamma a - \frac{k_F}{\pi} a^2 + O(a^3)\right), \tag{15}$$

where $\gamma = \int_0^1 dx[W(e^x) - x]^2 = 2(1 - c[1 + c(1 + c/3)]) \approx 0.100\,795$. Figure 5 shows that the analytical weak-coupling form (15) agrees with the numerical Born solution (13) for $|k_F a| \lesssim 0.3$. Finally, second-order perturbation theory for weakly repulsive interaction yields [43]

$$a_{\text{ind}}^{\text{PT}} = -\frac{k_F}{2\pi}\,\frac{(M+m)^2}{Mm}\, a^2 + O(a^3) \tag{16}$$

from the continuum of scattering states alone (green dotted line in Fig. 5). This result at order $O(a^2)$ fully agrees with the second-order term in the Born approximation (15) in the Born-Oppenheimer limit $M \gg m$. However, the first term in the Born approximation (15) that arises from the bound state is of *first order* in a and therefore dominates over the continuum contribution at weak coupling $R_0 < |a| \lesssim k_F^{-1}$. Hence, the usual perturbation theory for repulsive impurities is unable to describe attractive impurities even at weak coupling because it misses the leading bound-state contribution for $|a| > R_0$. In the exact solution of the Schrödinger equation, the bound-state contribution can become arbitrarily large near an Efimov resonance, depending on the value of the cutoff radius R_0. Only for very weak attraction with $|a| \lesssim R_0$ the bound-state contribution is small, and the induced scattering is dominated by the second-order contribution (16), as is the case in Ref. [14] where $k_F a \approx -0.012$, and in Ref. [15].

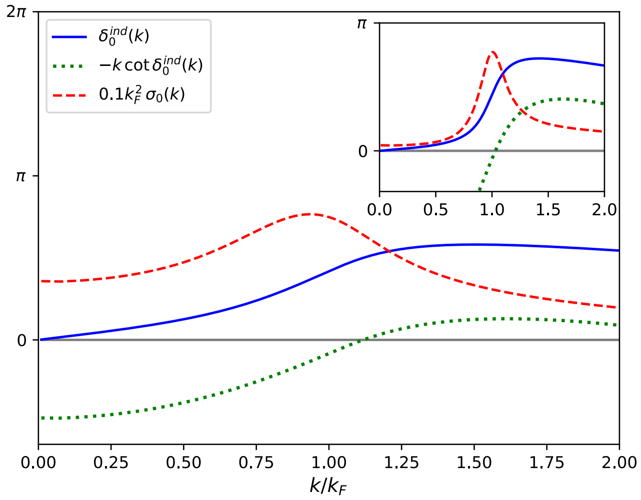

FIG. 6. Scattering resonance at positive energy above the continuum threshold and quasibound states. Enhanced scattering occurs at the upturn of the scattering phase shift $\delta_0^{\rm ind}(k)$ (blue solid line) at $k = 1.12\,k_F$, where $\cot\delta_0^{\rm ind}(k)$ has a zero crossing (green dotted line). Correspondingly, the s-wave differential cross section σ_0 (red dashed line) exhibits a maximum at energies near ε_F. The data shown are for the Cs-Li mass ratio $M/m = 22.17$ and $k_F R_0 = 0.1$ near the Efimov resonance at $a = 0.536\,k_F^{-1} \lesssim a_+^{(1)} = 0.542\,k_F^{-1}$. Inset: for larger mass ratio $M/m = 44.33$ there is a well-developed scattering resonance of Breit-Wigner form (17) with $E_{\rm qbnd} = 1.06\varepsilon_F$ and $\Gamma_{\rm qbnd} = 0.69\varepsilon_F$. This arises from a quasibound state at $a = 0.359k_F^{-1} \lesssim a_+^{(1)} = 0.360k_F^{-1}$.

C. Quasibound states

Beyond the Efimov threshold $1/a > 1/a_+^{(n)}$ at positive scattering length, the in-medium Efimov bound state is pushed out of the potential to energies above the continuum threshold, but it may be caught behind the repulsive barrier that is created by the fermionic medium and the two-body bound states (right panel of Fig. 2). How long the bound state can be caught behind the barrier depends on the effective height of the potential in the Schrödinger equation (8), which is proportional to the mass ratio M/m. The larger the mass ratio, the longer lived is the quasibound state even at positive energies. We find long-lived states approximately for $M/m \gtrsim 40$. In this case, the Efimov bound state goes over into a quasibound state at positive energies and with a small decay width, similar to the collisionally stable quasibound states found in Ref. [44]. We identify such a state when the scattering phase shift assumes the form of a Breit-Wigner resonance at positive energies $E = k^2/2m$ as shown in Fig. 6,

$$\cot\left[\delta_{\ell=0}^{\rm ind}(k)\right] = -\frac{E - E_{\rm qbnd}}{\Gamma_{\rm qbnd}/2} + \cdots . \tag{17}$$

From the position of the zero crossing and the slope we read off the energy $E_{\rm qbnd}$ and the full width at half maximum decay width $\Gamma_{\rm qbnd}$. For Cs-Li parameters $M/m = 22.17$, Fig. 6 shows enhanced scattering at positive energies but still large width $\Gamma_{\rm qbnd} > E_{\rm qbnd}$ so that we cannot yet speak of a well-defined quasibound state. For larger mass ratio $M/m = 44.33$, we find that for $1/a > 1/a_+$ the in-medium Efimov state can turn into a well-developed quasibound state as shown in the inset: it has a decay width $\Gamma_{\rm qbnd} < E_{\rm qbnd}$ smaller than its energy.

Based on Refs. [19,33], it appears reasonable to assume that the excited quasibound trimer state will eventually decay into two polarons, which form the continuum threshold for $1/a > 1/a_+$. The character of these polaron states depends on the scattering length across the polaron-to-molecule transition [26,28,29]. For strong binding $1/k_F a > (1/k_F a)_c \simeq 0.9$, which is the situation depicted in Fig. 3 near $a_+^{(1)}$, each impurity forms a tightly bound impurity-fermion dimer of energy μ embedded in the residual Fermi sea [19,33]. For weaker binding $1/k_F a < (1/k_F a)_c$, instead, each impurity forms a Fermi polaron, which would describe the continuum threshold near higher-lying Efimov states $a_+^{(n>1)}$.

A quasibound state is also manifest as a peak in the s-wave scattering cross section (red dashed line in Fig. 6)

$$\sigma_{\ell=0}(k) = \frac{4\pi}{k^2}\sin^2\left[\delta_{\ell=0}^{\rm ind}(k)\right] \tag{18}$$

at positive energy. For a finite density of heavy impurities in thermal equilibrium with the medium at $T \simeq E_{\rm qbnd}$ there will be enhanced scattering between the impurities, which would lead to a greater mean-field shift in the impurity spectra proportional to the impurity density.

Experimentally, the Efimov bound states in medium could be observed as a medium-density-dependent shift of the three-body loss peaks associated with the Efimov trimers [33]. The quasibound state and scattering resonance at positive energies above the continuum threshold would lead to an impurity-density-dependent shift in the polaron spectrum, estimated at a few percent in the case of Ref. [45], and to enhanced radio-frequency association of Efimov trimers [20] beyond $a_+^{(n)}$.

IV. CONCLUSION

The induced interaction between *attractive* impurities in a Fermi sea differs fundamentally from the RKKY interaction between nuclear spins in an electron gas, or repulsive impurities. While the continuum of scattering states yields a similar oscillating potential at large distance, the appearance of bound states implies a strong attraction at short distances. This singular $-1/R^2$ attraction gives rise to a series of three-body Efimov bound states down to the cutoff scale. Whenever a bound state crosses the continuum threshold, the induced scattering length $a_{\rm ind}$ exhibits resonances and changes sign. Attractive impurities can thus scatter strongly, and repulsively, in distinction to the weak induced attraction for repulsive impurities. For very weak attraction of order $k_F a \approx -0.01$, instead, our prediction for the induced scattering length is just slightly more attractive than in perturbation theory due to the additional attraction by the bound state, consistent with recent measurements [14,15].

While the impurity-impurity-fermion Efimov bound states below the continuum threshold have been discussed earlier, we find that at positive scattering length and large mass ratio the Efimov states can turn into quasibound states at positive energy. This corresponds to two impurities caught behind the repulsive potential barrier created by the Fermi sea: they can eventually tunnel through the barrier and escape, but as long as they are close, there is an enhanced probability to form a deeply bound state. This three-body recombination leads to a clear signature in experimental loss spectra [35–37].

Our investigation can be generalized to a dilute gas of heavy impurities, where it has been shown that the total Casimir energy is well approximated by a sum of pairwise two-body energies [4,24]. It is then justified to apply our results to a thermal gas of impurities at temperature T, where the scattering properties are evaluated at the thermal wave vector $\lambda_T^{-1} = \sqrt{mT/2\pi}$. This leads to the prediction of an enhanced mean-field shift when $T \simeq E_{\text{qbnd}}$. Furthermore, if three impurities are all nearby it would be interesting to explore the emergence of four-body impurity-impurity-impurity-fermion bound states. For smaller mass ratio, corrections beyond the Born-Oppenheimer approximation have to be included [30,46], in particular the scattering of trimers by the Fermi sea, which creates particle-hole excitations and alters the induced potential [5].

For the related case of impurities in a Bose-Einstein condensate, recent studies found many-body bound states of two impurities, or bipolarons, for moderately attractive interaction [45,47–49]. It will be interesting to extend these studies to the regime of strong attraction on the molecular side of the Feshbach resonance, where the impurities have been shown to strongly deform the surrounding Bose-Einstein condensate [50,51]. This again gives rise to an oscillating induced potential between the impurities that can be described using nonlocal Gross-Pitaevskii theory [52].

ACKNOWLEDGMENTS

We thank A. Volosniev for interesting discussions. This work is supported by the Deutsche Forschungsgemeinschaft (DFG, German Research Foundation), project ID 273811115 (SFB1225 ISOQUANT) and under Germany's Excellence Strategy EXC2181/1-390900948 (the Heidelberg STRUCTURES Excellence Cluster). E.L. acknowledges support by the IMPRS-QD.

---

[1] H. B. G. Casimir, On the attraction between two perfectly conducting plates, Proc. Kon. Ned. Akad. Wet. **51**, 793 (1948).

[2] Y. Yu, A. Bulgac, and P. Magierski, Shell Correction Energy for Bubble Nuclei, Phys. Rev. Lett. **84**, 412 (2000).

[3] G. Neergaard and J. Madsen, Does the quark-gluon plasma contain stable hadronic bubbles? Phys. Rev. D **62**, 034005 (2000).

[4] Y. Nishida, Casimir interaction among heavy fermions in the BCS-BEC crossover, Phys. Rev. A **79**, 013629 (2009).

[5] D. J. MacNeill and F. Zhou, Pauli Blocking Effect on Efimov States Near a Feshbach Resonance, Phys. Rev. Lett. **106**, 145301 (2011).

[6] A. Schirotzek, C.-H. Wu, A. Sommer, and M. W. Zwierlein, Observation of Fermi Polarons in a Tunable Fermi Liquid of Ultracold Atoms, Phys. Rev. Lett. **102**, 230402 (2009).

[7] S. Nascimbène, N. Navon, K. J. Jiang, L. Tarruell, M. Teichmann, J. McKeever, F. Chevy, and C. Salomon, Collective Oscillations of an Imbalanced Fermi Gas: Axial Compression Modes and Polaron Effective Mass, Phys. Rev. Lett. **103**, 170402 (2009).

[8] C. Kohstall, M. Zaccanti, M. Jag, A. Trenkwalder, P. Massignan, G. M. Bruun, F. Schreck, and R. Grimm, Metastability and coherence of repulsive polarons in a strongly interacting Fermi mixture, Nature (London) **485**, 615 (2012).

[9] M. Koschorreck, D. Pertot, E. Vogt, B. Fröhlich, M. Feld, and M. Köhl, Attractive and repulsive Fermi polarons in two dimensions, Nature (London) **485**, 619 (2012).

[10] M. Cetina, M. Jag, R. S. Lous, I. Fritsche, J. T. M. Walraven, R. Grimm, J. Levinsen, M. M. Parish, R. Schmidt, M. Knap, and E. Demler, Ultrafast many-body interferometry of impurities coupled to a Fermi sea, Science **354**, 96 (2016).

[11] F. Scazza, G. Valtolina, P. Massignan, A. Recati, A. Amico, A. Burchianti, C. Fort, M. Inguscio, M. Zaccanti, and G. Roati, Repulsive Fermi Polarons in a Resonant Mixture of Ultracold ^{6}Li Atoms, Phys. Rev. Lett. **118**, 083602 (2017).

[12] Z. Yan, P. B. Patel, B. Mukherjee, R. J. Fletcher, J. Struck, and M. W. Zwierlein, Boiling a Unitary Fermi Liquid, Phys. Rev. Lett. **122**, 093401 (2019).

[13] C. Mora and F. Chevy, Normal Phase of an Imbalanced Fermi Gas, Phys. Rev. Lett. **104**, 230402 (2010).

[14] B. J. DeSalvo, K. Patel, G. Cai, and C. Chin, Observation of fermion-mediated interactions between bosonic atoms, Nature (London) **568**, 61 (2019).

[15] H. Edri, B. Raz, N. Matzliah, N. Davidson, and R. Ozeri, Observation of Spin-Spin Fermion-Mediated Interactions between Ultracold Bosons, Phys. Rev. Lett. **124**, 163401 (2020).

[16] K. Mukherjee, S. I. Mistakidis, S. Majumder, and P. Schmelcher, Induced interactions and quench dynamics of bosonic impurities immersed in a Fermi sea, Phys. Rev. A **102**, 053317 (2020).

[17] V. Efimov, Energy levels arising from resonant two-body forces in a three-body system, Phys. Lett. B **33**, 563 (1970).

[18] E. Braaten and H. W. Hammer, Universality in few-body systems with large scattering length, Phys. Rep. **428**, 259 (2006).

[19] P. Naidon and S. Endo, Efimov physics: A review, Rep. Prog. Phys. **80**, 056001 (2017).

[20] T. Lompe, T. B. Ottenstein, F. Serwane, A. N. Wenz, G. Zürn, and S. Jochim, Radio-frequency association of Efimov trimers, Science **330**, 940 (2010).

[21] M. A. Ruderman and C. Kittel, Indirect exchange coupling of nuclear magnetic moments by conduction electrons, Phys. Rev. **96**, 99 (1954).

[22] T. Kasuya, A theory of metallic ferro- and antiferromagnetism on Zener's model, Prog. Theor. Phys. **16**, 45 (1956).

[23] K. Yosida, Magnetic properties of Cu-Mn alloys, Phys. Rev. **106**, 893 (1957).

[24] A. Bulgac and A. Wirzba, Casimir Interaction among Objects Immersed in a Fermionic Environment, Phys. Rev. Lett. **87**, 120404 (2001).

[25] F. Chevy, Universal phase diagram of a strongly interacting Fermi gas with unbalanced spin populations, Phys. Rev. A **74**, 063628 (2006).

[26] R. Schmidt and T. Enss, Excitation spectra and rf response near the polaron-to-molecule transition from the functional renormalization group, Phys. Rev. A **83**, 063620 (2011).

[27] P. Massignan, M. Zaccanti, and G. M. Bruun, Polarons, dressed molecules and itinerant ferromagnetism in ultracold Fermi gases, Rep. Prog. Phys. **77**, 034401 (2014).

[28] M. Punk, P. T. Dumitrescu, and W. Zwerger, Polaron-to-molecule transition in a strongly imbalanced Fermi gas, Phys. Rev. A **80**, 053605 (2009).

[29] C. Mora and F. Chevy, Ground state of a tightly bound composite dimer immersed in a Fermi sea, Phys. Rev. A **80**, 033607 (2009).

[30] S. Endo and M. Ueda, Perfect screening of the inter-polaronic interaction, arXiv:1309.7797.

[31] N. G. Nygaard and N. T. Zinner, Efimov three-body states on top of a Fermi sea, New J. Phys. **16**, 023026 (2014).

[32] F. F. Bellotti, T. Frederico, M. T. Yamashita, D. V. Fedorov, A. S. Jensen, and N. T. Zinner, Three-body bound states of two bosonic impurities immersed in a Fermi sea in 2D, New J. Phys. **18**, 043023 (2016).

[33] M. Sun and X. Cui, Efimov physics in the presence of a Fermi sea, Phys. Rev. A **99**, 060701(R) (2019).

[34] B. Tran, M. Rautenberg, M. Gerken, E. Lippi, B. Zhu, J. Ulmanis, M. Drescher, M. Salmhofer, T. Enss, and M. Weidemüller, Fermions meet two bosons—the heteronuclear Efimov effect revisited, Braz. J. Phys. (2020), doi: 10.1007/s13538-020-00811-5.

[35] J. Ulmanis, S. Häfner, R. Pires, E. D. Kuhnle, Y. Wang, C. H. Greene, and M. Weidemüller, Heteronuclear Efimov Scenario with Positive Intraspecies Scattering Length, Phys. Rev. Lett. **117**, 153201 (2016).

[36] R. Pires, J. Ulmanis, S. Häfner, M. Repp, A. Arias, E. D. Kuhnle, and M. Weidemüller, Observation of Efimov Resonances in a Mixture with Extreme Mass Imbalance, Phys. Rev. Lett. **112**, 250404 (2014).

[37] S.-K. Tung, K. Jimenez-Garcia, J. Johansen, C. V. Parker, and C. Chin, Geometric Scaling of Efimov States in a ^{6}Li-^{133}Cs Mixture, Phys. Rev. Lett. **113**, 240402 (2014).

[38] F. Calogero, *Variable Phase Approach to Potential Scattering* (Academic Press, New York, 1967).

[39] Y. Wang, J. Wang, J. P. D'Incao, and C. H. Greene, Universal Three-Body Parameter in Heteronuclear Atomic Systems, Phys. Rev. Lett. **109**, 243201 (2012).

[40] S. Häfner, J. Ulmanis, E. D. Kuhnle, Y. Wang, C. H. Greene, and M. Weidemüller, Role of the intraspecies scattering length in the Efimov scenario with large mass difference, Phys. Rev. A **95**, 062708 (2017).

[41] S. Endo, P. Naidon, and M. Ueda, Universal physics of $2+1$ particles with non-zero angular momentum, Few-Body Syst. **51**, 207 (2011).

[42] S. Moroz, Nonrelativistic scale anomaly, and composite operators with complex scaling dimensions, Ann. Phys. (NY) **326**, 1368 (2011).

[43] D. H. Santamore and E. Timmermans, Fermion-mediated interactions in a dilute Bose-Einstein condensate, Phys. Rev. A **78**, 013619 (2008).

[44] O. I. Kartavtsev and A. V. Malykh, Low-energy three-body dynamics in binary quantum gases, J. Phys. B: At. Mol. Opt. Phys. **40**, 1429 (2007).

[45] P. Naidon, Two impurities in a Bose-Einstein condensate: From Yukawa to Efimov attracted polarons, J. Phys. Soc. Jpn. **87**, 043002 (2018).

[46] M. Schecter and A. Kamenev, Phonon-Mediated Casimir Interaction between Mobile Impurities in One-Dimensional Quantum Liquids, Phys. Rev. Lett. **112**, 155301 (2014).

[47] N. T. Zinner, Efimov states of heavy impurities in a Bose-Einstein condensate, Europhys. Lett. **101**, 60009 (2013).

[48] A. Camacho-Guardian, L. A. Peña Ardila, T. Pohl, and G. M. Bruun, Bipolarons in a Bose-Einstein Condensate, Phys. Rev. Lett. **121**, 013401 (2018).

[49] A. Camacho-Guardian and G. M. Bruun, Landau Effective Interaction between Quasiparticles in a Bose-Einstein Condensate, Phys. Rev. X **8**, 031042 (2018).

[50] M. Drescher, M. Salmhofer, and T. Enss, Real-space dynamics of attractive and repulsive polarons in Bose-Einstein condensates, Phys. Rev. A **99**, 023601 (2019).

[51] M. Drescher, M. Salmhofer, and T. Enss, Exact quench dynamics of the ideal Bose polaron at zero and nonzero temperatures, arXiv:2011.06385.

[52] M. Drescher, M. Salmhofer, and T. Enss, Theory of a resonantly interacting impurity in a Bose-Einstein condensate, Phys. Rev. Research **2**, 032011(R) (2020).

Bibliography

Adlong, H. S., Liu, W. E., Scazza, F., Zaccanti, M., Oppong, N. D., Fölling, S., Parish, M. M., and Levinsen, J. "Quasiparticle Lifetime of the Repulsive Fermi Polaron". *Physical Review Letters*, **125** (13), 133401 (2020). doi:10.1103/PhysRevLett.125.133401. Cited on page 114

Adlong, H. S., Liu, W. E., Turner, L. D., Parish, M. M., and Levinsen, J. "Signatures of the orthogonality catastrophe in a coherently driven impurity". *Physical Review A*, **104** (4), 043309 (2021). doi:10.1103/PhysRevA.104.043309. Cited on pages 114, 122, and 126

Anderson, P. W. "Infrared Catastrophe in Fermi Gases with Local Scattering Potentials". *Physical Review Letters*, **18** (24), 1049–1051 (1967). doi:10.1103/PhysRevLett.18.1049. Cited on pages 2, 5, 81, and 89

Arias, A. "A reservoir optical dipole trap for creating a Bose-Einstein condensate of ^{133}Cs". Master's thesis, Ruprecht-Karls-Universität Heidelberg (2014). Cited on page 23

Arias de Saavedra, F., Boronat, J., Polls, A., and Fabrocini, A. "Effective mass of one He-4 atom in liquid He-3". *Physical Review B*, **50** (6), 4248–4251 (1994). doi:10.1103/PhysRevB.50.4248. Cited on pages 1 and 81

Arndt, M., Ben Dahan, M., Guéry-Odelin, D., Reynolds, M. W., and Dalibard, J. "Observation of a Zero-Energy Resonance in Cs-Cs Collisions". *Physical Review Letters*, **79** (4), 625–628 (1997). doi:10.1103/PhysRevLett.79.625. Cited on page 66

Arora, B., Safronova, M. S., and Clark, C. W. "Tune-out wavelengths of alkali-metal atoms and their applications". *Physical Review A*, **84** (4), 043401 (2011). doi:10.1103/PhysRevA.84.043401. Cited on pages 20, 26, and 66

Balakrishnan, N., Kharchenko, V., Forrey, R., and Dalgarno, A. "Complex scattering lengths in multi-channel atom–molecule collisions". *Chemical Physics Letters*, **280** (1-2), 5–9 (1997). doi:10.1016/S0009-2614(97)01052-X. Cited on page 97

Baranger, M. "General impact theory of pressure broadening". *Physical Review*, **112** (3), 855–865 (1958a). doi:10.1103/PhysRev.112.855. Cited on page 116

Baranger, M. "Simplified Quantum-Mechanical Theory of Pressure Broadening". *Physical Review*, **111** (2), 481–493 (1958b). Cited on page 116

Baroni, C., Huang, B., Fritsche, I., Dobler, E., Anich, G., Kirilov, E., Grimm, R., Bastarrachea-Magnani, M. A., Massignan, P., and Bruun, G. M. "Mediated interactions between Fermi polarons and the role of impurity quantum statistics". *Nature Physics*, **20** (1), 68–73 (2024a). doi:10.1038/s41567-023-02248-4. Cited on pages 2, 4, and 82

Baroni, C., Lamporesi, G., and Zaccanti, M. "Quantum Mixtures of Ultracold Atomic Gases". `arXiv:2405.14562`. Cited on pages 2 and 82

Barontini, G., Weber, C., Rabatti, F., Catani, J., Thalhammer, G., Inguscio, M., and Minardi, F. "Observation of Heteronuclear Atomic Efimov Resonances". *Physical Review Letters*, **103** (4), 043201 (2009). doi:10.1103/PhysRevLett.103.043201. Cited on page 3

Barontini, G., Weber, C., Rabatti, F., Catani, J., Thalhammer, G., Inguscio, M., and Minardi, F. "Erratum: Observation of heteronuclear atomic efimov resonances (Physical Review Letters (2009) 103 (043201))". *Physical Review Letters*, **104** (5), 59901 (2010). doi:10.1103/PhysRevLett.104.059901. Cited on page 3

Bedaque, P. F., Braaten, E., and Hammer, H.-W. "Three-body Recombination in Bose Gases with Large Scattering Length". *Physical Review Letters*, **85** (5), 908–911 (2000). doi:10.1103/PhysRevLett.85.908. Cited on page 77

Bell, S. C., Junker, M., Jasperse, M., Turner, L. D., Lin, Y. J., Spielman, I. B., and Scholten, R. E. "A slow atom source using a collimated effusive oven and a single-layer variable pitch coil Zeeman slower". *Review of Scientific Instruments*, **81** (1), 1–8 (2010). doi:10.1063/1.3276712. Cited on page 15

Berninger, M., Zenesini, A., Huang, B., Harm, W., Nägerl, H.-C., Ferlaino, F., Grimm, R., Julienne, P. S., and Hutson, J. M. "Universality of the Three-Body Parameter for Efimov States in Ultracold Cesium". *Physical Review Letters*, **107** (12), 120401 (2011). doi:10.1103/PhysRevLett.107.120401. Cited on pages 60 and 77

Berninger, M., Zenesini, A., Huang, B., Harm, W., Nägerl, H.-C., Ferlaino, F., Grimm, R., Julienne, P. S., and Hutson, J. M. "Feshbach resonances, weakly bound molecular states, and coupled-channel potentials for cesium at high magnetic fields". *Physical Review A*, **87** (3), 032517 (2013). doi:10.1103/PhysRevA.87.032517. Cited on pages 47, 48, 60, and 96

Bloom, R. S., Hu, M.-G., Cumby, T. D., and Jin, D. S. "Tests of Universal Three-Body Physics in an Ultracold Bose-Fermi Mixture". *Physical Review Letters*, **111** (10), 105301 (2013). doi:10.1103/PhysRevLett.111.105301. Cited on page 3

Bohn, J. L. and Julienne, P. S. "Prospects for influencing scattering lengths with far-off-resonant light". *Physical Review A*, **56** (2), 1486–1491 (1997). doi:10.1103/PhysRevA.56.1486. Cited on page 98

Borchers, F. C. "Modelling of Absorption Imaging of degenerate Fermi Gases in ultracold Atom Experiments". Bachelor's thesis, Ruprecht-Karls-Universität Heidelberg (2023). Cited on pages 39 and 79

Braaten, E. and Hammer, H.-W. “Three-Body Recombination into Deep Bound States in a Bose Gas with Large Scattering Length”. *Physical Review Letters*, **87** (16), 160407 (2001). doi:10.1103/PhysRevLett.87.160407. Cited on page 77

Braaten, E. and Hammer, H.-W. “Universality in few-body systems with large scattering length”. *Physics Reports*, **428** (5-6), 259–390 (2006). doi:10.1016/j.physrep.2006.03.001. Cited on page 77

Bredas, J. L. and Street, G. B. “Polarons, Bipolarons, and Solitons in Conducting Polymers”. *Accounts of Chemical Research*, **18** (10), 309–315 (1985). doi:10.1021/ar00118a005. Cited on page 1

Burchianti, A., Valtolina, G., Seman, J. A., Pace, E., De Pas, M., Inguscio, M., Zaccanti, M., and Roati, G. “Efficient all-optical production of large Li-6 quantum gases using D1 gray-molasses cooling”. *Physical Review A*, **90** (4), 043408 (2014). doi:10.1103/PhysRevA.90.043408. Cited on pages 53, 54, and 57

Catani, J., Lamporesi, G., Naik, D., Gring, M., Inguscio, M., Minardi, F., Kantian, A., and Giamarchi, T. “Quantum dynamics of impurities in a one-dimensional Bose gas”. *Physical Review A*, **85** (2), 1–6 (2012). doi:10.1103/PhysRevA.85.023623. Cited on page 2

Cetina, M., Jag, M., Lous, R. S., Fritsche, I., Walraven, J. T. M., Grimm, R., Levinsen, J., Parish, M. M., Schmidt, R., Knap, M., and Demler, E. “Ultrafast many-body interferometry of impurities coupled to a Fermi sea”. *Science*, **354** (6308), 96–99 (2016). doi:10.1126/science.aaf5134. Cited on pages 2, 5, 82, 121, and 126

Cetina, M., Jag, M., Lous, R. S., Walraven, J. T., Grimm, R., Christensen, R. S., and Bruun, G. M. “Decoherence of Impurities in a Fermi Sea of Ultracold Atoms”. *Physical Review Letters*, **115** (13), 135302 (2015). doi:10.1103/PhysRevLett.115.135302. Cited on pages 2, 5, 82, 121, and 126

Chen, X.-Y., Duda, M., Schindewolf, A., Bause, R., Bloch, I., and Luo, X.-Y. “Suppression of Unitary Three-Body Loss in a Degenerate Bose-Fermi Mixture”. *Physical Review Letters*, **128** (15), 153401 (2022). doi:10.1103/PhysRevLett.128.153401. Cited on pages 4, 79, and 93

Chen, Y., Li, W., Sun, Y., Chen, Q., Chang, P., and Tung, S. “Dual-species Bose-Einstein condensates of Li-7 and Cs-133”. *Physical Review A*, **108** (033301), 1–8 (2023). doi:10.1103/PhysRevA.108.033301. Cited on pages 3 and 48

Chevy, F. “Universal phase diagram of a strongly interacting Fermi gas with unbalanced spin populations”. *Physical Review A*, **74** (6), 063628 (2006). doi:10.1103/PhysRevA.74.063628. Cited on pages 84, 85, 86, and 124

Chin, C., Grimm, R., Julienne, P., and Tiesinga, E. “Feshbach resonances in ultracold gases”. *Reviews of Modern Physics*, **82** (2), 1225–1286 (2010). doi:10.1103/RevModPhys.82.1225. Cited on pages 2 and 46

Chin, C., Vuletić, V., Kerman, A. J., Chu, S., Tiesinga, E., Leo, P. J., and Williams, C. J. "Precision Feshbach spectroscopy of ultracold Cs2". *Physical Review A*, **70** (3), 032701 (2004). doi:10.1103/PhysRevA.70.032701. Cited on page 69

Christianen, A., Cirac, J. I., and Schmidt, R. "Bose polaron and the Efimov effect: A Gaussian-state approach". *Physical Review A*, **105** (5), 1–18 (2022). doi:10.1103/PhysRevA.105.053302. Cited on page 3

Cline, R. A., Miller, J. D., Matthews, M. R., and Heinzen, D. J. "Spin relaxation of optically trapped atoms by light scattering". *Optics Letters*, **19** (3), 207–209 (1994). Cited on page 67

Combescot, R., Recati, A., Lobo, C., and Chevy, F. "Normal State of Highly Polarized Fermi Gases: Simple Many-Body Approaches". *Physical Review Letters*, **98** (18), 180402 (2007). doi:10.1103/PhysRevLett.98.180402. Cited on pages 83, 84, 85, 86, 87, and 124

Cvitaš, M. T., Soldán, P., Hutson, J. M., Honvault, P., and Launay, J.-M. "Interactions and dynamics in Li+Li2 ultracold collisions". *The Journal of Chemical Physics*, **127** (7), 1–21 (2007). doi:10.1063/1.2752162. Cited on page 98

Dagotto, E. "Correlated electrons in high-temperature superconductors". *Reviews of Modern Physics*, **66** (3), 763–840 (1994). doi:10.1103/RevModPhys.66.763. Cited on page 1

Dalibard, J. "Collisional dynamics of ultra-cold atomic gases". In "Proceedings of the International School of Physics "Enrico Fermi"", 321–349 (1999). ISBN 0967335558. doi:10.3254/978-1-61499-225-7-321. Cited on page 44

Darkwah Oppong, N., Riegger, L., Bettermann, O., Höfer, M., Levinsen, J., Parish, M. M., Bloch, I., and Fölling, S. "Observation of Coherent Multiorbital Polarons in a Two-Dimensional Fermi Gas". *Physical Review Letters*, **122** (19), 193604 (2019). doi:10.1103/PhysRevLett.122.193604. Cited on pages 2, 82, and 114

Deiglmayr, J. "Structure, formation, and interactions of ultracold polar molecules". Ph.D. thesis, University of Freiburg (2009). Cited on page 49

Delannoy, G., Murdoch, S. G., Boyer, V., Josse, V., Bouyer, P., and Aspect, A. "Understanding the production of dual Bose-Einstein condensation with sympathetic cooling". *Physical Review A*, **63** (5), 051602 (2001). doi:10.1103/PhysRevA.63.051602. Cited on page 66

DeSalvo, B. J., Patel, K., Cai, G., and Chin, C. "Observation of fermion-mediated interactions between bosonic atoms". *Nature*, **568** (7750), 61–64 (2019). doi:10.1038/s41586-019-1055-0. Cited on pages 3, 4, 48, and 126

DeSalvo, B. J., Patel, K., Johansen, J., and Chin, C. "Observation of a Degenerate Fermi Gas Trapped by a Bose-Einstein Condensate". *Physical Review Letters*, **119** (23), 233401 (2017). doi:10.1103/PhysRevLett.119.233401. Cited on pages 3 and 48

Diessel, O. K., von Milczewski, J., Christianen, A., and Schmidt, R. "Probing molecular spectral functions and unconventional pairing using Raman spectroscopy". *Physical Review Research*, **6** (2), 023239 (2024). doi:10.1103/PhysRevResearch.6.023239. Cited on pages 6, 102, 119, 120, and 126

Drescher, M., Salmhofer, M., and Enss, T. "Real-space dynamics of attractive and repulsive polarons in Bose-Einstein condensates". *Physical Review A*, **99** (2), 023601 (2019). doi:10.1103/PhysRevA.99.023601. Cited on page 5

Drescher, M., Salmhofer, M., and Enss, T. "Bosonic Functional Determinant Approach and its Application to Polaron Spectra". `arXiv:2403.13582`. Cited on pages 90, 91, 92, 115, 117, and 124

Drewsen, M., Laurent, P., Nadir, A., Santarelli, G., Clairon, A., Castin, Y., Grison, D., and Salomon, C. "Investigation of sub-Doppler cooling effects in a cesium magneto-optical trap". *Applied Physics B*, **59** (3), 283–298 (1994). doi:10.1007/BF01081396. Cited on page 59

Duda, M., Chen, X.-Y., Schindewolf, A., Bause, R., von Milczewski, J., Schmidt, R., Bloch, I., and Luo, X.-Y. "Transition from a polaronic condensate to a degenerate Fermi gas of heteronuclear molecules". *Nature Physics*, **19** (5), 720–725 (2023). doi:10.1038/s41567-023-01948-1. Cited on page 126

Eberhard, R. "Imaging of a degenerate gas of ultracold Lithium atoms". Bachelor's thesis, Ruprecht-Karls-Universität Heidelberg (2016). Cited on page 39

Edri, H., Raz, B., Matzliah, N., Davidson, N., and Ozeri, R. "Observation of Spin-Spin Fermion-Mediated Interactions between Ultracold Bosons". *Physical Review Letters*, **124** (16), 163401 (2020). doi:10.1103/PhysRevLett.124.163401. Cited on page 4

Efimov, V. "Energy levels arising from resonant two-body forces in a three-body system". *Physics Letters B*, **33** (8), 563–564 (1970). doi:10.1016/0370-2693(70)90349-7. Cited on page 3

Enss, T., Tran, B., Rautenberg, M., Gerken, M., Lippi, E., Drescher, M., Zhu, B., Weidemüller, M., and Salmhofer, M. "Scattering of two heavy Fermi polarons: Resonances and quasibound states". *Physical Review A*, **102** (6), 063321 (2020). doi:10.1103/PhysRevA.102.063321. Cited on pages 4, 79, 83, 92, 93, and 94

Esry, B. D., Greene, C. H., and Burke, J. P. "Recombination of Three Atoms in the Ultracold Limit". *Physical Review Letters*, **83** (9), 1751–1754 (1999). doi:10.1103/PhysRevLett.83.1751. Cited on page 77

Etrych, J., Martirosyan, G., Cao, A., Ho, C. J., Hadzibabic, Z., and Eigen, C. "Universal quantum dynamics of Bose polarons". `arXiv:2402.14816`. Cited on page 2

Filzinger, M. “Improved manipulation and detection of an ultracold Li6-Cs133 mixture towards the investigation of the Bose polaron”. Master’s thesis, Ruprecht-Karls-Universität Heidelberg (2018). Cited on pages 35 and 39

Foot, C. J. Atomic Physics. Oxford University Press, Inc., New York (2005). Cited on pages 103 and 104

Forbes, M. M., Gezerlis, A., Hebeler, K., Lesinski, T., and Schwenk, A. “Neutron polaron as a constraint on nuclear density functionals”. *Physical Review C*, **89** (041301(R)), 1–5 (2014). doi:10.1103/PhysRevC.89.041301. Cited on pages 1 and 81

Freund, R. “Switching polarity of a magnetic gradient field using an H bridge in an ultracold mixture of Lithium and Caesium”. Bachelor’s thesis, Ruprecht-Karls-Universität Heidelberg (2019). Cited on pages 13, 118, 127, and 128

Freund, R. “Implementation of a movable optical microtrap for mixing ultracold Li-6 and Cs-133 towards studying the polaron scenario”. Master’s thesis, Ruprecht-Karls-Universität Heidelberg (2022). Cited on pages 23, 26, 27, 29, 30, and 51

Fritsche, I., Baroni, C., Dobler, E., Kirilov, E., Huang, B., Grimm, R., Bruun, G. M., and Massignan, P. “Stability and breakdown of Fermi polarons in a strongly interacting Fermi-Bose mixture”. *Physical Review A*, **103** (5), 053314 (2021). doi:10.1103/PhysRevA.103.053314. Cited on page 2

Fröhlich, H. “Electrons in lattice fields”. *Advances in Physics*, **3** (11), 325–361 (1954). doi:https://doi.org/10.1080/00018735400101213. Cited on page 2

Frye, M. D., Yang, B. C., and Hutson, J. M. “Ultracold collisions of Cs atoms in excited Zeeman and hyperfine states”. *Physical Review A*, **100** (2), 22702 (2019). doi:10.1103/PhysRevA.100.022702. Cited on pages 96, 97, 99, and 100

Fumi, F. “CXVI. Vacancies in monovalent metals”. *The London, Edinburgh, and Dublin Philosophical Magazine and Journal of Science*, **46** (380), 1007–1020 (1955). doi:10.1080/14786440908520622. Cited on pages 83, 84, and 87

Gehm, M. E. Properties of Li-6. North Carolina (2003). Cited on page 11

Gerken, M. “Gray Molasses Cooling of Lithium-6 Towards a Degenerate Fermi Gas”. Master’s thesis, Ruprecht-Karls-Universität Heidelberg (2016). Cited on pages 11 and 53

Gerken, M. “Exploring p-wave Feshbach Resonances in Ultracold Lithium and Lithium-Cesium Mixtures”. Ph.D. thesis, Ruprecht-Karls-Universität Heidelberg (2022). doi:10.11588/heidok.00031719. Cited on pages 11, 12, 31, 36, 45, 51, and 53

Gerken, M., Tran, B., Häfner, S., Tiemann, E., Zhu, B., and Weidemüller, M. “Observation of dipolar splittings in high-resolution atom-loss spectroscopy of Li-6 p-wave Feshbach resonances”. *Physical Review A*, **100** (5), 050701 (2019). doi:10.1103/PhysRevA.100.050701. Cited on pages 30 and 32

Giorgini, S., Pitaevskii, L. P., and Stringari, S. “Theory of ultracold atomic Fermi gases”. *Reviews of Modern Physics*, **80** (4), 1215–1274 (2008). doi:10.1103/RevModPhys.80.1215. Cited on pages 43 and 44

Goodstein, D. L. States of Matter. Dover Publications, Inc., Mineola, New York (1985). Cited on page 42

Grimm, R. “Ultracold Fermi gases in the BEC-BCS crossover: A review from the Innsbruck perspective”. In “Proceedings of the International School of Physics "Enrico Fermi"”, volume 164, 413–462 (2007). ISBN 9781586038465. doi:10.3254/978-1-58603-846-5-413. Cited on page 27

Grimm, R., Weidemüller, M., and Ovchinnikov, Y. B. “Optical Dipole Traps for Neutral Atoms”. In “Advances In Atomic, Molecular and Optical Physics”, volume 42, 95–170 (2000). doi:10.1016/S1049-250X(08)60186-X. Cited on page 20

Gross, C., Gan, H. C. J., and Dieckmann, K. “All-optical production and transport of a large Li-6 quantum gas in a crossed optical dipole trap”. *Physical Review A*, **93** (5), 053424 (2016). doi:10.1103/PhysRevA.93.053424. Cited on page 57

Gross, N., Shotan, Z., Kokkelmans, S., and Khaykovich, L. “Observation of Universality in Ultracold Li-7 Three-Body Recombination”. *Physical Review Letters*, **103** (16), 163202 (2009). doi:10.1103/PhysRevLett.103.163202. Cited on page 3

Grusdt, F. and Demler, E. “New theoretical approaches to Bose polarons”. In “Proceedings of the International School of Physics "Enrico Fermi"”, volume 191, 325–411 (2016). ISBN 9781614996934. doi:10.3254/978-1-61499-694-1-325. Cited on page 1

Guenther, N.-E., Schmidt, R., Bruun, G. M., Gurarie, V., and Massignan, P. “Mobile impurity in a Bose-Einstein condensate and the orthogonality catastrophe”. *Physical Review A*, **103** (1), 013317 (2021). doi:10.1103/PhysRevA.103.013317. Cited on page 2

Hadzibabic, Z., Stan, C. A., Dieckmann, K., Gupta, S., Zwierlein, M. W., Görlitz, A., and Ketterle, W. “Two-Species Mixture of Quantum Degenerate Bose and Fermi Gases”. *Physical Review Letters*, **88** (16), 160401 (2002). doi:10.1103/PhysRevLett.88.160401. Cited on page 49

Häfner, S. “From two-body to many-body physics in an ultracold Bose-Fermi mixture of Li and Cs atoms”. Ph.D. thesis, Ruprecht-Karls-Universität Heidelberg, Heidelberg (2017). doi:10.11588/heidok.00023852. Cited on pages 11, 12, 32, 39, and 44

Häfner, S., Ulmanis, J., Kuhnle, E. D., Wang, Y., Greene, C. H., and Weidemüller, M. “Role of the intraspecies scattering length in the Efimov scenario with large mass difference”. *Physical Review A*, **95** (6), 062708 (2017). doi:10.1103/PhysRevA.95.062708. Cited on pages 3 and 48

Heck, R. “All-Optical Formation of an Ultracold Gas of Fermionic Lithium Close to Quantum Degeneracy”. Master’s thesis, Ruprecht-Karls-Universität Heidelberg (2012). Cited on pages 21, 38, and 53

Hu, H. and Liu, X.-J. “Fermi polarons at finite temperature: Spectral function and rf spectroscopy”. *Physical Review A*, **105** (4), 043303 (2022). doi:10.1103/PhysRevA.105.043303. Cited on pages 90 and 115

Hu, M.-G., Van de Graaff, M. J., Kedar, D., Corson, J. P., Cornell, E. A., and Jin, D. S. “Bose Polarons in the Strongly Interacting Regime”. *Physical Review Letters*, **117** (5), 055301 (2016). doi:10.1103/PhysRevLett.117.055301. Cited on pages 2 and 4

Hutson, J. M. “Feshbach resonances in ultracold atomic and molecular collisions: threshold behaviour and suppression of poles in scattering lengths”. *New Journal of Physics*, **9** (5), 152–152 (2007). doi:10.1088/1367-2630/9/5/152. Cited on page 98

Idziaszek, Z. and Julienne, P. S. “Universal Rate Constants for Reactive Collisions of Ultracold Molecules”. *Physical Review Letters*, **104** (11), 113202 (2010). doi:10.1103/PhysRevLett.104.113202. Cited on page 97

Ivanov, V. V., Khramov, A., Hansen, A. H., Dowd, W. H., Münchow, F., Jamison, A. O., and Gupta, S. “Sympathetic Cooling in an Optically Trapped Mixture of Alkali and Spin-Singlet Atoms”. *Physical Review Letters*, **106** (15), 153201 (2011). doi:10.1103/PhysRevLett.106.153201. Cited on page 65

Jiang, J., Li, X.-J., Wang, X., Dong, C.-Z., and Wu, Z. W. “Tune-out wavelengths of the hyperfine components of the ground level of Cs-133 atoms”. *Physical Review A*, **102** (4), 042823 (2020). doi:10.1103/PhysRevA.102.042823. Cited on page 66

Jochim, S. “Bose-Einstein Condensation of Molecules”. Ph.D. thesis, University of Innsbruck (2004). Cited on page 54

Joffe, M. A., Ketterle, W., Martin, A., and Pritchard, D. E. “Transverse cooling and deflection of an atomic beam inside a Zeeman slower”. *Journal of the Optical Society of America B*, **10** (12), 2257 (1993). doi:10.1364/JOSAB.10.002257. Cited on page 15

Johansen, J., DeSalvo, B. J., Patel, K., and Chin, C. “Testing universality of Efimov physics across broad and narrow Feshbach resonances”. *Nature Physics*, **13** (8), 731–735 (2017). doi:10.1038/nphys4130. Cited on page 3

Jørgensen, N. B., Wacker, L., Skalmstang, K. T., Parish, M. M., Levinsen, J., Christensen, R. S., Bruun, G. M., and Arlt, J. J. “Observation of Attractive and Repulsive Polarons in a Bose-Einstein Condensate”. *Physical Review Letters*, **117** (5), 055302 (2016). doi:10.1103/PhysRevLett.117.055302. Cited on pages 2 and 4

Kaplan, A., Andersen, M. F., Grünzweig, T., and Davidson, N. “Hyperfine spectroscopy of optically trapped atoms”. *Journal of Optics B*, **7** (8), R103–R125 (2005). doi:10.1088/1464-4266/7/8/R01. Cited on page 67

Kerman, A. J., Vuletić, V., Chin, C., and Chu, S. "Beyond Optical Molasses: 3D Raman Sideband Cooling of Atomic Cesium to High Phase-Space Density". *Physical Review Letters*, **84** (3), 439–442 (2000). doi:10.1103/PhysRevLett.84.439. Cited on page 59

Ketterle, W., Durfee, D. S., and Stamper-Kurn, D. M. "Making, probing and understanding Bose-Einstein condensates". `arXiv:9904034 [cond-mat]`. Cited on pages 32, 36, 42, 43, and 58

Ketterle, W. and Zwierlein, M. W. "Making, probing and understanding ultracold Fermi gases". `arXiv:0801.2500`. Cited on pages 38, 43, 44, 46, and 75

Klaus, L. "Design and construction of an optical Microtrap to studz the polaron scenario in an ultracold Li6-Cs133 mixture". Master's thesis, Ruprecht-Karls-Universität Heidelberg (2019). Cited on pages 26 and 39

Knap, M., Shashi, A., Nishida, Y., Imambekov, A., Abanin, D. A., and Demler, E. "Time-Dependent Impurity in Ultracold Fermions: Orthogonality Catastrophe and Beyond". *Physical Review X*, **2** (4), 041020 (2012). doi:10.1103/PhysRevX.2.041020. Cited on pages 5, 89, 90, and 122

Knoop, S., Ferlaino, F., Mark, M., Berninger, M., Schöbel, H., Nägerl, H.-C., and Grimm, R. "Observation of an Efimov-like trimer resonance in ultracold atom–dimer scattering". *Nature Physics*, **5** (3), 227–230 (2009). doi:10.1038/nphys1203. Cited on page 3

Kohstall, C., Zaccanti, M., Jag, M., Trenkwalder, A., Massignan, P., Bruun, G. M., Schreck, F., and Grimm, R. "Metastability and coherence of repulsive polarons in a strongly interacting Fermi mixture". *Nature*, **485** (7400), 615–618 (2012). doi:10.1038/nature11065. Cited on pages 2, 82, 85, 114, and 115

Koschorreck, M., Pertot, D., Vogt, E., Fröhlich, B., Feld, M., and Köhl, M. "Attractive and repulsive Fermi polarons in two dimensions". *Nature*, **485** (7400), 619–622 (2012). doi:10.1038/nature11151. Cited on pages 2 and 82

Kraemer, T., Mark, M., Waldburger, P., Danzl, J. G., Chin, C., Engeser, B., Lange, A. D., Pilch, K., Jaakkola, A., Nägerl, H.-C., and Grimm, R. "Evidence for Efimov quantum states in an ultracold gas of caesium atoms". *Nature*, **440** (7082), 315–318 (2006). doi:10.1038/nature04626. Cited on pages 3, 60, and 77

Kraft, S. "Formation of ultracold LiCs molecules". Ph.D. thesis, University of Freiburg (2006). Cited on page 49

Landau, L. D. "Electron Motion In Crystal Lattices". In "Physikalische Zeitschrift der Sowjetunion", volume 3, 67–68 (1933). doi:10.1016/b978-0-08-010586-4.50015-8. Cited on page 1

Le Kien, F., Schneeweiss, P., and Rauschenbeutel, A. "Dynamical polarizability of atoms in arbitrary light fields: general theory and application to cesium". *The European Physical Journal D*, **67** (5), 92 (2013). doi:10.1140/epjd/e2013-30729-x. Cited on page 20

LeBlanc, L. J. and Thywissen, J. H. "Species-specific optical lattices". *Physical Review A*, **75** (5), 053612 (2007). doi:10.1103/PhysRevA.75.053612. Cited on pages 20, 21, 50, and 66

Levinsen, J., Parish, M. M., and Bruun, G. M. "Impurity in a Bose-Einstein Condensate and the Efimov Effect". *Physical Review Letters*, **115** (12), 125302 (2015). doi:10.1103/PhysRevLett.115.125302. Cited on pages 2, 3, and 126

Levitov, L. S. and Lesovik, G. B. "Charge distribution in quantum shot noise". *Journal of Experimental and Theoretical Physics Letters*, **58** (3), 230–235 (1993). Cited on page 90

Li, W.-X., Chen, Y.-D., Sun, Y.-T., Tung, S., and Julienne, P. S. "Feshbach resonances in an ultracold Li-7 - Cs-133 Bose-Bose mixture". *Physical Review A*, **106** (2), 023317 (2022). doi:10.1103/PhysRevA.106.023317. Cited on page 3

Linskens, A. F., Holleman, I., Dam, N., and Reuss, J. "Two-photon Rabi oscillations". *Physical Review A*, **54** (6), 4854–4862 (1996). doi:10.1103/PhysRevA.54.4854. Cited on pages 106 and 107

Liu, R., Peng, C., and Cui, X. "Emergence of crystalline few-body correlations in mass-imbalanced Fermi polarons". *Cell Reports Physical Science*, **3** (8), 100993 (2022). doi:10.1016/j.xcrp.2022.100993. Cited on page 2

Liu, W. E., Shi, Z.-Y., Parish, M. M., and Levinsen, J. "Theory of radio-frequency spectroscopy of impurities in quantum gases". *Physical Review A*, **102** (2), 023304 (2020). doi:10.1103/PhysRevA.102.023304. Cited on pages 83, 87, 90, 91, 92, and 115

Lobo, C., Recati, A., Giorgini, S., and Stringari, S. "Normal State of a Polarized Fermi Gas at Unitarity". *Physical Review Letters*, **97** (20), 200403 (2006). doi:10.1103/PhysRevLett.97.200403. Cited on page 84

Lompe, T. "Effimov Physics in a three-component Fermi gas". Ph.D. thesis, University of Heidelberg, Heidelberg (2011). doi:10.11588/heidok.00012212. Cited on page 54

Lompe, T., Ottenstein, T. B., Serwane, F., Wenz, A. N., Zürn, G., and Jochim, S. "Radio-Frequency Association of Efimov Trimers". *Science*, **330** (6006), 940–944 (2010). doi:10.1126/science.1193148. Cited on page 3

Loudon, R. The Quantum Theory of Light. Oxford University Press, Inc., New York (2000). Cited on pages 68 and 103

Lous, R. S., Fritsche, I., Jag, M., Huang, B., and Grimm, R. "Thermometry of a deeply degenerate Fermi gas with a Bose-Einstein condensate". *Physical Review A*, **95** (5), 053627 (2017). doi:10.1103/PhysRevA.95.053627. Cited on page 80

Lous, R. S., Fritsche, I., Jag, M., Lehmann, F., Kirilov, E., Huang, B., and Grimm, R. "Probing the Interface of a Phase-Separated State in a Repulsive Bose-Fermi Mixture". *Physical Review Letters*, **120** (24), 243403 (2018). doi:10.1103/PhysRevLett.120.243403. Cited on page 79

Luo, L., Clancy, B., Joseph, J., Kinast, J., Turlapov, A., and Thomas, J. E. "Evaporative cooling of unitary Fermi gas mixtures in optical traps". *New Journal of Physics*, **8** (9), 213–213 (2006). doi:10.1088/1367-2630/8/9/213. Cited on page 55

Mahan, G. D. Many-particle Physics. Kluwer Academic, New York (2000). Cited on pages 1, 2, and 81

Maier, R. A., Eisele, M., Tiemann, E., and Zimmermann, C. "Efimov Resonance and Three-Body Parameter in a Lithium-Rubidium Mixture". *Physical Review Letters*, **115** (4), 1–5 (2015). doi:10.1103/PhysRevLett.115.043201. Cited on page 4

Marti, G. E., Olf, R., Vogt, E., Öttl, A., and Stamper-Kurn, D. M. "Two-element Zeeman slower for rubidium and lithium". *Physical Review A*, **81** (4), 043424 (2010). doi:10.1103/PhysRevA.81.043424. Cited on page 15

Massignan, P., Zaccanti, M., and Bruun, G. M. "Polarons, dressed molecules and itinerant ferromagnetism in ultracold Fermi gases". *Reports on Progress in Physics*, **77** (3), 034401 (2014). doi:10.1088/0034-4885/77/3/034401. Cited on pages 81 and 88

Mathy, C. J. M., Parish, M. M., and Huse, D. A. "Trimers, Molecules, and Polarons in Mass-Imbalanced Atomic Fermi Gases". *Physical Review Letters*, **106** (16), 166404 (2011). doi:10.1103/PhysRevLett.106.166404. Cited on page 2

Matthies, J. "Towards Ultracold Lithium-Caesium Ground State Molecules". Master's thesis, Imperial College London, UK and Ruprecht-Karls-Universität Heidelberg (2018). Cited on page 26

Mattuck, R. A Guide to Feynman Diagrams of the Many-Body Problem. McGraw-Hill, Inc., New York (1976). Cited on page 1

Metcalf, H. J. and van der Straten, P. Laser cooling and trapping. Springer-Verlag New York, Inc., New York (1999). Cited on pages 14 and 15

Mosk, A., Kraft, S., Mudrich, M., Singer, K., Wohlleben, W., Grimm, R., and Weidemüller, M. "Mixture of ultracold lithium and cesium atoms in an optical dipole trap". *Applied Physics B*, **73** (8), 791–799 (2001). doi:10.1007/s003400100743. Cited on pages 65 and 66

Mott, N. "Polaron models of high-temperature superconductivity". *Physica C: Superconductivity*, **205** (1-2), 191–205 (1993). doi:10.1016/0921-4534(93)90187-U. Cited on page 1

Mudrich, M., Kraft, S., Singer, K., Grimm, R., Mosk, A., and Weidemüller, M. "Sympathetic Cooling with Two Atomic Species in an Optical Trap". *Physical Review Letters*, **88** (25), 253001 (2002). doi:10.1103/PhysRevLett.88.253001. Cited on page 66

Muir, J. B., Levinsen, J., Earl, S. K., Conway, M. A., Cole, J. H., Wurdack, M., Mishra, R., Ing, D. J., Estrecho, E., Lu, Y., Efimkin, D. K., Tollerud, J. O., Ostrovskaya, E. A., Parish, M. M., and Davis, J. A. "Interactions between Fermi polarons in monolayer WS2". *Nature Communications*, **13** (1), 6164 (2022). doi:10.1038/s41467-022-33811-x. Cited on pages 1 and 81

Nakajima, S., Horikoshi, M., Mukaiyama, T., Naidon, P., and Ueda, M. "Nonuniversal Efimov Atom-Dimer Resonances in a Three-Component Mixture of Li-6". *Physical Review Letters*, **105** (2), 023201 (2010). doi:10.1103/PhysRevLett.105.023201. Cited on page 3

Nakano, E., Iida, K., and Horiuchi, W. "Quasiparticle properties of a single α- particle in cold neutron matter". *Physical Review C*, **102** (5), 055802 (2020). doi:10.1103/PhysRevC.102.055802. Cited on pages 1 and 81

Neiczer, M. "Efficient creation of a molecular Bose-Einstein condensate of Lithium-6 using a spatially modulated dipole trap". Master's thesis, Ruprecht-Karls-Universität Heidelberg (2018). Cited on pages 11, 21, and 53

Ness, G., Shkedrov, C., Florshaim, Y., Diessel, O. K., von Milczewski, J., Schmidt, R., and Sagi, Y. "Observation of a Smooth Polaron-Molecule Transition in a Degenerate Fermi Gas". *Physical Review X*, **10** (4), 041019 (2020). doi:10.1103/PhysRevX.10.041019. Cited on pages 2, 6, 82, 89, 101, 102, 119, and 126

Nishida, Y. "Casimir interaction among heavy fermions in the BCS-BEC crossover". *Physical Review A*, **79** (1), 013629 (2009). doi:10.1103/PhysRevA.79.013629. Cited on page 4

Nozières, P. and De Dominicis, C. T. "Singularities in the X-Ray Absorption and Emission of Metals. III. One-Body Theory Exact Solution". *Physical Review*, **178** (3), 1097–1107 (1969). doi:10.1103/PhysRev.178.1097. Cited on pages 1 and 81

O'Hara, K. M., Gehm, M. E., Granade, S. R., and Thomas, J. E. "Scaling laws for evaporative cooling in time-dependent optical traps". *Physical Review A*, **64** (5), 051403 (2001). doi:10.1103/PhysRevA.64.051403. Cited on pages 55 and 57

Ospelkaus, S., Ospelkaus, C., Dinter, R., Fuchs, J., Nakat, M., Sengstock, K., and Bongs, K. "Degenerate K–Rb Fermi–Bose gas mixtures with large particle numbers". *Journal of Modern Optics*, **54** (5), 661–673 (2007). doi:10.1080/09500340600777763. Cited on page 49

Parish, M. M. and Levinsen, J. "Quantum dynamics of impurities coupled to a Fermi sea". *Physical Review B*, **94** (18), 184303 (2016). doi:10.1103/PhysRevB.94.184303. Cited on page 114

Patel, K., Cai, G., Ando, H., and Chin, C. "Sound Propagation in a Bose-Fermi Mixture: From Weak to Strong Interactions". *Physical Review Letters*, **131** (8), 083003 (2023). doi:10.1103/PhysRevLett.131.083003. Cited on pages 3, 4, 48, 79, 93, and 126

Pethick and Shmidt. Bose–Einstein Condensation in dilute gases. Cambridge University Press, Cambridge (2001). Cited on pages 27 and 43

Petrov, D. S. "The few-atom problem". In "Many-Body Physics with Ultracold Gases", 109–160. Oxford University Press, Oxford (2012). doi:10.1093/acprof:oso/9780199661886.003.0003. Cited on page 46

Petrov, D. S. and Werner, F. "Three-body recombination in heteronuclear mixtures at finite temperature". *Physical Review A*, **92** (2), 022704 (2015). doi:10.1103/PhysRevA.92.022704. Cited on page 77

Phillips, W. D. and Metcalf, H. "Laser Deceleration of an Atomic Beam". *Physical Review Letters*, **48** (9), 596–599 (1982). doi:10.1103/PhysRevLett.48.596. Cited on page 14

Pires, R. "Efimov Resonances in an Ultracold Mixture with Extreme Mass Imbalance". Ph.D. thesis, Ruprecht-Karls-Universität Heidelberg (2014). doi:10.11588/heidok.00017133. Cited on pages 3, 12, 13, 50, and 127

Pires, R., Repp, M., Ulmanis, J., Kuhnle, E. D., Weidemüller, M., Tiecke, T. G., Greene, C. H., Ruzic, B. P., Bohn, J. L., and Tiemann, E. "Analyzing Feshbach resonances: A Li-6 - Cs-133 case study". *Physical Review A*, **90** (1), 012710 (2014a). doi:10.1103/PhysRevA.90.012710. Cited on pages 3, 41, 48, 95, 96, and 99

Pires, R., Ulmanis, J., Häfner, S., Repp, M., Arias, A., Kuhnle, E. D., and Weidemüller, M. "Observation of Efimov Resonances in a Mixture with Extreme Mass Imbalance". *Physical Review Letters*, **112** (25), 250404 (2014b). doi:10.1103/PhysRevLett.112.250404. Cited on pages 3 and 118

Pollack, S. E., Dries, D., and Hulet, R. G. "Universality in Three- and Four-Body Bound States of Ultracold Atoms". *Science*, **326** (5960), 1683–1685 (2009). doi:10.1126/science.1182840. Cited on page 3

Prokof'ev, N. V. "Effective Masses of Ions in Superfluid in He-3 B". *Physical Review Letters*, **74** (14), 2748–2751 (1995). doi:10.1103/PhysRevLett.74.2748. Cited on pages 1 and 81

Punk, M., Dumitrescu, P. T., and Zwerger, W. "Polaron-to-molecule transition in a strongly imbalanced Fermi gas". *Physical Review A*, **80** (5), 053605 (2009). doi:10.1103/PhysRevA.80.053605. Cited on page 88

Rakshit, D., Karpiuk, T., Brewczyk, M., and Gajda, M. "Quantum Bose-Fermi droplets". *SciPost Physics*, **6** (6), 079 (2019a). doi:10.21468/SciPostPhys.6.6.079. Cited on page 126

Rakshit, D., Karpiuk, T., Zin, P., Brewczyk, M., Lewenstein, M., and Gajda, M. "Self-bound Bose–Fermi liquids in lower dimensions". *New Journal of Physics*, **21** (7), 073027 (2019b). doi:10.1088/1367-2630/ab2ce3. Cited on page 126

Ratkata, A., Gregory, P. D., Innes, A. D., Matthies, A. J., McArd, L. A., Mortlock, J. M., Safronova, M. S., Bromley, S. L., and Cornish, S. L. "Measurement of the tune-out wavelength for Cs-133 at 880 nm". *Physical Review A*, **104** (5), 052813 (2021). doi:10.1103/PhysRevA.104.052813. Cited on pages 20 and 66

Rautenberg, M. "Theoretical considerations concerning the relation of the Efimov scenario to Fermi polarons and upgrade of a polaron experiment". Master's thesis, Ruprecht-Karls-Universität Heidelberg (2021). Cited on pages 39 and 59

Renner, C. “Design and characterization of a dual-wavelength high-resolution imaging system”. Diploma’s thesis, Ruprecht-Karls-Universität Heidelberg, Heidelberg (2014). Cited on page 39

Rentrop, T., Trautmann, A., Olivares, F. A., Jendrzejewski, F., Komnik, A., and Oberthaler, M. K. “Observation of the Phononic Lamb Shift with a Synthetic Vacuum”. *Physical Review X*, **6** (4), 041041 (2016). doi:10.1103/PhysRevX.6.041041. Cited on page 2

Repp, M. “Interspecies Feshbach Resonances in an ultracold, optically trapped Bose-Fermi mixture of Cesium an Lithium”. Ph.D. thesis, Ruprecht-Karls-Universität Heidelberg (2013). doi:10.11588/heidok.00014993. Cited on pages 11, 12, 14, 16, 17, 18, and 95

Repp, M., Pires, R., Ulmanis, J., Heck, R., Kuhnle, E. D., Weidemüller, M., and Tiemann, E. “Observation of interspecies Li-6 - Cs-133 Feshbach resonances”. *Physical Review A*, **87** (1), 010701 (2013). doi:10.1103/PhysRevA.87.010701. Cited on pages 3, 41, 48, 97, and 118

Rose, F. and Schmidt, R. “Disorder in order: Localization without randomness in a cold-atom system”. *Physical Review A*, **105** (1), 013324 (2022). doi:10.1103/PhysRevA.105.013324. Cited on page 3

Roy, S., Landini, M., Trenkwalder, A., Semeghini, G., Spagnolli, G., Simoni, A., Fattori, M., Inguscio, M., and Modugno, G. “Test of the Universality of the Three-Body Efimov Parameter at Narrow Feshbach Resonances”. *Physical Review Letters*, **111** (5), 053202 (2013). doi:10.1103/PhysRevLett.111.053202. Cited on page 3

Savard, T. A., O’Hara, K. M., and Thomas, J. E. “Laser-noise-induced heating in far-off resonance optical traps”. *Physical Review A*, **56** (2), 514–518 (1997). Cited on page 29

Scazza, F., Valtolina, G., Massignan, P., Recati, A., Amico, A., Burchianti, A., Fort, C., Inguscio, M., Zaccanti, M., and Roati, G. “Repulsive Fermi Polarons in a Resonant Mixture of Ultracold Li-6 Atoms”. *Physical Review Letters*, **118** (8), 083602 (2017). doi:10.1103/PhysRevLett.118.083602. Cited on pages 2, 82, 84, 114, and 115

Scazza, F., Zaccanti, M., Massignan, P., Parish, M. M., and Levinsen, J. “Repulsive Fermi and Bose Polarons in Quantum Gases”. *Atoms*, **10** (2), 55 (2022). doi:10.3390/atoms10020055. Cited on pages 1, 81, and 83

Schirotzek, A., Wu, C.-H., Sommer, A., and Zwierlein, M. W. “Observation of Fermi Polarons in a Tunable Fermi Liquid of Ultracold Atoms”. *Physical Review Letters*, **102** (23), 230402 (2009). doi:10.1103/PhysRevLett.102.230402. Cited on pages 2, 82, 84, 95, and 115

Schlöder, U., Engler, H., Schünemann, U., Grimm, R., and Weidemüller, M. “Cold inelastic collisions between lithium and cesium in a two-species magneto-optical trap”. *The European Physical Journal D*, **7** (3), 331 (1999). doi:10.1007/s100530050576. Cited on pages 19 and 49

Schmidt, R. and Enss, T. “Excitation spectra and rf response near the polaron-to-molecule transition from the functional renormalization group”. *Physical Review A*, **063620**, 1–14 (2011). doi:10.1103/PhysRevA.83.063620. Cited on page 88

Schmidt, R., Knap, M., Ivanov, D. A., You, J.-S., Cetina, M., and Demler, E. “Universal many-body response of heavy impurities coupled to a Fermi sea: a review of recent progress”. *Reports on Progress in Physics*, **81** (2), 024401 (2018). doi:10.1088/1361-6633/aa9593. Cited on pages 1, 2, 5, 81, 83, 87, 89, 90, 121, and 126

Schoenhals, A. “Imaging of ultracold Cesium atoms at high magnetic fields”. Master’s thesis, Ruprecht-Karls-Universität Heidelberg (2013). Cited on pages 38 and 72

Schott, S., Chopra, U., Lemaur, V., Melnyk, A., Olivier, Y., Di Pietro, R., Romanov, I., Carey, R. L., Jiao, X., Jellett, C., Little, M., Marks, A., McNeill, C. R., McCulloch, I., McNellis, E. R., Andrienko, D., Beljonne, D., Sinova, J., and Sirringhaus, H. “Polaron spin dynamics in high-mobility polymeric semiconductors”. *Nature Physics*, **15** (8), 814–822 (2019). doi:10.1038/s41567-019-0538-0. Cited on page 1

Schünemann, U., Engler, H., Grimm, R., Weidemüller, M., and Zielonkowski, M. “Simple scheme for tunable frequency offset locking of two lasers”. *Review of Scientific Instruments*, **70** (1), 242–243 (1999). doi:10.1063/1.1149573. Cited on page 38

Schünemann, U., Engler, H., Zielonkowski, M., Weidemüller, M., and Grimm, R. “Magneto-optic trapping of lithium using semiconductor lasers”. *Optics Communications*, **158** (1-6), 263–272 (1998). doi:10.1016/S0030-4018(98)00517-3. Cited on pages 15 and 19

Schürg, A. “Optimisation of microsecond laser pulses for lithium absorption imaging”. Bachelor’s thesis, Ruprecht-Karls-Universität Heidelberg (2024). Cited on pages 38 and 79

Shkedrov, C., Ness, G., Florshaim, Y., and Sagi, Y. “In situ momentum-distribution measurement of a quantum degenerate Fermi gas using Raman spectroscopy”. *Physical Review A*, **101** (1), 013609 (2020). doi:10.1103/PhysRevA.101.013609. Cited on pages 6, 102, and 126

Sidler, M., Back, P., Cotlet, O., Srivastava, A., Fink, T., Kroner, M., Demler, E., and Imamoglu, A. “Fermi polaron-polaritons in charge-tunable atomically thin semiconductors”. *Nature Physics*, **13**, 255–262 (2017). doi:10.1038/NPHYS3949. Cited on pages 1 and 81

Silber, C., Günther, S., Marzok, C., Deh, B., Courteille, P. W., and Zimmermann, C. “Quantum-degenerate mixture of fermionic lithium and bosonic rubidium gases”. *Physical Review Letters*, **95** (17) (2005). doi:10.1103/PhysRevLett.95.170408. Cited on pages 49 and 65

Simonelli, C., Neri, E., Ciamei, A., Goti, I., Inguscio, M., Trenkwalder, A., and Zaccanti, M. “Realization of a high power optical trapping setup free from thermal lensing effects”. *Optics Express*, **27** (19), 27215 (2019). doi:10.1364/OE.27.027215. Cited on page 53

Skou, M. G., Nielsen, K. K., Skov, T. G., Morgen, A. M., Jørgensen, N. B., Camacho-Guardian, A., Pohl, T., Bruun, G. M., and Arlt, J. J. “Life and death of the Bose polaron”. *Physical Review Research*, **4** (4), 043093 (2022). doi:10.1103/PhysRevResearch.4.043093. Cited on page 2

Skou, M. G., Skov, T. G., Jørgensen, N. B., Nielsen, K. K., Camacho-Guardian, A., Pohl, T., Bruun, G. M., and Arlt, J. J. “Non-equilibrium quantum dynamics and formation of the Bose polaron”. *Nature Physics*, **17** (6), 731–735 (2021). doi:10.1038/s41567-021-01184-5. Cited on page 2

Spiegelhalder, F. M., Trenkwalder, A., Naik, D., Kerner, G., Wille, E., Hendl, G., Schreck, F., and Grimm, R. “All-optical production of a degenerate mixture of Li-6”. *Physical Review A*, **81** (4), 043637 (2010). doi:10.1103/PhysRevA.81.043637. Cited on page 49

Stan, C. A. and Ketterle, W. “Multiple species atom source for laser-cooling experiments”. *Review of Scientific Instruments*, **76** (6) (2005). doi:10.1063/1.1935433. Cited on page 11

Steck, D. A. Cesium D Line Data. http://steck.us/alkalidata, Oregon (2023). Cited on pages 11, 102, 103, and 104

Steck, D. A. Quantum and atomic optics. http://steck.us/teaching, Oregon (2024). Cited on pages 104 and 109

Sun, M. and Cui, X. “Enhancing the Efimov correlation in Bose polarons with large mass imbalance”. *Physical Review A*, **96** (2), 022707 (2017). doi:10.1103/PhysRevA.96.022707. Cited on pages 2 and 4

Sun, M. and Cui, X. “Efimov physics in the presence of a Fermi sea”. *Physical Review A*, **99** (6), 060701 (2019). doi:10.1103/PhysRevA.99.060701. Cited on page 4

Sun, M., Zhai, H., and Cui, X. “Visualizing the Efimov Correlation in Bose Polarons”. *Physical Review Letters*, **119** (1), 013401 (2017). doi:10.1103/PhysRevLett.119.013401. Cited on pages 2, 3, and 4

Tran, B. “From Efimov Physics to Polarons in an Ultracold Mixture of Li and Cs Atoms”. Ph.D. thesis, Ruprecht-Karls-Universität Heidelberg (2022). doi:10.11588/heidok.00031882. Cited on pages 12, 14, 21, 35, 36, 51, 59, 92, and 126

Tran, B., Rautenberg, M., Gerken, M., Lippi, E., Zhu, B., Ulmanis, J., Drescher, M., Salmhofer, M., Enss, T., and Weidemüller, M. “Fermions Meet Two Bosons—the Heteronuclear Efimov Effect Revisited”. *Brazilian Journal of Physics*, **51** (2), 316–322 (2021). doi:10.1007/s13538-020-00811-5. Cited on page 4

Trefzger, C. and Castin, Y. “Impurity in a Fermi sea on a narrow Feshbach resonance: A variational study of the polaronic and dimeronic branches”. *Physical Review A*, **85** (5), 053612 (2012). doi:10.1103/PhysRevA.85.053612. Cited on page 88

Treutlein, P., Chung, K. Y., and Chu, S. “High-brightness atom source for atomic fountains”. *Physical Review A*, **63** (5), 051401 (2001). doi:10.1103/PhysRevA.63.051401. Cited on page 59

Tung, S. K., Jiménez-García, K., Johansen, J., Parker, C. V., and Chin, C. “Geometric scaling of efimov states in a Li-6 - Cs-133 mixture”. *Physical Review Letters*, **113** (24), 1–5 (2014). doi:10.1103/PhysRevLett.113.240402. Cited on page 3

Tung, S. K., Parker, C., Johansen, J., Chin, C., Wang, Y., and Julienne, P. S. “Ultracold mixtures of atomic Li-6 and Cs-133 with tunable interactions”. *Physical Review A*, **87** (1), 1–4 (2013). doi:10.1103/PhysRevA.87.010702. Cited on pages 3, 41, 48, 74, and 120

Ulmanis, J. “Universality and non-universality in the heteronuclear Emov scenario with large mass imbalance”. Ph.D. thesis, Ruprecht-Karls-Universität Heidelberg (2015). doi:10.11588/heidok.00019214. Cited on pages 32, 66, 74, 75, 76, and 77

Ulmanis, J., Häfner, S., Kuhnle, E. D., and Weidemüller, M. “Heteronuclear Efimov resonances in ultracold quantum gases”. *National Science Review*, **3** (2), 174–188 (2016a). doi:10.1093/nsr/nww018. Cited on page 3

Ulmanis, J., Häfner, S., Pires, R., Kuhnle, E. D., Wang, Y., Greene, C. H., and Weidemüller, M. “Heteronuclear Efimov Scenario with Positive Intraspecies Scattering Length”. *Physical Review Letters*, **117** (15), 153201 (2016b). doi:10.1103/PhysRevLett.117.153201. Cited on pages 3, 4, 48, and 118

Ulmanis, J., Häfner, S., Pires, R., Kuhnle, E. D., Weidemüller, M., and Tiemann, E. “Universality of weakly bound dimers and Efimov trimers close to Li–Cs Feshbach resonances”. *New Journal of Physics*, **17** (5), 055009 (2015). doi:10.1088/1367-2630/17/5/055009. Cited on pages 3, 47, 48, 95, and 96

Ulmanis, J., Häfner, S., Pires, R., Werner, F., Petrov, D. S., Kuhnle, E. D., and Weidemüller, M. “Universal three-body recombination and Efimov resonances in an ultracold Li-Cs mixture”. *Physical Review A*, **93** (2), 022707 (2016c). doi:10.1103/PhysRevA.93.022707. Cited on pages 3, 48, and 50

Vale, C. J. and Zwierlein, M. “Spectroscopic probes of quantum gases”. *Nature Physics*, **17** (12), 1305–1315 (2021). doi:10.1038/s41567-021-01434-6. Cited on pages 32 and 101

Veeravalli, G., Kuhnle, E., Dyke, P., and Vale, C. J. “Bragg Spectroscopy of a Strongly Interacting Fermi Gas”. *Physical Review Letters*, **101** (25), 250403 (2008). doi:10.1103/PhysRevLett.101.250403. Cited on pages 6, 102, and 126

Vidaña, I. “Fermi polaron in low-density spin-polarized neutron matter”. *Physical Review C*, **103** (5), L052801 (2021). doi:10.1103/PhysRevC.103.L052801. Cited on pages 1 and 81

Vivanco, F. J., Schuckert, A., Huang, S., Schumacher, G. L., Assumpção, G. G. T., Ji, Y., Chen, J., Knap, M., and Navon, N. "The strongly driven Fermi polaron". `arXiv:2308.05746`. Cited on page 126

Viverit, L., Giorgini, S., Pitaevskii, L. P., and Stringari, S. "Adiabatic compression of a trapped Fermi gas". *Physical Review A*, **63** (3), 033603 (2001). doi:10.1103/PhysRevA.63.033603. Cited on page 55

Vuletic, V., Chin, C., Kerman, A. J., and Chu, S. "Degenerate raman sideband cooling of trapped cesium atoms at very high atomic densities". *Physical Review Letters*, **81** (26), 5768–5771 (1998). doi:10.1103/PhysRevLett.81.5768. Cited on page 59

Walraven, J. Quantum Gases. https://staff.fnwi.uva.nl/j.t.m.walraven, Amsterdam (2019). Cited on page 58

Wang, J., Liu, X.-j., and Hu, H. "Exact Quasiparticle Properties of a Heavy Polaron in BCS Fermi Superfluids". *Physical Review Letters*, **128** (17), 175301 (2022). doi:10.1103/PhysRevLett.128.175301. Cited on pages 122 and 126

Weber, T., Herbig, J., Mark, M., Naegerl, H.-C., and Grimm, R. "Bose-Einstein Condensation of Cesium". *Science*, **299** (5604), 232–235 (2003). doi:10.1126/science.1079699. Cited on page 17

Weiner, J., Bagnato, V. S., Zilio, S., and Julienne, P. S. "Experiments and theory in cold and ultracold collisions". *Reviews of Modern Physics*, **71** (1), 1–85 (1999). doi:10.1103/RevModPhys.71.1. Cited on page 49

Welz, K. "Gaining Deeper Understanding of Interaction-Induced Processes in Ultracold Gases". Master's thesis, Ruprecht-Karls-Universität Heidelberg (2024). Cited on pages 67, 68, 72, 103, 104, 108, and 109

Williams, J. R., Hazlett, E. L., Huckans, J. H., Stites, R. W., Zhang, Y., and O'Hara, K. M. "Evidence for an Excited-State Efimov Trimer in a Three-Component Fermi Gas". *Physical Review Letters*, **103** (13), 130404 (2009). doi:10.1103/PhysRevLett.103.130404. Cited on page 3

Wu, H. and Foot, C. J. "Direct simulation of evaporative cooling". *Journal of Physics B*, **29** (8), L321–L328 (1996). doi:10.1088/0953-4075/29/8/003. Cited on page 66

Yan, Z. Z., Ni, Y., Chuang, A., Dolgirev, P. E., Seetharam, K., Demler, E., Robens, C., and Zwierlein, M. "Collective flow of fermionic impurities immersed in a Bose–Einstein condensate". *Nature Physics* (2024a). doi:10.1038/s41567-024-02541-w. Cited on page 126

Yan, Z. Z., Ni, Y., Robens, C., and Zwierlein, M. W. "Bose polarons near quantum criticality". *Science*, **368** (6487), 190–194 (2020). doi:10.1126/science.aax5850. Cited on pages 2, 4, and 79

Yan, Z., Patel, P. B., Mukherjee, B., Fletcher, R. J., Struck, J., and Zwierlein, M. W. "Boiling a Unitary Fermi Liquid". *Physical Review Letters*, **122** (9), 093401 (2019). doi:10.1103/PhysRevLett.122.093401. Cited on pages 2, 82, 84, 89, and 115

Yan, Z., Patel, P. B., Mukherjee, B., Vale, C. J., Fletcher, R. J., and Zwierlein, M. W. "Thermography of the superfluid transition in a strongly interacting Fermi gas". *Science*, **383** (6683), 629–633 (2024b). doi:10.1126/science.adg3430. Cited on page 80

Zaccanti, M., Deissler, B., Derrico, C., Fattori, M., Jona-Lasinio, M., Müller, S., Roati, G., Inguscio, M., and Modugno, G. "Observation of an efimov spectrum in an atomicsystem". *Nature Physics*, **5** (8), 586–591 (2009). doi:10.1038/nphys1334. Cited on page 3

Zhang, Y., Ong, W., Arakelyan, I., and Thomas, J. E. "Polaron-to-Polaron Transitions in the Radio-Frequency Spectrum of a Quasi-Two-Dimensional Fermi Gas". *Physical Review Letters*, **108** (23), 235302 (2012). doi:10.1103/PhysRevLett.108.235302. Cited on pages 2 and 82

Zhu, B., Häfner, S., Tran, B., Gerken, M., Ulmanis, J., Tiemann, E., and Weidemüller, M. "High partial-wave Feshbach resonances in an ultracold Li-6 - Cs-133 mixture". `arXiv:1912.01264`. Cited on pages 3, 30, 32, and 48

Zhu, B., Häfner, S., Tran, B., Gerken, M., Ulmanis, J., Tiemann, E., and Weidemüller, M. "Spin-rotation coupling in p-wave Feshbach resonances". `arXiv:1910.12011`. Cited on pages 3, 30, 32, 48, and 118

Zürn, G., Lompe, T., Wenz, A. N., Jochim, S., Julienne, P. S., and Hutson, J. M. "Precise Characterization of Li-6 Feshbach Resonances Using Trap-Sideband-Resolved RF Spectroscopy of Weakly Bound Molecules". *Physical Review Letters*, **110** (13), 135301 (2013). doi:10.1103/PhysRevLett.110.135301. Cited on page 54

Acknowledgements

Here we are, at the end of this long journey. I will always remember the time in Heidelberg as a period of intense learning and research, of deep personal and scientific growth, made possible by the opportunity to meet amazing people and to have at disposal great research infrastructures. I would like to thank for that, but not only,...

...my supervisor *Prof. Matthias Weidemüller*, for the great opportunity to pursue my doctoral thesis in his group, in a very solid and stimulating environment. Your eclectic and outstanding personality has created an open and international atmosphere, and your great physical intuition was always inspiring to me. Your support and guidance have been fundamental to the completion of this thesis. Thank you for providing the necessary framework to work successfully in the group, from participation in schools and conferences to very good funding opportunities. Motivated by your positive attitude and by the confidence you gave me, I was able to prove myself and develop both professionally and personally under your guidance, taking on new challenges and responsibilities early on.

...my second referee *Prof. Markus Oberthaler* for have taken the responsability to reviewing this work, as well as *Prof. Tilman Enss* and *Prof. Joerg Evers* for being part of my defence committee.

...*Prof. Lauriane Chomaz*, for all the constructive discussions and close supervision you have provided to our experiment since you arrived. Your new ideas and perspectives have been very stimulating and helpful for me and the development of the lab work! Thank you also for sponsoring me to present our work in seminars and workshops.

...*Prof. Tilman Enss* for the active and constant collaboration on the SFB - C03 project. Thanks for the many meetings and journal clubs in which you patiently answered questions, always able to take the discussion one step further with your deep expertise.

...all *Li-Cs lab members*, because the maintenance and upgrading of such a complex experimental machine is the fruit of a joint effort. I thank my old fellow mates *Manuel Gerken* and *Binh Tran*. We enjoyed lots of discussions and pleasant moments, inside and outside the lab, that I will always remember with a smile. It was equally a pleasure to work with the new fellow mates *Michael Rautenberg* and *Tobias Krom*. I'm very grateful for your important contribution in translating many old Mathematica scripts into Python and creating new ones that made daily lab analysis much easier! Thanks a lot to all (four) for the hard work that you invested into the experiment and for the infinite time we spent together in trying to come up with new ideas and solutions to the challenges of the daily lab life. I wish you all good luck!

...all the students who choose our lab for their Master's and/or Bachelor's theses during these years, who all did a great job: *Kilian Welz*, *Robert Freund*, *Michael Rautenberg*, *Lauritz Klaus*, *Jonas Matthies*, *Markus Neiczer*, *Ron von Oppen*, *Adrian Schuerg*, *Felix Brochers*, *Marcia Kroker*. A special mention of those students for whom I have taken direct responsibility, *Robert Freund* and *Kilian Welz*: it was a pleasure to work with you guys and a fun opportunity to learn by teaching.

...the other SFB - C03 collaborators: *Dr. Moritz Drescher*, for his excellent cooperation both on the Bose- as well as on the Fermi-polaron project, and *Prof. Manfred Salmhofer*.

...*Dr. Bing Zhu*, because it was of great support to have you as postdoc in our group in the first few months of my PhD.

...the whole *Quantum Dynamics group*, including all Rydbergs, Haitraps and Digital-Twins members. I am grateful to all of them for always being so friendly, kind and helpful. A special mention to *Dr. Gerhard Zuern* for all the advice he gave me on which I could rely on as well as for helping with any kind of technical problems we had in the lab - which were uncountable! - while maintaining always patience and enthusiasm. I am also so grateful to have had *Saba Zia Hassan* sharing a lot of experiences from the very beginning of our interview at the IMPRS-QD. Your company was always relaxing and encouraging!

...the whole *Ultracold group* and to *Prof. Selim Jochim* for sharing all their impressive experimental know-how on Li-Fermi gases, radiofrequency spectroscopy, imaging techniques and many others. Thanks also for the fun chats during lunch breaks. A special mention to *Keerthan Subramanian* for taking the time on many occasions to explain us things in a very clear and pedagogical way and also for the interesting conversations beyond physics.

...the *Quantum Fluids*, *QUO* and *SynQS* groups for sharing knowledge and useful lab materials. In particular to to *Dr. Bing Yang* for his impressive enthusiasm and effort for fulfilling every scientific question we posed him and to *Dr. Helmut Strobel* for the great help on Ti:Sa cavity alignment and the exchanges with the Li-K group.

...*Prof. Nicolò Defenu* for sharing inspiring ideas on strongly interacting Fermi gases and on the Kibble-Zureck mechanism, and for the enlightening discussions about the scientific academic world.

...*Prof. Richard Schimdt*, *Arthur Christianen*, *Oriana Diessel* for their inspiration and support in developing the potential project on dressed dimers.

...the *Collaborative Research Center - IsoQuant*, for financial support and for the opportunity to be member of both the organizing committee of an international conference, QSEC 2022, as well as of the Jury for a SciArt 2021 residency. It was very instructive for me to gain insight into how selection processes work and to be part of the decision-making process. It was also a pleasure to represent the young researchers of IsoQuant together with *Robert Ott* and *Bruno Faigle-Cedzich* and to have the freedom for the organization of seminars as well as for the annual retreat. A special thanks goes to *Mrs. Tina Kuka* for the great help and support she gave us. Thank also to *Lisa Ringena* for finding the time to give to a bunch of italian high school guys a hands-on look at laser optics experiments. It was a lot of fun to join you in this activity and I would love to do something similar with you again!

...the mechanical and electronic workshops of the Institute for their assistance in extending and improving the experiment. Moreover, a special thanks to *Ralf Ziegler* and *Dominic Litsch* for their help while I was setting up the new didactic FP-MOT lab.

...*Dr. Philipp Preiss* for the remarkable initiative and guidance of the project on emergency mecahinical ventilators during the COVID-19 pandemic. I was really proud to get involved and contribute to something that could have made a real difference in that emergency situation.

...the group of secretaries and aministratives of the Physikalisches Institute, because without them any matter or problem would have been much more difficult to handle. Special thanks to *Mrs. Claudia Kramer* and *Mrs. Alexandra Holten*.

...the *Heidelberg Graduate School For Physics* and the *International Max Planck Research School for Quantum Dynamics* enabling conference trips and winter schools, as well as excellent seminars, symposia and graduate courses. A special thanks to *Mrs. Gesine Heiselmann* and *Mrs. Sibel Babacan* for their help in dealing with the bureaucracy.

...*mia mamma* e *mio babbo* per essermi sempre stati vicini e per farmi sentire il loro enorme amore in ogni momento, sia da vicino che da lontano. Grazie anche a mio fratello *Edoardo* per esserci sempre nei momenti più importanti.

...*Lorenzo*, per farmi sorridere ogni mattina quando mi sveglio, per avermi motivata ad arrivare in fondo a questo percorso e per rendere ogni giornata insieme un capolavoro!

...all the people who took the time to proofread this thesis, or help in any other way: *Michael Rautenberg*, *Lorenzo Tesi*, *Moritz Drescher*, *Tobias Krom* and *Matthias Weidemüller*.